UNIVERSITY OF OKLAHOMA

GRADUATE COLLEGE

SEARCHES FOR A HIGH-MASS HIGGS-LIKE DIBOSON RESONANCE IN THE $H \to WW \to \ell\nu qq$ DECAY CHANNEL USING pp COLLISIONS AT BOTH $\sqrt{s} = 8$ AND 13 TeV WITH THE ATLAS DETECTOR AT THE LHC

A DISSERTATION

SUBMITTED TO THE GRADUATE FACULTY

in partial fulfillment of the requirements for the

Degree of

DOCTOR OF PHILOSOPHY

By

BENJAMIN L. PEARSON
Norman, Oklahoma
2016

SEARCHES FOR A HIGH-MASS HIGGS-LIKE DIBOSON RESONANCE IN THE $H \to WW \to \ell\nu qq$ DECAY CHANNEL USING pp COLLISIONS AT BOTH $\sqrt{s} = 8$ AND 13 TeV WITH THE ATLAS DETECTOR AT THE LHC

A DISSERTATION APPROVED FOR THE
HOMER L. DODGE DEPARTMENT OF PHYSICS AND ASTRONOMY

BY

Dr. Michael Strauss, Chair

Dr. Braden Abbott

Dr. Chung Kao

Dr. Deborah Watson

Dr. Jeffrey Harwell

To my past, present, and future family.

"You're braver than you believe, and stronger than you seem, and smarter than you think."

- A.A. Milne, Christopher Robin

Acknowledgements

I would like to deeply thank all of my teachers and professors over the 20 years of my academic journey, for instilling in me a deep, unquenchable desire to learn.

"If you don't know, the thing to do is not to get scared, but to learn."

- Ayn Rand, Atlas Shrugged

I would also like to thank all of my family and friends who have helped motivate and encourage me in my pursuit of this degree.

"It's the job that's never started as takes longest to finish."

- J.R.R. Tolkien, The Lord of the Rings

Lastly, I would like to thank my wife for not only supporting me through the entire process, but actually pushing me to be the best me I could be. Thank you for living this adventure with me!

"I am a wife-made man."

- Danny Kaye

"I knew when I met you an adventure was going to happen."

- A.A. Milne, Winnie the Pooh

Table of Contents

List of Tables

List of Figures

Abstract

This work presents two searches for a high-mass Higgs boson in the $H \to WW \to \ell\nu qq$ decay channel using the ATLAS detector to analyze the high-energy proton-proton collisions provided by the Large Hadron Collider at two different center-of-mass energies, $\sqrt{s} = 8\,\text{TeV}$ in 2012 and $\sqrt{s} = 13\,\text{TeV}$ in 2015, corresponding to two independent datasets with sizes given by their integrated luminosities of 20.3 fb^{-1} and 3.2 fb^{-1}, respectively.

No significant excess of data above the expected background is observed in either analysis, so upper limits are set on the production cross-section times branching ratio, as a function of the hypothesized boson mass, for the various signal models tested. The derived limits substantially improve upon previous results.

Chapter 1

Introduction

> *"There is nothing like looking, if you want to find something. You certainly usually find something, if you look, but it is not always quite the something you were after."*
>
> - J.R.R. Tolkien, The Hobbit

It has been a driving question throughout the history of science: What are the fundamental constituents of matter and how do they interact with one another? Particle physics addresses this question directly. The contributions of many physicists over the decades, has culminated in an impressively descriptive and predictive theory of the fundamental constituents of matter and their interactions, referred to as the Standard Model.

The recent discovery of the Higgs boson, as predicted by the Standard Model, is a pinnacle moment in the validation of the particle physics theory. However, there are still many compelling reasons to search for physics beyond the Standard Model, particularly for additional higher mass scalar (Higgs-like) bosons.

This dissertation outlines these motivations in Chapter 2, after a description of the Standard Model. The ATLAS detector and Large Hadron Collider, used to search for the Higgs bosons, are described in Chapter 3, preceding the description of two searches at different center-of-mass collision energies $\sqrt{s} = 8\,\text{TeV}$ and $13\,\text{TeV}$ in Chapters 4 and 5, respectively. Both are searches for a high-mass Higgs boson in the

decay channel $H \to WW \to \ell\nu qq'$ (qq' referred to hereafter as simply qq). Finally, Chapter 6 discusses the conclusions from both analyses, which offer substantial improvements over the results of previous searches.

Chapter 2

The Standard Model and the Higgs Sector

The first section of this chapter gives a brief summary of the Standard Model of particle physics; a more complete and detailed description of the Standard Model can be found in [13]. This leads directly into the second section that describes the Higgs boson's role in electroweak symmetry breaking, as well as its production and detection at the Large Hadron Collider (LHC). The final section highlights some of the limitations of the Standard Model and outlines how these motivate searches for physics beyond the Standard Model, specifically an extended Higgs sector as presented in this work.

2.1 The Standard Model of Particle Physics

The Standard Model of particle physics (SM) [14, 15, 16] is a mathematical-based theory that describes the fundamental constituents of matter in the known universe and their interactions with each other, offering the best description of the subatomic world to date. It began over half a century ago and has developed through the collaborative effort of many theorists and experimentalists, making precise descriptions and predictions of particle physics validated and/or motivated by experiments, currently culminating in the recent discovery of the Higgs boson (discussed further in the next section).

In the SM, matter is made up of 12 spin-$\frac{1}{2}$ fermions divided into six quarks (up u,

down d, charm c, strange s, top t, and bottom b) and six leptons (electron e^-, muon μ^-, tau τ^-, and neutrinos: ν_e, ν_μ, ν_τ), each with a corresponding anti-particle of opposite electric charge (e.g. $\bar{s}$ and μ^+). The theory also includes three fundamental interactions (i.e. forces) between the fermions that are mediated by 12 spin-1 bosons: electromagnetic interactions by the massless photon (γ), weak interactions by the massive $W^\pm$ and Z^0 bosons, and strong interactions by eight massless gluons (g). Gravity is not included in the SM, but its contributions are negligible at the scales of particle physics. Lastly, the particle content of the SM is complete with the spin-0 Higgs boson, whose field enables particles to acquire masses in the theory.

The SM particles and their interactions are summarized in Figures 2.1a and 2.1b, respectively. Each particle is listed with its mass, electric charge, and spin, along with its most commonly used symbol and name. The columns of the quarks and leptons correspond to their generations (or families): 1^{st}, 2^{nd}, and 3^{rd} from left to right. The possible interactions between the particles are depicted by the lines connecting them, where each interaction line is attached to its corresponding mediating boson.

Combining special relativity and quantum mechanics, the SM is a quantum field theory (QFT) [17] that stems from quantizing the fields in the Dirac equation and considering elementary particles as the quanta of fields, e.g. fermion (or matter) fields commonly represented by Ψ with corresponding anti-particle fields $\overline{\Psi} = \Psi^\dagger\gamma^\circ$ (where $\dagger$ denotes the hermitian adjoint and γ° is the zeroth Dirac gamma matrix). The model culminates in a mathematical structure of these fields based on group theory

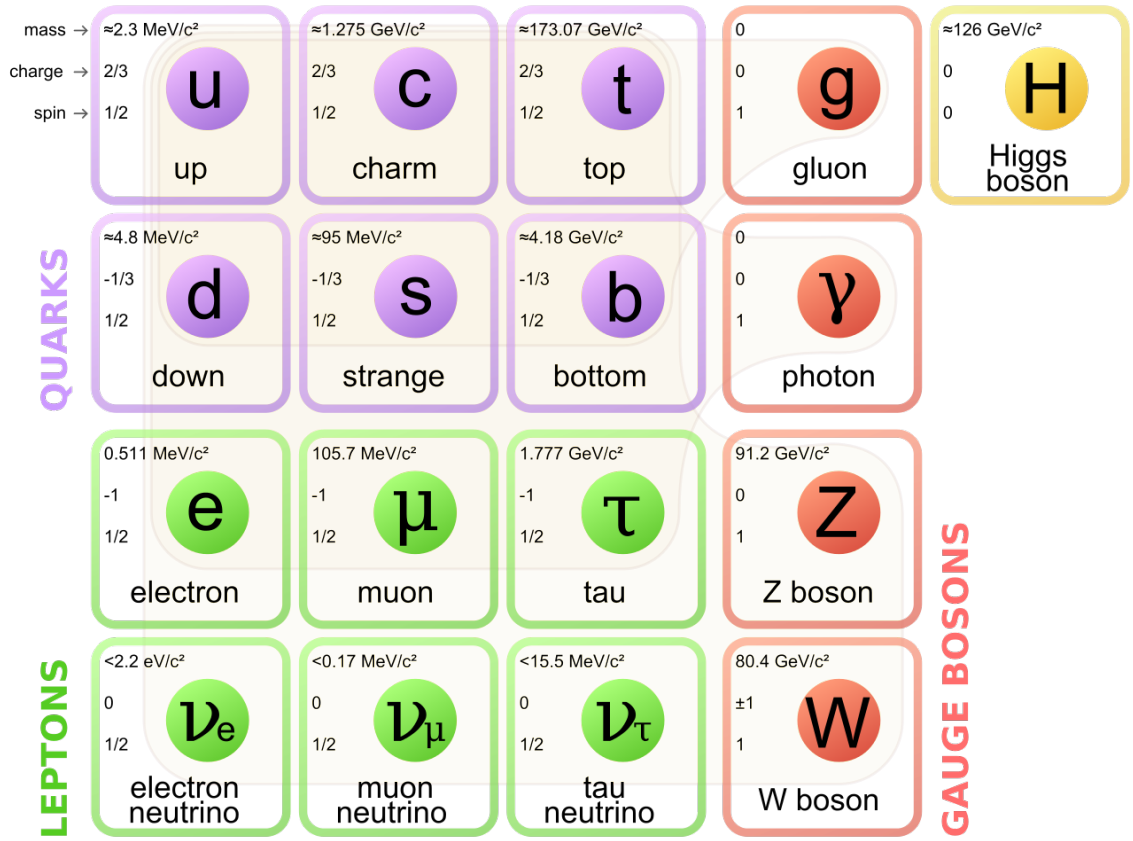

(a)

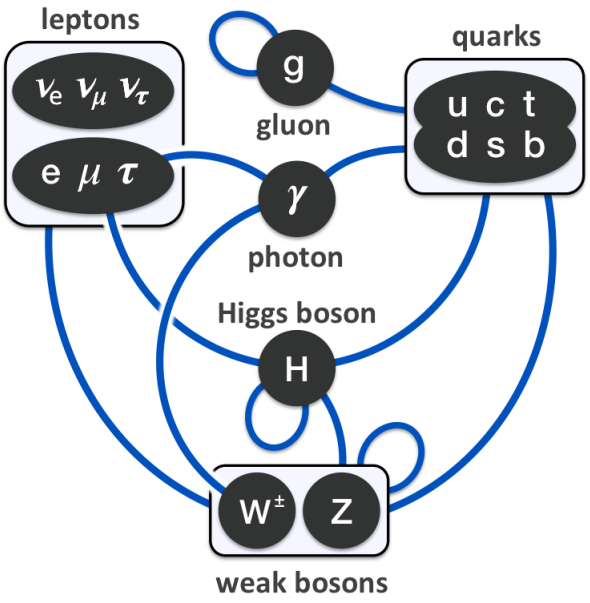

(b)

Figure 2.1: The particle content (a) and interactions (b) in the Standard Model (assuming massless neutrinos for the interactions). Taken from [1] and [2], respectively.

symmetries and local gauge invariance of the gauge group $\mathrm{SU}(3)_C \times \mathrm{SU}(2)_L \times \mathrm{U}(1)_Y$. The mathematical structure takes the form of a Lagrangian, L, that contains the products and derivatives of the quantized fields, describes the dynamics of the system through the Euler-Lagrange equations of motion, and is required to be renormalizable and invariant under the SM gauge group transformations. The invariance requirement necessitates the introduction of "gauge fields," whose interaction terms describe the strong and electroweak forces.

The gauge fields introduced due to invariance under the $\mathrm{SU}(3)_C$ gauge group ("C" for color, the charge of the strong force) are the eight gluon fields G^i_μ, $i = 1, \ldots, 8$. This part of the SM gauge theory is known as quantum chromodynamics (QCD) and describes the strong interactions between quarks and gluons. The quarks have color charge and couple to the gluon fields as triplets, while all other particles are colorless, i.e. $\mathrm{SU}(3)_C$ singlets, and therefore do not directly couple to gluons (i.e. experience the strong force). The QCD interactions are described by the Lagrangian (only including gauge and matter/kinetic terms):

$$L_{\mathrm{SU}(3)_C} = -\frac{1}{4} G^i_{\mu\nu} G^{\mu\nu i} + \sum_\alpha \overline{\Psi}^{(\alpha)}_a i \not{D}_{ab} \Psi^{(\alpha)}_b \quad , \tag{2.1}$$

where $\Psi^{(\alpha)}_a$ represents a quark field with flavor index $\alpha = u, d, s, \ldots$ and color index $a = 1, 2, 3$, and where there is an implicit sum over repeated color indices. Also in Equation 2.1, $G^i_{\mu\nu}$ is the field strength tensor for the i^{th} gluon field

$$G^i_{\mu\nu} = \partial_\mu G^i_\nu - \partial_\nu G^i_\mu - g_3 f^{ijk} G^j_\mu G^k_\nu \quad , \tag{2.2}$$

and $\not{D}_{ab} = \gamma^\mu D_{\mu ab}$ is the $\mathrm{SU}(3)_C$ covariant derivative, where

$$D_{\mu ab} = \partial_\mu \delta_{ab} + i g_3 \frac{\lambda^i_{ab}}{2} G^i_\mu \quad . \tag{2.3}$$

In Equations 2.2 and 2.3, g_3 is the SU(3) gauge coupling constant and λ^i are the eight SU(3) group generators, in the form of triplet representation matrices, whose commutation relations define the structure constants f^{ijk}: $[\lambda^i, \lambda^j] = 2i f^{ijk} \lambda^k$.

The gauge fields introduced due to invariance under the $\mathrm{SU}(2)_L$ gauge group ("L" for left-handed) are the three weak-isospin fields W^i_μ, $i = 1, 2, 3$. Left-handed components of fermion fields, $\Psi_L \equiv \frac{1}{2}(1 - \gamma_5)\Psi$, couple directly to these weak-isospin gauge fields as doublets, while right-handed components, $\Psi_R \equiv \frac{1}{2}(1 + \gamma_5)\Psi$, have zero weak-isospin as SU(2) singlets. In contrast, all fermions have a non-zero weak hypercharge, Y, in their coupling to the B_μ gauge field introduced due to invariance under the $\mathrm{U}(1)_Y$ gauge group ("Y" to distinguish it from the $\mathrm{U}(1)_Q$ gauge of quantum electrodynamics, QED, where Q is the electric charge operator $Q = \frac{1}{2}(\sigma^3 + Y)$, and $\frac{1}{2}\sigma^3$ is the third weak isospin generator [see below]).

The combined $\mathrm{SU}(2)_L \times \mathrm{U}(1)_Y$ local gauge group unifies the weak and electromagnetic interactions. Similar to QCD, the Lagrangian describing the interactions in this group contains gauge terms given by

$$L_{\text{gauge}} = -\frac{1}{4} W^i_{\mu\nu} W^{\mu\nu i} - \frac{1}{4} B_{\mu\nu} B^{\mu\nu} \quad , \tag{2.4}$$

where $i = 1, 2, 3$ and the field strength tensors $W^i_{\mu\nu}$ and $B_{\mu\nu}$ are given by

$$W^i_{\mu\nu} = \partial_\mu W^i_\nu - \partial_\nu W^i_\mu - g_2 \epsilon^{ijk} W^j_\mu W^k_\nu \tag{2.5}$$

and

$$B_{\mu\nu} = \partial_\mu B_\nu - \partial_\nu B_\mu \quad . \tag{2.6}$$

Here g_2 is the SU(2) gauge coupling constant and ϵ^{ijk} is the antisymmetric Levi-Civita symbol. Also, the Lagrangian includes a kinetic/fermion term in the form of $\overline{\Psi} i\gamma^\mu D_\mu \Psi$, with the $\mathrm{SU}(2)_L \times \mathrm{U}(1)_Y$ covariant derivative D_μ given by

$$D_\mu = \partial_\mu + ig_2 \frac{\sigma^i}{2} W_\mu^i + ig_1 \frac{Y}{2} B_\mu \quad , \tag{2.7}$$

where g_1 is the U(1) gauge coupling constant and σ^i are the three Pauli matrices that form the SU(2) group generators.

Unlike the gluon fields in QCD, the $\mathrm{SU}(2)_L \times \mathrm{U}(1)_Y$ gauge fields do not correspond directly to the physical gauge bosons observed in nature, but rather must be mixed to form combined fields that do:

Combined Field			Quanta	Interaction
$W_\mu^\pm$	$=$	$\frac{1}{\sqrt{2}}(W_\mu^1 \mp iW_\mu^2)$	$W^\pm$ bosons	Weak charged current
Z_μ	$=$	$\cos\theta_W W_\mu^3 - \sin\theta_W B_\mu$	Z^0 boson	Weak neutral current
A_μ	$=$	$\sin\theta_W W_\mu^3 + \cos\theta_W B_\mu$	γ photon	Electromagnetic (QED),

(2.8)

where θ_W is the weak mixing angle related to the gauge coupling constants by

$$\sin\theta_W = \frac{g_1}{\sqrt{g_1^2 + g_2^2}} \qquad \text{and} \qquad \cos\theta_W = \frac{g_2}{\sqrt{g_1^2 + g_2^2}} \quad . \tag{2.9}$$

Experimentally, the $W^\pm$ and Z^0 bosons are shown to be massive, but adding a mass term for them in the Lagrangian is forbidden as it would break the local $\mathrm{SU}(2)_L \times \mathrm{U}(1)_Y$ gauge symmetry. In fact, the same holds true for introducing explicit fermion mass terms. This is clearly a problem.

The SM solution to this problem is the Higgs mechanism [18, 19, 20], which is responsible for the electroweak gauge field mixing and generates the fermion and boson masses, all through its spontaneous symmetry breaking of $\mathrm{SU}(2)_L \times \mathrm{U}(1)_Y$.

2.2 The Standard Model Higgs boson

2.2.1 Spontaneous Electroweak Symmetry Breaking

The basic idea behind spontaneous symmetry breaking is that the ground (vacuum) state does not share the gauge symmetry of the underlying theory. In the case of spontaneous electroweak symmetry breaking (EWSB), the vacuum state should break the $\mathrm{SU}(2)_L \times \mathrm{U}(1)_Y$ symmetry in such a way as to provide a massless photon and massive $W^{\pm}$ and Z^0 bosons. This is possible with the right choice of parameters in the setup.

Maintaining the $\mathrm{SU}(2)_L \times \mathrm{U}(1)_Y$ symmetry of the Lagrangian, a scalar field can be added to the Lagrangian in the form of a complex $\mathrm{SU}(2)_L$ doublet (adding four degrees of freedom)

$$\Phi = \begin{pmatrix} \phi^+ \\ \phi^0 \end{pmatrix} = \frac{1}{\sqrt{2}} \begin{pmatrix} \phi_1 + i\phi_2 \\ \phi_3 + i\phi_4 \end{pmatrix} \tag{2.10}$$

with weak isospin $\frac{1}{2}$ and hypercharge $Y = 1$. The scalar part of the Lagrangian takes the form

$$L_\Phi = (D_\mu \Phi)^\dagger (D^\mu \Phi) - V(\Phi) \tag{2.11}$$

including a covariant derivative term (with D_μ as defined in Equation 2.7) and, vital for spontaneous symmetry breaking, a potential term $V(\Phi)$. The most general

renormalizable form of the scalar potential is given by

$$V(\Phi) = \mu^2 \Phi^\dagger \Phi + \lambda (\Phi^\dagger \Phi)^2, \tag{2.12}$$

where μ relates to the Higgs mass and λ is the quartic Higgs coupling. In order to obtain a stable vacuum $\lambda > 0$, and in order for spontaneous symmetry breaking to occur $\mu^2 < 0$. With these two requirements, there are an infinite number of solutions to the minimum of the potential (vacua) that satisfy

$$\sqrt{\sum_i (\langle 0|\phi_i|0\rangle)^2} = \sqrt{\frac{-\mu^2}{\lambda}} \equiv v, \tag{2.13}$$

where $\langle 0|\phi_i|0\rangle$ represents the vacuum expectation value (VEV) of the i^{th} field in Φ from Equation 2.10. Choosing a single vacuum from the continuum breaks the symmetry, and the choice to take $\langle 0|\phi_3|0\rangle = v$ as the only non-vanishing VEV leads to the desired particle content in the theory.

The quantum theory resulting from this choice of vacuum is obtained by considering perturbations around the minimum by defining a shifted field h (the Higgs field) with a vanishing VEV: $h = \phi_3 - v$. Of course there are also perturbations around the minimum in the other three dimensions, corresponding to shifted fields $\phi_i \to \xi_i$ $(i = 1, 2, 4)$. However, these fields can be absorbed through local gauge transformations of the gauge bosons into the unitary gauge, where the fields' aggregate three degrees of freedom are transferred to the vector gauge bosons ($W^\pm$ and Z^0), giving them each an additional degree of freedom, their mass. Note that the last degree of freedom from the originally introduced complex doublet takes the form of the new scalar particle, the physical Higgs boson. Thus, in the unitary gauge following

spontaneous symmetry breaking, Φ is simply given by

$$\Phi = \frac{1}{\sqrt{2}}\begin{pmatrix} 0 \\ v+h \end{pmatrix}, \tag{2.14}$$

which can be shown to break all of the individual $\mathrm{SU}(2)_L \times \mathrm{U}(1)_Y$ generators (i.e. $\sigma^i\Phi \neq 0$ and $Y\Phi \neq 0$). However, the $\mathrm{U}(1)_Q$ generator, Q, does not break because Φ carries no electric charge: $Q\Phi = \frac{1}{2}(\sigma^3 + Y)\Phi = 0$. Thus, the SM gauge symmetry is spontaneously broken from $\mathrm{SU}(3)_C \times \mathrm{SU}(2)_L \times \mathrm{U}(1)_Y \to \mathrm{SU}(3)_C \times \mathrm{U}(1)_Q$.

Plugging Equation 2.14 into the $(D_\mu\Phi)^\dagger(D^\mu\Phi)$ term of the scalar Lagrangian leads to mass terms for the gauge bosons found in terms $\propto v^2$. The masses of the physical gauge bosons are found to be:

$$m_{W^+} = m_{W^-} = \frac{1}{2}vg_2, \quad m_{Z^0} = \frac{1}{2}v\sqrt{g_1^2 + g_2^2}, \quad \text{and} \quad m_\gamma = 0. \tag{2.15}$$

The photon remains massless, which should be expected since the $\mathrm{U}(1)_Q$ gauge is unbroken. In similar fashion, the gluons remain massless with their gauge symmetry also intact. The covariant derivative term of the scalar Lagrangian also contains interaction terms between the Higgs boson and the gauge bosons found in terms $\propto vh$ (single Higgs couplings) and $\propto h^2$ (di-Higgs couplings). As the Higgs is both electric-charge-neutral and a singlet under $\mathrm{SU}(3)_C$, it does not couple at tree level to the massless photons or gluons. The most relevant of these couplings for this analysis is the single Higgs coupling to a pair of W bosons:

$$g_{HWW} = \frac{2m_W^2}{v} = \frac{1}{2}vg_2^2. \tag{2.16}$$

The potential term, $V(\Phi)$, of the scalar Lagrangian, following spontaneous symmetry breaking, contains the Higgs self-interactions and the mass term for the

Higgs boson, given by $m_h = \sqrt{2\lambda v^2}$. Although v can be calculated ($\approx 246\,\text{GeV}$) from its relation to the Fermi coupling G_F, λ is a free parameter which means that the mass of the Higgs boson is not explicitly predicted by the SM. Thus, searches for the Higgs boson covered a large range of masses.

Lastly, the introduced Higgs doublet also comes to the rescue of the fermions, whose explicit mass terms ($\propto \overline{\Psi}_L \Psi_R$) are not invariant under $\text{SU}(2)_L \times \text{U}(1)_Y$, and are therefore forbidden. The Higgs doublet can be used to create invariant singlet terms in the form $-\lambda_f \overline{\Psi}_L \Phi \Psi_R$, where λ_f is the Yukawa coupling of the f^{th} fermion. In the case that Φ has a non-zero VEV (as in spontaneous EWSB), these terms not only describe the interaction between the Higgs field and the fermions, but also provide mass terms for the fermions. The Higgs couplings to the fermions are related to the mass of the fermions by

$$g_{Hf\bar{f}} = \frac{\lambda_f}{\sqrt{2}} = \frac{m_f}{v}, \tag{2.17}$$

which is generally very small, except for the heaviest quarks.

It should be noted that although the Higgs mechanism provides the mass terms for particles in the SM Lagrangian, it does not predict what the masses are, they remain free parameters in the model like the Higgs mass itself. Also, with the large number of Higgs couplings to both fermions and massive bosons, there are many possible production and decay modes for the SM Higgs boson.

2.2.2 Production and Detection at the LHC

The production cross-sections (σ) and decay branching ratios (BR) of the SM Higgs boson are all calculable for a given Higgs mass (m_H) and are shown in Figure 2.2 for the LHC with pp collisions at $\sqrt{s} = 8\,\text{TeV}$, along with the Higgs decay cross-sections times BR for several decay channels. At the LHC (in the mass range plotted), the dominant Higgs production mode is gluon-gluon fusion (ggF: $pp \to H$ in the figure), followed by vector boson fusion (VBF: $pp \to qqH$ in the figure). Feynman diagrams for both of these processes are shown in Figure 2.3, where the necessary fermion loop in ggF production is dominated by contributions from the top quark.

As for the decay modes, since the Higgs couplings are proportional to the mass of the decay products, the largest branching ratio tends to correspond to the heaviest kinematically accessible final state for a given Higgs mass. Thus, $H \to bb$ dominates the BR at low mass and $H \to WW$ dominates at high mass (with ZZ being suppressed by the presence of identical particles in its final state). The analyses in this work are partly motivated by the large $H \to WW$ BR, and utilize both the ggF and VBF Higgs production modes.

Although a large cross-section and BR are helpful to produce more events, they do not tell the whole story of a decay channel's potential for discovery. The purity of the signal, i.e. how well the signal can be distinguished from backgrounds, also plays an important role. This is clearly evidenced by the fact that $H \to \gamma\gamma$ and $H \to ZZ \to \ell^+\ell^-\ell^+\ell^-$ (two very clean signals) were the primary discovery channels of the new boson, with mass $\sim 125\,\text{GeV}$, observed in 2012 by both the

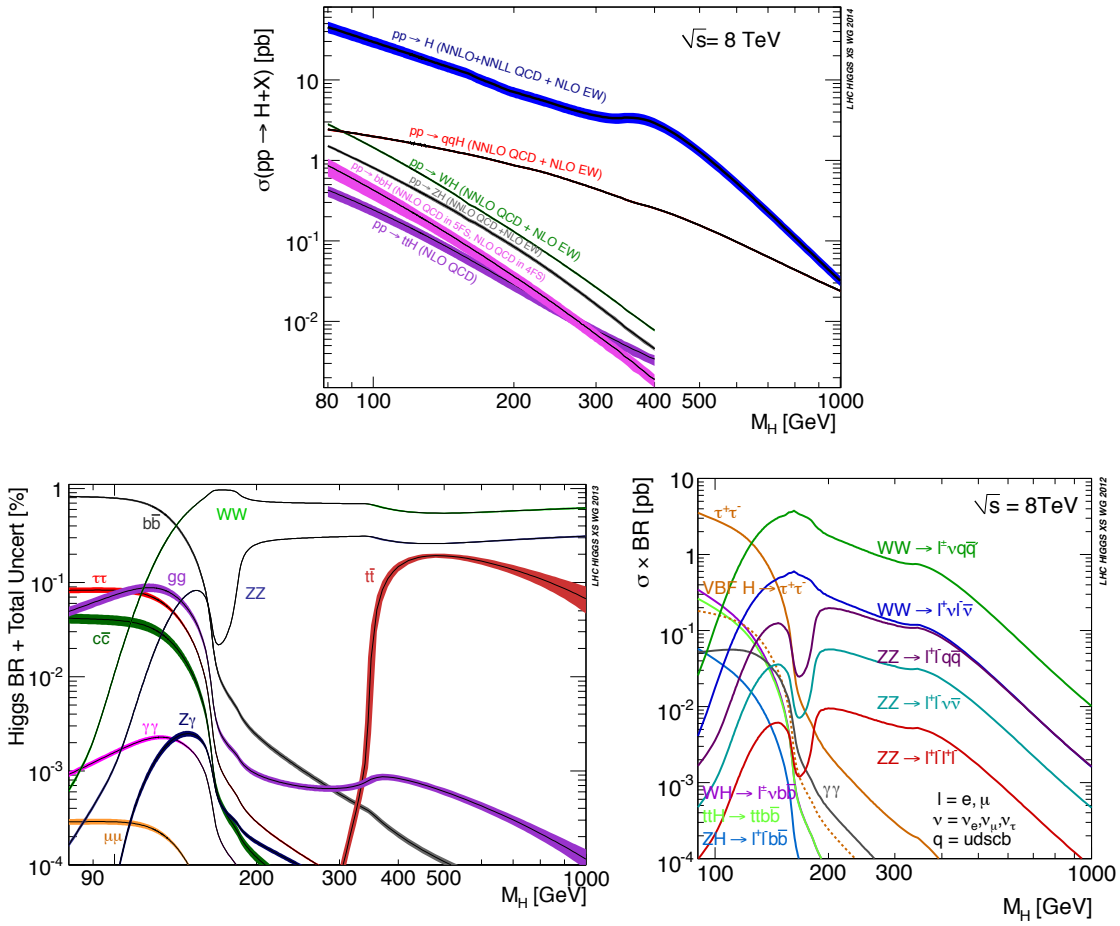

Figure 2.2: LHC Standard Model Higgs production cross-sections (top), decay branching ratios (bottom left), and decay cross-sections times branching ratios (bottom right) as a function of the Higgs mass, m_H, all at $\sqrt{s} = 8\,\text{TeV}$ [3].

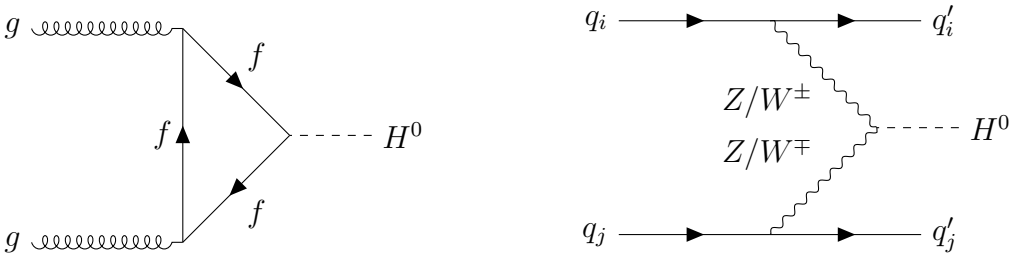

(a) ggF **(b)** VBF

Figure 2.3: Feynman diagrams of the two Higgs production mechanisms searched for in this work (and dominant at the LHC): gluon-gluon fusion (a) and vector boson fusion (b).

ATLAS [21] and CMS [22] collaborations at the LHC. Subsequent measurements of the new particle's properties have shown consistency with those predicted for the SM Higgs boson [23, 24]. The discovery of this keystone particle demonstrates a great accomplishment of the Standard Model, and led to the awarding of the 2013 Noble prize for its theoretical postulation nearly 50 years prior.

2.3 Beyond the Standard Model: Extended Higgs Sector

Although the SM has withstood an astounding range of precision tests over its lifetime and demonstrated great predictive power in physics at energies spanning several orders of magnitude, it is still incomplete. Most obviously, the SM does not include gravity, as there has yet to be a renormalizable theory of quantum gravity. Other missing pieces include: neutrino masses, evidenced by the discoveries of neutrino flavor oscillations; a source or description of dark matter and dark energy, evidenced by astrophysical measurements as together making up more than 95% of the energy density in the universe today; and a mechanism to explain the apparent large level of matter-antimatter asymmetry found in the universe today, assuming the universe began in a symmetric matter-antimatter state. All of these and more, including theoretical arguments, serve as strong motivations to search for physics *beyond* the Standard Model (BSM).

Specifically in regards to the Higgs mechanism, current measurements (and lack thereof) leave room for BSM interpretations that the observed Higgs boson is only a part of an extended Higgs sector. This was especially the case at the time of the

8 TeV analysis ($\sim$ 2013), where the analysis motivation was partly to continue the SM-like Higgs boson search over the full explorable mass range at the LHC without being biased by the nature of the recently discovered 125 GeV resonance, and partly to include a more model-independent result as a springboard for future BSM searches, such as the 13 TeV search also presented in this work.

Some of the extended Higgs sectors are partly motivated by the open question of whether or not the observed Higgs boson at 125 GeV is the only contributor to the cancellation of the divergent W/Z scattering terms, necessary to preserve unitarity. Two motivating examples of BSM extensions to the Higgs sector, that are both compatible with current results and predict the existence of an additional neutral Higgs-like resonance in the high-mass regime, are electroweak singlet (EWS) models [25, 26, 27] and Two Higgs Doublet Models (2HDM's) [28, 3].

2.3.1 Electroweak Singlet Models

One of the simplest extensions of the SM Higgs sector is the addition of a real electroweak singlet field to the original complex Higgs doublet. The two fields mix and, following electroweak symmetry breaking, result in two neutral CP-even scalar bosons, h and H. Their masses are assumed to be non-degenerate, with the less massive scalar h corresponding to the observed boson at 125 GeV. Also, each scalar's couplings to fermions and vector bosons are scaled by a common factor with respect to the SM: κ for h and κ' for H, where unitarity requires

$$\kappa^2 + \kappa'^2 = 1. \tag{2.18}$$

The light scalar h retains the branching ratios of the SM Higgs and its cross-section and width are simply those in the SM scaled by κ^2. As for the heavy scalar H, non-SM decay modes (such as $H \to hh$) are possible if they are kinematically allowed, which complicates the scaling of the cross-section and width for H. With respect to the SM Higgs' production cross-section ($\sigma_{H,\mathrm{SM}}$), decay width ($\Gamma_{H,\mathrm{SM}}$), and branching ratios into decay mode i ($\mathrm{BR}_{H,\mathrm{SM},i}$), those for H are scaled as:

$$\begin{aligned} \sigma_H &= \kappa'^2 \times \sigma_{H,\mathrm{SM}} \\ \Gamma_H &= \frac{\kappa'^2}{1 - \mathrm{BR}_{H,\mathrm{new}}} \times \Gamma_{H,\mathrm{SM}} \\ \mathrm{BR}_{H,i} &= (1 - \mathrm{BR}_{H,\mathrm{new}}) \times \mathrm{BR}_{H,\mathrm{SM},i}. \end{aligned} \tag{2.19}$$

where $\mathrm{BR}_{H,\mathrm{new}}$ is the total branching ratio of H into its non-SM modes.

Since measurements of the observed Higgs boson (h in EWS) show good agreement with the SM predictions, κ^2 must be close to one, which implies a small κ'^2. This indicates that the width of the new resonance H should be quite narrow, unless $\mathrm{BR}_{H,\mathrm{new}}$ is close to 1.

2.3.2 Two Higgs Doublet Models

2HDM's (such as appear in supersymmetry) introduce a second electroweak doublet (that also receives a VEV from spontaneous electroweak symmetry breaking) that adds four new degrees of freedom to the system, which translate to a total of five particles in the Higgs sector: h, H, $H^{\pm}$, and A. There are again two neutral CP-even scalar bosons h and H; where, like before, h is less massive and corresponds to the observed 125 GeV boson. Of the remaining particles, $H^{\pm}$ are charged scalars and A

is a neutral CP-odd pseudo-scalar.

There are two additional parameters in 2HDM's in the form of rotation angles α, which diagonalizes the mass-squared matrix of the neutral scalars, and β, which diagonalizes the mass-squared matrices of both the pseudo-scalar and charged bosons. The angle β is often expressed in its relation to the ratio of the VEV's of the two doublets: $\tan\beta = v_2/v_1$. These two angles play a vital role in determining the interactions of the various Higgs fields with both fermions and vector bosons.

Lastly, unlike the ESW models, h's (H's) couplings to the fermions and vector bosons are scaled by two different factors: $\kappa_f^{(\prime)}$ and $\kappa_V^{(\prime)}$, respectively. However, as in the case of EWS, these scaling factors must obey sum rules to maintain unitarity, which in this more general case take the form

$$\kappa_V^2 + \kappa_V'^2 = 1 \quad \text{and} \quad \kappa_V\kappa_f + \kappa_V'\kappa_f' = 1, \tag{2.20}$$

and must hold true for each vector boson (W and Z) and each fermion species.

Although the results presented in this work are never directly interpreted in 2HDM, the models still serve as a source of motivation for the searches, and the narrow width approximation results are meant to be extendible to many models, including 2HDM.

Chapter 3

The ATLAS Detector

ATLAS (A Toroidal LHC ApparatuS) is a nearly hermetic general-purpose particle detector designed to analyze the high-energy particle collisions produced by the Large Hadron Collider (LHC) at the CERN (*Conseil Européen pour la Recherche Nucléaire*) laboratory, located astride the Franco-Swiss border near Geneva, Switzerland. The first section of this chapter highlights some aspects of the LHC most relevant to the subsequent chapters and the rest of this chapter gives an overview of the ATLAS detector. Detailed technical design reports of the LHC and ATLAS can be found in [29] and [6], respectively.

3.1 LHC Overview

The LHC is an enormous circular particle accelerator with a circumference of nearly 26.7 km, capable of accelerating protons to ultra-relativistic speeds and colliding them at unprecedented center-of-mass collision energies: $\sqrt{s} = 8$ TeV in 2012 (Run-I) and $\sqrt{s} = 13$ TeV in 2015-present (Run-II). The LHC does not operate alone in the acceleration of these protons, but is complimented by a whole complex of other accelerators, boosters, and storage rings shown in Figure 3.1. The protons originate from hydrogen atoms stripped of their electrons and are incrementally accelerated up to around 450 GeV for injection into the LHC. They are injected into the two LHC beam pipes in opposite directions, circulating around the LHC in bunches consisting

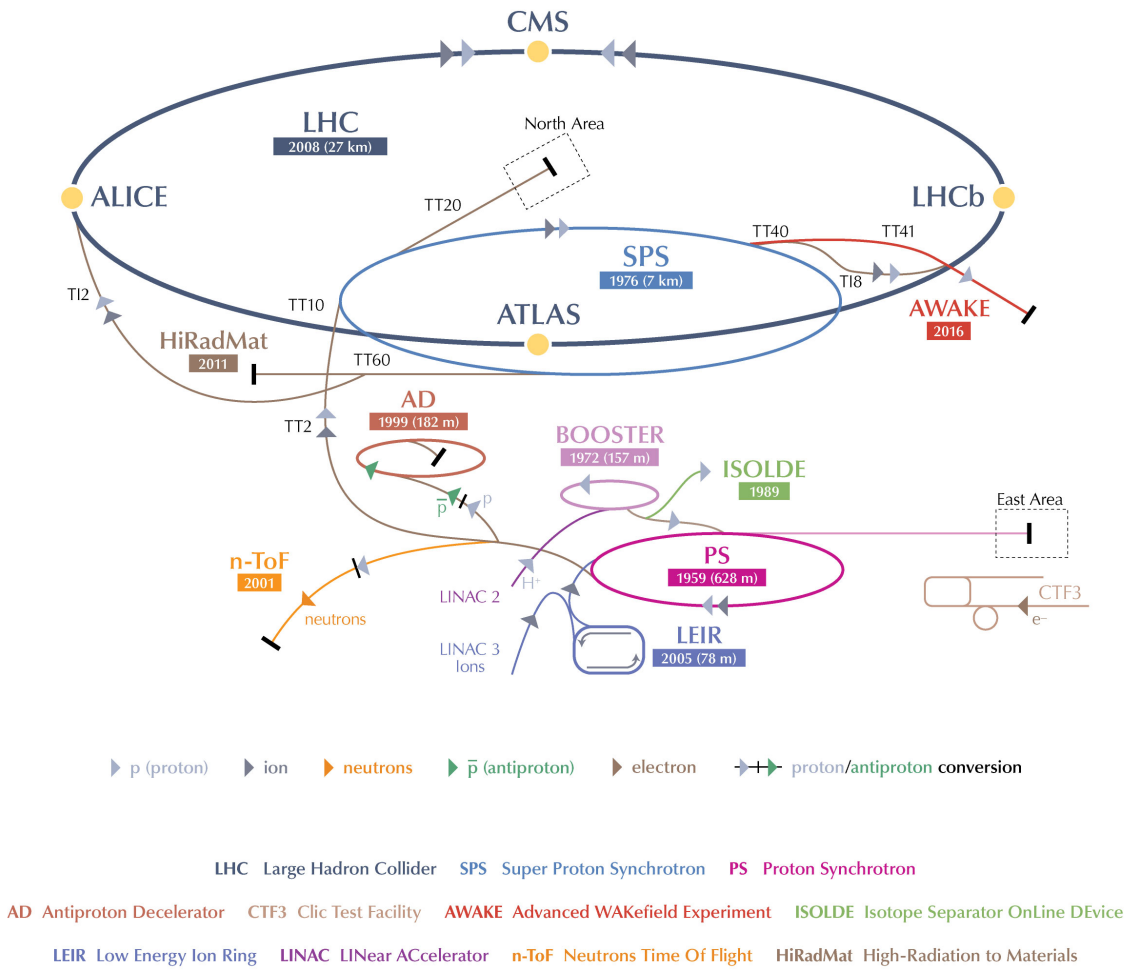

Figure 3.1: CERN's accelerator complex in 2013 [CERN]

of around 10^{11} protons each (at injection). Nominally, each proton beam contains more than 2,000 bunches spaced about 50 ns apart (25 ns in Run-II).

The impressive proton energies reached in the LHC are achieved and maintained (compensating for energy losses) by superconducting electromagnetic resonator cavities, delivering radio-frequency (RF) power to the proton beams and keeping the protons tightly bunched. The maneuvering of these high-energy proton beams

is accomplished using about 9,600 powerful magnets to guide and focus them in the LHC. Large superconducting dipole magnets (1,232 of them), each capable of creating a magnetic field of up to 8.33 T along its entire length, bend the proton beams into their nearly-circular paths and special quadrupole magnets focus/squeeze the beams to the smallest size possible at the interaction points (IP), e.g. ATLAS, in order to maximize the chance of collisions.

The proton-proton collisions actually consist of interactions between the quarks and gluons inside the colliding protons that are each carrying some fraction of the protons' momenta, thus creating a wide variety of high-energy particle interactions. The rate at which a given physics process is produced at the LHC (R_{process}), in number of events per second, is related to the production cross-section of that process (σ_{process}) by a proportionality factor called the instantaneous luminosity ($\mathcal{L}$):

$$R_{\text{process}} = \sigma_{\text{process}} \cdot \mathcal{L} \quad . \tag{3.1}$$

The cross-section represents the probability for the process to occur and the luminosity characterizes the rate of interactions in a given area with units $\text{cm}^{-2}\text{s}^{-1}$. The instantaneous luminosity of the LHC only depends on the beam characteristics and, assuming Gaussian beam distributions, can be expressed as [29]

$$\mathcal{L} = \frac{N_{\text{p}}^2 n_{\text{b}} f_{\text{rev}} \gamma_{\text{r}}}{4\pi \epsilon_{\text{n}} \beta^*} F \quad , \tag{3.2}$$

where N_{p} is the number of protons in each bunch, n_{b} is the number of bunches in each beam, f_{rev} is the beam revolution frequency, γ_{r} is the relativistic Lorentz factor, ϵ_{n} is the normalized transverse beam emittance, β^* is the beta function evaluated at

the IP, and F is the geometric luminosity reduction factor coming from the small crossing angle of the beams at the IP. The denominator in the luminosity expression is related to the transverse area of a bunch.

This is where the LHC excels yet again! Not only does it create proton beams at very high energies, but also high intensities and extremely focussed, striving to maximize the instantaneous luminosity (designed to reach a peak luminosity of 10^{34} $\mathrm{cm}^{-2}\mathrm{s}^{-1}$) in order to maximize the production of rare processes at the interaction points for the detectors, such as ATLAS, to detect and analyze.

3.2 ATLAS Design

ATLAS has the largest volume of any collider-detector ever constructed with its roughly cylindrical shape measuring 44 m long and 25 m in diameter. It weighs in at approximately 7,000 tons and is located nearly 100 m underground where it concentrically surrounds the LHC beam pipe and is nominally forward-backward symmetric, centered length-wise at the nominal IP.

The nominal IP defines the origin of the coordinate system used to describe the detector and the particles traversing it, with the $+z$-axis aligned with the beam axis pointing in the direction of the counter-clockwise rotating beam (viewed from above), the $+x$-axis pointing from the IP toward the center of the LHC ring, and the $+y$-axis pointing upward (slightly off from vertical as the LHC ring has a slight tilt). Due to the detector's cylindrical shape, it can be more convenient to use polar coordinates where the azimuthal angle ϕ is measured around the beam axis from the

$+x$-axis and the polar angle θ is measured from the $+z$-axis.

Since the collisions in the detector take place between partons (gluons and quarks) contained within the protons, with unknown fractions of the incoming protons' momenta, conservation of momentum can only be applied in the plane transverse to the beam (the x-y plane). Thus, it is practical to define transverse variables that refer to projections in the x-y plane, such as the transverse momentum p_{T}. It is also useful to replace the previously defined polar angle θ by a quantity called the pseudorapidity (η), which is the ultra-relativistic approximation of the rapidity (y):

$$y = \frac{1}{2}\ln\left(\frac{E+p_z}{E-p_z}\right) \qquad \xrightarrow{pc \gg mc^2} \qquad \eta = -\ln\left(\tan\frac{\theta}{2}\right) \quad .$$

The pseudorapidity ranges from $-\infty$ (at $\theta = \pi$) to $+\infty$ (at $\theta = 0$), and is 0 at $\theta = \pi/2$ (i.e. the transverse plane). Its usefulness stems from the fact that the center-of-mass frame of the interacting partons in the collision is rarely coincident with the detector rest frame along the beam axis, and unlike θ, the pseudorapidity difference ($\Delta\eta$) between two particles is invariant with respect to Lorentz boosts along the z-axis. Another commonly used parameter with the same invariant property is the separation between particles in $\eta - \phi$ space, ΔR, defined as

$$\Delta R = \sqrt{\Delta\eta^2 + \Delta\phi^2} \quad .$$

ATLAS is considered a "general-purpose" detector because of its wide-reaching physics goals: from the search for the Higgs boson and precision SM measurements, to searches for physics beyond the SM such as supersymmetry, dark matter, extra

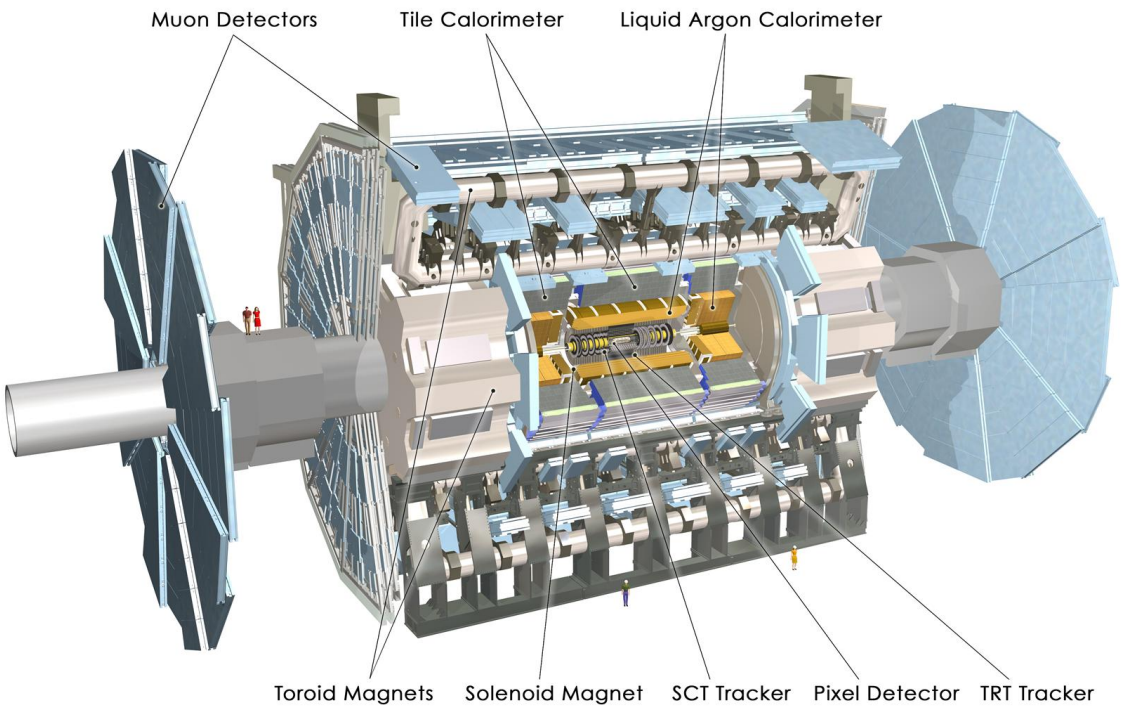

Figure 3.2: A cut-away graphic of the entire ATLAS detector, highlighting each major sub-detector system [4].

dimensions, and even simply unexpected new phenomena at these unexplored collision energies (perhaps the most exiting). In order to meet these ambitious goals and to handle the high luminosity delivered by the LHC, ATLAS was designed to have fast radiation-hard sensors and electronics, nearly hermetic coverage (especially in the direction transverse to the beams), and high detector granularity for excellent particle identification and reconstruction.

As shown in Figure 3.2, ATLAS is composed of many concentric sub-detectors, almost all of which are in a barrel+end-caps configuration. The sub-detectors can be categorized into three main components: an inner detector for distinguishing and measuring the momentum and position of charged particles by precisely tracking their

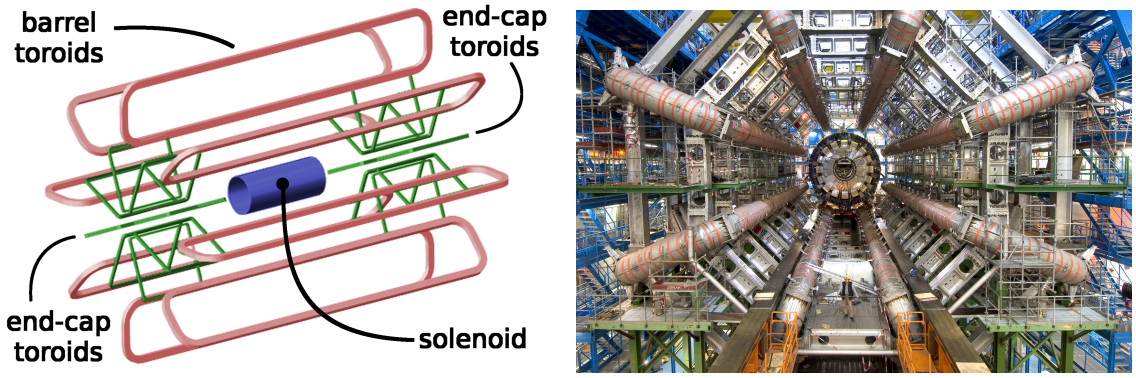

(a) **(b)**

Figure 3.3: (a) The ATLAS magnet system configuration [5]. (b) A photo of the barrel toroid magnets [CERN].

trajectories, calorimeters for measuring particle energies, and a muon spectrometer for identifying and measuring the momentum of muons from their tracks. An overview of each sub-detector category is given in the dedicated sections below, starting with the innermost detector layer and moving radially outward (following the trajectory of a transverse energetic particle created in a collision).

Much of the design of ATLAS was driven by the choice of its magnet system (shown in Figure 3.3a) consisting of an inner barrel superconducting solenoid surrounding the inner detector, and three outer superconducting toroids (one barrel and two end-caps) encasing the calorimeters. Figure 3.3b shows the barrel toroid (likely the most recognizable attribute of ATLAS) during construction and displays the immense size of the magnet system that all-together provides a magnetic field, of at least 50 mT, throughout a volume of approximately 12,000 m^3. These powerful magnets are required in order to bend the trajectories of high-momentum charged particles within the detector to provide for the precise measurement of their momenta and

the identification of their charge.

The solenoid provides a 2 T axial magnetic field for the inner detector and is thin (only $\sim$ 10 cm thick and only contributes $\sim$ 0.66 radiation lengths at normal incidence) in order to minimize the amount of material in front of the barrel calorimeters. The barrel and end-cap toroids are each made up of eight nearly-rectangular coils aligned radially and spaced symmetrically in ϕ about the beam-axis, with both end-cap coil arrangements offset by 22.5° in ϕ from the barrel coil arrangement. Together they provide a toroidal magnetic field for the muon spectrometer of $\sim$ 0.5 T in the barrel region and $\sim$ 1 T in the end-cap regions.

With the magnetic system defined, the various sub-detectors fall into place.

3.3 ATLAS Inner Detector

The Inner Detector (ID) fills the solenoid magnet cavity and closely surrounds the beam pipe. It is made up of three sub-detector systems and is designed to precisely track charged particles in order to provide primary and secondary vertex measurements and excellent momentum resolution. Other important design considerations for the ID include the high-radiation environment, due to its close proximity to the interaction point, as well as the desire to minimize the amount of material in front of the calorimeters for optimal performance. The ID sub-detectors consist of an innermost detector utilizing silicon pixel layers (Pixel), surrounded by a detector of silicon micro-strip layers (or "semiconductor tracker" - SCT), and finally an outermost detector of straw tubes creating a transition radiation tracker (TRT).

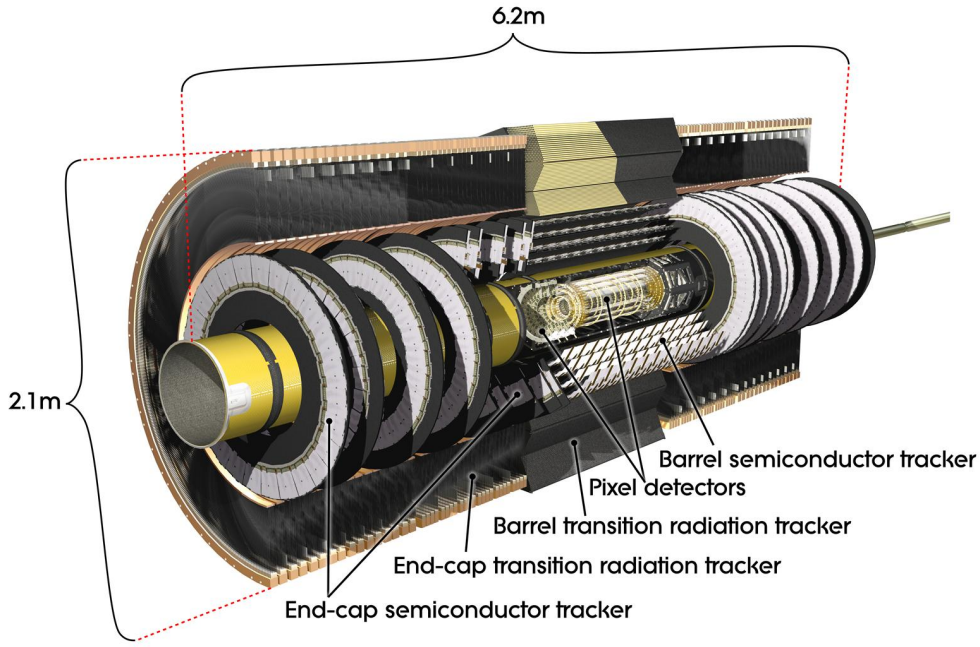

Figure 3.4: A cut-away view of the ATLAS inner detector with both the barrel and end-cap components of its three sub-detectors (Pixel, Semiconductor Tracker, and Transition Radiation Tracker) visible and labelled [6].

These sub-detectors are detailed further in the following sections and are shown in Figure 3.4, with the radial and longitudinal positioning of their barrel and end-cap components shown in Figures 3.5 and 3.6, respectively.

3.3.1 Pixel

The Pixel detector [30] is the closest detector system to the interaction point and therefore subject to a high density of particles coming from the collisions. Thus, to maintain precise tracking, the Pixel detector requires the highest granularity possible. There are a total of 1,744 modules arranged in three cylindrical barrel layers and six end-cap disks (three at each end of the barrel region) with each module containing roughly 50,000 pixels of nominal size 50×400 μm^2. With more than 80 million

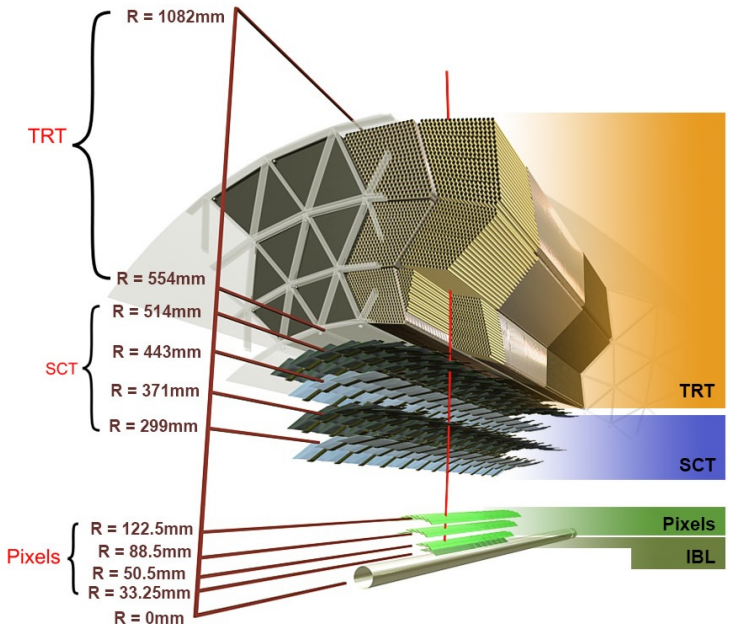

Figure 3.5: A partial cross-sectional view of the inner detector, displaying the radial positioning of each sub-detector in the barrel region [7]. The red line is demonstrative of the reconstructed track from a charged particle (with p_{T} of 10 GeV) traversing the ID. Note the inclusion of the IBL (see Section 3.3.1).

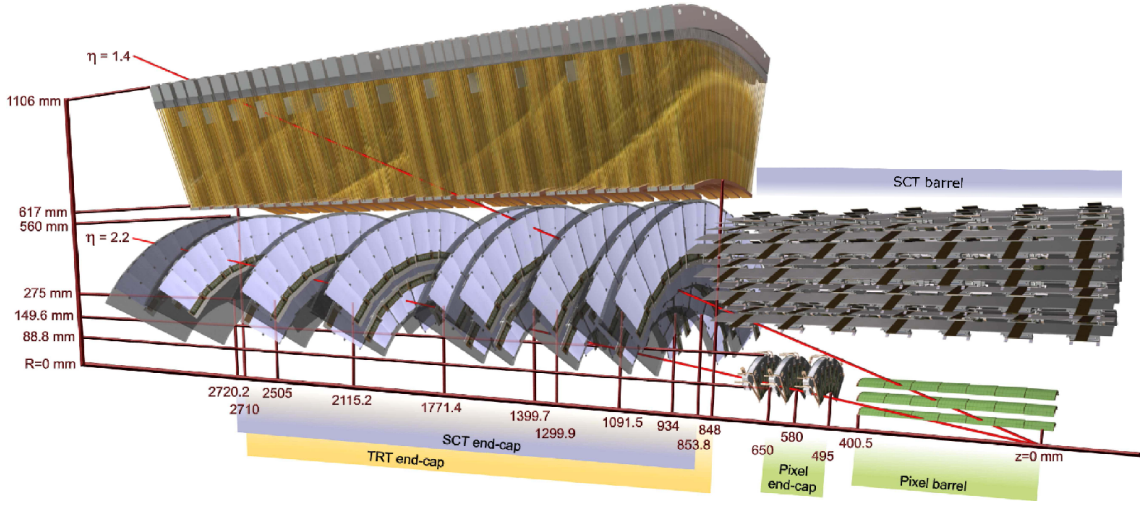

Figure 3.6: A partial profile view of the inner detector, highlighting the longitudinal positioning of each sub-detector [8]. The red lines are demonstrative of reconstructed tracks from charged particles (with p_{T} of 10 GeV) traversing the sub-detectors. Note the omission of the TRT barrel region.

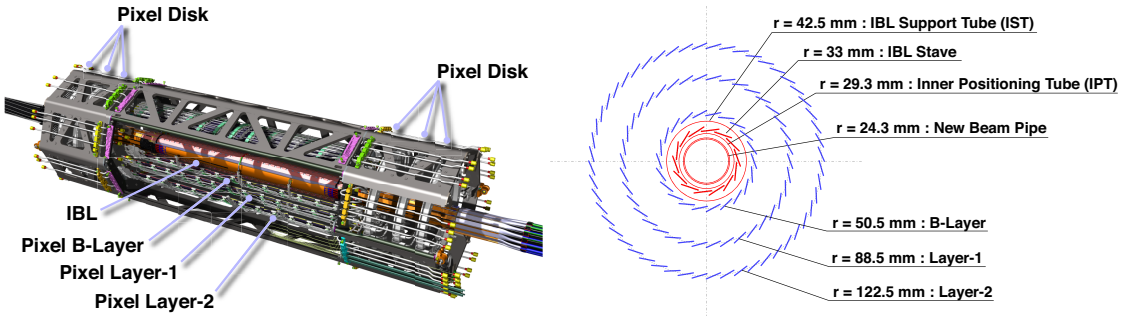

Figure 3.7: On the left is a cut-away graphic of the Pixel detector including the IBL, the three barrel Pixel layers (B-Layer [Layer-0], Layer-1, and Layer-2), and the end-cap Pixel disks along with the support structure and cooling system. On the right is an illustration of the barrel Pixel and IBL layers in the R-ϕ plane [9].

pixels (i.e. readout channels) in total, the Pixel detector has a total active area of about 1.7 m^2, a pseudorapidity coverage of $|\eta| < 2.5$, and an impressive intrinsic accuracy of 10 μm in R-ϕ and 115 μm in z (R) in the barrel (end-cap) region(s). The radial distance of the innermost Pixel barrel layer (the so called B-layer) from the beam-line is only 5 cm, but during the "long shutdown" between LHC Run-I and Run-II, a fourth silicon pixel layer was added even closer to the beam-line in the form of a new sub-detector named the Insertable B-Layer (IBL). Figure 3.7 shows a schematic of the Pixel detector with the IBL included.

IBL The IBL [31] [32], as its name suggests, was inserted between the Pixel B-layer and a new smaller radius beam-pipe with the purpose of improving the tracking and vertex reconstruction performance (especially that related to the tagging of b-quark jets [b-tagging]) of the ID. With a radius of only 3.3 cm, the IBL is designed to handle even greater pixel occupancy and radiation doses through the use of two newly developed silicon sensor technologies and new faster read-out electronics. The IBL

is made up of 14 carbon fiber staves arranged cylindrically around the beam-pipe, providing full ϕ coverage (each stave is tilted by 14° to create some overlap) and pseudorapidity coverage of $|\eta| \leq 2.9$. Each stave supports and supplies cooling to 20 silicon sensors that each contain nearly 27,000 pixels. The IBL pixels are even smaller than those in the Pixel detector with a size of 50×250 μm^2, offering the desired increased granularity.

Following the brief interlude of turning inward toward the IBL, the next detector out from the Pixel detector is the SCT.

3.3.2 SCT

The SCT [33] surrounds the Pixel detector and has a similar layout with four concentric cylindrical layers in the barrel region and a series of nine disks in each of the end-cap regions. However, instead of silicon pixels the SCT sensors are composed of silicon micro-strips. There are a total of 8,448 rectangular barrel sensors and 6,944 various wedge-shaped end-cap sensors, each with 768 active single-sided p-in-n silicon strips of around 6 cm in length and 80 μm in width. The modules on each layer of the detector actually consist of pairs of sensors mounted flatly back-to-back with one sensor rotated by 40 mrad with respect to the other that is aligned along the beam-axis on the barrel layers and radially on the end-cap disks. All in all, the SCT has approximately 6.3 million readout channels, continuing the high-granularity tracking of the Pixel detector by providing at least four precise space point measurements within the fiducial coverage of the ID with an accuracy of 17 μm in R-ϕ and 580 μm

in z (R) in the barrel (end-cap) region(s).

The high-precision of the Pixel and SCT silicon trackers is essential to ATLAS, but comes at a high monetary cost, especially for the relatively low number of space points measured (only seven [eight including the IBL] for a typical track). Thus, the remainder of the ID volume contains the complimentary and cost-effective TRT that offers less granularity but many more space points per track (typically 36).

3.3.3 TRT

The TRT [34] radially surrounds the SCT and is composed of a matrix of gas-filled thin-walled proportional drift tubes (referred to as straws hereafter), providing continued tracking up to $|\eta| < 2.0$. The barrel region consists of 52,544 144 cm long straws aligned parallel to the beam axis and arranged in an axial array with an average spacing of approximately 7 mm, forming roughly 73 layers of straws. The end-cap regions each consist of 122,880 37 cm long straws aligned radially to the beam axis and arranged in 160 planes, each containing the same number of straws with uniform azimuthal spacing. Each successive end-cap straw-plane is positioned 8 - 15 mm apart and is rotated in ϕ with respect to the previous plane by 3/8 of the azimuthal straw spacing.

All of the TRT straws are 4 mm in diameter, have a 35 μm wall thickness, and are made from multi-layer polyimide films coated with aluminum and graphite, and structurally stabilized by carbon fibers. Each straw contains a 31 μm diameter gold-plated tungsten anode wire at its center and is filled with a Xe-based gas

mixture (70% Xe, 27% CO_2, and 3% O_2) at an over-pressure of 5 -10 mbar. The anode wires are held at ground potential while the straws are held at a high voltage (typically around -1530 V) in order to quickly collect the freed electrons coming from the ionization of the gas by charged particles passing through the straws. The time it takes the freed electrons to "drift" to the anode wire gives the distance between the particle track and the wire. Each TRT straw has an intrinsic precision of 130 μm in R-ϕ.

In addition to extended tracking, the TRT (as its name suggests) creates the opportunity for particles to emit transition radiation photons through the use of polypropylene fibers (foils) interspersed with the straw layers in the barrel (end-cap) region(s). This offers a level of particle identification/discrimination (primarily aimed at electron identification) as the probability of a particle to emit transition radiation grows with its Lorentz factor, γ. The electron identification provided by the TRT compliments that of the calorimeters.

3.4 ATLAS Calorimeters

Moving outward from the ID and the solenoid magnet that encloses it, one finds the calorimeters. In stark contrast to the ID that prioritized minimizing the amount of material, the calorimeters are designed to absorb and measure the energy of particles using passive layers of dense absorbing material, which cause the particles to "shower" into cascades of lower-energy particles, interspersed with active sampling layers. Figure 3.8 shows the calorimeter system in ATLAS, which is composed of a set of

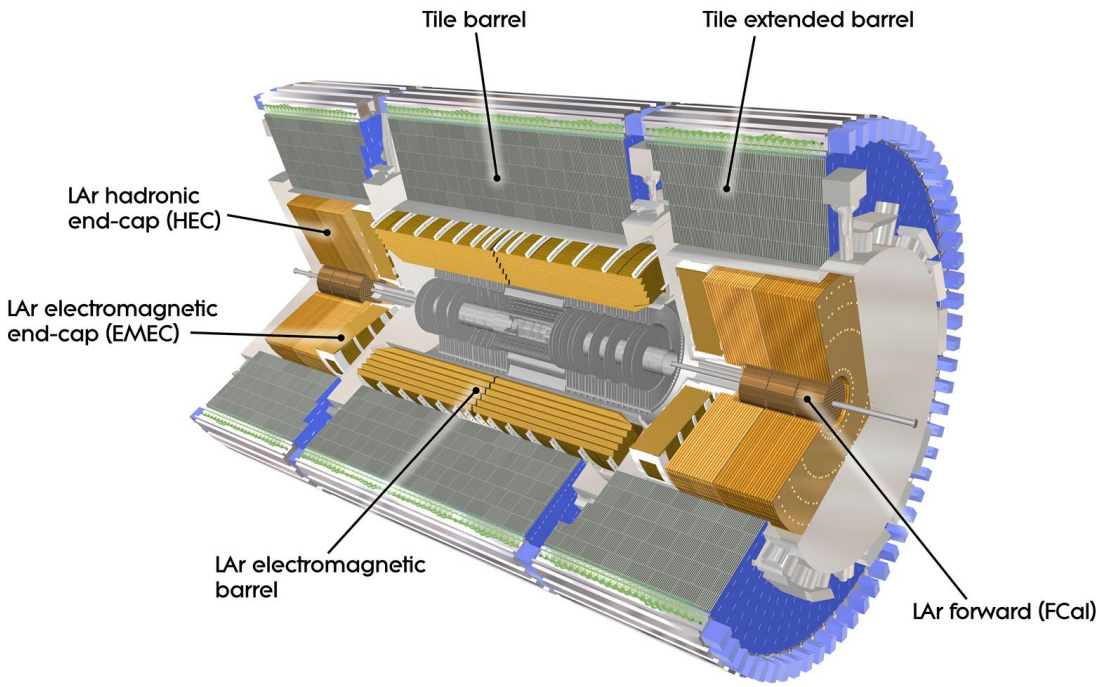

Figure 3.8: A cut-away view of ATLAS, highlighting the calorimeters [10].

electromagnetic (EM) calorimeters surrounded by hadronic calorimeters and has a layout similar to the ID with barrel and end-cap regions. Altogether, the calorimeter system provides coverage for nearly the entire 4π solid angle (with pseudorapidity up to $|\eta| < 4.9$) and good containment of both electromagnetic and hadronic showers. This is critical to ensure a good measurement of the missing transverse energy, which is essential to many physics analyses, including those presented in this work.

An important unit of measure for the EM calorimeters is the radiation length, X_0, which is defined as the average distance a high-energy electron ($E > 100\,\text{MeV}$) will travel in a given material before bremsstrahlung radiation reduces its energy to $1/e$ ($\approx 36.8\%$) of its original value. The radiation length is equivalent to 7/9 of the mean free path for high-energy photons, which lose energy primarily through pair

production and Compton scattering. As the energy loss of hadrons is dominated by strong interactions in the calorimeters, a more useful measure of the material is the interaction length, λ_{int}, which is the mean free path of a hadron in the calorimeter.

3.4.1 Electromagnetic Calorimeter

The EM calorimeter surrounds the ID volume and consists of a barrel calorimeter ($> 22\ X_0$) split into two identical halves, end-cap calorimeters ($> 24\ X_0$) on each side split into two coaxial wheels, and forward calorimeters ($\sim 27.6\ X_0$) on each side coaxial with the end-caps but recessed about 1.2 m further away from the interaction point. All of them use liquid argon (LAr) as the active material to be ionized by the cascading charged particles. The barrel and end-cap EM calorimeters have the finest granularity (especially in their first layer) and feature accordion-shaped lead absorber plates and Kapton electrodes that provide complete azimuthal coverage with no cracks thanks to the unique geometry. The forward EM calorimeter features copper as the absorbing metal in the form of stacked copper plates with a matrix of 12,260 holes filled with electrode structures, each made of a coaxial copper rod and copper tube with LAr in-between.

3.4.2 Hadronic Calorimeter

The hadronic calorimeter surrounds the EM calorimeter and consists of a barrel calorimeter ($\sim 9.7\ \lambda_{\text{int}}$) split into central and extended regions, end-cap calorimeters ($10\ \lambda_{\text{int}}$) on each side split into two stacked wheels, and forward calorimeters (10

λ_{int}) on each side also split into two stacked wheels.

The hadronic end-cap and forward calorimeter wheels are positioned directly behind their corresponding EM counterparts and actually all share the same end-cap cryostats (minimizing gaps between the calorimeter systems) as they also use LAr for their active material. The end-cap wheels are divided azimuthally into 32 identical wedge-shaped modules. The front (rear) end-cap wheel modules consist of 25 (17) copper plates, each 25 mm (50 mm) thick except for the first plate of each wheel at half that thickness. For all of the end-cap wheel modules the LAr and electrodes are contained in the 8.5 mm gap between successive plates. The hadronic forward wheels are similar in design to the forward EM calorimeter wheels, but use tungsten rods instead of copper, have successively fewer electrodes, and only have two copper end-plates with tungsten slugs filling the volume in between.

The hadronic barrel calorimeter (or tile calorimeter), including the central and two extended barrels, uses a different technology than the other calorimeters with steel plates for absorbers and scintillating tiles for the active material. When traversed by ionizing particles (e.g. hadronic showers), the plastic tiles emit scintillation light that is then read out by optical fibers and transformed into electrical signals by photo-multiplier tubes. The entire tile calorimeter has a pseudorapidity coverage of $|\eta| < 1.7$, with its inner (outer) radius of 2.28 m (4.25 m) and central (extended) barrel measuring 5.8 m (2.6 m) in length. Each barrel section is evenly divided azimuthally into 64 wedge-shape modules with 11 stacked and staggered layers of radially oriented scintillating tiles and steel plates.

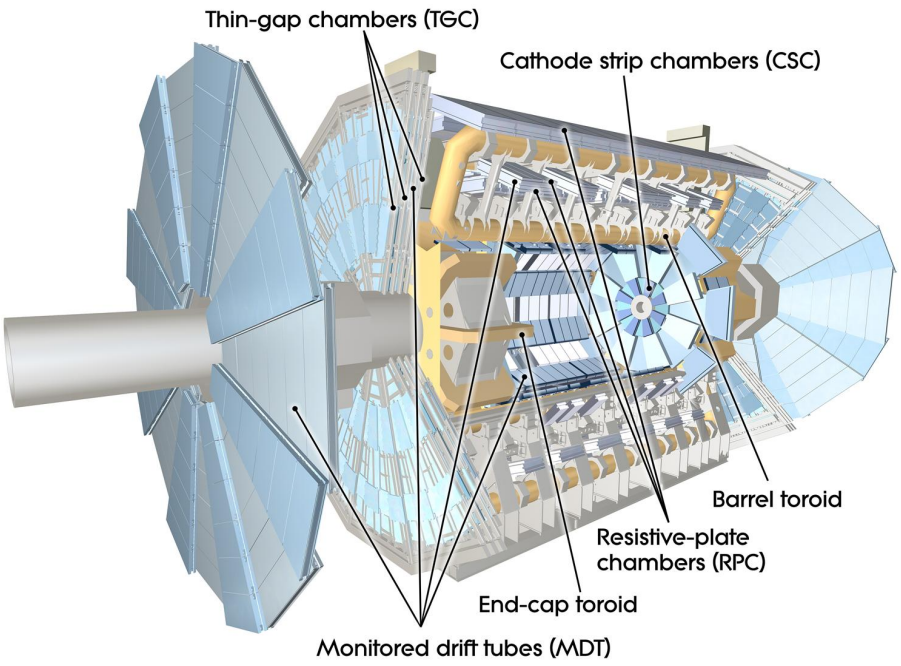

Figure 3.9: A cut-away view of the ATLAS muon spectrometer, including the toroid magnet system [11].

Altogether, the calorimeters will stop nearly all electrons, photons, and hadrons within $|\eta| < 4.9$. However, neutrinos and high-energy muons will continue on through the entire detector.

3.5 ATLAS Muon Spectrometer

The muon spectrometer, in conjunction with the bending power of the toroid magnet system, is designed to provide precise standalone measurements of muon momenta and charge within $|\eta| < 2.7$ as well as to trigger on them in the region $|\eta| < 2.4$. As the outermost detector system it defines the overall dimensions of the ATLAS detector, as seen in Figure 3.9. The muon detector system employs four different detector technologies: two for precision tracking and two primarily for triggering.

The primary tracking technology used is that of monitored drift tubes (MDTs), which provide muon position precision of ~ 80 μm per tube. MDTs are arranged parallel to the beam axis in three cylindrical shells in the barrel region and arranged perpendicular to the beam axis in three large wheels in each end-cap region. MDTs cover the entire tracking pseudorapidity range of $|\eta| < 2.7$, except for the innermost end-cap wheel layer ($2 < |\eta| < 2.7$) where cathode-strip chambers (CSC) are used instead due to their higher rate capability and resolution (~ 80 μm).

A system of fast trigger chambers compliments the tracking chambers, with resistive plate chambers (RPC) in the barrel region, $|\eta| < 1.05$, and thin gap chambers (TGC) in the end-cap regions, $1.05 < |\eta| < 2.4$. Both types of trigger chambers actually measure two coordinates of the muon tracks, one in the ϕ (non-bending) plane and one in the η (bending) plane, thus directly complimenting the tracking chambers' measurement of the coordinate in the bending plane. The trigger chambers also provide well-defined p_{T} thresholds and identification of bunch-crossings.

3.6 ATLAS Data Acquisition Process

With bunch crossings occurring every 50 ns in Run-I, the ATLAS Data Acquisition (DAQ) system requires a trigger system to reduce the 20 MHz event rate down to a more manageable and recordable rate of a few hundred Hz. This massive reduction from produced to recorded events is expected, as the physics processes of most interest are rare. The trigger system is made up of three levels of event selection: Level-1 (L1), Level-2 (L2), and an event filter; where each level refines the previous

selection.

The L1 trigger reduces the 20 MHz event rate down to around 75 kHz, making its decision to keep or toss an event within 2.5 μs of its associated bunch-crossing. It does this by analyzing reduced-granularity information from the calorimeters (L1Calo) and muon systems (L1Muon), searching for high p_{T} particles (muons, electrons/photons, jets, etc.) and/or a large amount of missing transverse energy.

The L2 trigger further reduces the event rate to < 3.5 kHz, taking an average of 40 ms to process each event. It uses all of the available detector data within the Regions-of-Interest (RoI's) defined by the L1 trigger as areas of the detector containing objects that triggered the event.

Finally, the event filter reduces the event rate to ~ 200 Hz for recording, taking an average of four seconds to process each event. It uses offline analysis, with the entire event information available, to make the final refined selections.

3.6.1 Changes in Run-II

In Run-II the event rate increased to 40 MHz because of the decreased bunch spacing, and the probability of producing high-energy particles that meet the trigger thresholds also increased because of the increased collision energy. Together, these changes increase the trigger rate by a factor of five, which is handled by an upgrade of the trigger system [35]. The L1 hardware-based trigger system gained topological trigger processors (L1Topo) that run topological algorithms on data from the calorimeters and muon detectors, performing geometrical cuts/corrections and calculating complex

observables like the invariant mass. Also, the L2 and event filter stages were combined into a single software-based high-level trigger (HLT), which features fast algorithms that access data from an RoI (or sometimes the full-event information) and run on a special PC farm with an average processing time of 0.2 s.

In the end, the upgraded L1 trigger reduces the 40 MHz event rate down to 100 kHz, and the HLT further reduces the rate to an average of 1 kHz for recording.

3.7 Other Design Aspects

There are many more services and entire systems used in ATLAS that are not detailed here including radiation shielding, the LHC interface, and the immense cooling system to only name a few. There are layers upon layers of services managed by a multitude of people.

Chapter 4

8 TeV Analysis

4.1 Introduction

This chapter details the search for a high-mass Higgs boson in the $H \to WW \to \ell\nu qq$ decay channel utilizing 20.3 fb^{-1} of pp collision data recorded by the ATLAS detector at a center-of-mass energy of $\sqrt{s} = 8\,\text{TeV}$. The analysis was combined with a parallel $H \to WW \to \ell\nu\ell\nu$ high-mass Higgs search for publication in Ref. [36]. The results of the search improve upon the 7 TeV results [37], extend the mass range, and expand the breadth of model interpretations. The search results are interpreted using three different signal hypotheses (described further in Section 4.2.1):

- A Higgs boson with a SM width and a lineshape modeled by the complex-pole scheme (CPS) [38] for most mass points.
- A narrow width Higgs boson with a lineshape referred to as the narrow-width approximation (NWA).
- A Higgs boson with an intermediate-width (IW).

The chapter begins with a description of the Monte Carlo (MC) modeling of signal and background physics processes in Section 4.2, followed by an overview of the utilized LHC data in Section 4.3, and a detailing of the pertinent physics object reconstructions in ATLAS and their preliminary selection criteria in Section 4.5. Next, Section 4.6 lays out the primary event selection criteria and explains the

categorization of events into signal and control regions. This is followed by a look at the WW invariant mass reconstruction, resolution, and related studies in Section 4.7, with the final mass-dependent event selection criteria outlined in Section 4.8. Prior to the end results, an explanation of the data-driven background estimations is given in Section 4.9 along with an overview of the systematic uncertainties in Section 4.10, culminating in a final check of the MC modeling against data in Section 4.11. Finally, with satisfactory modeling of the MC in the control regions, Section 4.12 presents the final results with an outline of the maximum likelihood fit to the data and the subsequent limit setting infrastructure due to the absence of a discovery.

4.2 Physics Modeling

MC simulations are used to model all signal and background processes in the analysis except for the multi-jet QCD background where a data-driven method is used (see Section 4.9.1). The production of MC can be generalized into three stages: generation, simulation, and digitization [39].

Generation

Various MC programs are used in this generation stage due to the wide range of physics processes in this analysis. For a single event, the generation begins with the production of a single parton-parton hard-scatter interaction. The generators are then responsible for modeling any prompt decays (such as W, Z, and Higgs bosons) along with any initial- and final-state parton showering, hadronization, and

underlying events (e.g. multiple parton-parton interactions and beam remnants); resulting in a set of stable (proper lifetime $c\tau > 10$ mm) final-state particles. Lastly, at this stage, "truth" information is recorded for each generated event, detailing every particle's interaction history from the generator (e.g. parent-daughter information and four-momenta) including incoming and outgoing particles.

Simulation

Before entering the simulation stage, the vertex of the hard-scatter in each generated event is smeared (as originally all were unrealistically located exactly at the geometric center of the detector) to better represent the luminous region within ATLAS.

Each generated event is then fed into the simulation stage, in which every final-state particle is propagated through the ATLAS detector using the GEANT4 simulation framework [40, 41]. This framework is a powerful, versatile, and configurable tool that simulates the passage of particles through matter, including ionization and energy deposition in materials, as well as intermediate particle decays, radiation, and scattering. The matter, in this case, is the ATLAS detector with all of its tracking, calorimetry, magnets, support structures, cooling pipes, cables, etc. The simulation also takes faulty or unpowered detector components into account.

The energies deposited in the sensitive segments of the ATLAS detector are recorded as "hits", along with their corresponding position and time, and written to a simulation output hit file. Also at this stage, select information is added to the truth record, such as truth tracks and decays, for certain particles (only those of

most interest to physics analyses).

The CPU time required to run an event through the full GEANT4 simulation (FullSim) is understandably very large due to its detailed detector geometry and physics description. This limits the MC statistics achievable in a reasonable amount of time and is basically a showstopper for analyses requiring samples with either very large statistics or fast turn-arounds. In order to speed up the processing time, fast simulations were developed to complement GEANT4 and, as almost 80% of the FullSim CPU time is spent simulating particles traversing the calorimeters, calorimetry simulation is the primary target for improvement.

Nearly half of the samples in this analysis use the ALTFAST-II (AFII or AF2) [39] fast simulation that utilizes the Fast Calorimeter Simulation (FastCaloSim) while retaining the full simulation for the inner detector and muon system. FastCaloSim takes, as input, the truth information of all the interacting particles at the outer edge of the inner detector and instead of simulating the interactions between the particles and the calorimeter material directly (as done in FullSim), it uses parameterizations of the longitudinal and lateral energy profiles of showers based on substantial FullSim MC samples of single photons (used to approximate electron and photon showers) and charged pions (used to approximate all hadronic showers). Compared to FullSim, AFII reduces the simulation CPU time by a factor of 10!

Whenever possible, the kinematics of the AFII simulated samples in this analysis have been validated against those of corresponding FullSim samples. A selection of the object-level kinematic distributions compared for one such validation (for CPS

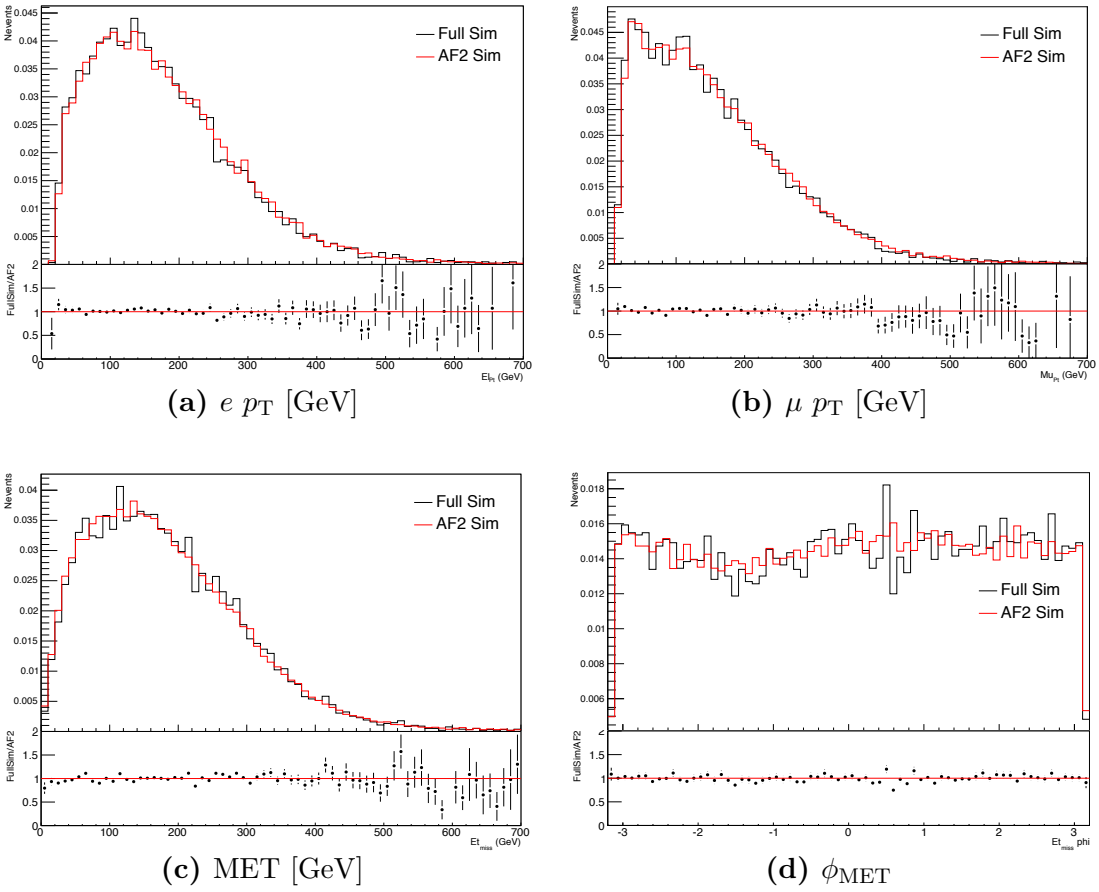

(a) e p_{T} [GeV] **(b)** μ p_{T} [GeV]

(c) MET [GeV] **(d)** ϕ_{MET}

Figure 4.1: Object-level kinematic distribution comparisons between AFII and FullSim simulated CPS VBF 800 GeV signal samples. Each upper sub-plot distribution is normalized to unity and the lower sub-plots show the bin-by-bin ratio of the two distributions (FullSim/AFII).

VBF 800 GeV signal) are shown in Figures 4.1 and 4.2. The distributions shown are nearly inclusive of the entire samples, with only minor requirements on the number of jets and leptons. The larger statistics of the AFII sample can be seen clearly in the figures in the form of smoother distributions. No obvious mis-modeling or trend is observed between the two simulations.

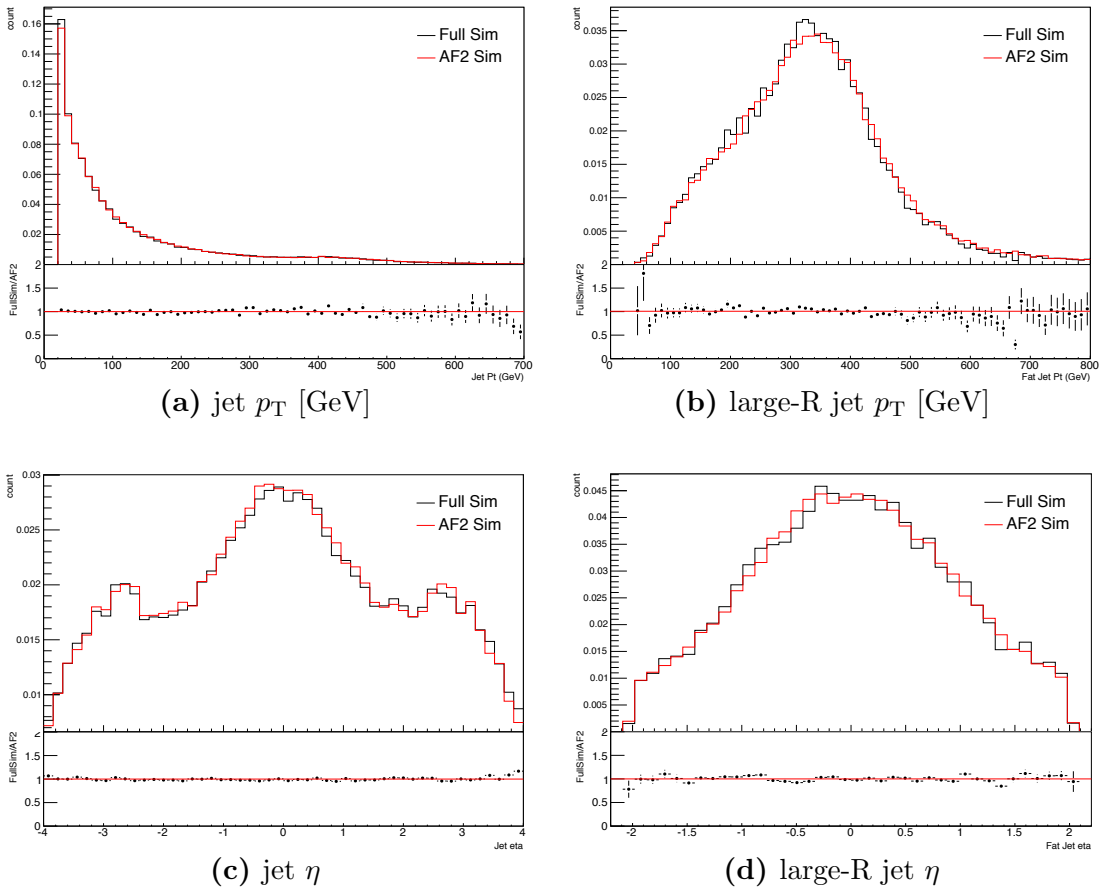

(a) jet p_{T} [GeV] **(b)** large-R jet p_{T} [GeV]

(c) jet η **(d)** large-R jet η

Figure 4.2: Object-level kinematic distribution comparisons between AFII and FullSim simulated CPS VBF 800 GeV signal samples. Each upper sub-plot distribution is normalized to unity and the lower sub-plots show the bin-by-bin ratio of the two distributions (FullSim/AFII).

Digitization

The end-goal of the digitization stage is to simulate the detector readout. However, in the previous two steps, an event only consisted of a single hard-scatter interaction from a single bunch crossing, which is a very unrealistic environment for simulating the detector readout. In reality, in addition to the hard-scatter interaction there are most often multiple other proton-proton interactions in each bunch crossing (referred to as in-time pile-up), detector noise from beam and cavern related interactions, and detector response effects due to interactions from nearby bunch crossings (referred to as out-of-time pile-up).

Thus, to prepare for a realistic detector response simulation, hits from the hard scattering are overlaid with separately generated and simulated hits from the additional interactions mentioned above.

The hits are then converted into "digits" by the ATLAS digitization software for inputs to the read out drivers (RODs) in the detector electronics. A digit is generally produced when the current or voltage on a given readout channel exceeds a predefined threshold within a certain time period. Depending on the sub-detector, the digit's format can include the shape of the signal over this time or just the fact that the threshold was exceeded. Finally, the ROD functionality is emulated, resulting in the output of a Raw Data Object (RDO) file.

Lastly, the digitization process also creates Simulated Data Objects (SDOs), created from the truth information provided by the previous stages, that map the hits in the detector to the truth particles that deposited the hits.

The final output of this process, the RDO file, is in the exact same format as the raw data (except for the additional truth information stored for MC), allowing for identical reconstruction of MC and data events.

4.2.1 Signal MC

The processes for the three signal interpretation scenarios are all modeled using the POWHEG [42] generator in combination with PYTHIA8 [43] (POWHEG+PYTHIA8) and are produced separately for ggF and VBF Higgs production modes. The cross-section calculations for the ggF signals include next-to-leading order (NLO) electroweak (EW) corrections [44], next-to-next-to-leading order (NNLO) QCD corrections [45], and QCD soft-gluon resummations up to next-to-next-to-leading logarithmic order (NNLL) [46]. As for the VBF signals, their cross-section calculations include NLO EW and QCD corrections [47], as well as approximate NNLO QCD corrections [48]. Lastly, the branching ratios of $H \to WW$ have been calculated as a function of the hypothesized Higgs mass using PROPHECY4F [49].

The modeling of the various signal interpretation samples diverges from here as detailed below.

CPS and Breit-Wigner: Samples are generated to model a Higgs boson with a SM-like width and lineshape. Samples with $m_H < 400\,\text{GeV}$ are generated using a running-width Breit-Wigner (BW) lineshape [38]. The reason for stopping at this mass point is that the increasing width has become comparable to the mass ($\Gamma/m \sim 7.3\%$ at 400 GeV) which signals the breakdown of the BW model.

Thus, samples with $m_H \geq 400\,\text{GeV}$ are generated using the CPS lineshape instead as it provides a more accurate description. Table 4.1 summarizes both sets of SM-like samples. Neither set of signal samples includes the effect of interference between resonant and non-resonant $gg \to WW$ production at the generator level. Therefore, the effect is taken into account through an event weighting procedure detailed in Ref. [3] and outlined below.

Interference between the signal and non-resonant WW background increases with increasing Higgs width (and therefore m_H in this case) and affects both the production cross-section and kinematic distributions. This interference effect was shown to be small enough to neglect for $m_H < 400\,\text{GeV}$, but must be taken into account for higher masses [38]. Therefore, since none of the signal samples include this effect, all of them must have a correction applied in the form of an interference event weight at particle level. This weight is calculated differently for ggF and VBF samples.

For ggF signal samples, interference weights are computed at leading order (LO) accuracy in QCD using the MCFM [50] program. Following the procedure in Ref. [3], these weights are then rescaled to next-to-next-to-leading order (NNLO) in order to match the signal cross-section order of calculation. For VBF signal samples, interference weights are computed using the Repolo (Reweighting Powheg at Leading Order) tool from the VBFNLO Monte Carlo generator framework [51, 52, 53]. Both procedures have associated uncertainties to be included in the total theoretical uncertainty (see Section 4.10.3).

IW: Samples are not directly generated, but are derived by weighting the CPS samples to running-width Breit-Wigner line shapes with widths in the range $0.2 \leq \Gamma_H/\Gamma_{H,\mathrm{SM}} \leq 0.8$, where Γ_H is the width of the hypothetical particle and $\Gamma_{H,\mathrm{SM}}$ is the width of a SM Higgs boson at the same mass. Interference weights are derived in the same manor as for the CPS samples and are computed as a function of the modified width.

NWA: Samples are generated using a Breit-Wigner lineshape with a fixed width of 4.07 MeV and are summarized in Table 4.2. The samples span the mass range $300 \leq m_H \leq 1500$ GeV in 50 GeV increments. Due to the fact that this narrow width is much smaller than the experimental mass resolution, the actual lineshape is hidden in the reconstruction, making this a more model-independent scenario. The narrow width also creates a situation in which the effect of the interference is negligible between the signal and the non-resonant WW background, so no interference weights are applied to these samples.

4.2.2 Background MC

The dominant background contribution to the $H \to WW \to \ell\nu qq$ signal comes from $W+$jets production, followed by the production of $t\bar{t}$ and minor contributors: single top, $Z+$jets, diboson (WW, WZ, ZZ, $W\gamma$, and Z/γ), and QCD multi-jet. Simulations of these background processes are described briefly below with summaries of the samples used in Tables 4.3, 4.4, and 4.5.

Table 4.1: SM-like signal samples used in the analysis, with corresponding lineshape, MC generator (and tune), PDF set, and detector simulation information.

m_H [GeV]	Lineshape	Generator (Tune)	PDF Set	Simulation	
				ggF	VBF
300	Breit-Wigner	Powheg + Pythia8 (AU2)	CT10	FullSim	FullSim
320	Breit-Wigner	Powheg + Pythia8 (AU2)	CT10	FullSim	FullSim
340	Breit-Wigner	Powheg + Pythia8 (AU2)	CT10	FullSim	FullSim
360	Breit-Wigner	Powheg + Pythia8 (AU2)	CT10	FullSim	FullSim
380	Breit-Wigner	Powheg + Pythia8 (AU2)	CT10	FullSim	FullSim
400	CPS	Powheg + Pythia8 (AU2)	CT10	FullSim	AFII
420	CPS	Powheg + Pythia8 (AU2)	CT10	FullSim	AFII
440	CPS	Powheg + Pythia8 (AU2)	CT10	FullSim	AFII
460	CPS	Powheg + Pythia8 (AU2)	CT10	FullSim	AFII
480	CPS	Powheg + Pythia8 (AU2)	CT10	FullSim	AFII
500	CPS	Powheg + Pythia8 (AU2)	CT10	FullSim	AFII
520	CPS	Powheg + Pythia8 (AU2)	CT10	FullSim	AFII
540	CPS	Powheg + Pythia8 (AU2)	CT10	FullSim	AFII
560	CPS	Powheg + Pythia8 (AU2)	CT10	FullSim	AFII
580	CPS	Powheg + Pythia8 (AU2)	CT10	FullSim	AFII
600	CPS	Powheg + Pythia8 (AU2)	CT10	FullSim	AFII
650	CPS	Powheg + Pythia8 (AU2)	CT10	FullSim	AFII
700	CPS	Powheg + Pythia8 (AU2)	CT10	FullSim	AFII
750	CPS	Powheg + Pythia8 (AU2)	CT10	FullSim	AFII
800	CPS	Powheg + Pythia8 (AU2)	CT10	FullSim	AFII
850	CPS	Powheg + Pythia8 (AU2)	CT10	FullSim	AFII
900	CPS	Powheg + Pythia8 (AU2)	CT10	FullSim	AFII
950	CPS	Powheg + Pythia8 (AU2)	CT10	FullSim	AFII
1000	CPS	Powheg + Pythia8 (AU2)	CT10	FullSim	AFII

Table 4.2: NWA signal samples used in the analysis, with corresponding lineshape, MC generator (and tune), PDF set, and detector simulation information.

m_H [GeV]	Lineshape	Generator (Tune)	PDF Set	Simulation ggF & VBF
300	NWA	Powheg + Pythia8 (AU2)	CT10	FullSim
350	NWA	Powheg + Pythia8 (AU2)	CT10	AFII
400	NWA	Powheg + Pythia8 (AU2)	CT10	FullSim
450	NWA	Powheg + Pythia8 (AU2)	CT10	AFII
500	NWA	Powheg + Pythia8 (AU2)	CT10	FullSim
550	NWA	Powheg + Pythia8 (AU2)	CT10	AFII
600	NWA	Powheg + Pythia8 (AU2)	CT10	FullSim
650	NWA	Powheg + Pythia8 (AU2)	CT10	AFII
700	NWA	Powheg + Pythia8 (AU2)	CT10	FullSim
750	NWA	Powheg + Pythia8 (AU2)	CT10	AFII
800	NWA	Powheg + Pythia8 (AU2)	CT10	FullSim
850	NWA	Powheg + Pythia8 (AU2)	CT10	AFII
900	NWA	Powheg + Pythia8 (AU2)	CT10	FullSim
950	NWA	Powheg + Pythia8 (AU2)	CT10	AFII
1000	NWA	Powheg + Pythia8 (AU2)	CT10	FullSim
1050	NWA	Powheg + Pythia8 (AU2)	CT10	AFII
1100	NWA	Powheg + Pythia8 (AU2)	CT10	AFII
1150	NWA	Powheg + Pythia8 (AU2)	CT10	AFII
1200	NWA	Powheg + Pythia8 (AU2)	CT10	AFII
1250	NWA	Powheg + Pythia8 (AU2)	CT10	AFII
1300	NWA	Powheg + Pythia8 (AU2)	CT10	AFII
1350	NWA	Powheg + Pythia8 (AU2)	CT10	AFII
1400	NWA	Powheg + Pythia8 (AU2)	CT10	AFII
1450	NWA	Powheg + Pythia8 (AU2)	CT10	AFII
1500	NWA	Powheg + Pythia8 (AU2)	CT10	AFII

$W+$ jets: The production of a leptonically decaying W-boson with associated jets is the dominant background in this analysis and is modeled by version 1.4.1. of the SHERPA [54] MC generator, with constraints from data taken into account in a dedicated $W+$ jets-enriched control region. The final normalization of this background is determined from the final fit to data in the signal and control regions.

In order to have sufficient statistics for this dominant background in the entire mass range considered in this analysis, it isn't enough to simply add more events because these would preferentially populate the low-mass region as the majority of $W+$ jets events in general have correspondingly low W-boson p_{T} (p_{T}^{W}). To circumvent this issue, SHERPA samples are generated in specific ranges of p_{T}^{W}: 40–70 GeV, 70–140 GeV,140–280 GeV, 280–500 GeV, and > 500 GeV with an inclusive sample used for $p_{\mathrm{T}}^{W} < 40$ GeV. For the benefit of other physics groups, the non-inclusive samples are further divided by quark content using b-, c-, and light-jet filters. Lastly, in continued pursuance of large statistics for the $W+$ jets background, AFII simulated samples are used whenever available.

Top: Single top and $t\bar{t}$ pair productions introduce backgrounds with their $t \to Wb$ decays. All of the top samples are modeled by MC and generated with the AFII simulation in order to have better statistics in the high-mass region. All of the top backgrounds are generated using POWHEG+PYTHIA6 [55], except for the single top t-channel process that trades POWHEG for ACERMC [56]. Similar

to the $W+$jets background, a top-enriched control region is defined in order to constrain the normalization of the top background (in the end determined by the final fit) and observe its modeling with respect to data. Finally, two prescribed weights are applied sequentially to events in the $t\bar{t}$ sample in order to correct for disagreements between data and the POWHEG prediction in the p_{T} distributions of both the $t\bar{t}$ system and the individual top quarks [57].

$Z+$jets and Diboson: The production of a leptonically decaying Z-boson with associated jets, along with the production of dibosons (WW, WZ, ZZ, $W\gamma$, and Z/γ), have much smaller contributions to the background in this analysis. The normalization and kinematics for all of these samples are modeled solely by MC. The MC generators for the diboson processes include ALPGEN [58]+JIMMY [59], HERWIG [60], and SHERPA. SHERPA is also used to generate the $Z+$jets samples, which are divided by the same p_{T} binning and quark-content filters as the $W+$jets samples for both consistency and welcomed larger statistics.

Mullti-jet: The production of QCD multi-jet events, with a jet that fakes an electron or muon, contributes to the background in this analysis, but is greatly suppressed at high m_H and only has a minor contribution. However, it is difficult to model this background well using MC, so a data-driven estimation is used (see Section 4.9.1).

Table 4.3: Top and diboson Monte Carlo samples used in the analysis, with information on the process, MC generator (and tune), cross-section, and detector simulation.

Process	Generator (Tune)	PDF Set	$\sigma\times$ BR [pb] ($@\ \sqrt{s} = 8$ TeV)	AFII/FullSim
$t\bar{t}$	Powheg + Pythia6 (P2011C)	CTEQ6L1	252.89	AFII
Single top (t-channel)	AcerMC + Pythia6 (P2011C)	CTEQ6L1	28.44	AFII
Single top (s-channel)	Powheg + Pythia6 (P2011C)	CTEQ6L1	1.818	AFII
Wt (inclusive)	Powheg + Pythia6 (P2011C)	CTEQ6L1	22.37	AFII
WW	Herwig (AUET2)	CTEQ6L1	32.501	FullSim
WZ	Herwig (AUET2)	CTEQ6L1	12.009	FullSim
ZZ	Herwig (AUET2)	CTEQ6L1	4.6914	FullSim
$Z/\gamma^* \to ee$ ($p_{\mathrm{T}} > 10$ GeV)	Sherpa	CT10	32.26	FullSim
$Z/\gamma^* \to \mu\mu$ ($p_{\mathrm{T}} > 10$ GeV)	Sherpa	CT10	32.317	FullSim
Wγ	Alpgen + Jimmy (AUET2)	CTEQ6L1	229.88	FullSim
Wγ + 1 parton, (Lepton/Photon Filter)	Alpgen + Jimmy (AUET2)	CTEQ6L1	59.518	FullSim
Wγ + 2 partons, (Lepton/Photon Filter)	Alpgen + Jimmy (AUET2)	CTEQ6L1	21.39	FullSim
Wγ + 3 partons, (Lepton/Photon Filter)	Alpgen + Jimmy (AUET2)	CTEQ6L1	7.1203	FullSim
Wγ + 4 partons	Alpgen + Jimmy (AUET2)	CTEQ6L1	2.1224	FullSim
Wγ + 5 partons	Alpgen + Jimmy (AUET2)	CTEQ6L1	0.46612	FullSim

Table 4.4: $W+$jets Monte Carlo samples used in the analysis, with information on the process, MC generator (and tune), cross-section, and detector simulation.

Process	Generator (Tune)	PDF Set	$\sigma\times$ BR [pb] (@ $\sqrt{s} = 8$ TeV)	AFII/FullSim
W$\to e\nu$	Sherpa	CT10	11866.0	FullSim
W$\to e\nu$, $40 < p_{\mathrm{T}} < 70$, b-jet filter	Sherpa	CT10	652.82	AFII
W$\to e\nu$, $40 < p_{\mathrm{T}} < 70$,c-jet filter, b-jet veto	Sherpa	CT10	652.83	AFII
W$\to e\nu$, $40 < p_{\mathrm{T}} < 70$, c-jet veto, b-jet veto	Sherpa	CT10	653.16	AFII
W$\to e\nu$, $70 < p_{\mathrm{T}} < 140$, b-jet filter	Sherpa	CT10	250.55	AFII
W$\to e\nu$, $70 < p_{\mathrm{T}} < 140$, c-jet filter, b-jet veto	Sherpa	CT10	250.71	AFII
W$\to e\nu$, $70 < p_{\mathrm{T}} < 140$, c-jet veto, b-jet veto	Sherpa	CT10	250.43	AFII
W$\to e\nu$, $140 < p_{\mathrm{T}} < 280$, b-jet filter	Sherpa	CT10	31.155	AFII
W$\to e\nu$, $140 < p_{\mathrm{T}} < 280$, c-jet filter, b-jet veto	Sherpa	CT10	31.189	AFII
W$\to e\nu$, $140 < p_{\mathrm{T}} < 280$, c-jet veto, b-jet veto	Sherpa	CT10	31.112	AFII
W$\to e\nu$, $280 < p_{\mathrm{T}} < 500$, b-jet filter	Sherpa	CT10	1.8413	FullSim
W$\to e\nu$, $280 < p_{\mathrm{T}} < 500$, c-jet filter, b-jet veto	Sherpa	CT10	1.8370	FullSim
W$\to e\nu$, $280 < p_{\mathrm{T}} < 500$, c-jet veto, b-jet veto	Sherpa	CT10	1.8426	FullSim
W$\to e\nu$, $p_{\mathrm{T}} > 500$, b-jet filter	Sherpa	CT10	0.10188	FullSim
W$\to e\nu$, $p_{\mathrm{T}} > 500$, c-jet filter, b-jet veto	Sherpa	CT10	0.10101	FullSim
W$\to e\nu$, $p_{\mathrm{T}} > 500$, c-jet veto, b-jet veto	Sherpa	CT10	0.10093	FullSim
W$\to \mu\nu$	Sherpa	CT10	11867.0	FullSim
W$\to \mu\nu$, $40 < p_{\mathrm{T}} < 70$, b-jet filter	Sherpa	CT10	652.73	AFII
W$\to \mu\nu$, $40 < p_{\mathrm{T}} < 70$, c-jet filter, b-jet veto	Sherpa	CT10	653.14	AFII
W$\to \mu\nu$, $40 < p_{\mathrm{T}} < 70$, c-jet veto, b-jet veto	Sherpa	CT10	653.06	AFII
W$\to \mu\nu$, $70 < p_{\mathrm{T}} < 140$, b-jet filter	Sherpa	CT10	250.55	AFII
W$\to \mu\nu$, $70 < p_{\mathrm{T}} < 140$, c-jet filter, b-jet veto	Sherpa	CT10	250.57	AFII
W$\to \mu\nu$, $70 < p_{\mathrm{T}} < 140$, c-jet veto, b-jet veto	Sherpa	CT10	250.77	AFII
W$\to \mu\nu$, $140 < p_{\mathrm{T}} < 280$, b-jet filter	Sherpa	CT10	31.164	AFII
W$\to \mu\nu$, $140 < p_{\mathrm{T}} < 280$, c-jet filter, b-jet veto	Sherpa	CT10	31.165	AFII
W$\to \mu\nu$, $140 < p_{\mathrm{T}} < 280$, c-jet veto, b-jet veto	Sherpa	CT10	31.173	AFII
W$\to \mu\nu$, $280 < p_{\mathrm{T}} < 500$, b-jet filter	Sherpa	CT10	1.8380	FullSim
W$\to \mu\nu$, $280 < p_{\mathrm{T}} < 500$, c-jet filter, b-jet veto	Sherpa	CT10	1.8395	FullSim
W$\to \mu\nu$, $280 < p_{\mathrm{T}} < 500$, c-jet veto, b-jet veto	Sherpa	CT10	1.8433	FullSim
W$\to \mu\nu$, $p_{\mathrm{T}} > 500$, b-jet filter	Sherpa	CT10	0.10163	FullSim
W$\to \mu\nu$, $p_{\mathrm{T}} > 500$, c-jet filter, b-jet veto	Sherpa	CT10	0.10210	FullSim
W$\to \mu\nu$, $p_{\mathrm{T}} > 500$, c-jet veto, b-jet veto	Sherpa	CT10	0.10186	FullSim
W$\to \tau\nu$	Sherpa	CT10	11858.0	FullSim
W$\to \tau\nu$, $40 < p_{\mathrm{T}} < 70$, b-jet filter	Sherpa	CT10	652.84	AFII
W$\to \tau\nu$, $40 < p_{\mathrm{T}} < 70$, c-jet filter, b-jet veto	Sherpa	CT10	652.58	AFII
W$\to \tau\nu$, $40 < p_{\mathrm{T}} < 70$, c-jet veto, b-jet veto	Sherpa	CT10	652.99	AFII
W$\to \tau\nu$, $70 < p_{\mathrm{T}} < 140$, b-jet filter	Sherpa	CT10	250.57	FullSim
W$\to \tau\nu$, $70 < p_{\mathrm{T}} < 140$, c-jet filter, b-jet veto	Sherpa	CT10	250.61	FullSim
W$\to \tau\nu$, $70 < p_{\mathrm{T}} < 140$, c-jet veto, b-jet veto	Sherpa	CT10	250.60	FullSim
W$\to \tau\nu$, $140 < p_{\mathrm{T}} < 280$, b-jet filter	Sherpa	CT10	31.162	FullSim
W$\to \tau\nu$, $140 < p_{\mathrm{T}} < 280$, c-jet filter, b-jet veto	Sherpa	CT10	31.151	FullSim
W$\to \tau\nu$, $140 < p_{\mathrm{T}} < 280$, c-jet veto, b-jet veto	Sherpa	CT10	31.176	FullSim
W$\to \tau\nu$, $280 < p_{\mathrm{T}} < 500$, b-jet filter	Sherpa	CT10	1.8362	FullSim
W$\to \tau\nu$, $280 < p_{\mathrm{T}} < 500$, c-jet filter, b-jet veto	Sherpa	CT10	1.8395	FullSim
W$\to \tau\nu$, $280 < p_{\mathrm{T}} < 500$, c-jet veto, b-jet veto	Sherpa	CT10	1.8368	FullSim
W$\to \tau\nu$, $p_{\mathrm{T}} > 500$, b-jet filter	Sherpa	CT10	0.10208	FullSim
W$\to \tau\nu$, $p_{\mathrm{T}} > 500$, c-jet filter, b-jet veto	Sherpa	CT10	0.10139	FullSim
W$\to \tau\nu$, $p_{\mathrm{T}} > 500$, c-jet veto, b-jet veto	Sherpa	CT10	0.10201	FullSim
VBF W$\to e\nu$	Sherpa	CT10	4.2114	FullSim
VBF W$\to \mu\nu$	Sherpa	CT10	4.2128	FullSim

Table 4.5: $Z+$jets Monte Carlo samples used in the analysis, with information on the process, MC generator (and tune), cross-section, and detector simulation.

Process	Generator (Tune)	PDF Set	$\sigma\times$ BR [pb] (@ $\sqrt{s} = 8$ TeV)	AFII/FullSim
Z$\to ee$	Sherpa	CT10	1207.8	FullSim
Z$\to ee$, $40 < p_{\mathrm{T}} < 70$, b-jet filter	Sherpa	CT10	70.48500	AFII
Z$\to ee$, $40 < p_{\mathrm{T}} < 70$, c-jet filter, b-jet veto	Sherpa	CT10	70.53000	AFII
Z$\to ee$, $40 < p_{\mathrm{T}} < 70$, c-jet veto, b-jet veto	Sherpa	CT10	70.43100	AFII
Z$\to ee$, $70 < p_{\mathrm{T}} < 140$, b-jet filter	Sherpa	CT10	29.49400	AFII
Z$\to ee$, $70 < p_{\mathrm{T}} < 140$, c-jet filter, b-jet veto	Sherpa	CT10	29.48700	AFII
Z$\to ee$, $70 < p_{\mathrm{T}} < 140$, c-jet veto, b-jet veto	Sherpa	CT10	29.49100	AFII
Z$\to ee$, $140 < p_{\mathrm{T}} < 280$, b-jet filter	Sherpa	CT10	3.987700	AFII
Z$\to ee$, $140 < p_{\mathrm{T}} < 280$, c-jet filter, b-jet veto	Sherpa	CT10	3.981100	AFII
Z$\to ee$, $140 < p_{\mathrm{T}} < 280$, c-jet veto, b-jet veto	Sherpa	CT10	3.989000	AFII
Z$\to ee$, $280 < p_{\mathrm{T}} < 500$, b-jet filter	Sherpa	CT10	0.241600	FullSim
Z$\to ee$, $280 < p_{\mathrm{T}} < 500$, c-jet filter, b-jet veto	Sherpa	CT10	0.241280	FullSim
Z$\to ee$, $280 < p_{\mathrm{T}} < 500$, c-jet veto, b-jet veto	Sherpa	CT10	0.241580	FullSim
Z$\to ee$, $p_{\mathrm{T}} > 500$, b-jet filter	Sherpa	CT10	0.013235	FullSim
Z$\to ee$, $p_{\mathrm{T}} > 500$,c-jet filter, b-jet veto	Sherpa	CT10	0.013454	FullSim
Z$\to ee$, $p_{\mathrm{T}} > 500$, c-jet veto, b-jet veto	Sherpa	CT10	0.013307	FullSim
Z$\to \mu\mu$	Sherpa	CT10	1207.7	FullSim
Z$\to \mu\mu$, $40 < p_{\mathrm{T}} < 70$, b-jet filter	Sherpa	CT10	70.48600	AFII
Z$\to \mu\mu$, $40 < p_{\mathrm{T}} < 70$, c-jet filter, b-jet veto	Sherpa	CT10	70.46900	AFII
Z$\to \mu\mu$, $40 < p_{\mathrm{T}} < 70$, c-jet veto, b-jet veto	Sherpa	CT10	70.53400	AFII
Z$\to \mu\mu$, $70 < p_{\mathrm{T}} < 140$, b-jet filter	Sherpa	CT10	29.49100	AFII
Z$\to \mu\mu$, $70 < p_{\mathrm{T}} < 140$, c-jet filter, b-jet veto	Sherpa	CT10	29.44700	AFII
Z$\to \mu\mu$, $70 < p_{\mathrm{T}} < 140$, c-jet veto, b-jet veto	Sherpa	CT10	29.52100	AFII
Z$\to \mu\mu$, $140 < p_{\mathrm{T}} < 280$, b-jet filter	Sherpa	CT10	3.984200	AFII
Z$\to \mu\mu$, $140 < p_{\mathrm{T}} < 280$, c-jet filter, b-jet veto	Sherpa	CT10	3.991100	AFII
Z$\to \mu\mu$, $140 < p_{\mathrm{T}} < 280$, c-jet veto, b-jet veto	Sherpa	CT10	3.984100	AFII
Z$\to \mu\mu$, $280 < p_{\mathrm{T}} < 500$, b-jet filter	Sherpa	CT10	0.242190	FullSim
Z$\to \mu\mu$, $280 < p_{\mathrm{T}} < 500$, c-jet filter,b-jet veto	Sherpa	CT10	0.241690	FullSim
Z$\to \mu\mu$, $280 < p_{\mathrm{T}} < 500$, c-jet veto, b-jet veto	Sherpa	CT10	0.242720	FullSim
Z$\to \mu\mu$, $p_{\mathrm{T}} > 500$, b-jet filter	Sherpa	CT10	0.013161	AFII
Z$\to \mu\mu$, $p_{\mathrm{T}} > 500$, c-jet filter, b-jet veto	Sherpa	CT10	0.013480	AFII
Z$\to \mu\mu$, $p_{\mathrm{T}} > 500$, c-jet veto, b-jet veto	Sherpa	CT10	0.013264	AFII
Z$\to \tau\tau$	Sherpa	CT10	1206.9	FullSim
Z$\to \tau\tau$, $40 < p_{\mathrm{T}} < 70$, b-jet filter	Sherpa	CT10	70.44100	AFII
Z$\to \tau\tau$, $40 < p_{\mathrm{T}} < 70$, c-jet filter, b-jet veto	Sherpa	CT10	70.53800	AFII
Z$\to \tau\tau$, $40 < p_{\mathrm{T}} < 70$, c-jet veto, b-jet veto	Sherpa	CT10	70.52800	AFII
Z$\to \tau\tau$, $70 < p_{\mathrm{T}} < 140$, b-jet filter	Sherpa	CT10	29.48900	FullSim
Z$\to \tau\tau$, $70 < p_{\mathrm{T}} < 140$, c-jet filter, b-jet veto	Sherpa	CT10	29.49900	FullSim
Z$\to \tau\tau$, $70 < p_{\mathrm{T}} < 140$, c-jet veto, b-jet veto	Sherpa	CT10	29.49400	FullSim
Z$\to \tau\tau$, $140 < p_{\mathrm{T}} < 280$, b-jet filter	Sherpa	CT10	3.988700	FullSim
Z$\to \tau\tau$, $140 < p_{\mathrm{T}} < 280$, c-jet filter, b-jet veto	Sherpa	CT10	3.988000	FullSim
Z$\to \tau\tau$, $140 < p_{\mathrm{T}} < 280$, c-jet veto, b-jet veto	Sherpa	CT10	3.987100	FullSim
Z$\to \tau\tau$, $280 < p_{\mathrm{T}} < 500$, b-jet filter	Sherpa	CT10	0.241900	FullSim
Z$\to \tau\tau$, $280 < p_{\mathrm{T}} < 500$, c-jet filter, b-jet veto	Sherpa	CT10	0.241020	FullSim
Z$\to \tau\tau$, $280 < p_{\mathrm{T}} < 500$, c-jet veto, b-jet veto	Sherpa	CT10	0.241470	FullSim
Z$\to \tau\tau$, $p_{\mathrm{T}} > 500$, b-jet filter	Sherpa	CT10	0.013285	FullSim
Z$\to \tau\tau$, $p_{\mathrm{T}} > 500$, c-jet filter, b-jet veto	Sherpa	CT10	0.013308	FullSim
Z$\to \tau\tau$, $p_{\mathrm{T}} > 500$, c-jet veto, b-jet veto	Sherpa	CT10	0.013284	FullSim

4.3 Dataset

The 20.3 fb^{-1} of data used in this analysis corresponds to the entire $\sqrt{s} = 8\,\text{TeV}$ dataset recorded by the ATLAS detector in 2012 and deemed *good for physics*. As shown in Figure 4.3, the ATLAS detector did not record all of the luminosity delivered by the LHC, but had a data-recording efficiency of 93.5% (the fraction of delivered data effectively recorded by ATLAS) [61]. As a subset of ATLAS detector systems only start to operate after the LHC has announced stable beams, their turn-on time contributes to the recording inefficiency. Other factors range from issues with the trigger or data acquisition systems to large-scale hardware problems.

Following the recording and reconstruction of the data, further data-quality checks are performed, where any "bad data" is assigned as a *defect* to an interval of validity (period of data taking). If the defect is found to be *intolerable*, the data in that defined interval of validity are rejected from physics analysis. Possible intolerable defects include noisy readout cells and portions of detectors being temporarily switched off. In order to smoothly inform analyses of which data are *good for physics*, a Good Run List (GRL) is provided that only contains periods of intolerable-defect-free data. In the end, an impressive 95.5% of the data recorded by ATLAS in 2012 were determined to be usable for physics analyses [61].

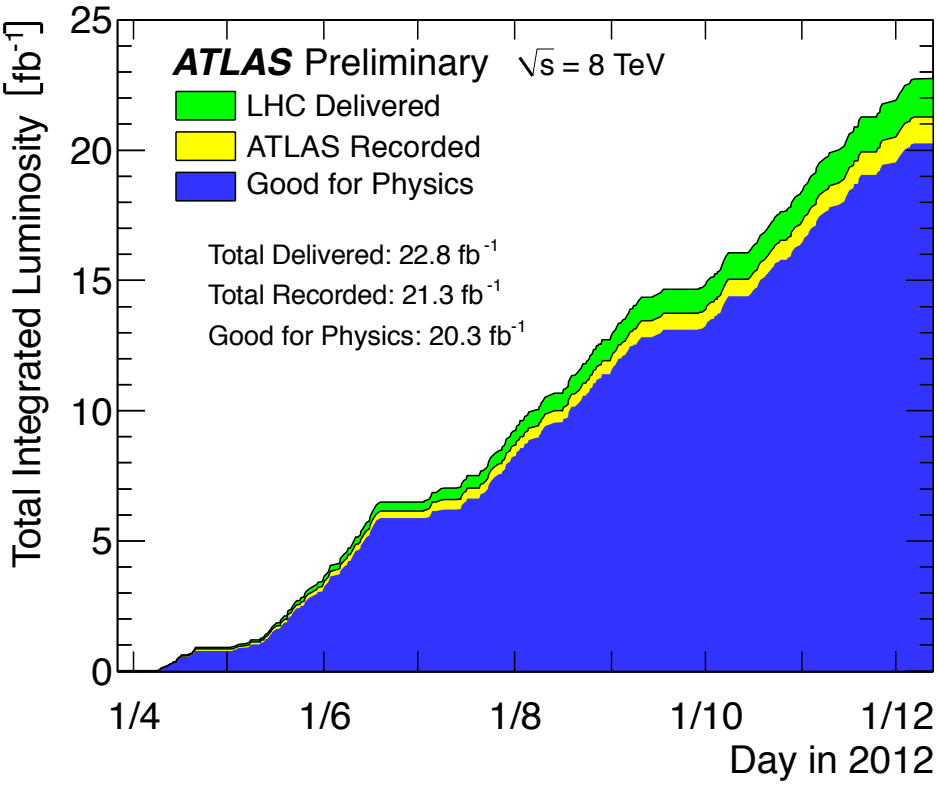

Figure 4.3: The cumulative luminosity versus time delivered to ATLAS by the LHC (green), recorded by ATLAS (yellow), and determined to be *good for physics* (blue) in 2012 with pp collisions at $\sqrt{s} = 8\,\text{TeV}$ [12]. The histograms are overlaid, i.e. not stacked, and the time axis is in units of months with the date format (D/M).

4.4 Triggers

Out of the entire 2012 ATLAS dataset, this analysis uses events triggered by single leptons in order to select events with $W \to \ell\nu$ decays. The specific triggers are listed in Table 4.6 along with their p_{T} thresholds and combined efficiencies. The trigger names contain a good deal of information; following the particle type (e or μ) and p_{T} threshold the letters v, h, and i along with the suffix (medium or tight) refer to further features and requirements of the trigger:

v: The trigger technically has an η dependent p_{T} threshold due to compensations for the varying amount of non-instrumented material (not uniform in η) in front of the calorimeters.

h: The trigger contains a hadronic leakage cut that vetoes events where the triggering object deposits $\geq 1\,\mathrm{GeV}$ of energy in the hadronic calorimeter within a region of 0.2×0.2 in $\eta \times \phi$ behind the EM calorimeter energy deposit.

i: The trigger has a track isolation requirement. In order to measure the level of track isolation, the quantity p_{T}^{iso} is first calculated by taking the scalar p_{T} sum of all tracks having $p_{\mathrm{T}} > 1\,\mathrm{GeV}$ found in the ID within a cone of ΔR centered around the triggering object, but excluding the object itself. The relative track isolation is then measured as the ratio of p_{T}^{iso} to the p_{T} of the triggering object.

- e24vhi: Requires a relative track isolation of $p_{\mathrm{T}}^{iso}/p_{\mathrm{T}}(e) < 0.1$ using a cone size of $\Delta R = 0.2$.

Table 4.6: Triggers used for 8 TeV analysis.

Triggered Object	**Trigger Name**	**p_{T} Threshold [GeV]**	**Combined Efficiency**
	e24vhi_medium	24	
e	**or**		$\geq 95\%$ for $\lvert\eta\rvert < 2.40$
	e60_medium	60	
	mu24i_tight	24	$\sim 70\%$ ($\sim 90\%$)
μ	**or**		for
	mu36_tight	36	$\lvert\eta\rvert < 1.05$ ($1.05 < \lvert\eta\rvert < 2.40$)

- mu24i: Requires a relative track isolation of $p_{\mathrm{T}}^{iso}/p_{\mathrm{T}}(\mu) < 0.12$ using a cone size of $\Delta R = 0.2$.

medium/tight: Refers to a specific level of electron or muon identification criteria that the trigger utilizes.

Combining the triggers for each lepton flavor, i.e. accepting events that pass either trigger, helps to maintain a high trigger efficiency across a larger kinematic range. The triggers with higher p_{T} thresholds and no isolation requirement compensate for the loss of efficiency at high p_{T} due to the isolation requirements of the lower p_{T} threshold triggers.

The electron trigger efficiencies are measured using the tag-and-probe technique in which offline reconstructed $Z \to e^+e^-$ decays are selected by requiring a pair of oppositely charged electrons with an invariant mass near that of the Z boson. One of these offline-electrons (the tag) is required to have an *associated* trigger-electron

that satisfies the criteria of an unprescaled single electron trigger, while the other offline-electron serves as the probe. To be considered *associated*, the separation between the tag and trigger electrons must satisfy $\Delta R < 0.15$. The efficiency of the electron triggers is simply the fraction of the selected e^+e^- events in which the probe electron also has an *associated* trigger-electron. A similar method is applied to measure the muon trigger efficiencies using $Z \to \mu^+\mu^-$ decays.

Since the MC samples do not flawlessly reproduce the observed trigger efficiencies in data, scale factors (ratios between measured and simulated efficiencies) are applied to the MC samples, making small corrections to better model the data. These efficiency scale factors, as well as those for reconstruction, identification, and isolation of electrons and muons (mentioned in the following sections), are provided to analysis groups by the ATLAS Electron and Muon Combined Performance groups through the use of ATLAS software packages. Public results regarding the various efficiency measurements can be found in [62] for electrons and in [63, 64] for muons.

4.5 Object Reconstruction and Preliminary Selection

Data events collected with the triggers described above, as well as simulated MC events, are filtered by requiring a loose event selection which gives high efficiency for all sub-channels and production modes of $H \to WW \to \ell\nu qq$. The basic signature of a $H \to WW \to \ell\nu qq$ candidate event is the presence of a high p_{T} electron or muon, at least two jets (or at least one merged jet) from the two quarks, and large missing transverse momentum ($E_{\mathrm{T}}^{\mathrm{miss}}$) corresponding to the neutrino p_{T}. This section details

the reconstruction and preliminary selection of these physics objects for this analysis.

4.5.1 Primary Vertex

The large amount of data delivered to ATLAS is made possible in part by the high luminosity provided by the LHC through both the very short time elapsed between proton-bunch crossings (50 ns in 2012) and the large average number of pp interactions per bunch crossing ($\langle\mu\rangle = 20.7$ in 2012). The in-time and out-of-time pile-up created in these bunch crossings require the use of dedicated algorithms and corrections to mitigate their negative impact on particle identification, event reconstruction, and energy calibrations. The pp collision vertices in each bunch crossing are reconstructed by the ID tracking system. In order to remove cosmic-ray and beam-induced backgrounds, events are required to have at least one vertex with at least three associated tracks, each with $p_{\mathrm{T}} > 400\,\mathrm{MeV}$. If more than one qualifying collision vertex is reconstructed, the one with the largest Σp_{T}^2 of its associated tracks is selected as the primary vertex.

4.5.2 Electrons

Electron candidates are reconstructed from clustered energy deposits in the EM calorimeter with an associated track in the ID and are required to pass a set of identification cuts (*Tight++* electrons) [62]. While the energy measurement is taken from the EM calorimeter, the pseudorapidity η and azimuthal angle ϕ are taken from the associated track. The cluster is required to be in the range $|\eta| < 2.47$, excluding

the transition region between the barrel and end-cap calorimeters, $1.37 < |\eta| < 1.52$. The track associated with the electron candidate is required to point back to the reconstructed primary vertex with a transverse impact parameter significance of $|d_0/\sigma_{d_0}| < 3$ and an impact parameter along the beam direction of $|z_0 \cdot \sin\theta| < 0.4$ mm. Finally, electrons are required to pass both calorimeter and track based isolation cuts; the variables used for these cuts are $topoEtCone Cor30$ and $PtCone30$ respectively.

The quantity $topoEtCone Cor30$ is constructed by summing the E_{T} of all the calorimeter cells within a cone of $\Delta R \leq 0.3$ around the electron and then subtracting the E_{T} that comes from the electron itself as well as energy deposits not related to the underlying event (primarily from pile-up). The ratio of $topoEtCone Cor30$ to the electron E_{T} provides the needed estimate of the electron calorimeter isolation. The isolation cut applied is E_{T} dependant, and is summarized in Table 4.7.

$PtCone30$ is analogously constructed, but instead of summing the E_{T} as measured by the calorimeters, it takes the scalar sum of the p_{T} from the tracker. The tracks included in the sum must be within a cone of $\Delta R \leq 0.3$ around the electron, point back to the same primary vertex as the electron track, and have $p_{\mathrm{T}} > 400\,\mathrm{MeV}$. Contributions from pile-up and the electron itself are subtracted from the sum, and the ratio of $PtCone30$ to the electron E_{T} provides the estimate of the electron track isolation. As with the calorimeter isolation, the cut value is dependent on the electron E_{T} and is also summarized in Table 4.7.

As with the triggers, the MC does not perfectly model the electron reconstruction, isolation, or identification efficiencies observed in data. Thus, to correct for this,

additional scale factors are applied to MC events containing reconstructed electrons (calculated/applied in bins of electron E_{T} and η) [62].

Table 4.7: Calorimeter and track isolation cuts for electron identification.

Isolation Base	**Isolation Variable**	**Isolation Cut**	**Electron E_{T} [GeV]**
Calorimeter	$topoEtCone Cor30/E_{\mathrm{T}}$	< 0.24	$15 \leq E_{\mathrm{T}} < 20$
		< 0.28	$E_{\mathrm{T}} \geq 20$
Track	$PtCone30/E_{\mathrm{T}}$	< 0.08	$15 \leq E_{\mathrm{T}} < 20$
		< 0.10	$E_{\mathrm{T}} \geq 20$

4.5.3 Muons

Muon candidates are reconstructed by combining tracks in the inner detector and muon spectrometer using the *Staco* combined muon algorithm [64]. Muons are required to pass basic quality cuts on the number and type of hits in the inner detector. The muons must satisfy $|z_0 \cdot \sin\theta| < 1.0$ mm and $|d_0/\sigma_{d_0}| < 3$. As with electrons, the muons must also pass track and calorimeter based isolation requirements summarized in Table 4.8.

Similar to the trigger and electron efficiency scale factors, muon reconstruction, isolation, and identification efficiency scale factors are applied to MC events containing reconstructed muons to ensure proper modeling of the data (calculated/applied in bins of muon ϕ and η) [64].

Table 4.8: Calorimeter and track isolation cuts for muon identification.

Isolation Base	**Isolation Variable**	**Isolation Cut**	**Electron E_{T} [GeV]**
Calorimeter	$topoEtCone Cor30/E_{\mathrm{T}}$	< 0.12	$15 \leq p_{\mathrm{T}} < 20$
		< 0.18	$20 \leq p_{\mathrm{T}} < 25$
		< 0.30	$p_{\mathrm{T}} \geq 25$
Track	$PtCone30/E_{\mathrm{T}}$	< 0.08	$15 \leq p_{\mathrm{T}} < 20$
		< 0.12	$p_{\mathrm{T}} \geq 20$

4.5.4 Jets

Jet candidates are also reconstructed from topological clusters of calorimeter cells, but create a much more diffuse deposit of energy because they are not discrete objects but rather *showers* of hadronic and EM particles. The primary role of jets in this analysis is to reconstruct the hadronic showers of the two quarks coming from the $W \to qq$ decay. Due to the large kinematic range (m_H range) studied in this analysis, two different jet reconstruction algorithms are used, creating two types of jets: *resolved* and *merged*. The *resolved* (or small-R) jets are reconstructed using the anti-k_t algorithm [65] with radius parameter $R = 0.4$ and a JVF (jet vertex fraction) [66] cut of > 0.5. The *merged* (or large-R) jets are reconstructed using the Cambridge-Aachen (C/A) algorithm [67] with radius parameter $R = 1.2$ and are then groomed using a standard mass-drop filtering algorithm described below.

The inclusion of large-R jets helps to mitigate the efficiency loss at very heavy Higgs boson masses near the upper end of our search region. The W bosons decayed from such a heavy Higgs are highly boosted, i.e. having significantly less mass than the Higgs they receive a "boost" in their momentum. This in turn leads to a narrower opening angle between the decay products of the W boson, e.g. the jets, as the opening angle (ΔR) between two-body decay products can be approximated as

$$\Delta R \approx \frac{2m}{p_{\mathrm{T}}} \tag{4.1}$$

where m and p_{T} are the mass and transverse momentum of the decaying particle, respectively. Thus, sometimes in the highly boosted regime the small-R jet algorithm cannot resolve the pair of jets coming from the hadronic W decay, while the large-R jet algorithm can reconstruct both jets in a single large-R jet and save the event from potential rejection/mis-identification. However, expanding the jet size increases the probability of including unwanted energy deposits in the jet area such as contributions from pile-up. This is typically where *jet substructure techniques* come into play to mitigate these unwanted contributions, as well as to examine the structure of the subjets and clusters that make up the large-R jet.

Mass-Drop Filter on large-R C/A Jets The mass-drop filter [68] seeks to isolate two relatively symmetric energy deposits within a large-R jet, that would arise from a two-body decay, and to remove unrelated and unwanted energy deposits. Originally developed for $H \to b\bar{b}$ decay searches [69], this mass-drop filter is a two stage procedure illustrated in Figure 4.4 and described below:

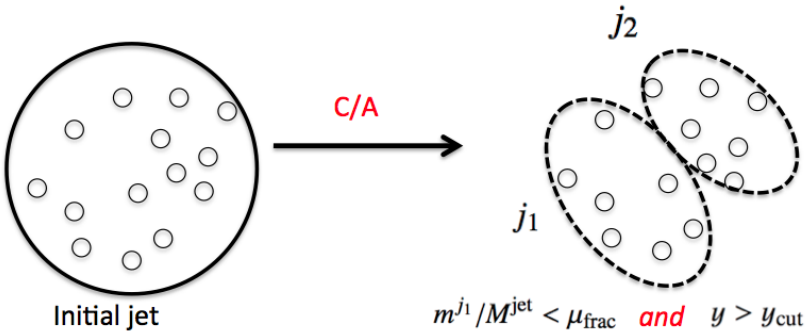

(a) Mass-drop and symmetry criteria.

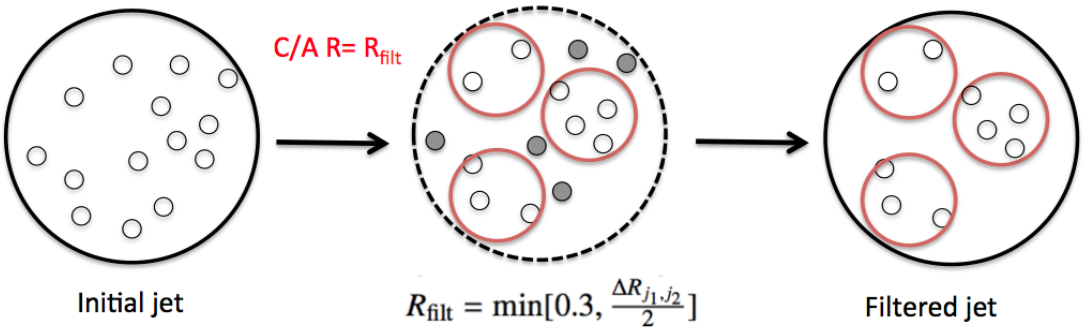

(b) Filtering

Figure 4.4: Illustration of the two-stage mass-drop filter on a large-R C/A jet.

1. **Mass-drop and symmetry criteria:** The last step in the C/A jet reconstruction algorithm (referenced above) is undone, which results in splitting the original jet into two mass-ordered subjets j_1 and j_2, as illustrated in Figure 4.4a. The mass-drop criteria is then applied, which ensures that there is a large mass difference between the original C/A jet (mass m^J) and the hardest of the two subjets (mass m^{j_1}):

$$m^{j_1}/m^J < \mu_{\text{frac}}. \tag{4.2}$$

Here, μ_{frac} is the mass-drop parameter. The symmetry criteria requires the two

subjets to satisfy a cut on y_{cut}, which represents the energy sharing between the two subjets in the original jet, and is given by the following formula:

$$\frac{\min[(p_{\text{T}}^{j_1})^2, (p_{\text{T}}^{j_2})^2]}{(m^J)^2} \times \Delta R_{j_1,j_2}^2 > y_{\text{cut}}. \tag{4.3}$$

This basically requires both subjets to carry some significant fraction of the original jet's momentum.

2. **Filtering:** Jets passing the mass-drop and symmetry criteria in the previous step are then filtered in order to remove the soft components and preserve the hardest components. First, the constituents of j_1 and j_2 are re-clustered using the C/A algorithm again, but with a new R_{filt} given by $R_{\text{filt}} = \min[0.3, \Delta R_{j_1,j_2}/2]$. Afterwards, all but the three hardest re-clustered subjets are discarded. Keeping three subjets for a two-body final state decay is done to allow for a radiation from the decay to be captured. This stage of the mass-drop filter is illustrated in Figure 4.4b.

If the C/A jet fails either the mass-drop or symmetry criteria, the jet is discarded. In this analysis the values of the parameters used are $\mu_{\text{frac}} = 0.67$ and $y_{\text{cut}} = 0.09$. These are the default values for this mass-drop filter algorithm on ATLAS and are recommended by the ATLAS Jet Substructure group.The resulting filtered large-R jet mass is calculated from the energies and momenta of the final jet constituents as:

$$m_J = \sqrt{\left(\sum_i E_i\right)^2 - \left(\sum_i \vec{\boldsymbol{p}}_i\right)^2} \tag{4.4}$$

where E_i and $\vec{\boldsymbol{p}}_i$ are the energy and three-momentum of the ith constituent.

***b*-tagging** A very helpful discriminant between our signal and top quark backgrounds is the identification of small-R jets originating from the hadronization of b-quarks since the branching ratio for $t \to Wb$ decays is $\sim$95%. Small-R jets within $|\eta| < 2.5$ are considered b-tagged if they are consistent with having originated from the decay of a b-quark. This is determined by a b-tagging multivariate neural network algorithm, MV1 [70, 71], which utilizes a combination of impact parameter significance and secondary vertex information to exploit the topology of b- and c-hadron weak decays. The algorithm is used at a working point that offers an 85% b-jet identification efficiency and a mis-tag rate for light-flavor jets of 10.3% in simulated $t\bar{t}$ events. Lastly, in order to have good agreement with data, b-tag scale factors are applied to the MC.

4.5.5 $\boldsymbol{E}_{\mathrm{T}}^{\mathrm{miss}}$

Missing transverse momentum $\boldsymbol{E}_{\mathrm{T}}^{\mathrm{miss}}$ in a given event is reconstructed by taking the negative vector sum of the energies deposited in the detector by identified and calibrated jets, leptons and photons, as well as soft clustered energy in the calorimeters [72, 73]. Energy deposits from isolated muons in the calorimeters are subtracted in the $\boldsymbol{E}_{\mathrm{T}}^{\mathrm{miss}}$ calculation to avoid double counting, as the muons' momentum contributions are measured from the muon spectrometers which already takes into account the energy deposited in the calorimeters. The $\boldsymbol{E}_{\mathrm{T}}^{\mathrm{miss}}$ vector sum is

separated into x and y components given by:

$$\begin{aligned} E_x^{\text{miss}} &= -\sum^{\text{term}} \left(\sum_{i=1}^{N_{\text{cell}}^{\text{term}}} E_i \sin\theta_i \cos\phi_i \right) \\ E_y^{\text{miss}} &= -\sum^{\text{term}} \left(\sum_{i=1}^{N_{\text{cell}}^{\text{term}}} E_i \sin\theta_i \sin\phi_i \right), \end{aligned} \tag{4.5}$$

where the first summation is over the various contributing terms from jets, leptons, etc. and the second summation is over the number of contributing calorimeter cells associated to a given term. Using these two components, the magnitude and azimuthal angle of the $\boldsymbol{E}_{\text{T}}^{\text{miss}}$ are given respectively by:

$$E_{\text{T}}^{\text{miss}} = \sqrt{(E_x^{\text{miss}})^2 + (E_y^{\text{miss}})^2} \quad \text{and} \quad \phi^{\text{miss}} = \arctan(\text{E}_{\text{y}}^{\text{miss}}/\text{E}_{\text{x}}^{\text{miss}}). \tag{4.6}$$

Although a minimum amount of $E_{\text{T}}^{\text{miss}}$ is required in the signal regions of this analysis, the full range of $E_{\text{T}}^{\text{miss}}$ is utilized in the estimation of the multi-jet background, as described in Section 4.9.1.

4.6 Selection and Categorization of Events

This section describes the categorization, classification, and selection applied to MC and data events alike.

4.6.1 Signal Event Preselection

This section describes the "preselection" that consists of various object and topology based selections aimed at distinguishing signal-like events and categorizing them. The selections will later be tightened to improve their discriminating power, but this

preselection provides a baseline/springboard for optimization studies, further event categorizations, and early (higher statistic) checks on MC/data agreement.

Object Selection A signal-like event is required to have exactly one reconstructed lepton candidate (electron or muon) with $p_{\mathrm{T}} > 25\,\mathrm{GeV}$. No additional leptons with $p_{\mathrm{T}} > 15\,\mathrm{GeV}$ are allowed. The selected lepton must match the object that triggered the event and be fairly central with $|\eta| < 2.4$. Events are also required to have $E_{\mathrm{T}}^{\mathrm{miss}} > 60\,\mathrm{GeV}$ in order to suppress the multi-jet background. Small-R jets in the event are only considered with $p_{\mathrm{T}} > 30\,\mathrm{GeV}$ and $|\eta| < 4.5$ and large-R jets only with $p_{\mathrm{T}} > 100$ GeV, $m_J > 40\,\mathrm{GeV}$, and $|\eta| < 1.2$. Lastly, a jet candidate of either size must satisfy $\Delta R > 0.3$ with respect to the selected lepton.

Production Categories For the purpose of distinguishing between production modes, events are classified into two orthogonal categories, ggF and VBF, based on the jet topology in the event.

VBF Designed to be most sensitive to the VBF production process, events in this category are required to have at least four small-R jets or at least two small-R jets and one large-R jet. In other words, events are required to have at least enough jets to reconstruct the hadronic W and to tag the two VBF-characteristic forward jets coming from the hadronization of the recoiling partons.

These tagging jets provide the main discriminating power between production modes and are identified as the pair of small-R jets with the largest

invariant mass in the event that satisfy the following criteria. The pair must have an invariant mass $m_{j_{tag1}j_{tag2}} > 600\,\text{GeV}$, leading jet $p_\text{T} > 40\,\text{GeV}$, and be well-separated in rapidity such that $|\Delta y_{j_{tag1}j_{tag2}}| > 3$.

If an event contains a pair of VBF tagging jets, along with enough other jets to reconstruct the hadronic W, it enters the VBF category. This is referred to as the VBF selection, along with any further selections explicitly specific to the category.

ggF Events in the ggF category are required to have at least two small-R jets or at least one large-R jet (again, enough to reconstruct the hadronic W). For events with at least four small-R jets or two small-R jets and one large-R jet (i.e. potential VBF category events), orthogonality between the two production categories is enforced in the ggF selection by vetoing events containing a pair of VBF tagging jets.

Together, this veto on VBF tagging jets and the requirement for a minimum number of jets, is referred to as the ggF selection, along with any further selections explicitly specific to the category.

All further selections apply to both the ggF and VBF categories, unless explicitly stated otherwise.

Hadronic W Reconstruction Events either use two small-R jets (classified as "resolved" events) or one large-R jet (classified as "merged" events) to reconstruct the hadronic W. The small-R "W-jet" candidates are identified from all small-R

jets in the event within $|\eta| < 2.4$ that are not identified as VBF tagging jets. The pair with an invariant mass closest to the W boson mass (using the current PDG value of 80.385 GeV) are considered to be the W-jets unless there are more than one such pair that fall into the Signal Region m_{jj} window ($65 \leq m_{jj} \leq 96$); in this case the pair having the largest scalar sum p_{T} is chosen. However, if there is a large-R jet in the event with a mass closer to the W boson mass than the invariant mass of the best di-jet pair, the large-R jet replaces the two W-jets as the candidate for the hadronically decaying W boson. This selection method has a 90-97% efficiency of picking both reconstructed jets that correspond to the truth jets (closest in $\Delta R < 0.3$) in resolved signal MC events following the entire signal region selection.

Decay Topology Additionally, events are required to have decay topologies consistent with semi-leptonic WW decays. For resolved events, at least one of the two W-jets must have $p_{\mathrm{T}} > 60\,\mathrm{GeV}$ and the pair is expected to be close together in ϕ (especially at high m_H) with the angular-separation requirement of $|\Delta\phi(j,j)| < 2.5$. Similarly, for both resolved and merged events, the angular separation between the lepton and neutrino is required to be small: $|\Delta\phi(\ell, E_{\mathrm{T}}^{\mathrm{miss}})| < 2.5$. Lastly, the angular separation between the leptonic and hadronic W bosons is expected to be large because they are decaying from a high-mass Higgs boson that is most often produced with negligible transverse momentum of its own. This is enforced by requiring both $|\Delta\phi(j,\ell)| > 1.0$ and $|\Delta\phi(j, E_{\mathrm{T}}^{\mathrm{miss}})| > 1.0$ for all W-jets, including the selected large-R W-jet in merged events.

***b*-tagging** Events are also vetoed from the signal region based on the presence of small-R b-tagged jets within the b-tagging acceptance of $|\eta| < 2.4$. This is done in order to suppress the $t\bar{t}$ background contribution in the region. For resolved events, if both of the W jets are b-tagged the event is vetoed, while if only one of the W jets is b-tagged the event is kept since a large fraction of jets from $W \to c\bar{s}$ decays are b-tagged due to the mistag rate of charm quarks. Furthermore, for both resolved and merged events, if any other small-R jet in the event (with $|\eta| < 2.4$ and including the VBF tagging jets) is b-tagged, the event is vetoed. However, in the case of merged events, small-R jets within $\Delta R \leq 0.4$ from the center of the large-R W-jet, are not considered in the b-tagging. There is no flavor tagging of the large-R jets in this analysis.

***W*-mass Window** The final requirement of the signal region preselection is that the invariant mass of the W-jet(s) be within the interval $65 \leq m_{J(jj)} \leq 96\,\text{GeV}$ (i.e. close to the W boson mass).

A summary of the signal region preselection described above is seen in Table 4.9.

Large-*R* Jet Impact on Preselection

As mentioned before, large-R jets are included in this analysis to make up for the observation that, with heavier and heavier Higgs mass, the preselection efficiency on the signal gets smaller and smaller. This is partly a result of more and more events with resolved di-jet pairs failing to fall within the W-mass window, which in turn is a result of the highly boosted hadronically decaying W bosons. Including the large-R

Table 4.9: Summary of the signal region event preselection. The small-R (large-R) jets passing the object selection are denoted by j (J) and their count by N_j (N_J). Also, VBF tagging jets are denoted by j_1 and j_2, with j_1 having the higher-p_{T}. The hadronic W boson candidate can be reconstructed as a pair of small-R jets ($j_w j_w$) or as a single large-R jet (J_w). The leading j_w is denoted $j_{w_{\mathrm{lead}}}$ and if only a single j_w is referenced, the requirement is applied to both.

Object selection	1 isolated charged lepton (e or μ): $p_{\mathrm{T}} > 25\,\mathrm{GeV}$, $\lvert\eta\rvert < 2.4$	
	$E_{\mathrm{T}}^{\mathrm{miss}} > 60\,\mathrm{GeV}$	
	small-R jets: $p_{\mathrm{T}} > 30\,\mathrm{GeV}$, $\lvert\eta\rvert < 4.5$	
	large-R jets: $p_{\mathrm{T}} > 100\,\mathrm{GeV}$, $\lvert\eta\rvert < 1.2$, $m_J > 40\,\mathrm{GeV}$	
VBF selection	$(N_j \geq 4)$ OR $(N_j \geq 2$ AND $N_J \geq 1)$	
	VBF tag: $m_{j_1 j_2} > 600\,\mathrm{GeV}$	
	VBF tag: $p_{\mathrm{T}}^{j_1} > 40\,\mathrm{GeV}$	
	VBF tag: $\lvert\Delta y(j_1, j_2)\rvert > 3.0$	
ggF selection	**not** VBF tagged AND $(N_j \geq 2$ OR $N_J \geq 1)$	
Further selection, hadronic W boson reconstructed as:	small-R jet pair	large-R jet
Decay topology	$p_{\mathrm{T}}^{j_{w_{\mathrm{lead}}}} > 60\,\mathrm{GeV}$	-
	$\Delta\phi(j_w, j_w) < 2.5$	-
	$\Delta\phi(j_w, \ell) > 1.0$	$\Delta\phi(J_w, \ell) > 1.0$
	$\Delta\phi(j_w, E_{\mathrm{T}}^{\mathrm{miss}}) > 1.0$	$\Delta\phi(J_w, E_{\mathrm{T}}^{\mathrm{miss}}) > 1.0$
	$\Delta\phi(\ell, E_{\mathrm{T}}^{\mathrm{miss}}) < 2.5$	
b-tagging veto events with:	both j_w b-tagged OR any other jet b-tagged	any b-tagged jet with $\Delta R(j, J_w) > 0.4$
W-mass window	$65\,\mathrm{GeV} \leq m_{j_w j_w} \leq 96\,\mathrm{GeV}$	$65\,\mathrm{GeV} \leq m_{J_w} \leq 96\,\mathrm{GeV}$

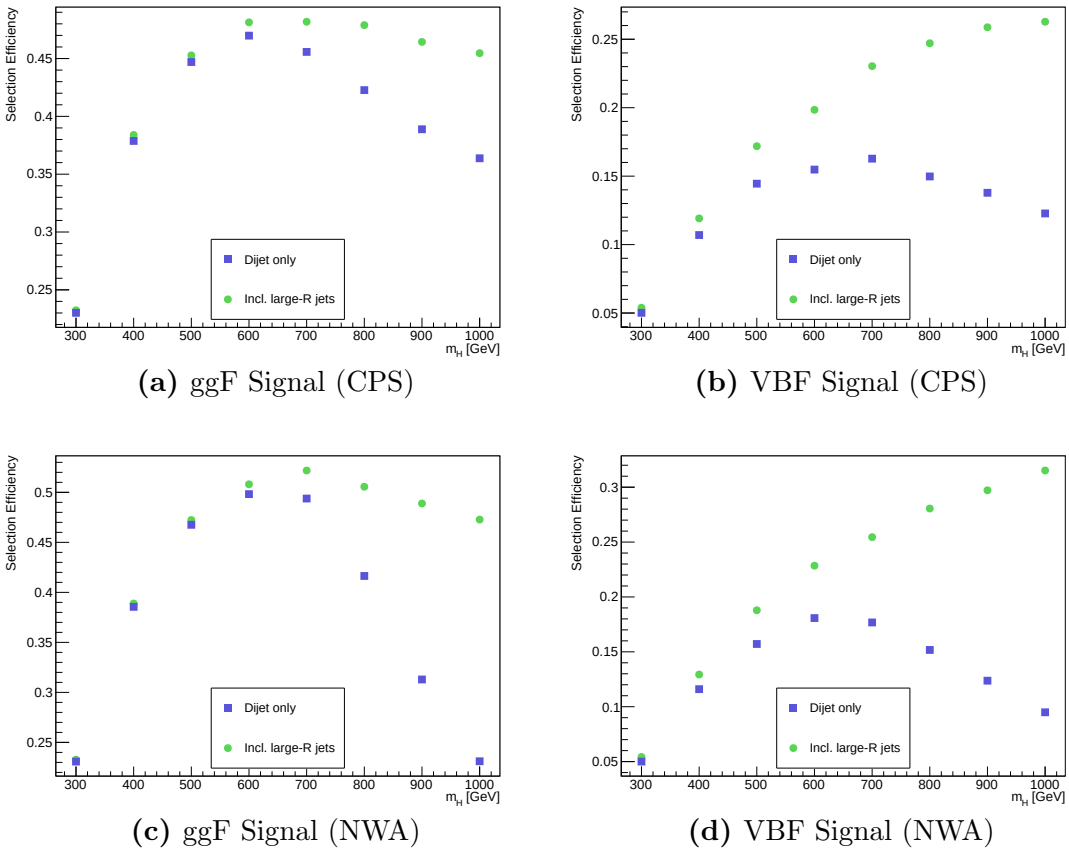

(a) ggF Signal (CPS) **(b)** VBF Signal (CPS)

(c) ggF Signal (NWA) **(d)** VBF Signal (NWA)

Figure 4.5: The preselection efficiency for CPS and NWA signal sample events. The blue squares show the preselection efficiency using only resolved jets to reconstruct the hadronic W, while the green circles show the preselection efficiency with the inclusion of large-R jets.

jets increases the selection efficiency dramatically in the heavy Higgs mass region for all of the signal samples (ggF/VBF and CPS/NWA), as shown in Figure 4.5. Also, as expected, the fraction of events that utilize a large-R jet to reconstruct the W increases as the hypothesized Higgs mass increases (see Figure 4.6).

4.6.2 Event Categorization and Region Definitions

In addition to the ggF and VBF production-mode categories discussed in the previous section, events are further divided into exclusive subcategories according to lepton

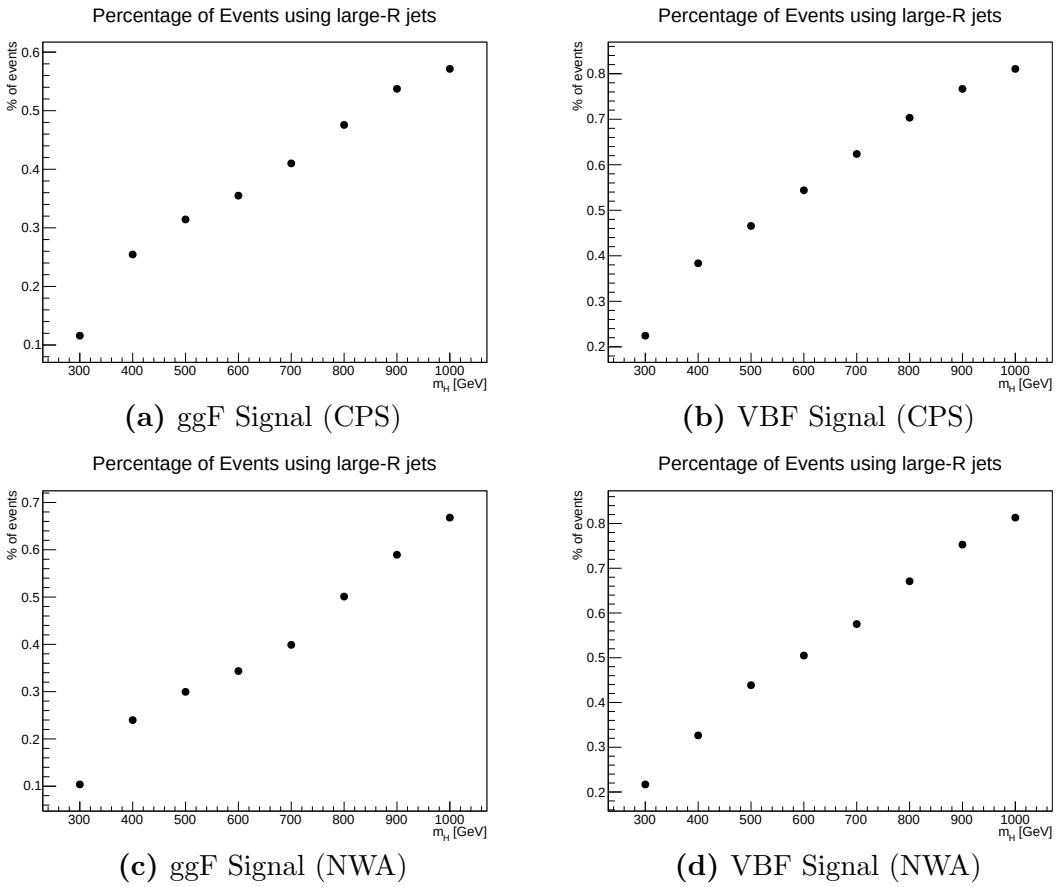

(a) ggF Signal (CPS) **(b)** VBF Signal (CPS)

(c) ggF Signal (NWA) **(d)** VBF Signal (NWA)

Figure 4.6: The percentage of preselected CPS and NWA signal events that use a large-R jet (as opposed to two small-R jets) to reconstruct the hadronic W.

flavor and charge: e^-, e^+, μ^-, or μ^+. The separation by lepton charge is particularly useful given the charge correlation present for W+jets production in pp collisions. In general, the categorization of events improves the sensitivity of the final combined result by exploiting any differences in the background or signal falling into the particular categories.

The events selected according to the description in Section 4.6.1 are assigned to the *Signal Region* (SR) of their respective categories. The SR contains events that provide optimal discovery potential for the signal. The collision data that falls

into the SR is initially "blinded" (meaning not analyzed or even looked at) to limit the experimenter bias in the analysis. The unblinding of the data in the SR takes place only after all selections are frozen/fixed, along with any corrections applied to the MC, and the MC demonstrates satisfactory modeling of the data. In order to test this data modeling in an unbiased way before unblinding, the collision data is compared to MC predictions in two control regions (CR). Separate CRs are defined for ggF and VBF categories, but merged for lepton flavor and charge.

***W*+jets CR:** The first control region is the $W+$jets control region (WCR), which is dominated by $W \to \ell\nu$+jets events. The selection defining this control region is identical to that of the SR, except for the hadronic W-mass window. The signal contributions are suppressed in the WCR by selecting an orthogonal set of events to the SR with a reconstructed hadronic W mass (m_{jj} for resolved events or m_J for merged events) that falls outside of the W-mass window and into upper and lower W-mass sidebands, effectively vetoing the most signal-like events and creating a $W+$jets enriched region.

The W-mass sidebands for the ggF category are defined as:

$$52\,\text{GeV} \leq m_{jj/J} < 65\,\text{GeV} \quad : \text{ ggF lower sideband} \tag{4.7}$$

$$96\,\text{GeV} < m_{jj/J} \leq 126\,\text{GeV} : \text{ ggF upper sideband.} \tag{4.8}$$

Due to lower statistics for both data and Monte Carlo in the VBF category, the

W-mass sidebands are extended:

$$43\,\text{GeV} \leq m_{jj/J} < 65\,\text{GeV} \quad : \text{ VBF lower sideband} \tag{4.9}$$

$$96\,\text{GeV} < m_{jj/J} \leq 200\,\text{GeV} : \text{ VBF upper sideband.} \tag{4.10}$$

Both sets of sideband ranges are chosen such that the signal contribution to the WCR is sufficiently depleted, while the kinematics of the WCR stay similar to the SR. The choice of ranges also takes into consideration keeping the number of background events close to the same in the upper and lower sidebands, so that when combined into one control region there is no bias in one direction with respect to the signal region.

Top CR: The second control region is the top control region (TopCR), which is designed to be as pure as possible for the second largest background, $t\bar{t} \to WbWb \to \ell\nu jj + bb$, while retaining similar kinematics to the SR. This background looks like the Higgs boson signal, but contains two characteristic b-jets. Therefore, the selection defining the TopCR is defined to be identical to the SR selection, but with the b-jet veto basically reversed, requiring at least one b-tagged jet that is not a small-R W-jet (in the case of a resolved event) and is distinct from the large-R W-jet with $\Delta R(j, J_w) > 0.4$ (in the case of a merged event). Also, to avoid introducing mis-modeling that is not present in the SR, resolved events are vetoed from the TopCR if both W-jets are b-tagged.

4.7 WW Invariant Mass Reconstruction and Resolution

Following the selection outlined in the previous section, each event contains all the necessary four-momenta components to fully reconstruct the four-body final state of a $H \to WW \to \ell\nu qq$ decay, except for one. While the hadronic W boson is fully reconstructed using the four-momentum(a) of the W-jet(s) selected in the event, as described in Section 4.6.1, the leptonic W boson cannot be unambiguously reconstructed because there is no measurement of the neutrino momentum along the beam axis (p_{ν_z}).

This section outlines the solution to the missing p_{ν_z} problem in this analysis and the resolution of the resulting fully-reconstructed WW invariant mass, along with a study of the effects of an alternate method for selecting W-jets.

4.7.1 Leptonic W Reconstruction and the Neutrino p_{ν_z}

To reiterate, knowledge of the neutrino momentum is required to reconstruct the leptonic W. The transverse momentum of the neutrino $\boldsymbol{p}_{\nu_{\mathrm{T}}}$ is taken to be the measured $\boldsymbol{E}_{\mathrm{T}}^{\mathrm{miss}}$ in the event, while the neutrino longitudinal momentum p_{ν_z} is not even indirectly measurable. However, p_{ν_z} can be computed (up to a two-fold ambiguity) by constraining the invariant mass of the $\ell\nu$ system to be equal to the

W boson mass (80.385 GeV) such that

$$\begin{aligned} m_W^2 = m_{\ell\nu}^2 &\equiv (p_\ell + p_\nu)^2 \\ &= \underbrace{p_\ell^2}_{\equiv m_\ell^2 \approx 0} + \underbrace{p_\nu^2}_{\equiv m_\nu^2 \approx 0} + 2p_\ell \cdot p_\nu \\ &= 2(E_\ell E_\nu - \vec{\boldsymbol{p}}_\ell \cdot \vec{\boldsymbol{p}}_\nu), \end{aligned} \tag{4.11}$$

where in this equation p represents a particle's four-momentum and $\vec{\boldsymbol{p}}$ its three-momentum. The final expression requires neglecting the small masses of the lepton and neutrino, which also leads to the relation $E_\nu = |\vec{\boldsymbol{p}}_\nu|$. Using this relation, along with the momentum conversions from cartesian coordinates (p_x, p_y) to (p_T, ϕ): $p_x = p_\mathrm{T}\cos\phi$ and $p_y = p_\mathrm{T}\sin\phi$, Equation 4.11 can be expanded in terms of p_{ν_z}:

$$m_W^2 = 2\left(E_\ell\sqrt{p_{\nu_\mathrm{T}}^2 + p_{\nu_z}^2} - p_{\ell_\mathrm{T}}p_{\nu_\mathrm{T}}\cos(\phi_\ell - \phi_\nu) - p_{\ell_z}p_{\nu_z}\right). \tag{4.12}$$

Defining

$$\alpha \equiv \frac{m_W^2}{2} + p_{\ell_\mathrm{T}}p_{\nu_\mathrm{T}}\cos(\phi_\ell - \phi_\nu) \tag{4.13}$$

and solving for p_{ν_z} leads to a quadratic solution with a two-fold ambiguity:

$$p_{\nu_z} = \frac{\alpha p_{\ell_z}}{E_\ell^2 - p_{\ell_z}^2} \pm \left[\underbrace{\left(\frac{\alpha E_\ell}{E_\ell^2 - p_{\ell_z}^2}\right)^2 - \frac{E_\ell^2\, p_{\nu_\mathrm{T}}^2}{E_\ell^2 - p_{\ell_z}^2}}_{\equiv\beta}\right]^{1/2}. \tag{4.14}$$

In the case of two real solutions (or $\beta > 0$) to Equation 4.14, the solution with the smaller $|p_{\nu_z}|$ is chosen. This choice is based on signal simulation studies that show it results more often in a better match to the real p_{ν_z}. In the case of complex solutions (or $\beta \leq 0$), only the real part of the solution is used.

Post-preselection distributions of the "low" and "high" $|p_{\nu_z}|$ solutions, along with the real part of the imaginary solutions and the truth p_{ν_z}, are shown in Figure

4.7 for several ggF and VBF signal MC samples. Also, the superior accuracy of the low $|p_{\nu_z}|$ solution is shown in Figure 4.8, which compares the resolutions (truth p_{ν_z} − reconstructed p_{ν_z}) of the various p_{ν_z} solutions, and in Table 4.10, which shows the percentage of post-preselection events in which the truth p_{ν_z} is closer to the low $|p_{\nu_z}|$ solution than the high solution. As evidenced in both the aforementioned figure and table, the efficiency of the lower $|p_{\nu_z}|$ solution with respect to the high solution worsens with increasing Higgs mass, but always stays above 58%.

Table 4.10: Percentage of post-preselection NWA signal events with a truth p_{ν_z} closer to the low $|p_{\nu_z}|$ solution than the high solution.

Sample	300 GeV	500 GeV	700 GeV	900 GeV	1100 GeV	1300 GeV	1500 GeV
ggF	71.0	64.9	62.5	60.7	59.3	58.6	58.6
VBF	78.4	66.9	62.8	60.9	60.2	59.0	58.1

Further studies were performed to address expressed concerns that our method of choosing the p_{ν_z} solution might depend on the number of primary vertices (NPV) in the event, or in other words, that it might depend on the pile-up. These studies show no significant correlation between the NPV and the quality (efficiency and resolution) of our neutrino p_{ν_z} choice in our MC signal samples, as can be seen in Figures 4.9 and 4.10.

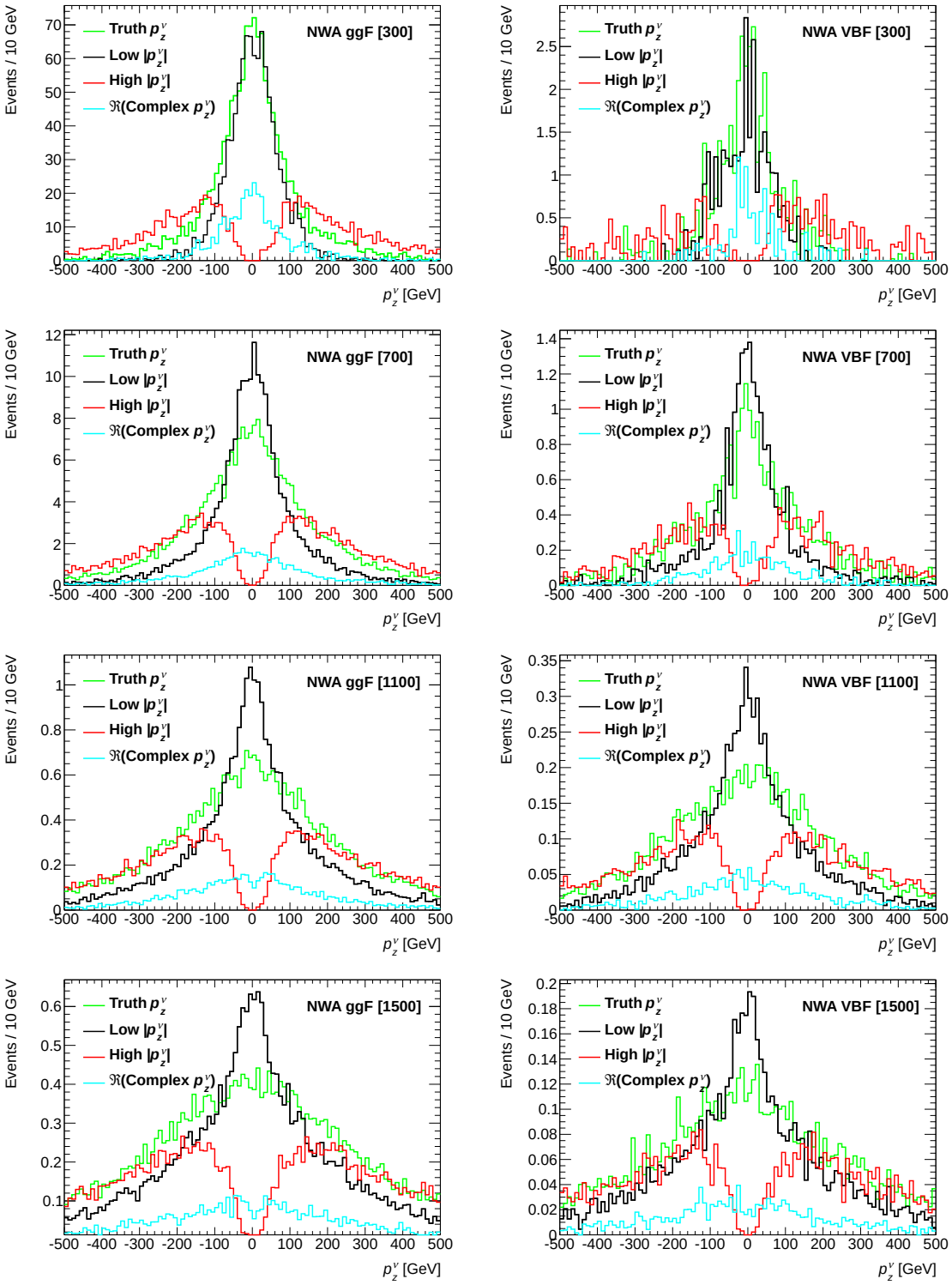

Figure 4.7: p_{ν_z} distributions comparing the low and high solutions, along with the real part of the imaginary solutions and the truth value, for events that pass the ggF or VBF preselection corresponding to the respective sample type.

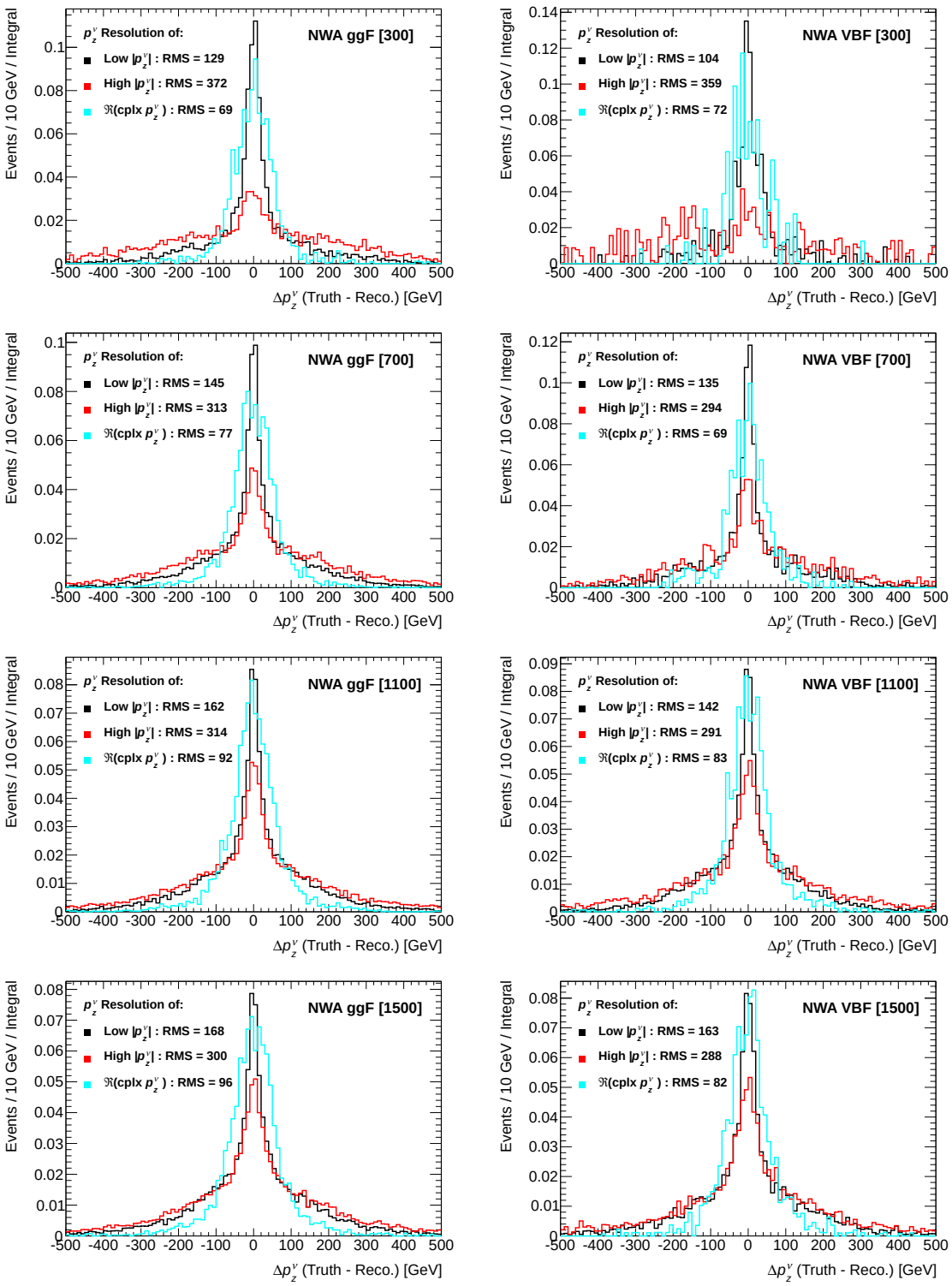

Figure 4.8: p_{ν_z} resolutions (truth - reconstruction) for the low, high, and real part of the imaginary solutions for events that pass the ggF or VBF preselection corresponding to the respective sample type.

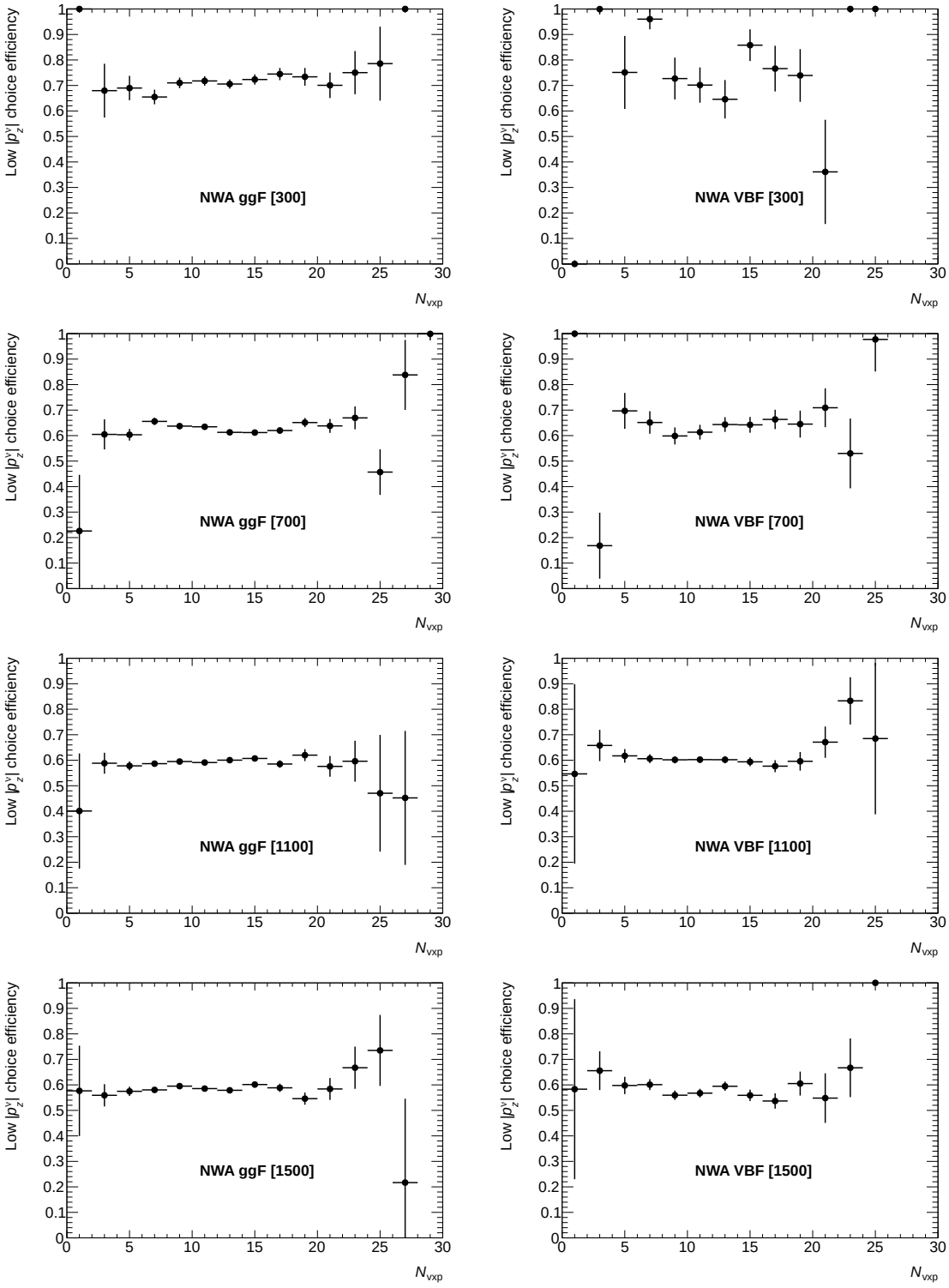

Figure 4.9: Profile histograms of the average efficiency of the low $|p_{\nu_z}|$ choice in bins of the number of primary vertices for events that pass the ggF or VBF preselection corresponding to the respective sample type.

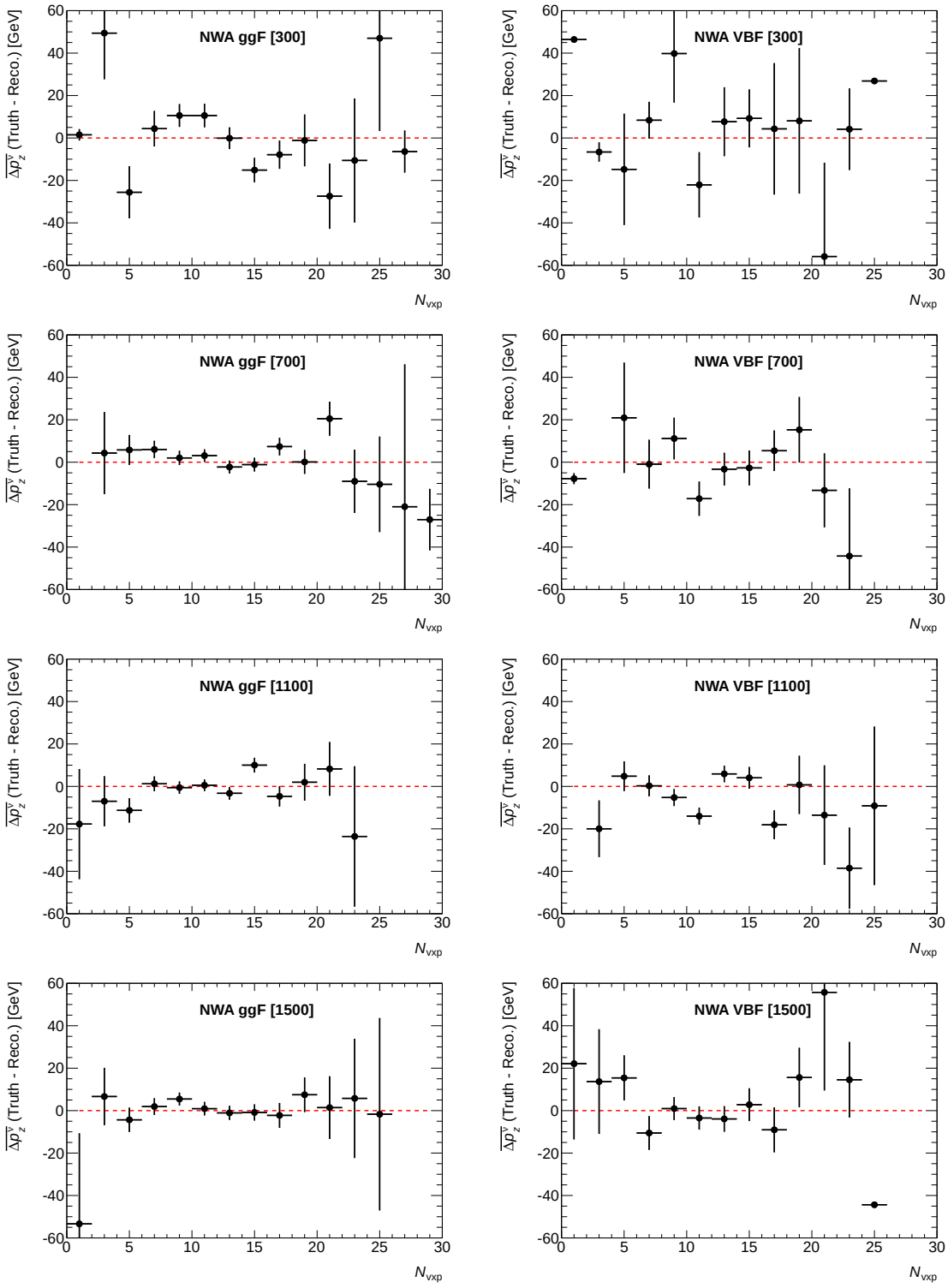

Figure 4.10: Profile histograms of the average p_{ν_z} resolution (for the low $|p_{\nu_z}|$ choice) in bins of the number of primary vertices for events that pass the ggF or VBF preselection corresponding to the respective sample type.

4.7.2 Experimental mass resolution

Now with the p_{ν_z} chosen, the WW system (i.e. the theorized high-mass Higgs boson) can be fully reconstructed including most importantly its invariant mass $m_{\ell\nu jj}$. The experimental resolution of $m_{\ell\nu jj}$ depends on the kinematic resolutions of the constituent objects and is thereby limited by the resolutions of the jet momentum, $E_{\mathrm{T}}^{\mathrm{miss}}$, and lepton momentum. In addition, if a jet not originating from $W \to q\bar{q}$ is used to reconstruct the hadronic W Lorentz vector, large tails in the reconstructed Higgs mass can be introduced.

The Narrow Width Approximation (NWA) signal samples are used to study the experimental mass resolution. Since these samples are generated with a mass distribution width of 4 MeV, the observed mass resolution following reconstruction can almost entirely be attributed to the experimental resolution.

Figure 4.11 shows the experimental mass resolution as a function of the boson mass (m_H) of the signal samples, where the resolution is taken to be the σ of a Gaussian fit to the peak region of the reconstructed $m_{\ell\nu jj}$ distribution following the signal preselection. The VBF resolution is slightly better than the ggF resolution, and both resolutions worsen slowly with increasing mass.

Also in Figure 4.11, the natural width of a SM-like Higgs boson is shown. The search for a light ($m_H \leq 400\,\mathrm{GeV}$) SM-like Higgs boson is limited by the experimental resolution, but since the SM natural width increases faster than the experimental resolution the search for a heavier SM-like Higgs boson is completely dominated by the natural width of the boson. At $m_H = 1\,\mathrm{TeV}$ the experimental resolution is similar

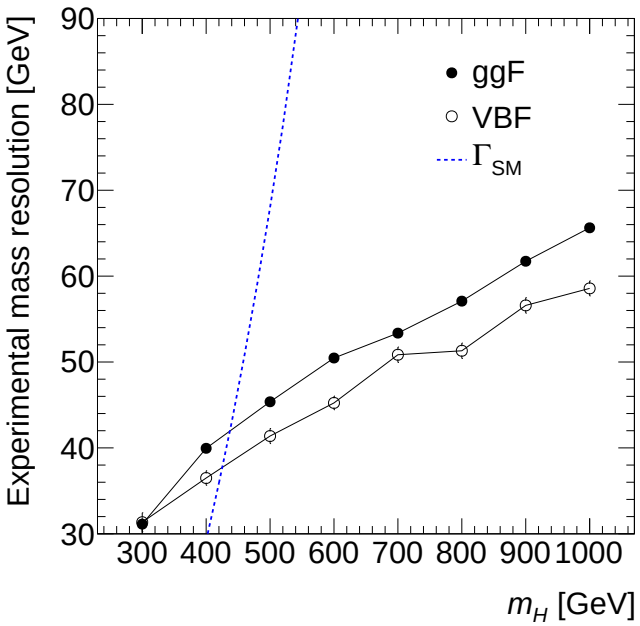

Figure 4.11: The experimental mass resolution as a function of m_H. The dashed line indicates the natural width of a SM-like Higgs boson.

to 0.1 Γ_{SM}, which is thus the smallest fraction of Γ_{SM} that is directly accessible in this analysis.

Further studies analyze the experimental mass resolution's dependence on the type of jet(s) used to reconstruct the Higgs and on the quality of the p_{ν_z} choice. Figure 4.12a shows the experimental mass resolution similarly to the previous figure, but this time with the merged and resolved event categories separated. The large uncertainties for some mass points come from Gaussian fits to low statistic categories. For both the ggF and VBF samples the resolved events have a poorer mass resolution than the merged events and the separation grows with increasing m_H. However, this is not a direct comparison of the two hadronic W reconstruction methods, but rather a comparison between the final categories.

For a more direct comparison of the two hadronic W reconstruction methods'

mass resolutions, the two methods are compared using the same events. In order to do this comparison after the entire event preselection, events for the comparison are required to pass both the merged and resolved category requirements. This comparison is shown in Figure 4.12b where the resolutions of the two methods are consistent with each other within uncertainties for the ggF and VBF cases. The large uncertainties in this figure at high m_H come from the small number of events passing both the resolved and boosted selections in the primarily boosted region.

Lastly, Figure 4.13 shows the contributions to the reconstructed NWA Higgs mass for several ggF and VBF sample mass points from the various p_{ν_z} cases: keeping the real part of the imaginary solutions, taking the lower $|p_{\nu_z}|$ solution and being closer than the higher $|p_{\nu_z}|$ solution to the truth value (labelled as "Correct"), and taking the lower $|p_{\nu_z}|$ solution and being further than the higher solution from the truth value (labelled as "Incorrect"). The incorrect p_{ν_z} solution events contribute significantly to the low-mass tails of the distributions, show a general shift toward lower masses, and have worse resolutions than the other two components.

The latter two points are highlighted even more clearly in Figure 4.14 where the three components are put on equal footing via normalization to better compare their shapes. In this second figure it is also shown that the correct p_{ν_z} solution events and the complex solution events have very similar resolutions and shapes for all sample mass points. Note that the length of the x-axis range of all plots in both figures is the same in order to visually display the changing mass resolution with m_H.

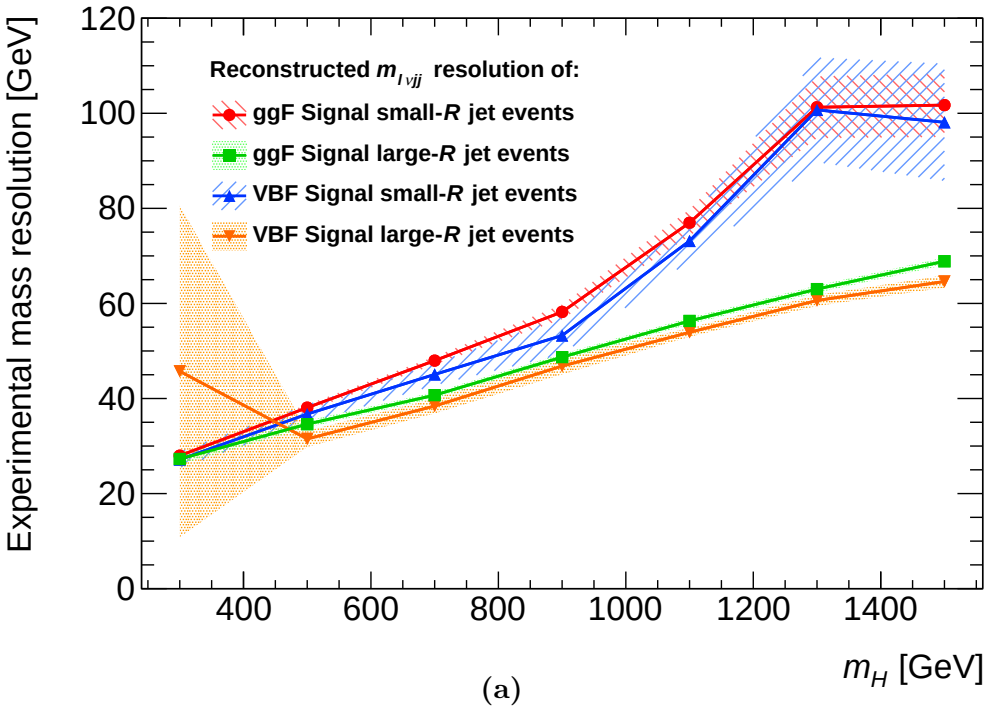

(a)

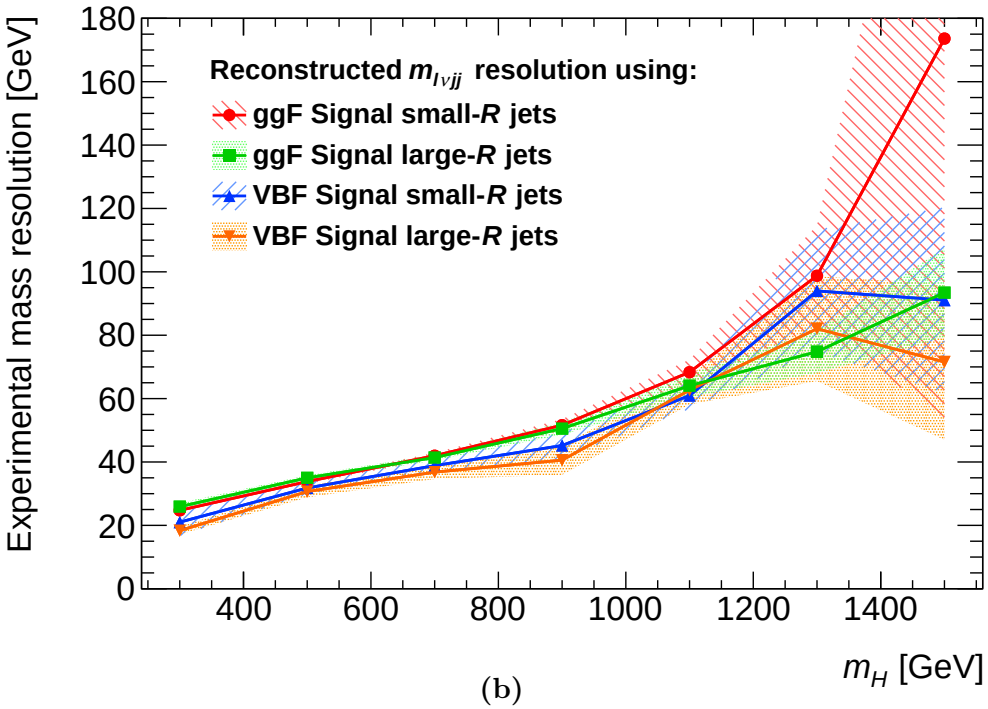

(b)

Figure 4.12: The experimental mass resolution as a function of m_H split into ggF and VBF signal events. The uncertainties of the Gaussian fits to the mass distributions are shown as shaded/hatched bands. **(a)** Comparison between the orthogonal merged (large-R) and resolved (small-R) event categories. **(b)** Comparison between the use of small-R jets and a single large-R jet in reconstructing the Higgs within events that would have passed both the merged and resolved preselections.

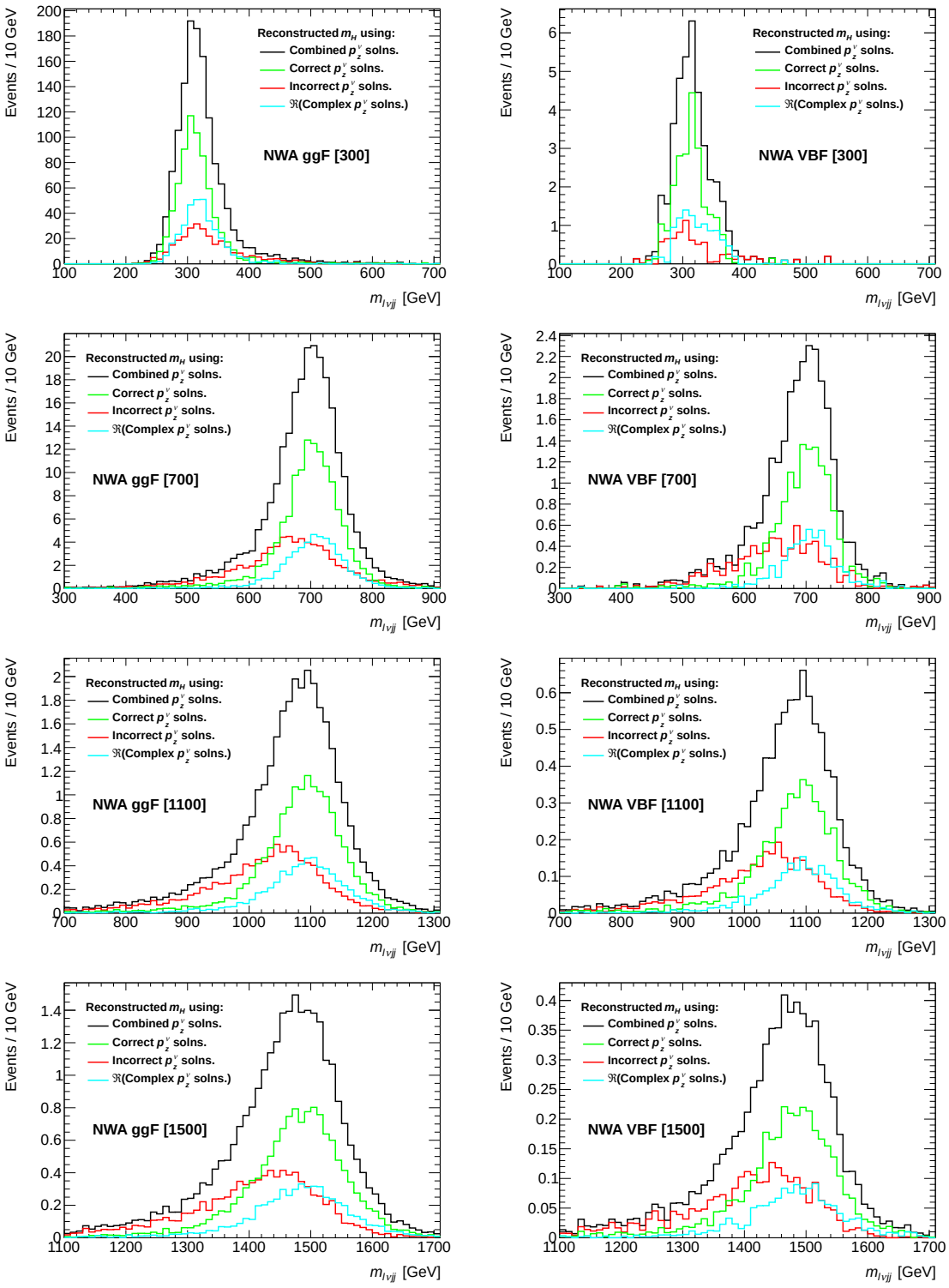

Figure 4.13: $m_{\ell\nu jj}$ distribution split into components based on the p_{ν_z} solution used: "Correct" meaning the low $|p_{\nu_z}|$ is closer to the truth, "Incorrect" meaning the unused high $|p_{\nu_z}|$ is closer to the truth, and the real component of complex p_{ν_z} solutions. Events are shown that pass the ggF or VBF SR preselection corresponding to the respective sample type.

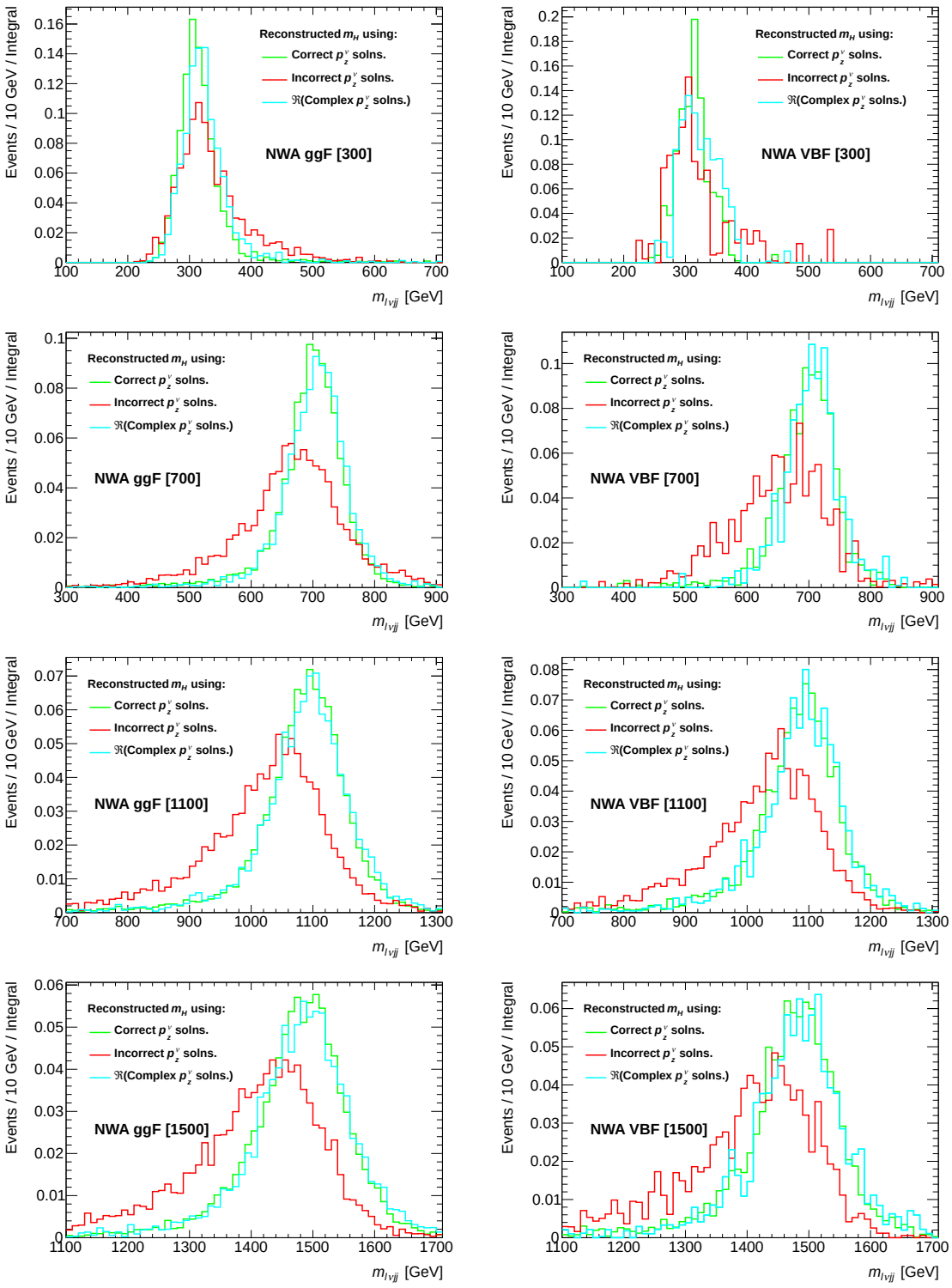

Figure 4.14: Components of the $m_{\ell\nu jj}$ distribution normalized by their respective integrals and split based on the p_{ν_z} solution used: "Correct" meaning the low $|p_{\nu_z}|$ is closer to the truth, "Incorrect" meaning the unused high $|p_{\nu_z}|$ is closer to the truth, and the real component of complex p_{ν_z} solutions. Events are shown that pass the ggF or VBF SR preselection corresponding to the respective sample type.

4.7.3 Alternate W-Jet Selection Method

An alternate method for selecting the pair of small-R jets from the hadronic W decay is studied, but was ultimately not used in the final analysis for reasons stated at the end of this section. As a reminder, the nominal selection method for the pair of small-R W-jets consists of finding the pair of small-R jets (from a subset of jets passing some minimum kinematic/overlap requirements) with an invariant mass in closest proximity to the W pole mass, except when multiple pairs fall within a small window around the W mass in which case the pair with the highest p_{T} sum is chosen. The alternate selection method, referred to hereafter as the "kinematic fitter," is quite similar to the nominal method in that it searches for a pair of jets from the same subset of jets and favorably biases pairs with invariant masses close to the W mass.

The kinematic fitter is based on a χ^2 minimization using the known W boson mass as a constraint and allowing the jet p_{T}'s to vary within their uncertainties (given by their jet energy resolutions provided by the Jets and Etmiss Combined Performance Group). The χ^2 to be minimized for each possible jet pair in an event is given by

$$\chi^2 = \left(\frac{m_W - m_{jj}^{\mathrm{fit}}}{\Gamma_W}\right)^2 + \sum_{i=1,2}\left(\frac{p_{\mathrm{T}_i} - p_{\mathrm{T}_i}^{\mathrm{fit}}}{\sigma_i}\right)^2, \tag{4.15}$$

where m_W and Γ_W are the known mass and width of a W boson; m_{jj}^{fit} is the iteratively calculated invariant mass of the jet pair using the iteratively varied $p_{\mathrm{T}_i}^{\mathrm{fit}}$ of each jet along with each jet's original η, ϕ, and mass; and σ_i is the jet energy resolution of the i^{th} jet. After the minimized χ^2 of each jet pair has been calculated, the pair with

the smallest minimized χ^2 is selected to be the W-jet pair. The selected jets are then used, with their altered p_{T}'s, throughout the rest of the analysis including the reconstruction of the $m_{\ell\nu jj}$.

The primary potential benefits of using the kinematic fitter are an improved $m_{\ell\nu jj}$ resolution and an increased signal significance due to the much narrower signal m_{jj} distribution coming from the mass constraint in the χ^2 minimization. Using $s/\sqrt{s+b}$ as a measure of the signal significance, where s is the number of signal events selected in the SR and b is the number of background events, it is seen that the kinematic fitter does provide improvement for some mass points, but only about a 3% improvement at best. The improvement in the $m_{\ell\nu jj}$ resolution is equally marginal.

The absence of significant improvement in the signal significance seems to mostly stem from the fact that the background m_{jj} distributions also peak at the W pole mass when the kinematic fitter is used. The best improvement is found with the 400 GeV ggF CPS signal and the kinematic fitter actually gives worse signal significance for signals above 600 GeV. The decline of performance with increasing m_H is likely due to the merging of the jets coming from the highly boosted hadronic W which should be picked up as a single large-R jet by the merged selection, but rather the kinematic fitter grabs at least one incorrect small-R jet and manages to form a pair of jets with an invariant mass close to the W mass, resulting in a skewed result.

An approach to deal with the declining performance with increasing signal m_H is

to make a "sliding" cut on the χ^2 such that if the χ^2 is greater than the cut value the kinematic fitter jets are not used for that event and the nominal jet selection (including large-R jets) is used instead. The cut value gets smaller and smaller until above 600 GeV it goes to 0, thus eliminating the use of the kinematic fitter at higher masses.

However, due to the limited level of improvements shown, the complications to the analysis of a sliding χ^2 cut and altered jet p_{T}'s, and finally due to time constraints limiting further studies, it was decided to not include the kinematic fitter in the nominal analysis.

4.8 Final (Mass-Dependent) Selection

The sensitivity to a heavy Higgs boson is improved by applying tighter and additional cuts beyond the event preselection (described in Section 4.6.1) that depend on the hypothesized mass of the Higgs boson. The primary reason for the sensitivity improvement comes from the fact that the average kinematics of the final state objects change quite drastically with increasing m_H, especially their p_{T} and angular separation. This section describes the mass-dependent selection along with its optimization.

4.8.1 Procedure

The variables chosen for the mass-dependent selection are those that exhibit increasingly good separation of the signal and background distributions with increasing

m_H. They are listed below and their distributions following the event preselection are shown in Figures 4.15 – 4.17, highlighting the shapes of various SM-like signal mass hypotheses overlaying the background. The variables used depend on the production-mode category determined in the preselection. Those used for the ggF category are

- $p_{\mathrm{T},j}^{\mathrm{leading}}$: The leading small-R W-jet p_{T} (resolved events only).
- $p_{\mathrm{T},j}^{\mathrm{subleading}}$: The sub-leading small-R W-jet p_{T} (resolved events only).
- $p_{\mathrm{T},J}^{\text{large-}R}$: The large-R W-jet p_{T} (merged events only).
- $p_{\mathrm{T,lep}}$: The lepton p_{T}.
- $\Delta\phi_{jj}$: The azimuthal angle between the two small-R W-jets (resolved events only).
- $\Delta\phi_{\ell\nu}$: The azimuthal angle between the lepton and neutrino.
- $E_{\mathrm{T}}^{\mathrm{miss}}$: The magnitude of the missing transverse momentum.

Those used for the VBF category are

- $\Delta\phi_{jj}$: The same as for ggF.
- $\Delta\phi_{\ell\nu}$: The same as for ggF.
- p_{T}-balance : The balance in p_{T} of the final state particles.

There are fewer mass-dependent cuts for VBF events than for ggF events because of the lower statistics in the VBF category, which is partly due to the more stringent

VBF preselection. The p_{T}-balance cut is only used for VBF events (as it only shows significant improvement there) and is defined by

$$p_{\mathrm{T}}\text{-balance} = \frac{|\,(\vec{\mathbf{p}}_{\ell} + \vec{\mathbf{p}}_{\nu} + \vec{\mathbf{p}}_{j_1} + \vec{\mathbf{p}}_{j_2})_{\mathrm{T}}\,|}{p_{\mathrm{T},\ell} + p_{\mathrm{T},\nu} + p_{\mathrm{T},j_1} + p_{\mathrm{T},j_2}} \tag{4.16}$$

where j_1 and j_2 are the leading and sub-leading small-R W-jets in the case of resolved events. In the case of merged events, the terms representing j_1 and j_2 are replaced with a single term $p_{\mathrm{T},J}$ representing the single large-R W-jet.

The optimal mass-dependent cut values for the selected variables are determined based on maximizing an estimator of the signal significance $s/\sqrt{s+b}$, where s is the number of signal events and b is the number of background events. Other estimators for the significance, namely $s/\sqrt{b}$ and $s/\sqrt{b+\Delta b}$ (where $\Delta b = 0.1b$ or $0.3b$), provide the same optimal cut values. Since the majority of signal events are localized to a small, defined region in $m_{\ell\nu jj}$, the significance calculation does not include all signal and background events that pass the preselection, but rather includes only those which fall into this signal-rich optimization $m_{\ell\nu jj}$ region. The range of the optimization region is m_H dependent as it is defined as including 90% of the signal events (post-preselection) centered about the mean of the reconstructed Higgs mass distribution.

The mass-dependent cut values are optimized for the mass range $300\,\mathrm{GeV} \leq m_H \leq 1000\,\mathrm{GeV}$ in $100\,\mathrm{GeV}$ steps. The optimal cut value for each selected variable and mass point is determined by a scan over a range of cut values at each of which the significance is calculated. The cut value that corresponds to the largest significance is selected as the optimal cut for that variable and mass point. Optimization cut-scans

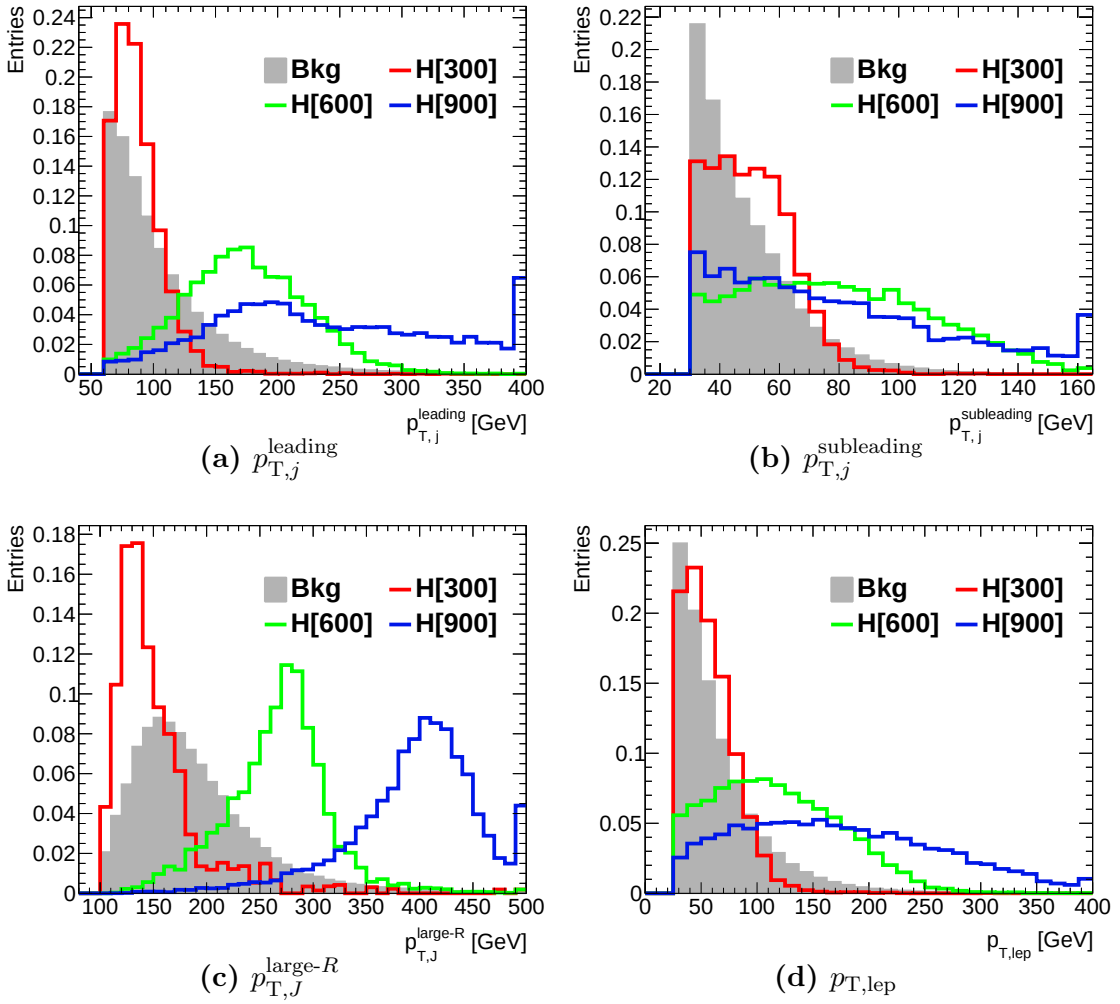

(a) $p_{\mathrm{T},j}^{\mathrm{leading}}$ (b) $p_{\mathrm{T},j}^{\mathrm{subleading}}$

(c) $p_{\mathrm{T},J}^{\text{large-}R}$ (d) $p_{\mathrm{T,lep}}$

Figure 4.15: Post-preselection distributions of the discriminating variables used in the mass-dependent selections in the ggF category. Three ggF SM-like signals are shown along with the total background. All distributions are normalized to unity.

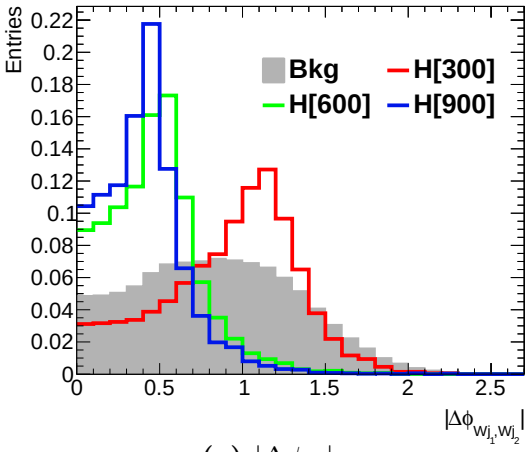

(a) $|\Delta\phi_{jj}|$

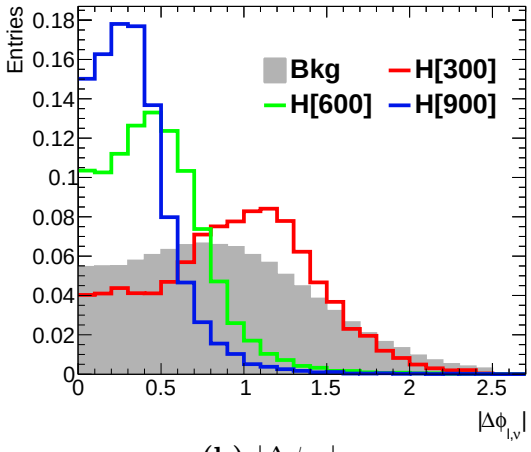

(b) $|\Delta\phi_{\ell\nu}|$

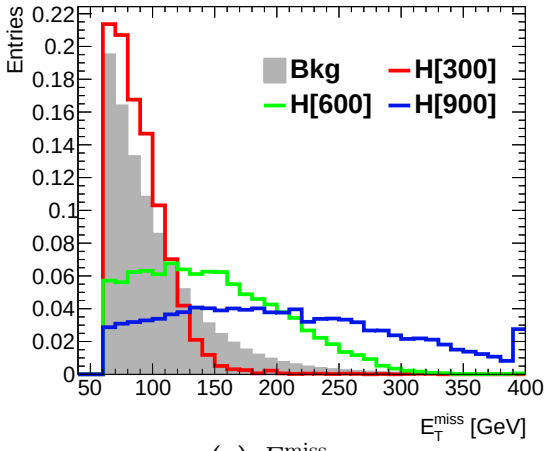

(c) $E_{\mathrm{T}}^{\mathrm{miss}}$

Figure 4.16: Post-preselection distributions of the discriminating variables used in the mass-dependent selections in the ggF category. Three ggF SM-like signals are shown along with the total background. All distributions are normalized to unity.

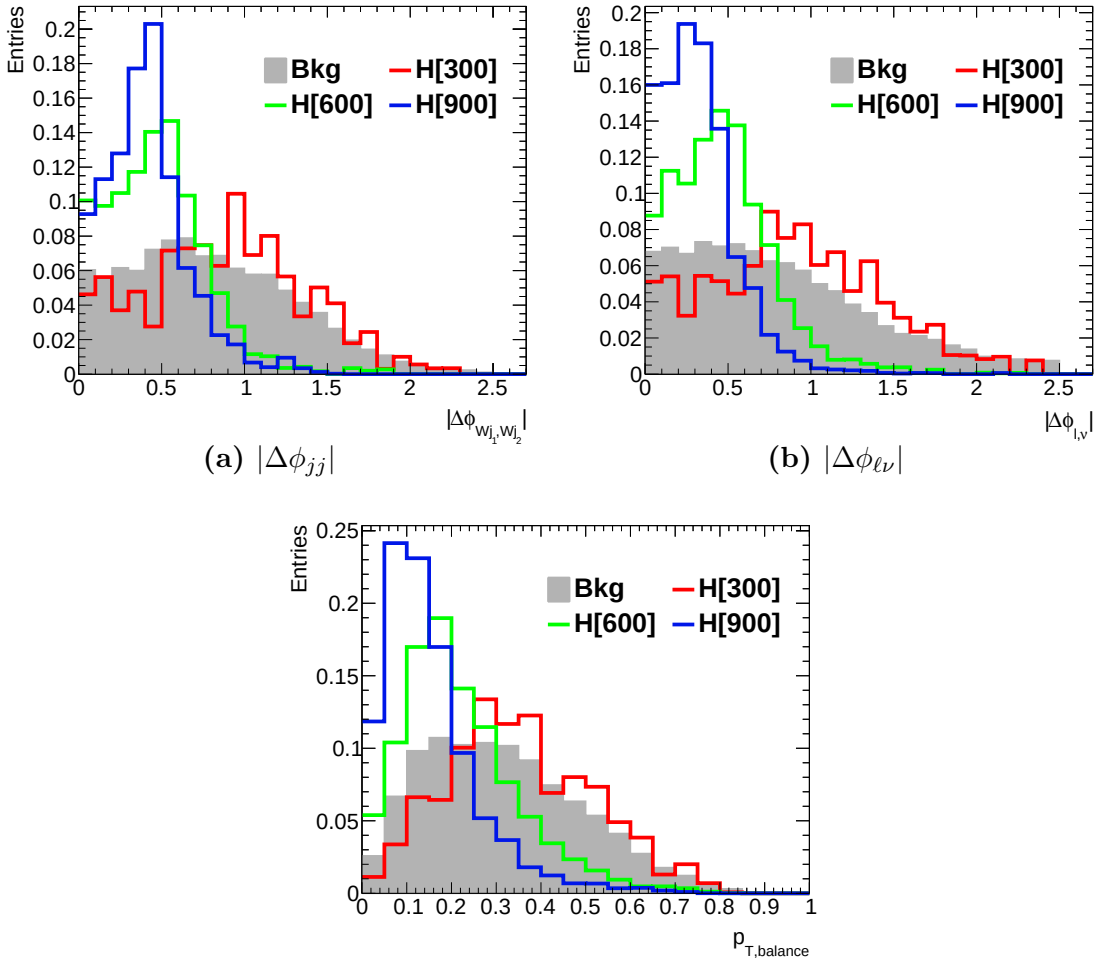

(a) $|\Delta\phi_{jj}|$ **(b)** $|\Delta\phi_{\ell\nu}|$

(c) p_{T}-balance

Figure 4.17: Post-preselection distributions of the discriminating variables used in the mass-dependent selections of the VBF category. Three VBF SM-like signals are shown along with the total background. All distributions are normalized to unity.

are shown in Figures 4.18 and 4.19 for the variables $|\Delta\phi_{\ell\nu}|$ and $p_{\mathrm{T},j}^{\mathrm{leading}}$, respectively (the rest are cataloged in the ATLAS internal note for this analysis). These figures give yet another feel for how much the kinematics shift with m_H. Note that this procedure neglects correlations between the variables being optimized, because each cut-scan is done on a single variable with all other cuts fixed at their preselection values.

4.8.2 Final Cuts

Although this cut optimization procedure provides cut values for the best significance, it does not take into account the negative effects of too-low statistics due to the harshness of the cuts. Since this is not simply a cut-and-count analysis, but an analysis in which the shape of the $m_{\ell\nu jj}$ invariant mass is used in the fit, low statistics can diminish the shape information and therefore degrade the sensitivity in the final fit. In this analysis for the ggF category, when the optimized cuts are used, the statistics for both signal and background events are too low, especially at high mass, to even get a stable shape fit in the limit setting code. This is not the case for the VBF category as it is already protected by having fewer optimized cuts.

Thus, in order to regain statistics in the ggF category, the optimized $E_{\mathrm{T}}^{\mathrm{miss}}$ and p_{T} cuts found in the cut-scans are loosened at each mass point from their optimal value to the next-lower ($m_H - 100\,\mathrm{GeV}$) mass point's optimal value. The corresponding loss in significance is generally moderate, on the order of a few percent. Also, since the 300 GeV mass point cannot be loosened in this way, the $E_{\mathrm{T}}^{\mathrm{miss}}$ and p_{T} cuts for this

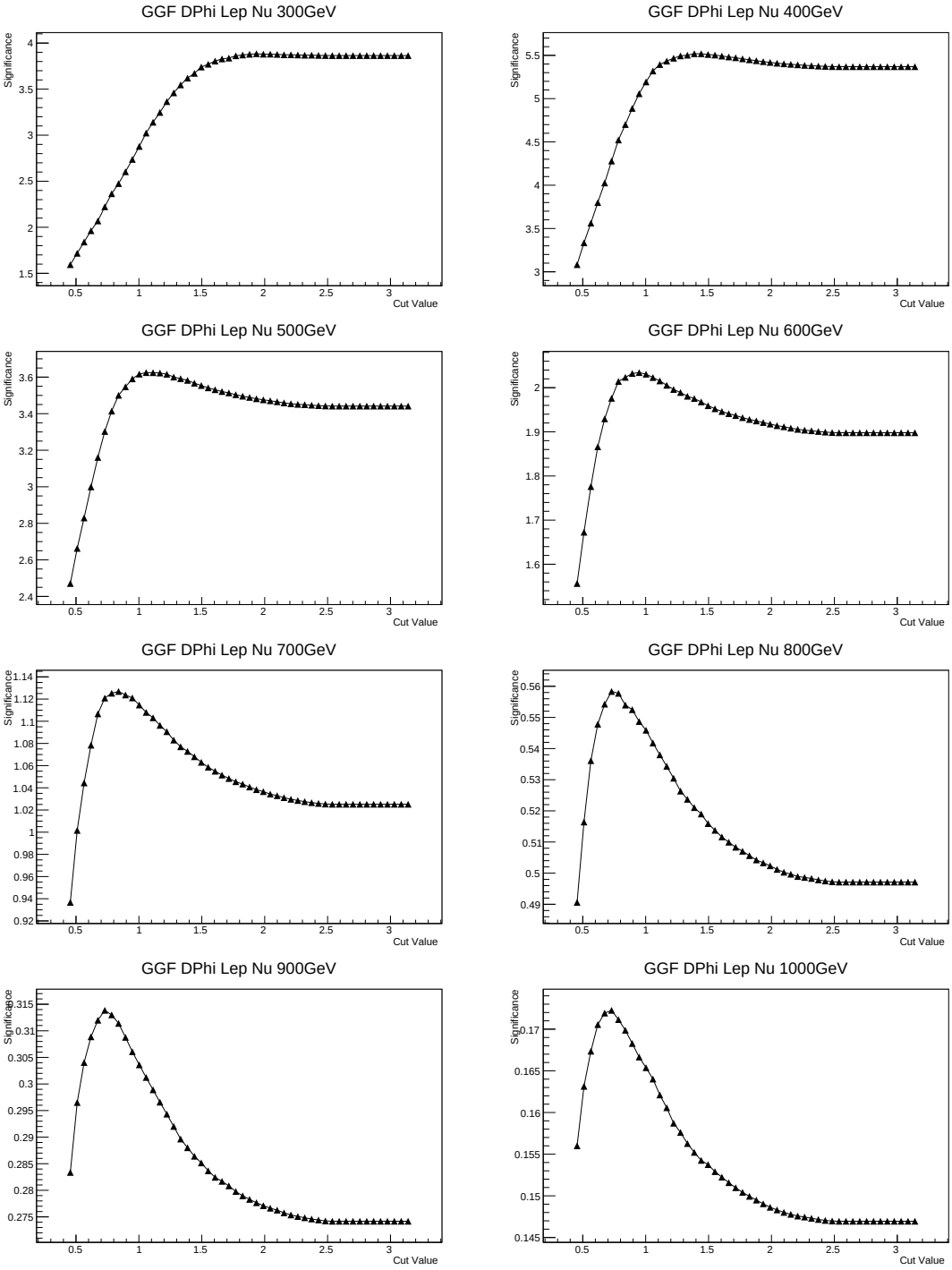

Figure 4.18: Significance as a function of cut value for $|\Delta\phi_{\ell\nu}|$ in the full m_H range of SM-like ggF samples.

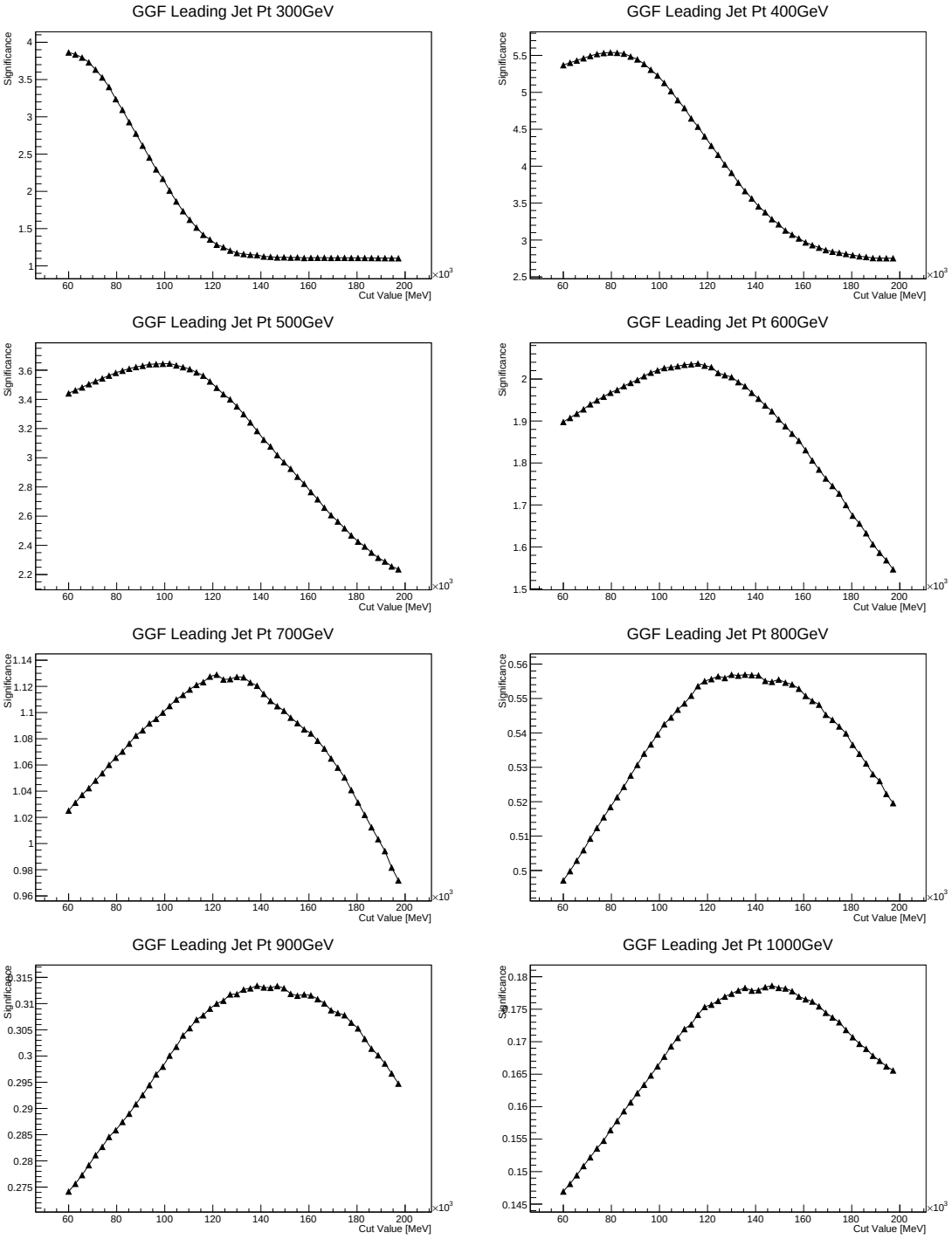

Figure 4.19: Significance as a function of cut value for the leading small-R W-jet p_{T} in the full m_H range of SM-like ggF samples.

mass point are kept at the preselection values. The last tweak to the optimized results is that the p_{T}-balance cut is not applied (i.e. p_{T}-balance ≤ 1) for $m_H < 500\,\mathrm{GeV}$ because the benefits in terms of significance gain are very small, with the optimal cut value determined by small statistical fluctuations.

The final mass-dependent cut values used in the analysis at each mass point are shown in Figures 4.20 and 4.21 for the ggF and VBF category variables, respectively. For comparison, the optimized cut values are also shown in both figures.

For both the ggF and VBF categories, the mass-dependent cut values for intermediate mass points are determined using a linear interpolation between the cut values of adjacent mass points. Also, for both production mode categories, the extended NWA signal search selections for mass hypotheses with $m_H > 1000\,\mathrm{GeV}$ use the $m_H = 1000\,\mathrm{GeV}$ optimized cut values.

4.9 Background Estimation

Recall that the background contributions in this analysis are estimated using a variety of methods as outlined in Section 4.2.2. The normalizations of the minor backgrounds, including diboson and $Z+$jets, are taken directly from the theory/MC, while the multi-jet, $W+$jets, and top backgrounds utilize the data in their estimations. This section outlines these data driven estimates.

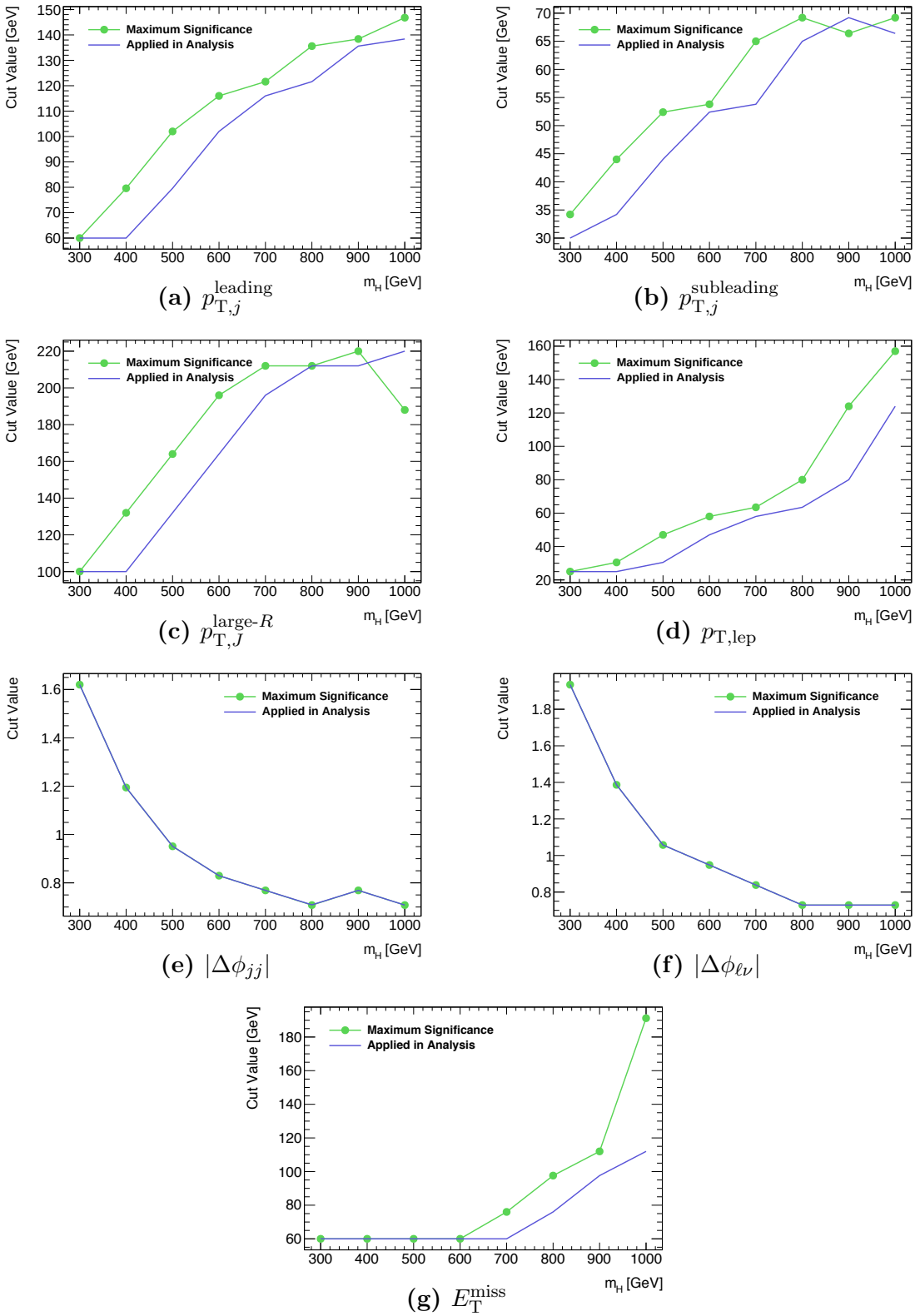

Figure 4.20: Cut values used in the analysis and optimal cut values (determined by maximum significance), as a function of m_H for each of the mass-dependent discriminating variables used in the ggF category.

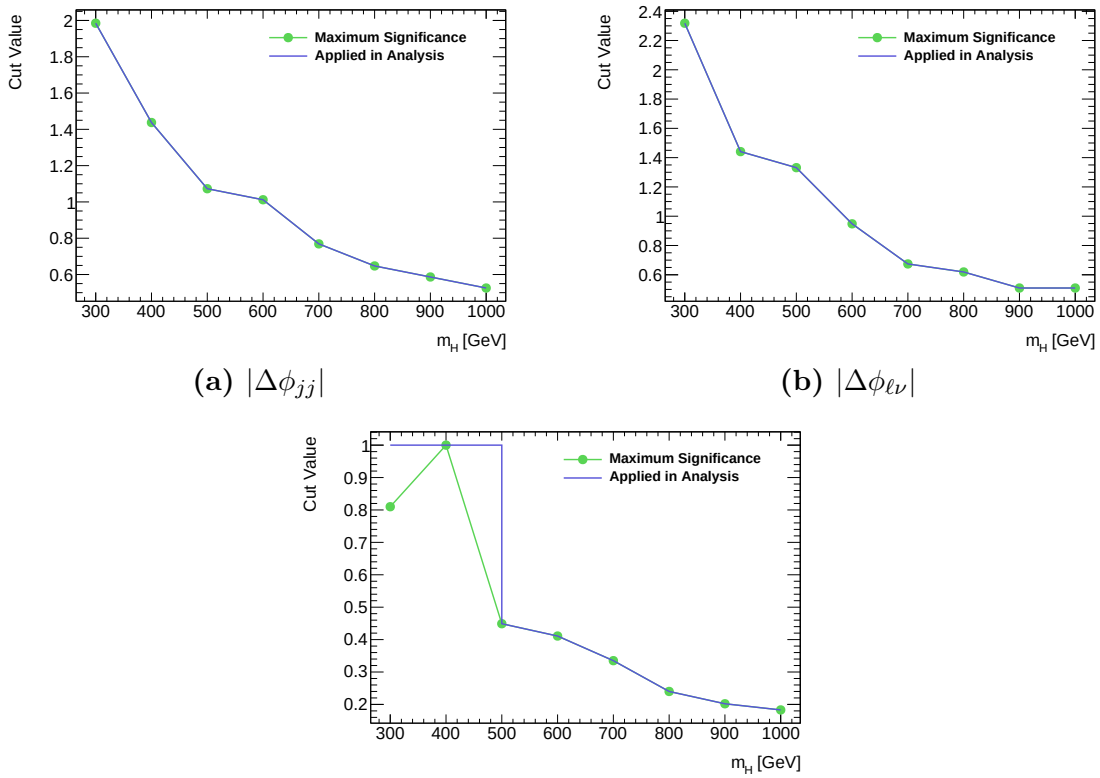

(a) $|\Delta\phi_{jj}|$ **(b)** $|\Delta\phi_{\ell\nu}|$

(c) p_{T}-balance

Figure 4.21: Cut values used in the analysis and optimal cut values (determined by maximum significance), as a function of m_H for each of the mass-dependent discriminating variables used in the VBF category.

4.9.1 Multi-Jet Background

The multi-jet (MJ) background contaminates the region of low $m_{\ell\nu jj}$ with multi-jet QCD events containing fake leptons. The contributions of the MJ background are difficult to model with MC, so a data-driven technique is employed, in which additional control regions and template fits to $E_{\mathrm{T}}^{\mathrm{miss}}$ spectra are used to estimate the MJ contributions in the various event regions. The primary items needed for this technique are MJ kinematic distribution templates from the data, rich with (ideally pure with) MJ events that are still kinematically close to the event regions they are

estimating contributions to.

For this purpose, every event region described in Section 4.6.2 (the SR, WCR, and TopCR) has an associated multi-jet control region (MJCR) with the same selection except for no $E_{\mathrm{T}}^{\mathrm{miss}}$ cut and an orthogonal loosened lepton definition. The loosened selection for electrons requires them to fail the *tight* identification requirements but still pass the *medium* identification requirements. For muons, the loosened selection requires the reversal of the impact parameter significance cut.

The amount of signal MC that enters these MJCRs is negligible, but there is a non-negligible contamination in each MJCR from the background MC. An example of this contamination can be seen in Figure 4.22, which shows the $m_{\ell\nu jj}$ distribution of the MJCR corresponding to the WCR $m_H = 300\,\mathrm{GeV}$ selection. These contributions are subtracted from the data in the kinematic distributions of the MJCRs in order to form the MJ distribution shape templates in each region.

Each control-region's MJ $E_{\mathrm{T}}^{\mathrm{miss}}$ template, together with all of the MC background $E_{\mathrm{T}}^{\mathrm{miss}}$ distributions (at their SM cross-sections and normalized to the data luminosity), is then fit to the data $E_{\mathrm{T}}^{\mathrm{miss}}$ spectrum in its corresponding control region (WCR or TopCR), with all cuts applied except for the $E_{\mathrm{T}}^{\mathrm{miss}}$ cut. The fits are template fits, in which the shapes of the $E_{\mathrm{T}}^{\mathrm{miss}}$ spectra are fixed and only their normalizations are free parameters. Thus, a fit results in a MJ scale factor to be used to normalize the MJ background in a given control region. Examples of the $E_{\mathrm{T}}^{\mathrm{miss}}$ template fits are shown in Figure 4.23 for the WCR $m_H = 300\,\mathrm{GeV}$ selection.

The SR cannot use such a fitting procedure because the data in the region could

contain significant amounts of signal. So although the shape of the MJ background in the SR is taken from the MJCR with the SR selection applied, its normalization uses the MJ scale factor derived in the WCR.

Lastly, to be clear, both the derivation and fitting of the MJ templates is done separately not only for the SR, WCR, and TopCR but also for ggF and VBF categories, for each signal mass point (because of the mass-dependent selections), for each lepton flavor, and for each lepton charge.

4.9.2 $W+$jets and Top Backgrounds

The $W+$jets and top-quark backgrounds are the most important in this analysis. The shapes of their $m_{\ell\nu jj}$ distributions and their overall normalizations are corrected using the data observed in their corresponding control regions (WCR and TopCR respectively). Their normalizations are determined from the final simultaneous fit (described in Section 4.12.1) to the signal and control regions. The modeling of their $m_{\ell\nu jj}$ distribution shapes is best observed by isolating their contributions to the data in their respective control regions.

This isolation is done by subtracting all of the non-$W+$jets (non-top) background contributions from the data in the ggF and VBF WCRs (TopCRs). The $W+$jets (top) MC is then normalized to the remaining data in the WCRs (TopCRs) for a shape comparison. The observed distributions (data - other backgrounds) differ significantly from the predicted distributions in all control regions as shown in Figure 4.24. The mismodeling is present in all lepton flavor and charge categories as

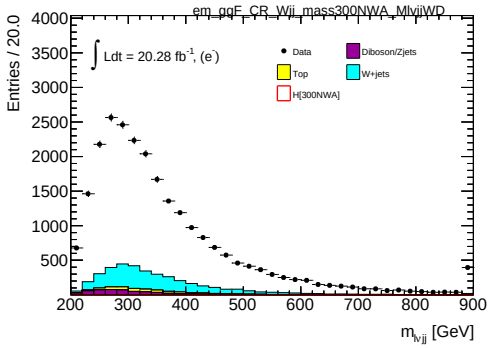

(a) WCR, ggF Selection, e^-

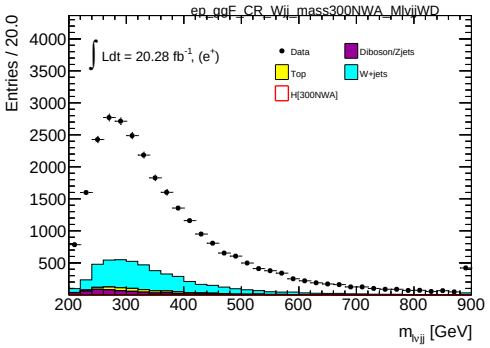

(b) WCR, ggF Selection, e^+

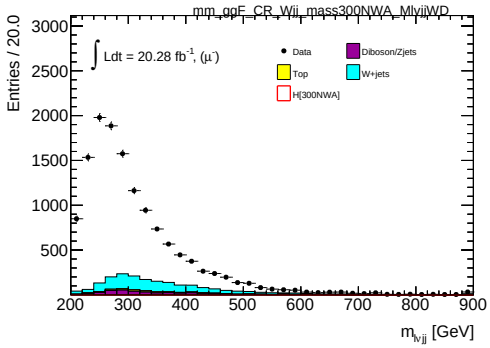

(c) WCR, ggF Selection, μ^-

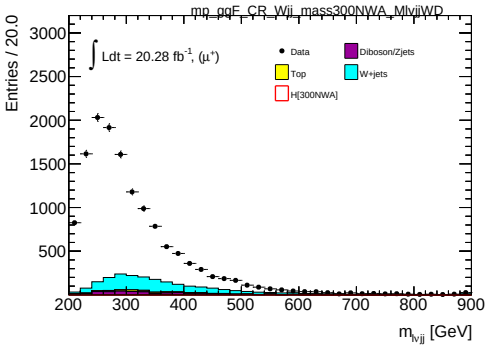

(d) WCR, ggF Selection, μ^+

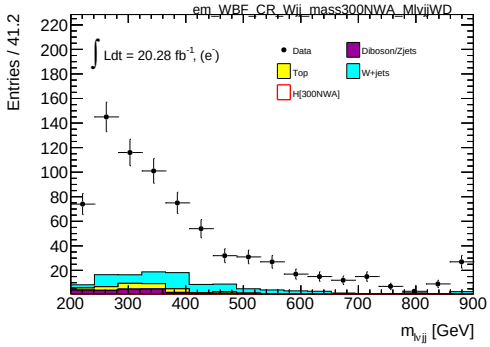

(e) WCR, VBF Selection, e^-

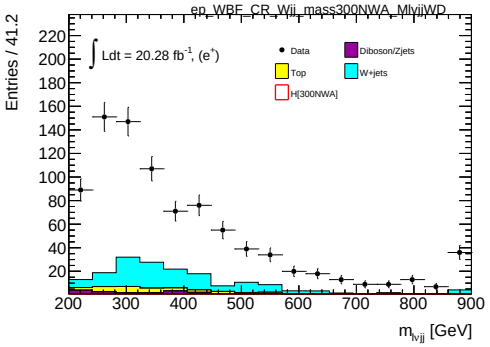

(f) WCR, VBF Selection, e^+

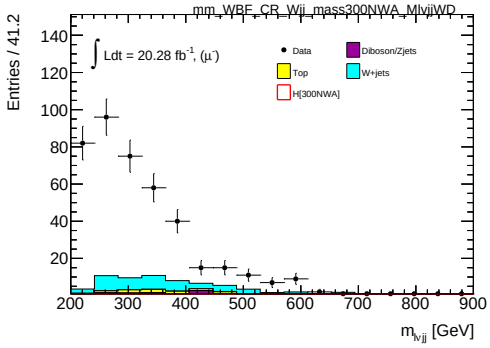

(g) WCR, VBF Selection, μ^-

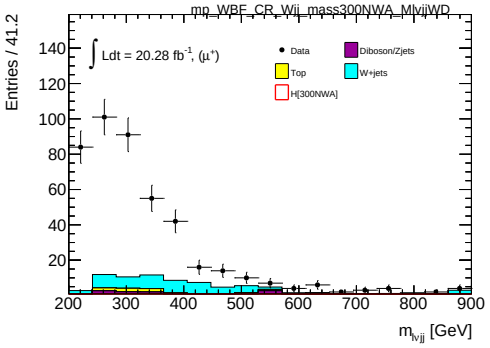

(h) WCR, VBF Selection, μ^+

Figure 4.22: $m_{\ell\nu jj}$ distributions in the MJCR with WCR, $m_H = 300\,\text{GeV}$ selections.

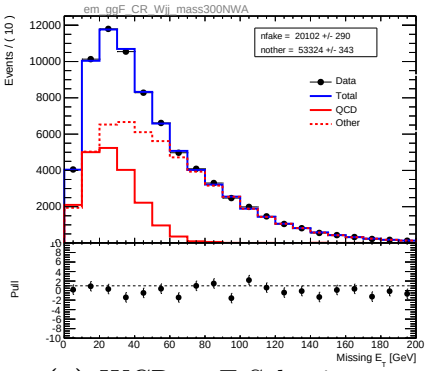

(a) WCR, ggF Selection, e^-

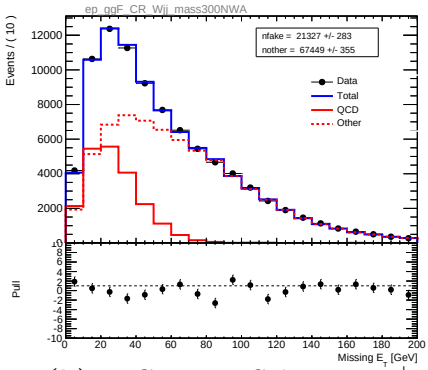

(b) WCR, ggF Selection, e^+

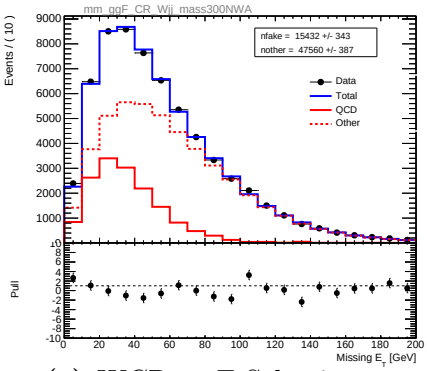

(c) WCR, ggF Selection, μ^-

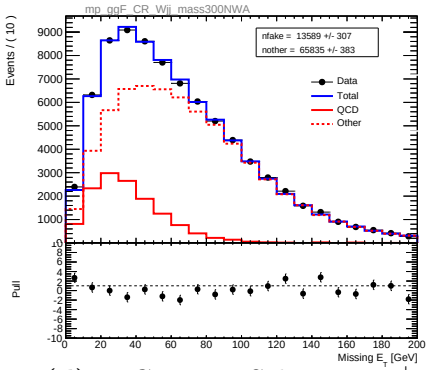

(d) WCR, ggF Selection, μ^+

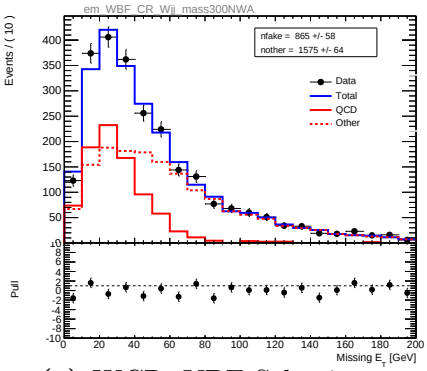

(e) WCR, VBF Selection, e^-

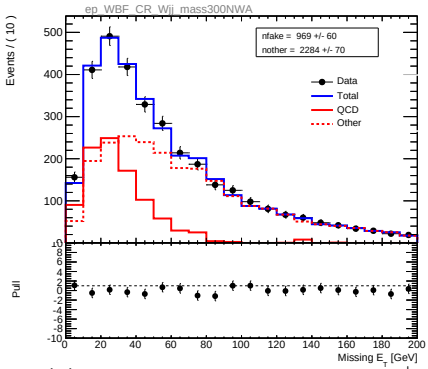

(f) WCR, VBF Selection, e^+

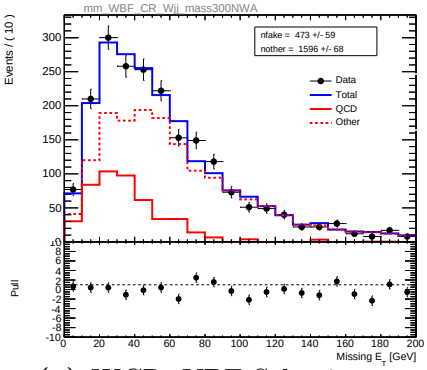

(g) WCR, VBF Selection, μ^-

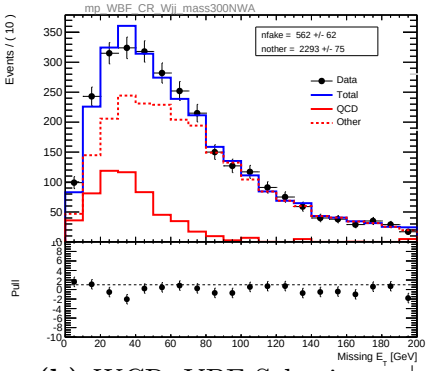

(h) WCR, VBF Selection, μ^+

Figure 4.23: Multi-jet $E_{\mathrm{T}}^{\mathrm{miss}}$ template fits in the WCR with 300 GeV selections.

well as in both merged and resolved W-jet categories.

W+jets shape correction The upper two plots in Figure 4.24 show the W+jets modeling in the ggF and VBF WCRs (with the $m_H = 300\,\text{GeV}$ selections applied) following the subtraction of all non-W+jets SM contributions and normalization to the remaining data. The W+jets mismodeling observed (most evident in the lower panels of the plots that show the data/MC ratio) is most likely due to mismodeling in the SHERPA MC samples because the mismodeling mostly goes away with the use of alternate W+jets samples, generated using ALPGEN+PYTHIA6. However, these alternate samples cannot be used in the analysis because they lack sufficient statistics in the SR, especially for large values of m_H.

Thus, the option chosen to deal with the mismodeling is to reweight the SHERPA W+jets MC events according to their invariant mass ($m_{\ell\nu jj}$) using the lowest-order polynomial function that reasonably fits the data/MC ratio. The mismodeling is corrected separately for ggF and VBF categories. The ggF reweighting function, shown in Figure 4.24a, is a second-order polynomial fit up to $m_{\ell\nu jj} = 1.7\,\text{TeV}$. The VBF reweighting function, shown in Figure 4.24b, is a third-order polynomial fit up to $m_{\ell\nu jj} = 0.9\,\text{TeV}$. Any event with $m_{\ell\nu jj}$ above the range of its category's fitted polynomial is reweighted using the same weight as that at the upper boundary of the fit.

Top shape correction The upper two plots in Figure 4.24 show the top modeling in the ggF and VBF TopCRs (with the $m_H = 300\,\text{GeV}$ selections applied) following

the subtraction of all non-top SM contributions and normalization to the remaining data. Due to the high purity of the TopCR, the subtracted $W+$jets contribution does not have the previously described $m_{\ell\nu jj}$ reweighting applied. As with the $W+$jets in the WCRs, differences in the $m_{\ell\nu jj}$ shapes are observed. The mismodeling is corrected by using first-order polynomial fits to the data/MC ratios in both the ggF and VBF TopCRs, as shown in Figures 4.24c and 4.24d.

As with the $W+$jets MC event reweighting, each top MC event passing the $m_H = 300\,\text{GeV}$ selection of any region (SR, WCR, or TopCR) is reweighted according to its invariant mass $m_{\ell\nu jj}$ using the fitted function of the category (ggF or VBF) it falls into. This actually encompasses all the $W+$jets and top MC events present in the final analysis, as all of the higher-mass cuts select subsets of the most inclusive set of events from the $m_H = 300\,\text{GeV}$ selection.

Result of corrections The effect of both reweightings on the predicted $m_{\ell\nu jj}$ distributions is shown in Figure 4.25 for the ggF and VBF WCRs and in Figure 4.26 for the ggF and VBF TopCRs. The plots on the left (right) of both figures show the predicted $m_{\ell\nu jj}$ distributions, and associated data/MC ratios, before (after) the reweightings are applied.

Although the $W+$jets and top MC mismodeling is also evident in several other kinematic variables, reweighting the $m_{\ell\nu jj}$ distributions proved to do the best job of simultaneously providing corrections to all of them. The systematic uncertainties assigned to the $W+$jets and top reweighting procedures are discussed in Section 4.10.4.

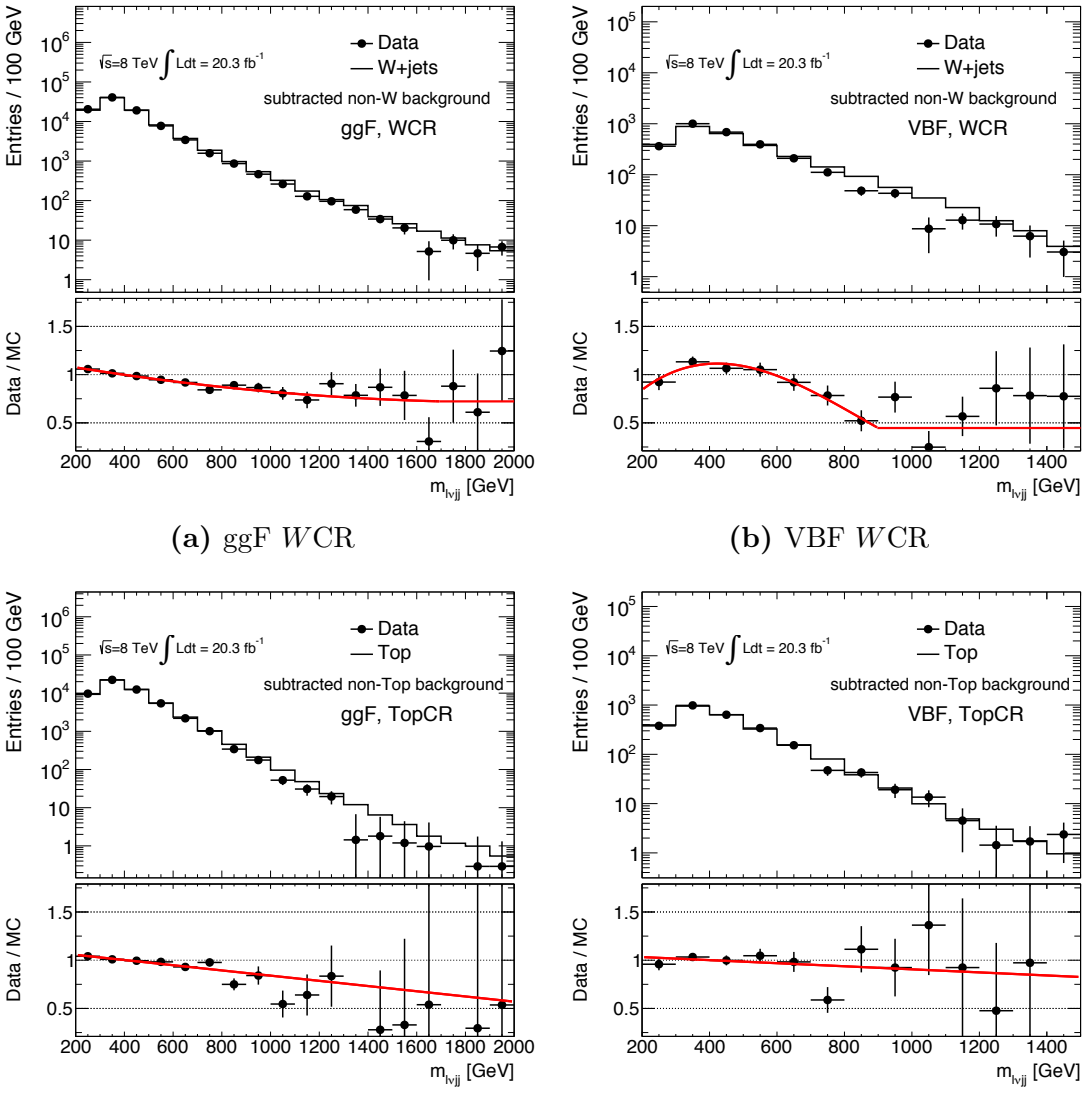

(a) ggF WCR **(b)** VBF WCR

(c) ggF TopCR **(d)** VBF TopCR

Figure 4.24: Data and MC shape comparison of the reconstructed Higgs mass in the (a) ggF WCR, (b) VBF WCR, (c) ggF TopCR, and (d) VBF TopCR after the $m_H = 300\,\text{GeV}$ selection. All the lepton flavor and charge categories are summed together. To isolate the effects of the $W+$jets [top-quark] background modeling, other contributions (top [$W+$jets], diboson, $Z+$jets, multi-jet) are subtracted from the data and the $W+$jets [top-quark] distribution is normalized to the remaining data in the WCR [TopCR]. The ratio of the data to the MC is shown in the bottom panel, along with a red line showing the fitted reweighting function.

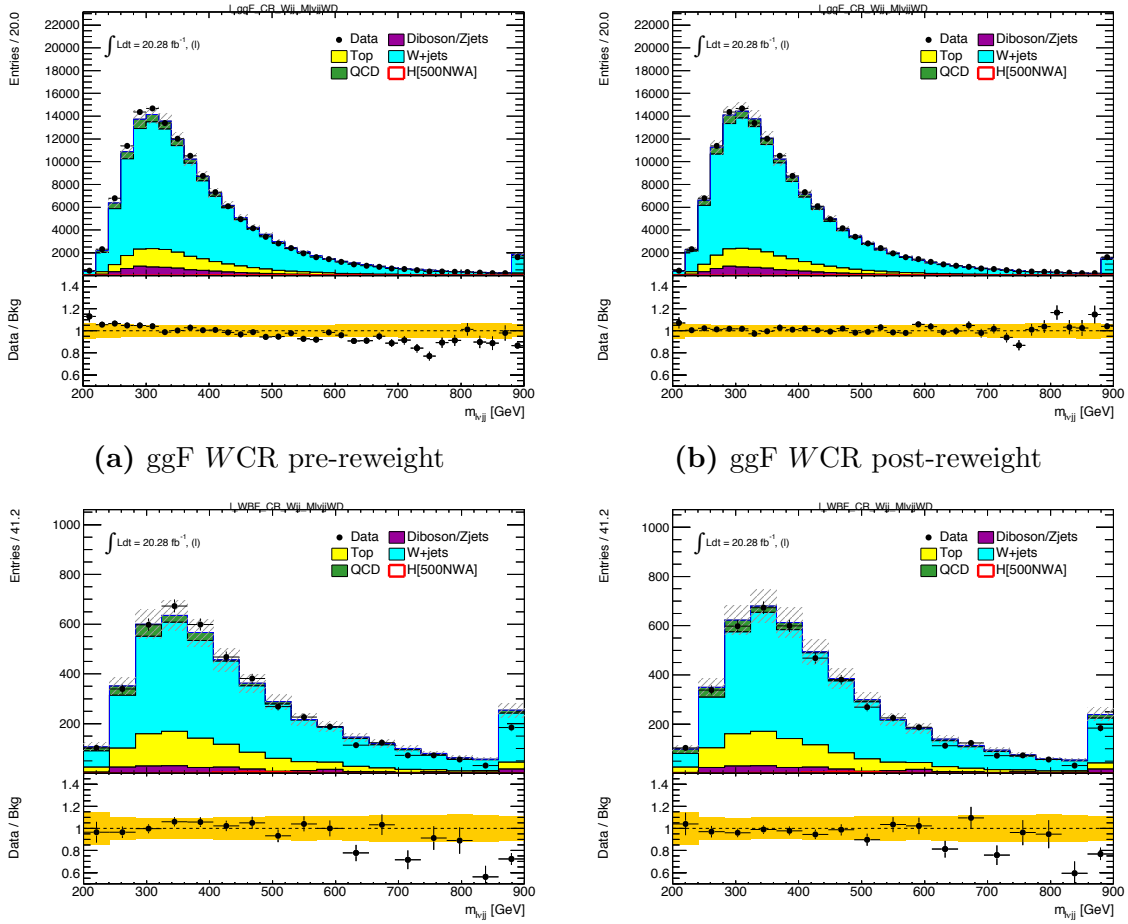

(a) ggF WCR pre-reweight

(b) ggF WCR post-reweight

(c) VBF WCR pre-reweight

(d) VBF WCR post-reweight

Figure 4.25: Comparison between data and MC of the reconstructed Higgs mass distributions before (left) and after (right) reweighting in the ggF (upper) and VBF (lower) WCRs. The ratio of the data to the MC is shown in the bottom panels along with the yellow band representing an early estimation of the combined statistical and systematic uncertainties on the background.

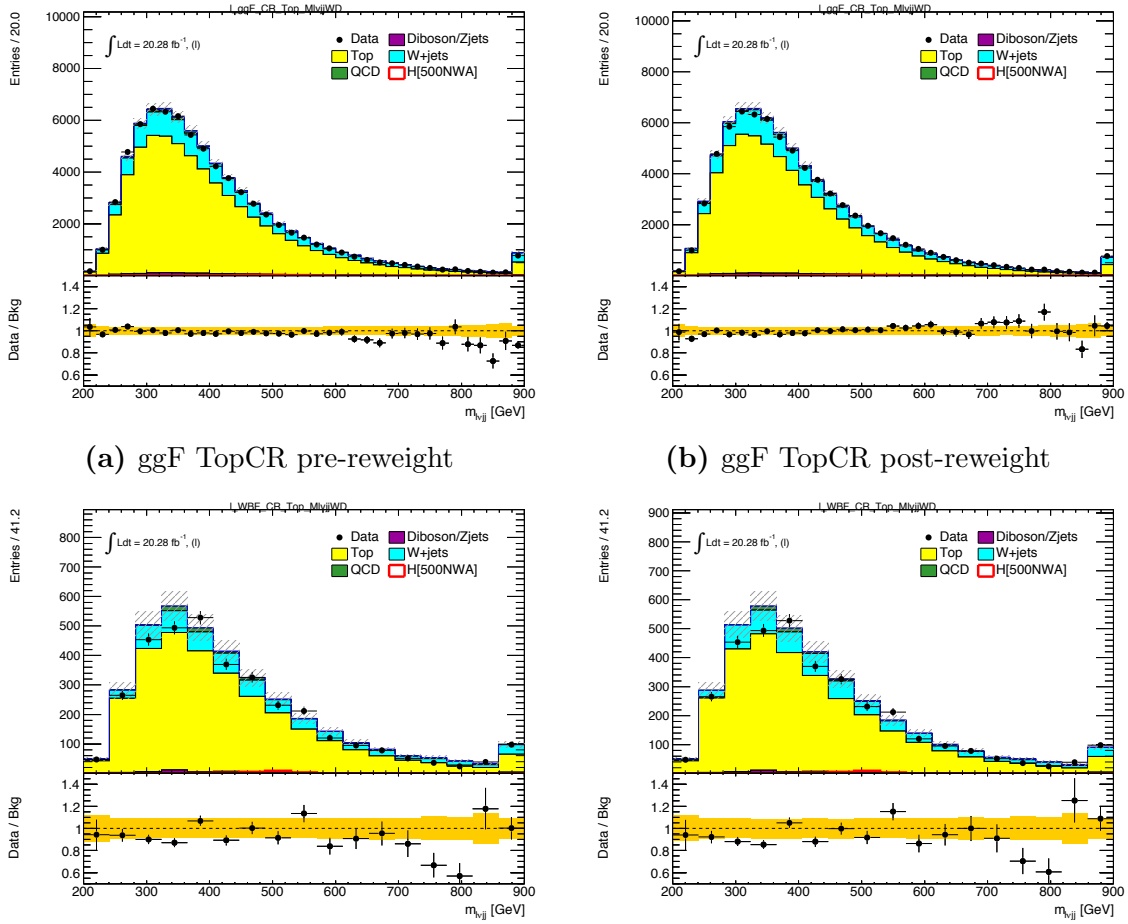

(a) ggF TopCR pre-reweight

(b) ggF TopCR post-reweight

(c) VBF TopCR pre-reweight

(d) VBF TopCR post-reweight

Figure 4.26: Comparison between data and MC of the reconstructed Higgs mass distributions before (left) and after (right) reweighting in the ggF (upper) and VBF (lower) TopCRs. The ratio of the data to the MC is shown in the bottom panels along with the yellow band representing an early estimation of the combined statistical and systematic uncertainties on the background.

4.10 Uncertainties

There are numerous sources of uncertainty in this complex analysis, especially due to the use of a broad range of reconstructed physics objects and background estimation techniques. The uncertainties roughly fall into three main categories:

Statistical: Uncertainties on the event yields simply determined by the number of observed data events in a given region: $N_{\text{obs}} \pm \sqrt{N_{\text{obs}}}$.

Theoretical: Systematic uncertainties primarily on aspects of the MC generation.

Experimental: Systematic uncertainties primarily on the reconstruction/modeling of objects and their properties in the detector, leading to uncertainties in the signal and background MC event yields.

Most experimental systematic uncertainties are implemented by varying the corresponding object property by one standard deviation ($\pm 1\sigma$) from its nominal value and re-running the full event selection (called a systematic variation). These consist of the uncertainties on the various reconstructed objects' energy scales and resolutions, and are listed in Table 4.11. Uncertainties that do not require a dedicated systematic variation include those that simply alter the scaling applied to an event, as is the case with uncertainties on the integrated data luminosity, as well as b-tagging and lepton scale factors.

Regardless of the need for a dedicated run variation, nearly all of the object uncertainties are calculated and provided by dedicated ATLAS Combined Performance groups in order to keep consistency between the many analyses using the same objects.

These are outlined below. The large-R jet resolution systematics are an exception to this and will be described, along with uncertainties on the interference reweighting and multi-jet background normalization, in proceeding dedicated subsections.

The lepton systematic uncertainties include those on the energy scale and resolution, as well as identification, isolation, reconstruction, and trigger efficiency of muons and electrons, all of which are estimated using $Z \to ee, \mu\mu$; $J/\psi \to ee, \mu\mu$; and $W \to e\nu, \mu\nu$ decays [64, 62, 74]. The uncertainty on the electron energy resolution is less than 10% for $E_{\mathrm{T}} < 50\,\mathrm{GeV}$ and asymptotically increases to ≈40% at higher energies, while the uncertainty on the electron energy scale is $|\eta|$ and E_{T} dependent, but the approximate range is 0.03-0.22% for $E_{\mathrm{T}} = 40\,\mathrm{GeV}$ and 0.27-2.25% for $E_{\mathrm{T}} = 200\,\mathrm{GeV}$ [74]. The uncertainty on the muon energy scale is 0.05% for $|\eta| < 1$ and increases to ≈0.2%, while the uncertainty on the combined muon momentum resolution ranges from 3-10% depending on $|\eta|$ and p_{T} [64]. The quoted muon resolution uncertainty actually contains two components coming from the independent resolutions of the inner detector and muon spectrometer. Finally, the uncertainties on the various lepton efficiency scale factors are nearly all smaller than 1%. The exceptions are the uncertainties on the electron identification and lepton (both electron and muon) isolation efficiency scale factors, which are still all smaller than 2.7%.

The $E_{\mathrm{T}}^{\mathrm{miss}}$ systematic variations only include variations on the soft terms (unassociated deposits of energy) because the systematic variations on the other reconstructed objects already alter the associated terms in the $E_{\mathrm{T}}^{\mathrm{miss}}$ calculation. The soft term

Table 4.11: Experimental systematic variations.

Category	Description
Leptons	Muon energy scale
	Electron energy scale
	Muon spectrometer track resolution
	Inner detector muon track resolution
	Electron energy resolution
MET	Soft term scale
	Soft term resolution
Small-R jets	Jet energy scale: • high-p_{T} jets • in-time pile-up • out-of-time pile-up • residual p_{T} dependence from pile-up • residual dependence on unrelated energy due to jet-area based pile-up correction • flavor composition • flavor response • b-jet response • in-situ modeling • in-situ detector related • statistical systematic • modeling systematic • closure systematic for AFII samples
	Jet energy resolution
Large-R jets	Jet energy scale
	Jet energy resolution
	Jet mass scale
	Jet mass resolution

variations consist of uncertainties on the energy scale and energy resolution. Comparing data and MC $Z \to \ell\ell$ events using methods developed in Ref. [72], these uncertainties are found to be on the order of a few percent [73].

The small-R jets have systematic uncertainties corresponding to the jet energy scale (JES), the jet energy resolution (JER), and the b-tagging algorithm. The JES uncertainty is broken into thirteen components (listed in Table 4.11) corresponding to different aspects of the jet calibration procedure, which utilizes a combination of simulation, test-beam data, and *in situ* measurements [75]. For the small-R anti-k_t jets used in this analysis, the combined uncertainty on the JES ranges from 1-7%, depending on $|\eta|$ and p_{T}. The relative uncertainty on the JER ranges from 2-40%, while the resolution itself varies from 5-20%, where the jets with p_{T} just above the selection cut have the largest uncertainty and worst resolution. Finally, the b-tagging uncertainty is broken into eight components by a method that utilizes a data sample dominated by di-leptonic decays of top-quark pairs [70, 71]. There are six uncorrelated components corresponding to the b-jet identification uncertainty (ranging from <1-7.8%), along with components corresponding to the uncertainties on the misidentification rates of light-quark jets (9-19% depending on p_{T} and $|\eta|$) and c-jets (6-14% depending on p_{T}).

The systematic uncertainty on the integrated luminosity is 2.8% for the 8 TeV dataset used in this analysis. The uncertainty is calculated using the same method as Ref. [76] for the 7 TeV dataset, in which beam-separation scans are used to calibrate the luminosity scale.

Similar to the small-R jets, the large-R jets have their own systematic uncertainties on JES and JER, but, unlike small-R jets, they also have uncertainties on the jet mass scale (JMS) and jet mass resolution (JMR). The two scale uncertainties, JES and JMS, are evaluated and provided by the ATLAS JetEtMiss group and are on the order of a few percent. However, the resolution systematic uncertainties have to be calculated by the individual analyses, as described below.

4.10.1 Large-R Jet Mass and Energy Resolutions

A previous ATLAS study indicated that large-R jet energy and mass resolutions could vary by up to 20% [77]. Therefore the recommendation from the JetEtMiss group is to estimate systematic uncertainties by smearing the jet energies and masses by Gaussian distributions, such that the energy and mass resolutions are increased by 20%. This requires knowing what the resolutions are in the first place.

The resolutions are evaluated by matching large-R jets to their associated truth jets in our signal samples, taking the ratio of their corresponding masses and energies (reconstructed/truth), and fitting a Gaussian to the central portion of each resulting distribution. Prior to the fitting, the jets are actually separated into three bins in p_{T} and two bins in $|\eta|$ based on the observation that the mass and energy resolutions vary as a function of the jet p_{T} and $|\eta|$. The widths (square root of the variances) of the fitted Gaussians, $\sigma^{i}_{\mathrm{res}}$, are taken to be the energy and mass resolutions, and are shown in Table 4.12 separated into their p_{T} and $|\eta|$ bins.

In order to smear (i.e. increase) the observed resolutions by the recommended 20%,

Table 4.12: Extracted mass and energy resolutions (before smearing) for the large-R jets used in this analysis

Mass Resolution	$100 < p_{\mathrm{T}} < 200$	$200 < p_{\mathrm{T}} < 500$	$p_{\mathrm{T}} > 500$
$0 < \|\eta\| < 0.6$	9.75%	7.26%	6.36%
$0.6 < \|\eta\| < 1.2$	9.81%	7.56%	6.92%
Energy Resolution	$100 < p_{\mathrm{T}} < 200$	$200 < p_{\mathrm{T}} < 500$	$p_{\mathrm{T}} > 500$
$0 < \|\eta\| < 0.6$	7.58%	5.05%	3.76%
$0.6 < \|\eta\| < 1.2$	7.91%	5.51%	4.27%

they are convoluted by Gaussians of widths $\sigma^{i}_{\mathrm{smear}} = 0.6633 \times \sigma^{i}_{\mathrm{res}}$ (where i represents JER and JMR), determined by the variance relation $(1.2\sigma_{\mathrm{res}})^2 = \sigma^2_{\mathrm{res}} + \sigma^2_{\mathrm{smear}}$. To create the systematic variations on the large-R JER and JMR, the nominal jet energy and mass are smeared by their corresponding unit Gaussians of width $\sigma^{i}_{\mathrm{smear}}$ and run back through the analysis just like the other systematic variations.

4.10.2 Multi-jet Background Estimate Uncertainty

The systematic uncertainty on the normalization of the MJ background is determined by comparing the default MJ estimate (described in Section 4.9.1) to an alternate estimate in which the electron isolation requirements are reversed and the muon impact parameter significance requirement is dropped. The relative difference between the two estimates is evaluated for each production mode (ggF and VBF), lepton channel (flavor and charge), and mass hypothesis (because of the mass-dependent

selection). However, only the average systematic value is taken for each lepton channel to avoid unphysical fluctuations between mass hypotheses.

The systematics uncertainties evaluated for the ggF signal regions vary between 10-100% depending on the lepton channel, with the muon channels having substantially lower uncertainty (10-30%) due to better compatibility of the two MJ estimates. Although these uncertainties are large, they only have a small impact on the final sensitivity of the analysis due to the small size of the multi-jet background, especially for higher mass hypotheses with the increasing $E_{\mathrm{T}}^{\mathrm{miss}}$ cut. In the case of VBF signal regions, the statistical uncertainty on the default template fit is taken as the systematic uncertainty because it dominates with respect to the uncertainty coming from the alternate estimate.

4.10.3 WW Interference Uncertainty

The systematic uncertainty on the interference weights applied to ggF signal samples comes from the theoretical uncertainty associated with the LO to NNLO scaling [3, 78]. However, in the case of VBF interference, the difference between LO and NNLO is expected to be small [47, 48, 79]. Therefore, a closure test systematic uncertainty is determined by comparing the nominal signal-plus-interference ($\mathcal{SI}$) m_{WW} (truth level mass) spectrum, determined by reweighting the $\mathcal{S}$-only POWHEG samples using REPOLO, to the spectrum evaluated as the difference between the VBFNLO generated background ($\mathcal{B}$) and complete $\mathcal{SBI}$ spectrums. The reason for the subtraction is that VBFNLO cannot generate interference by itself without including the signal

and background that cause the interference.

A visual comparison between the alternate background subtracted $\mathcal{SBI} - \mathcal{B}$ spectrum and the nominal $\mathcal{SI}$ spectrum is shown in the right frame of Figure 4.27 for the 800 GeV mass point. The frame on the left includes all of the components involved in the estimation: the original POWHEG $\mathcal{S}$, the REPOLO reweighted $\mathcal{SI}$, the VBFNLO generated $\mathcal{B}$ and $\mathcal{SBI}$, to be compared with the distribution obtained adding $\mathcal{B} + \mathcal{SI}$.

The ratio of the two spectrums, $\mathcal{SI}$ and $\mathcal{SBI} - \mathcal{B}$, is shown in Figure 4.28 as a function of m_{WW}/m_H for several mass points. The Figure is split into two frames in order to highlight the two assigned systematic uncertainty bands (shaded regions) based on symmetrically enveloping the ratios from the different mass hypothesis. The parametrization of the uncertainties is laid out in Table 4.13.

Table 4.13: Interference closure systematic as a function of m_{WW}/m_H

Signal Mass	Parametrization	Assigned Systematic [%]
$m_H < 500\,\text{GeV}$	$m_{WW}/m_H < 0.6$	2
	$0.6 \leq m_{WW}/m_H < 0.9$	8
	$0.9 \leq m_{WW}/m_H$	4
$m_H \geq 500\,\text{GeV}$	$m_{WW}/m_H < 0.9$	$(1 - m_{WW}/m_H) \times 20$
	$0.9 \leq m_{WW}/m_H < 1.1$	1.5
	$1.1 \leq m_{WW}/m_H$	$(m_{WW}/m_H - 1) \times 15$

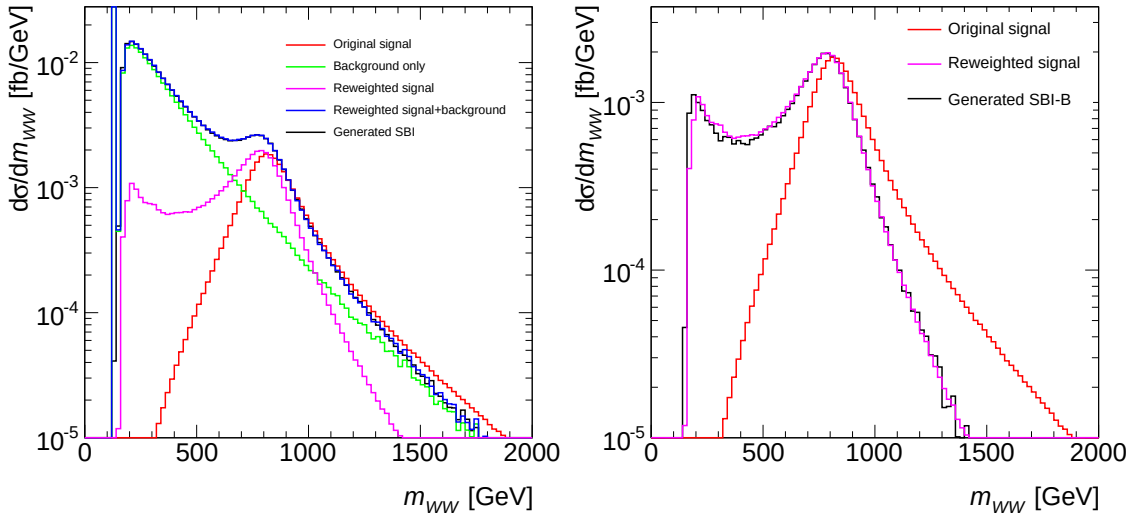

(a) Inclusive **(b)** Background subtracted

Figure 4.27: The effect of interference between signal and WW background for VBF production at $m_H = 800\,\text{GeV}$. The original signal $\mathcal{S}$ is shown in red, while the $\mathcal{S} \to \mathcal{SI}$ reweighted signal (using REPOLO) is shown in magenta. The left figure also shows the WW background $\mathcal{B}$ in green, the VBFNLO generated inclusive $\mathcal{SBI}$ in black, and the sum of $\mathcal{B} + \mathcal{SI}$ in blue. The right figure shows the comparison between $\mathcal{SI}$ and the background subtracted $\mathcal{SBI} - \mathcal{B}$, the ratio of which is used to assign the systematic uncertainty on the VBF interference reweighting.

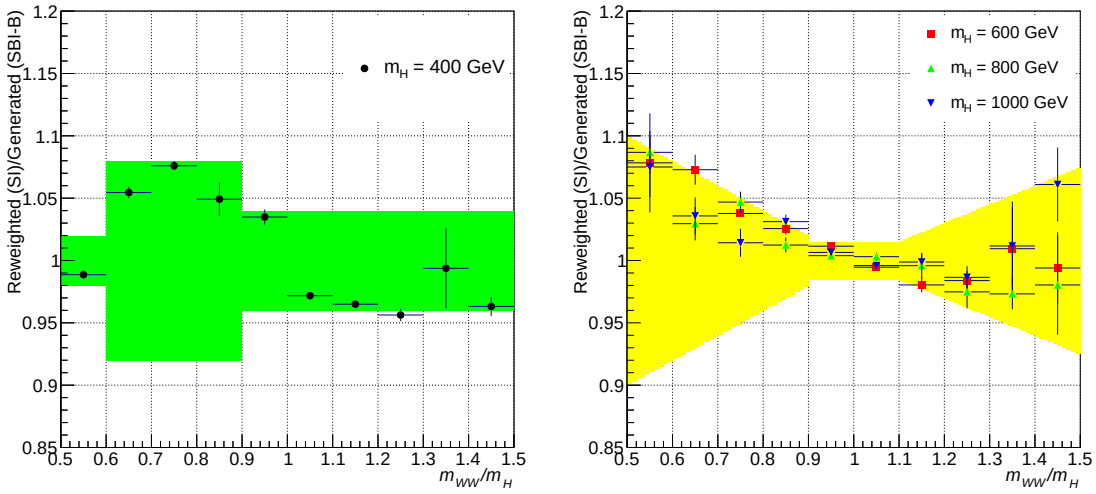

(a) Low Mass **(b)** High Mass

Figure 4.28: The ratio between the m_{WW} spectrums of the REPOLO reweighted $\mathcal{SI}$ and VBFNLO generated $\mathcal{SBI} - \mathcal{B}$ as a function of m_{WW}/m_H, for several mass points. The plots are split by low and high m_H for assigning the systematic uncertainties on the VBF interference reweighting (shown by the colored bands) based on the ratios.

4.10.4 $W+$jets and Top $m_{\ell\nu jj}$ Shape Reweighting Uncertainties

Finally, the dominant uncertainties on the background modeling are those on the reweighting of the $W+$jets and top MC events to correct their $m_{\ell\nu jj}$ shape mis-modeling (described in Section 4.9.2). A symmetric 50% uncertainty on the scaling coming from the reweighting functions of each background, is applied. The inclusion of these uncertainties, as Gaussian constraints in the final fit, allows the fit to adjust the $m_{\ell\nu jj}$ shapes of the $W+$jets and top backgrounds in the signal regions using the shape of the data.

4.11 Pre-fit MC Predictions Compared to Data

The background MC model the data in the control regions quite well (within uncertainties) following the event preselection, the reweighting of both $W+$jets and top MC $m_{\ell\nu jj}$ shapes, and the inclusion of all uncertainties. Figure 4.29 shows the $m_{\ell\nu jj}$ distributions and the ratio of data to background expectation for the WCR, TopCR, and SR after the ggF or VBF preselection. A slight deficit of data is observed in the VBF SR and TopCR as seen in the middle- and lower-right panels of Figure 4.29, but it is mitigated by the application of the mass-dependent selection (see Figure 4.30). Note that the distributions shown in Figure 4.29 do not include the final background normalizations applied by the fit to the control regions, but the $W+$jets and top $m_{\ell\nu jj}$ shape reweightings described in Section 4.9.2 are applied and the distributions are summed over lepton flavor and charge categories.

The corresponding $m_{\ell\nu jj}$ distributions separated by lepton flavor and charge can

be found in Appendix A.1. In order to get a more complete picture of the pre-fit MC modeling of the data following the preselection, distributions of many other kinematic variables used in the analysis can be found in Appendix A.2.

For a more quantitative view of the comparison between pre-fit MC predictions and data, Tables 4.14 and 4.15 show the pre-fit event yields (summed over lepton flavor and charge) for the ggF and VBF categories, respectively. The event yields are determined for every 100 GeV step in the mass hypothesis m_H (in the range $300 \leq m_H \leq 1200$ GeV) with the corresponding mass-dependent selection applied. Finally, the yields include the $m_{\ell\nu jj}$ shape reweighting of the $W+$jets and top MC events.

4.12 Results

With all of the systematics defined, the final signal and background yields in each final state and mass hypothesis are determined by a binned maximum likelihood fit to the observed data $m_{\ell\nu jj}$ distribution, as described in Section 4.12.1. Figure 4.30 shows the result of fitting for the $m_H = 500$ GeV hypothesis with the corresponding $m_H = 500$ GeV selection applied, where the CR and SR distributions are shown with their background normalizations corrected using the results of the fit.

Following the fits, no significant excess of data above the SM background expectation is observed for any mass hypothesis or production mode. Therefore, upper limits are set on the $\sigma_H \times \mathrm{BR}(H \to WW)$ for each mass hypothesis in each of the three signal scenarios. These are shown and discussed in Section 4.12.2.

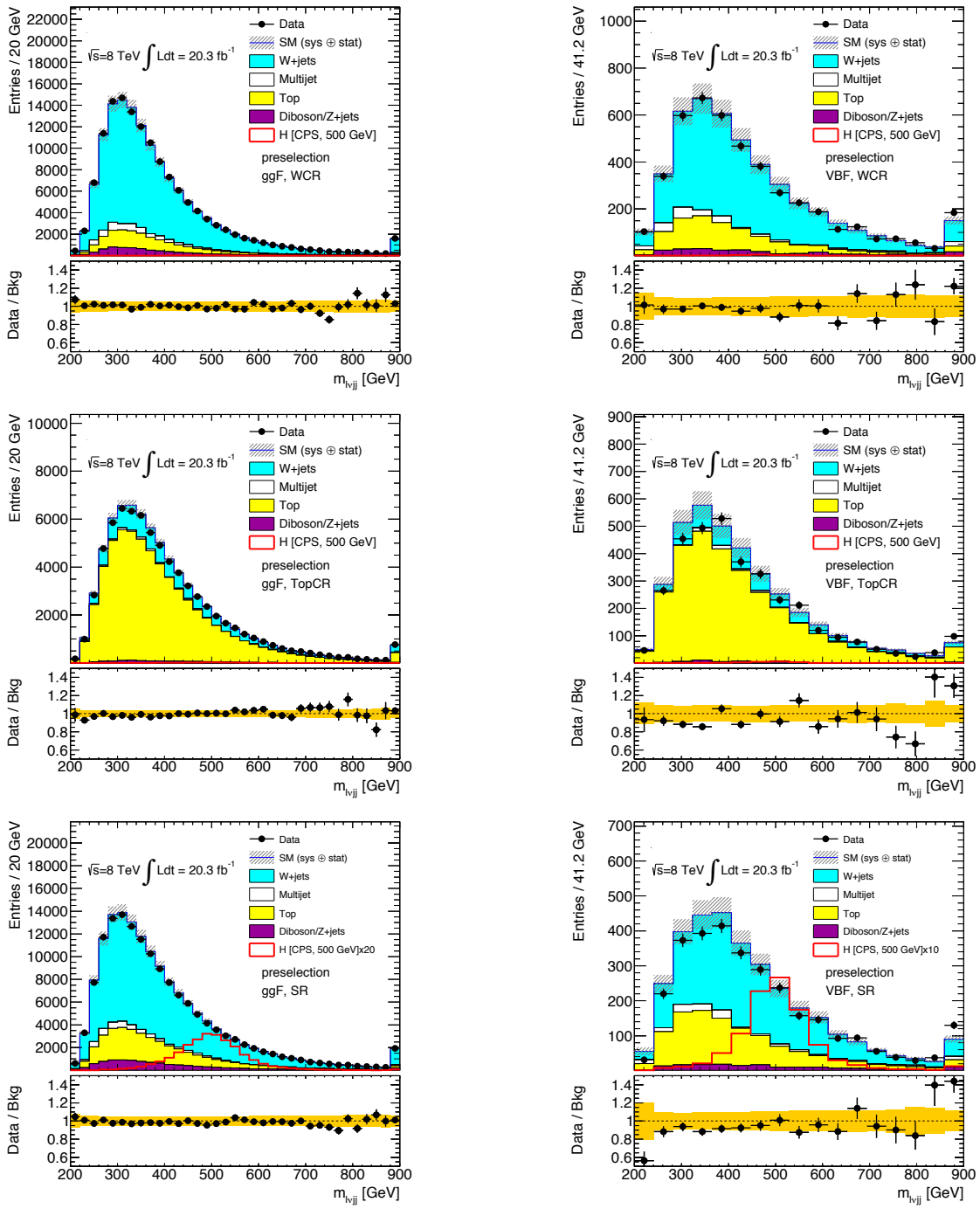

Figure 4.29: Reconstructed Higgs mass $m_{\ell\nu jj}/m_{\ell\nu J}$ in the WCR (top), TopCR (middle), and SR (bottom) after the ggF preselection (left) or the VBF preselection (right). All flavor and charge categories are summed in each plot. The upper panel of each plot shows the background processes (normalized by their theoretical cross-sections) stacked, with the data and a hypothetical CPS signal ($m_H = 500\,\text{GeV}$) overlaid. The lower panels show the ratio of data to background. The hatched gray band in the upper panel and the shaded yellow band in the lower panel show the combined statistical and systematic uncertainties on the background.

Table 4.14: Pre-fit event yields for the ggF category in the signal (SR) and control regions (WCR and TopCR) with the mass-dependent selection applied at the signal mass points (m_H). All lepton flavor and charge channels are combined. Signal yields assume SM Higgs production cross-sections and branching ratios. All uncertainties shown are statistical except for the multi-jet with systematic uncertainties.

Selection [m_H]	Region	ggF Signal CPS	ggF Signal NWA	VBF Signal CPS	VBF Signal NWA	W+jets	Top	Z+jets/ Diboson	Multi-jet	Data
	SR	1344 ± 17	1309 ± 21	103 ± 2	100 ± 4	97010 ± 227	27043 ± 33	9617 ± 63	4457 ± 1752	136310 ± 369
300 GeV	WCR	294 ± 8	282 ± 10	26.1 ± 0.8	26 ± 2	95447 ± 244	12216 ± 22	6140 ± 54	4769 ± 1871	118414 ± 344
	TopCR	154 ± 6	145 ± 7	16.0 ± 0.7	19 ± 2	11613 ± 69	54657 ± 47	1240 ± 26	895 ± 344	67854 ± 260
	SR	1815 ± 17	1879 ± 21	93 ± 2	100 ± 3	70902 ± 180	19217 ± 28	7103 ± 54	3189 ± 1245	99176 ± 315
400 GeV	WCR	263 ± 6	279 ± 8	13.2 ± 0.5	16 ± 1	69255 ± 197	7565 ± 17	4532 ± 48	3808 ± 1470	84809 ± 291
	TopCR	251 ± 6	258 ± 8	15.2 ± 0.6	17 ± 1	9061 ± 56	40617 ± 41	1043 ± 25	700 ± 272	51181 ± 226
	SR	987 ± 8	997 ± 10	65.9 ± 0.9	71 ± 2	41943 ± 122	11140 ± 21	4359 ± 43	1622 ± 624	58265 ± 241
500 GeV	WCR	109 ± 3	105 ± 3	7.9 ± 0.3	8 ± 1	37506 ± 127	3910 ± 12	2522 ± 35	1868 ± 700	45845 ± 214
	TopCR	134 ± 3	133 ± 4	10.4 ± 0.4	11 ± 1	5693 ± 38	24184 ± 31	690 ± 20	402 ± 156	30829 ± 176
	SR	453 ± 4	453 ± 4	45.1 ± 0.7	50 ± 1	23059 ± 79	6143 ± 15	2419 ± 31	780 ± 287	32022 ± 179
600 GeV	WCR	43 ± 1	42 ± 1	4.6 ± 0.2	3.9 ± 0.3	18715 ± 76	1990 ± 9	1248 ± 24	716 ± 264	22907 ± 151
	TopCR	59 ± 1	61 ± 2	6.6 ± 0.3	7.1 ± 0.4	3194 ± 25	13247 ± 23	384 ± 14	206 ± 76	17049 ± 131
	SR	219 ± 2	212 ± 2	31.2 ± 0.5	34.5 ± 0.8	14315 ± 56	3774 ± 12	1559 ± 24	522 ± 190	19971 ± 141
700 GeV	WCR	21.4 ± 0.7	20 ± 1	3.2 ± 0.2	2.8 ± 0.2	10893 ± 51	1201 ± 7	737 ± 17	434 ± 167	13388 ± 116
	TopCR	30.2 ± 0.9	27 ± 1	4.2 ± 0.2	4.3 ± 0.3	2021 ± 19	8147 ± 17	231 ± 12	105 ± 41	10597 ± 103
	SR	110.4 ± 1	99.2 ± 0.9	22.7 ± 0.4	23.6 ± 0.5	8340 ± 39	2126 ± 9	912 ± 18	144 ± 54	11418 ± 107
800 GeV	WCR	11.6 ± 0.4	10.9 ± 0.3	2.2 ± 0.1	2.9 ± 0.2	6019 ± 35	656 ± 5	406 ± 13	162 ± 66	7218 ± 85
	TopCR	14.6 ± 0.5	13.2 ± 0.4	2.7 ± 0.1	2.8 ± 0.3	1206 ± 13	4553 ± 13	131 ± 9	53 ± 25	6014 ± 78
	SR	55.7 ± 0.6	47.4 ± 0.5	16.3 ± 0.3	15.7 ± 0.4	4942 ± 28	1220 ± 7	557 ± 14	68 ± 28	6635 ± 81
900 GeV	WCR	6.1 ± 0.2	6.0 ± 0.2	1.8 ± 0.1	2.1 ± 0.1	3262 ± 23	368 ± 4	223 ± 9	44 ± 17	3943 ± 63
	TopCR	7.9 ± 0.3	6.5 ± 0.2	1.8 ± 0.1	1.5 ± 0.1	736 ± 9	2566 ± 10	76 ± 7	25 ± 10	3420 ± 58
	SR	23.7 ± 0.3	22.3 ± 0.2	10.2 ± 0.2	9.9 ± 0.3	1742 ± 14	376 ± 4	207 ± 8	25 ± 11	2243 ± 47
1000 GeV	WCR	3.3 ± 0.1	3.20 ± 0.09	1.24 ± 0.06	1.4 ± 0.1	1108 ± 11	117 ± 2	83 ± 5	15 ± 7	1317 ± 36
	TopCR	3.5 ± 0.1	2.84 ± 0.09	1.10 ± 0.08	1.01 ± 0.08	287 ± 5	830 ± 5	26 ± 4	16 ± 7	1165 ± 34
	SR	-	23.2 ± 0.21	-	10.0 ± 0.1	1742 ± 14	376 ± 4	207 ± 8	25 ± 11	2243 ± 47
1100 GeV	WCR	-	3.53 ± 0.08	-	1.54 ± 0.05	1108 ± 11	117 ± 2	83 ± 5	15 ± 7	1317 ± 36
	TopCR	-	3.23 ± 0.08	-	0.82 ± 0.03	287 ± 5	830 ± 5	26 ± 4	16 ± 7	1165 ± 34
	SR	-	23.8 ± 0.2	-	10.3 ± 0.1	1742 ± 14	376 ± 4	207 ± 8	25 ± 11	2243 ± 47
1200 GeV	WCR	-	4.12 ± 0.09	-	1.72 ± 0.05	1108 ± 11	117 ± 2	83 ± 5	15 ± 7	1317 ± 36
	TopCR	-	3.31 ± 0.08	-	0.91 ± 0.04	287 ± 5	830 ± 5	26 ± 4	16 ± 7	1165 ± 34

Table 4.15: Pre-fit event yields for the VBF category in the signal (SR) and control regions (WCR and TopCR) with the mass-dependent selection applied at the signal mass points (m_H). All lepton flavor and charge channels are combined. Signal yields assume SM Higgs production cross-sections and branching ratios. All uncertainties shown are statistical except for the multi-jet with systematic uncertainties.

Selection $[m_H]$	**Region**	**ggF Signal** **CPS**	**NWA**	**VBF Signal** **CPS**	**NWA**	$W+$**jets**	**Top**	$Z+$**jets/** **Diboson**	**Multi-jet**	**Data**
	SR	25 ± 2	25 ± 3	41 ± 1	41 ± 2	2011 ± 31	969 ± 6	155 ± 8	131 ± 48	3020 ± 55
300 GeV	WCR	10 ± 2	6 ± 1	11.5 ± 0.6	13 ± 1	3220 ± 39	771 ± 5	224 ± 10	226 ± 81	4215 ± 65
	TopCR	8 ± 1	8 ± 2	6.9 ± 0.4	8 ± 1	618 ± 17	2881 ± 10	61 ± 6	61 ± 23	3401 ± 58
	SR	53 ± 3	53 ± 3	52 ± 1	59 ± 2	1645 ± 26	765 ± 5	132 ± 7	88 ± 35	2480 ± 50
400 GeV	WCR	16 ± 2	15 ± 2	10.7 ± 0.5	11.6 ± 0.9	2546 ± 33	541 ± 4	177 ± 9	195 ± 70	3258 ± 57
	TopCR	17 ± 2	18 ± 2	9.7 ± 0.5	10.2 ± 0.8	491 ± 13	2297 ± 9	49 ± 5	51 ± 20	2742 ± 52
	SR	39 ± 2	40 ± 2	43.9 ± 0.7	48.2 ± 1	1103 ± 21	500 ± 4	88 ± 6	59 ± 25	1693 ± 41
500 GeV	WCR	9.2 ± 0.8	8.0 ± 0.9	6.7 ± 0.3	7.8 ± 0.5	1739 ± 27	346 ± 4	120 ± 7	127 ± 48	2241 ± 47
	TopCR	11.3 ± 0.9	10 ± 1	6.8 ± 0.3	7.8 ± 0.6	306 ± 10	1464 ± 7	31 ± 4	8 ± 4	1794 ± 42
	SR	24.8 ± 0.9	24 ± 1	36.6 ± 0.6	40 ± 1	775 ± 15	346 ± 4	67 ± 5	44 ± 20	1196 ± 35
600 GeV	WCR	5.3 ± 0.4	5.5 ± 0.5	5.0 ± 0.2	5.1 ± 0.4	1175 ± 20	235 ± 3	84 ± 6	72 ± 27	1548 ± 39
	TopCR	5.3 ± 0.4	5.5 ± 0.5	5.1 ± 0.2	5.4 ± 0.4	210 ± 7	981 ± 6	22 ± 3	8 ± 4	1200 ± 35
	SR	12.8 ± 0.5	12.7 ± 0.5	25.8 ± 0.4	26.6 ± 0.7	421 ± 11	179 ± 3	41 ± 4	24 ± 10	672 ± 26
700 GeV	WCR	2.7 ± 0.4	2.4 ± 0.2	3.6 ± 0.2	4.3 ± 0.3	610 ± 13	121 ± 2	50 ± 5	36 ± 13	806 ± 28
	TopCR	2.3 ± 0.2	2.5 ± 0.2	3.2 ± 0.2	3.4 ± 0.2	113 ± 5	466 ± 4	13 ± 3	7 ± 4	550 ± 23
	SR	7.7 ± 0.3	7.5 ± 0.3	19.6 ± 0.3	20.5 ± 0.5	260 ± 8	101 ± 2	27 ± 3	9 ± 4	394 ± 20
800 GeV	WCR	1.3 ± 0.1	1.5 ± 0.1	2.7 ± 0.1	2.7 ± 0.2	371 ± 10	73 ± 2	34 ± 4	11 ± 4	477 ± 22
	TopCR	1.3 ± 0.2	1.2 ± 0.1	1.9 ± 0.1	2.0 ± 0.2	58 ± 3	234 ± 3	5 ± 1	5 ± 3	292 ± 17
	SR	4.1 ± 0.2	4.4 ± 0.1	14.4 ± 0.3	15.6 ± 0.4	141 ± 5	55 ± 1	16 ± 2	7 ± 3	223 ± 15
900 GeV	WCR	0.81 ± 0.07	0.7 ± 0.1	2.33 ± 0.09	2.7 ± 0.2	208 ± 6	42 ± 1	25 ± 4	12 ± 5	279 ± 17
	TopCR	0.62 ± 0.06	0.7 ± 0.1	1.34 ± 0.09	1.3 ± 0.1	30 ± 2	119 ± 2	2.5 ± 0.9	0.5 ± 0.3	145 ± 12
	SR	2.8 ± 0.1	2.92 ± 0.09	12.6 ± 0.2	13.6 ± 0.3	100 ± 4	38 ± 1	12 ± 2	4 ± 2	159 ± 13
1000 GeV	WCR	0.60 ± 0.05	0.61 ± 0.04	2.44 ± 0.09	2.1 ± 0.1	154 ± 4	33 ± 1	20 ± 3	7 ± 3	215 ± 15
	TopCR	0.40 ± 0.04	0.34 ± 0.03	0.82 ± 0.05	1.0 ± 0.1	21 ± 2	76 ± 2	2.1 ± 0.8	0.3 ± 0.2	98 ± 10
	SR	-	3.33 ± 0.08	-	14.2 ± 0.1	100 ± 4	38 ± 1	12 ± 2	4 ± 2	159 ± 13
1100 GeV	WCR	-	0.73 ± 0.04	-	2.72 ± 0.06	154 ± 4	33 ± 1	20 ± 3	7 ± 3	215 ± 15
	TopCR	-	0.42 ± 0.03	-	0.92 ± 0.04	21 ± 2	76 ± 2	2.1 ± 0.8	0.3 ± 0.2	98 ± 10
	SR	-	3.60 ± 0.08	-	15.5 ± 0.2	100 ± 4	38 ± 1	12 ± 2	4 ± 2	159 ± 13
1200 GeV	WCR	-	0.94 ± 0.04	-	3.30 ± 0.07	154 ± 4	33 ± 1	20 ± 3	7 ± 3	215 ± 15
	TopCR	-	0.52 ± 0.03	-	1.03 ± 0.04	21 ± 2	76 ± 2	2.1 ± 0.8	0.3 ± 0.2	98 ± 10

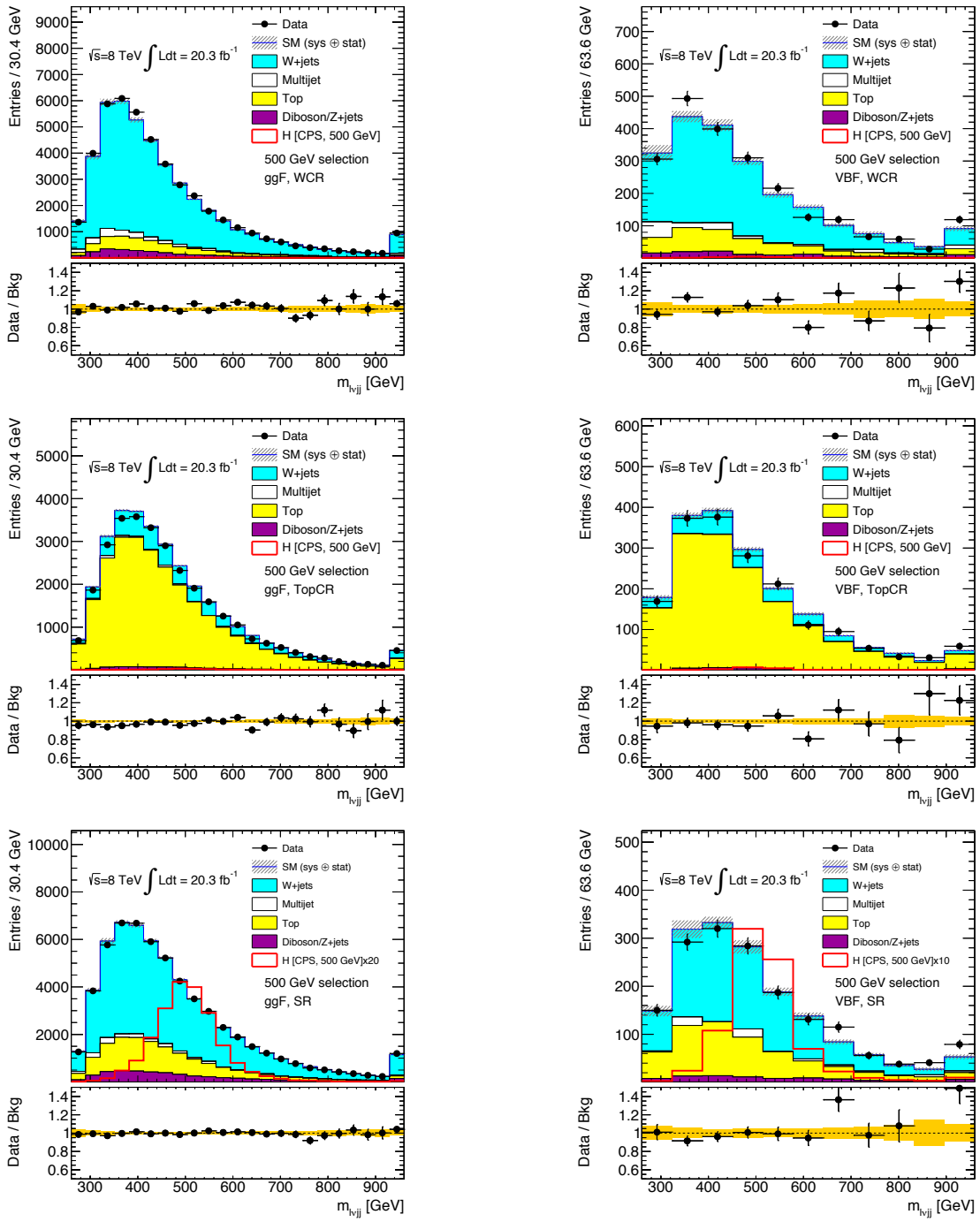

Figure 4.30: Post-fit reconstructed Higgs mass $m_{\ell\nu jj}/m_{\ell\nu J}$ in the WCR (top), TopCR (middle), and SR (bottom) after the ggF (left) or VBF (right) 500 GeV selection. The binning corresponds to the binning used in the fit. All flavor and charge categories are summed in each plot. The upper panel of each plot shows the background processes stacked, with the data and a hypothetical CPS signal ($m_H = 500\,\text{GeV}$) overlaid. The lower panels show the ratio of data to background. The hatched gray band in the upper panel and the shaded yellow band in the lower panel show the combined statistical and systematic uncertainties on the background.

4.12.1 Statistical Methods

The statistical method used for fitting and setting limits is detailed in Ref. [80] and outlined here. A likelihood function L is defined as the product of Poisson probability functions corresponding to each bin of the SR $m_{\ell\nu jj}$ distribution and total yields in the CRs (as they simply help constrain the normalization of the background, not the shape), multiplied by unit Gaussian functions that constrain each systematic uncertainty (parameterized by a nuisance parameter θ_i in the statistical treatment) about its nominal value. These nuisance parameters are also used to parameterize log-normal distributions used to implement modifications to the nominal signal and background yields in the Poisson functions.

The 95% CL (confidence level) upper limits are calculated using a combination of the $\mathrm{CL_s}$ modified frequentist method [81] and the asymptotic approximation [82], which define a test statistic $q(\mu)$ based on a ratio of likelihood functions:

$$q(\mu) = -2\ln\left(\frac{L\left(\mu;\hat{\hat{\theta}}(\mu)\right)}{L\left(\hat{\mu};\hat{\theta}\right)}\right), \tag{4.17}$$

where μ is the signal strength defined in this analysis as the ratio of the measured to SM-predicted $\sigma_H \times \mathrm{BR}(H{\to}WW)$ and $\hat{\hat{\theta}}(\mu)$ represents the values of all of the nuisance parameters θ_i that maximize L for a given value of μ. The other two quantities in the definition, $\hat{\mu}$ and $\hat{\theta}$, are defined as the values of μ and all the θ_i that unconditionally maximize L.

The fit range of the $m_{\ell\nu jj}$ distributions varies with each m_H hypothesis, but is always 700 GeV wide: starting with 200-900 GeV for $m_H = 300$ GeV and increasing

to 500-1200 GeV for $m_H = 1000\,\text{GeV}$. The number of bins within each fit range also varies with m_H, but unlike the fit ranges, is not the same between ggF and VBF production modes because of the lower statistics in the VBF regions. In fact, for each mass hypothesis, the number of bins for VBF is half that for ggF (rounding down to the nearest whole number): starting with 17 (35) bins at $m_H = 300\,\text{GeV}$ and decreasing to 6 (12) bins at $m_H = 1000\,\text{GeV}$ for the VBF (ggF) production mode. Also, the last bin in the fit range contains the overflow and the bins within a given fit range and production mode all have the same width. Note that in the case of the NWA scenario, the mass hypotheses tested with $m_H > 1000\,\text{GeV}$ use the $m_H = 1000\,\text{GeV}$ fit range and binning, due to the lack of data and background MC statistics at higher $m_{\ell\nu jj}$.

Although the analysis defines orthogonal ggF- and VBF-optimized SRs, they are not exclusive (as can readily be seen back in Tables 4.14 and 4.15. Therefore, the presence of both processes is accounted for when setting limits on one or the other. To accomplish this, the ggF (VBF) production cross-section is treated as a nuisance parameter in the fit when deriving the observed limits on the VBF (ggF) production. However, in order for the expected limits to correspond to the background-only hypothesis, the ggF (VBF) production cross-section is set to zero to derive the expected limits on the VBF (ggF) production.

4.12.2 Upper Limits

The 95% CL upper limits on $\sigma_H \times \mathrm{BR}(H \to WW)$ as a function of m_H are shown, separated by production mode, in Figures 4.31 and 4.32 for the CPS and NWA scenarios, respectively. The mass range of the CPS limits is $300\,\mathrm{GeV} \leq m_H \leq 1000\,\mathrm{GeV}$, while that of the NWA limits is $300\,\mathrm{GeV} \leq m_H \leq 1500\,\mathrm{GeV}$.

The corresponding upper limits for the IW scenario are shown in Figure 4.33 for three values of κ'^2, and are plotted in terms of $\frac{\sigma_H}{\kappa'^2} \times \mathrm{BR}(H \to WW)$ for better visual separation. In contrast to the limits set in the CPS and NWA scenarios, the ggF and VBF limits in the IW scenario can be combined, because EWS models (which this scenario is based on) assume the ratio between the production modes to be the same as that for the SM Higgs, whereas the other two scenarios have no such relation. In this analysis, the possible non-SM decay modes of the EWS scalar are not considered (i.e. $\mathrm{BR}_{H,\mathrm{new}} = 0$).

As expected, the limits improve as m_H increases for a given lineshape, and worsen over the full mass range as the width of the signal lineshape Γ_H increases. The dips seen in the observed limits, further than -2σ below the expected limits, were investigated and no underlying systematic effect was identified. A coincidence of deficits in the data is attributed to the simultaneous dip at $m_H \approx 750\,\mathrm{GeV}$ in both the ggF and VBF limits on the NWA scenario.

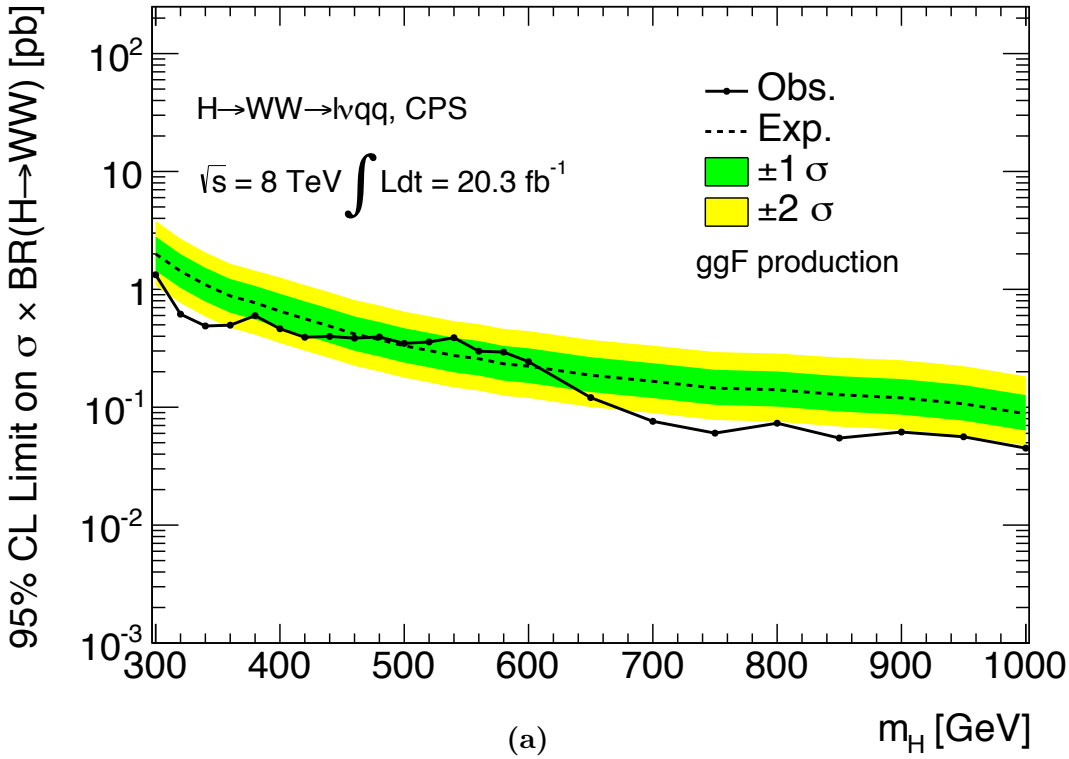

(a)

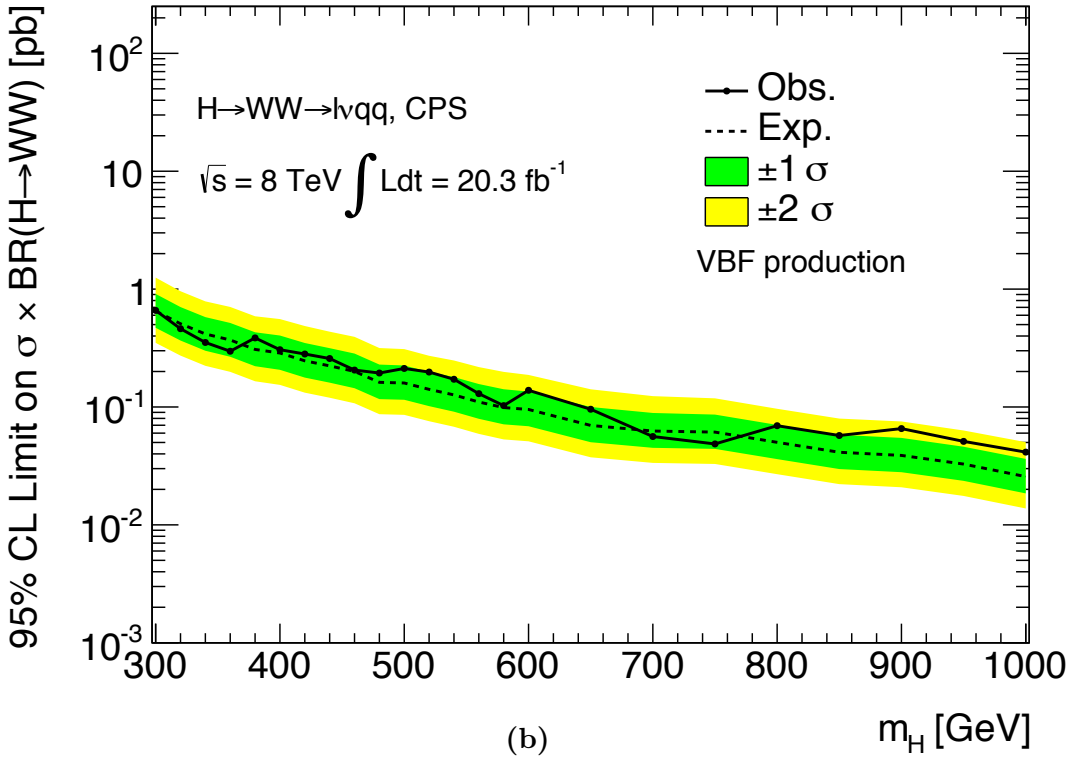

(b)

Figure 4.31: 95% CL upper limits on the $\sigma \times$ BR in the CPS (SM-like) scenario for ggF production (a) and VBF production (b). The green and yellow bands display the $\pm 1\sigma$ and $\pm 2\sigma$ uncertainties on the expected limits, respectively.

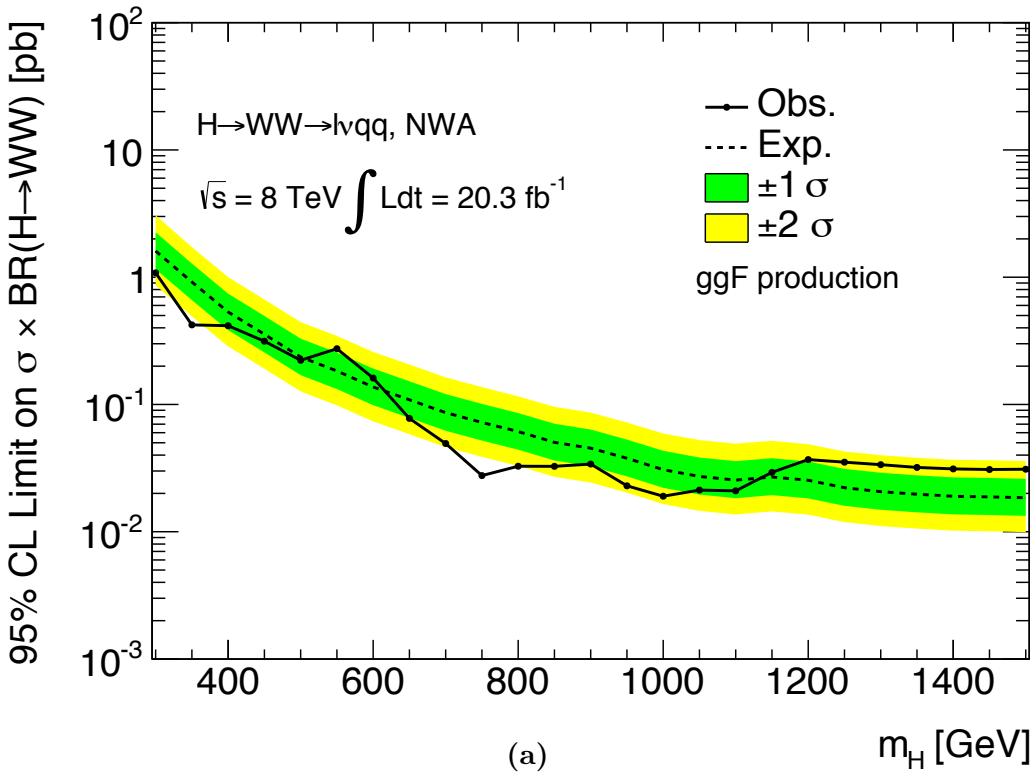

(a)

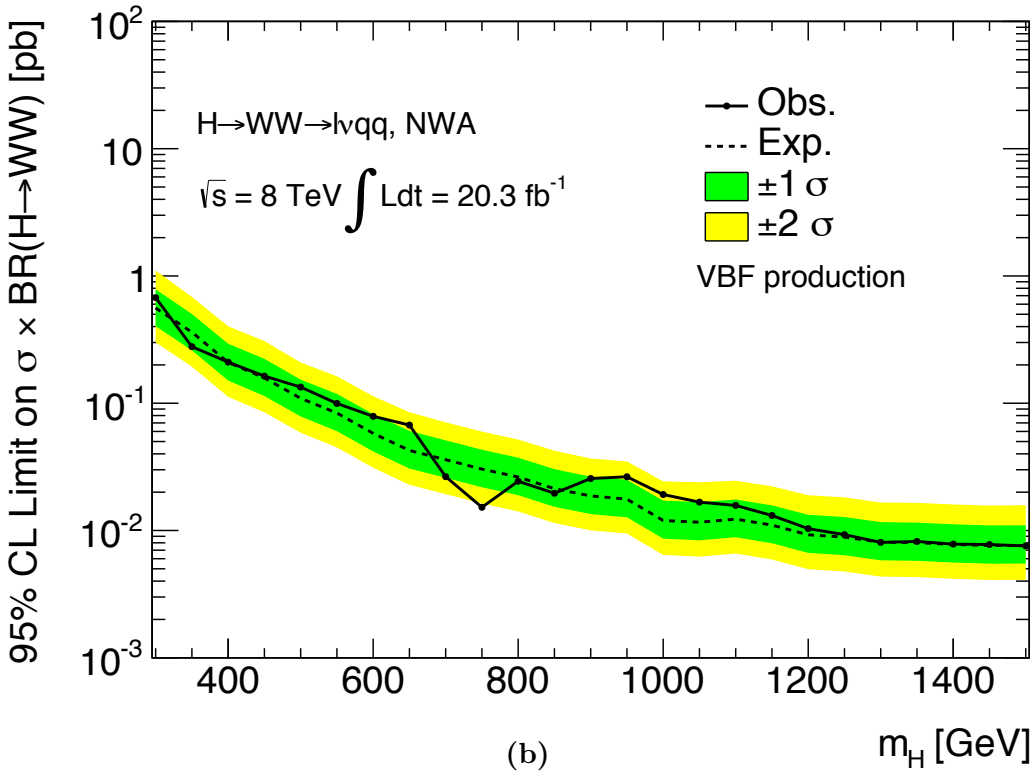

(b)

Figure 4.32: 95% CL upper limits on the $\sigma \times$ BR in the NWA scenario for ggF production (a) and VBF production (b). The green and yellow bands display the $\pm 1\sigma$ and $\pm 2\sigma$ uncertainties on the expected limits, respectively.

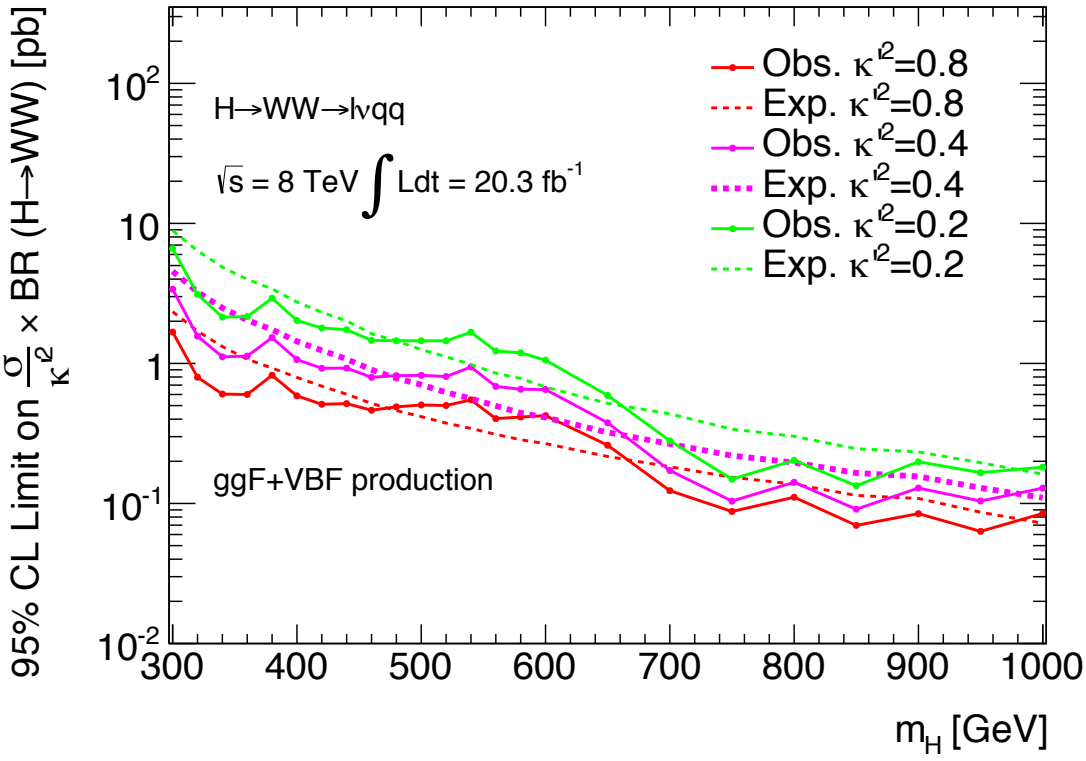

Figure 4.33: 95% CL upper limits on the $\frac{\sigma_H}{\kappa'^2}$ × BR for a heavy scalar resonance in the intermediate-width scenario ($0.2\Gamma_{H,\mathrm{SM}} \leq \Gamma_H \leq 0.8\Gamma_{H,\mathrm{SM}}$), with ggF and VBF production modes combined.

Chapter 5

13 TeV Analysis: The Search Continues

In contrast to the previous chapter, this chapter is brief, with a focus on highlighting the important differences between the analyses in the two chapters, as well as the new results.

5.1 Introduction

After the two-year *long shutdown* of the LHC, between 2013 and 2015, the collision energy increased from 8 to 13 TeV and the bunch spacing decreased from 50 to 25 ns, resulting in greater instantaneous luminosity and even more opportunities to explore the world of particle physics. There were also many upgrades to the ATLAS detector, a few of which are discussed in Section 3.6.1, including the installation of an additional Pixel detector layer (the IBL) closer to the interaction point.

The analysis described in this chapter is a continued search for a high-mass neutral scalar (still referred to simply as H) with the same final state: $H \to WW \to \ell\nu qq$. The search uses the 2015 ATLAS dataset, consisting of 3.2 fb^{-1} of pp collision data at $\sqrt{s} = 13$ TeV. Although the dataset is much smaller than that for the 8 TeV analysis, the nearly doubled center-of-mass collision energy makes the search competitive for high masses due to the associated mass-dependent increase in gg-produced processes, shown in Figure 5.1, along with the scaling of the cross-sections of multiple physics processes. Taking into account the scaling of the signal and major background

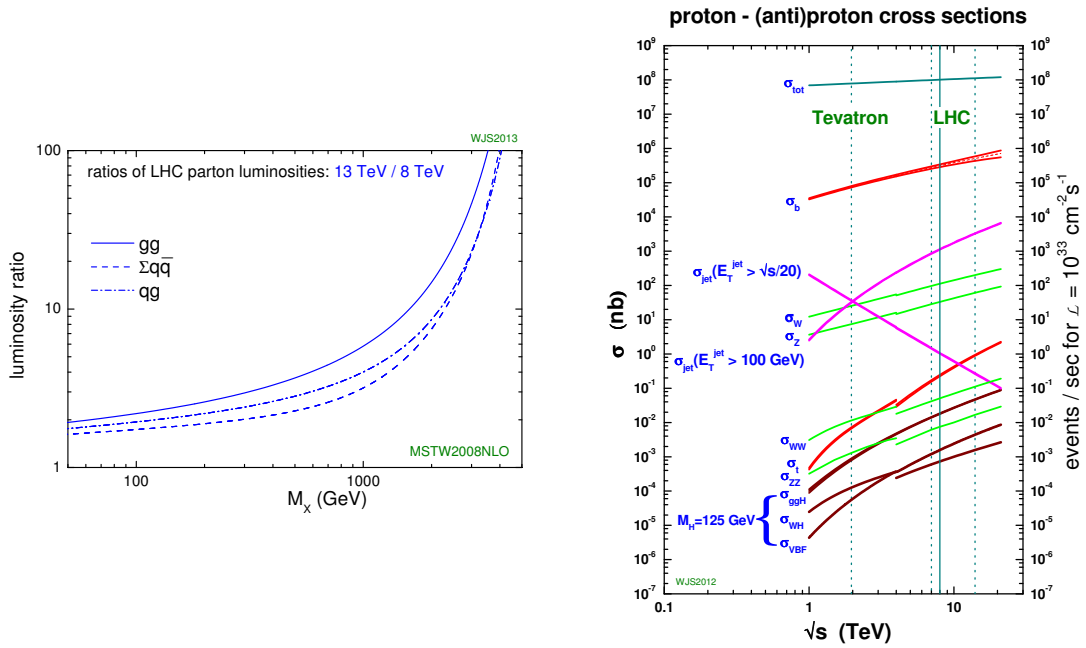

Figure 5.1: Comparisons of the expected luminosity (left) and cross-sections for several processes (right) provided by the LHC at 8 and 13 TeV [W.J. Stirling, private communication]. The calculations are done using MSTW2008 (NLO) parton distributions and the discontinuity in some of the cross-sections at 4 TeV is due to switching from proton-antiproton to proton-proton collisions.

production cross-sections, the analysis (using the NWA) was projected to regain similar sensitivity to the 8 TeV analysis at high m_H with only the first few fb^{-1} of 13 TeV data.

In order to analyze the new data quickly, it was made a priority to simplify the analysis and to join other analysis groups searching for the same final state. Thus, the heavy scalar search presented in this chapter was first made public in Ref. [83], where it was combined with a search for a spin-2 Kaluza-Klein graviton based on an extended Randall-Sundrum model of a warped extra dimension [84], as well as a search for a new heavy vector boson based on a Heavy Vector Triplet (HVT)

model [85]. No significant excess above the SM predictions was observed for any of the interpretations with this early analysis, but the search range was significantly extended up to $800\,\text{GeV} \leq m_H \leq 3000\,\text{GeV}$.

The scalar interpretation results were later updated with a few additional mass hypotheses, filling in gaps and extending the lower mass range ($800\,\text{GeV} \rightarrow 600\,\text{GeV}$), and were combined with the $H \rightarrow WW \rightarrow \ell\nu\ell\nu$ decay channel in Ref. [86]. Other than the additional mass points and updating to the Combined Performance (CP) groups' latest recommendations (for object selections and uncertainties), the scalar analysis remained the same.

These updated results are shown following a summary of the general analysis strategy.

5.2 Analysis Summary

This section summarizes the most significant aspects of the analysis needed to understand the results shown in the next section. More details can be found in the two public conference notes referenced earlier, namely Refs. [83] and [86].

5.2.1 Simplifications from the 8 TeV Analysis

Considering the small amount of data and the pressure for an early analysis, the focus is on the high-mass/boosted regime and analysis simplicity.

One of the most significant analysis simplifications, in reference to the 8 TeV analysis, is that there is only **one signal region** (when lepton channels are combined);

there are no selections that depend on the mass hypothesis, and only the ggF production mode is considered (although there is no explicit VBF veto).

With the focus solely on the boosted regime, the qq final state is exclusively reconstructed as a single large-R jet. Also, such a focus allows for a harsh cut on $E_{\mathrm{T}}^{\mathrm{miss}}$ ($> 100\,\mathrm{GeV}$ in this case), which is shown to effectively eliminate the multi-jet background in the analysis.

5.2.2 MC and Data

With the aim of producing results as model-independent as possible, the signal hypotheses tested in this analysis include the NWA heavy Higgs (from the 8 TeV analysis) in addition to a large width approximation (LWA) heavy Higgs (generated using MadGraph5_aMC@NLO), where the widths are equal to 5%, 10%, and 15% of m_H. Interference effects for NWA are again negligible and those for LWA are mitigated by only analyzing events with a truth mass within $\pm 2\Gamma_H$ of m_H. The mass hypotheses span the range from 0.6 TeV to 3 TeV in steps of 100 GeV up to 1 TeV and in steps of 200 GeV afterward. An additional mass point at 750 GeV was also added, motivated by a small excess of events observed near that invariant mass in the scalar resonance search for a diphoton final state [87].

The background processes are the same as for the 8 TeV analysis, with the exception of the now neglected multi-jet background, and the dataset used corresponds to all of the 13 TeV data recorded by ATLAS and deemed *good for physics* in 2015. Single lepton triggers are used again, along with a $E_{\mathrm{T}}^{\mathrm{miss}}$ trigger that regains the

inefficiency in the muon trigger.

5.2.3 Kinematic Selection and Event Region Definitions

The object selections are very similar to the previous analysis. One notable difference is the use of a different large-R jet collection, reconstructed with a distance parameter of $R = 1.0$ using the anti-k_t algorithm that was and is used for the small-R jets. These jets are analyzed in a dedicated boson tagger [88] that distinguishes jets originating from W boson decays from those originating from single gluons or quarks. It is configured to have 90% background rejection and 50% signal efficiency. The tagging can be broken into two requirements: one on W jet substructure and the other on the mass. This makes it possible to reverse only part of the tagging requirement to define a CR, as is done for the $W+$jets CR.

The event selection is shown in Table 5.1 for the various regions of the analysis starting with the preselection of exactly one lepton and at least one large-R jet passing the requirements. The new selections, compared to the previous analysis, are those on the p_{T} to $m_{\ell\nu J}$ ratios. They are shown to give good separation between the signal and background, as resonant signals should peak around a value of 0.5. The definitions of the CRs are also shown and are very similar to those in the previous analysis: a mass window side-band for the $W+$jets CR and a reversal of the b-tag veto for the Top CR.

Table 5.1: Event selections for the SR, W+jets CR and Top CR. Small-R jets that are b-tagged are denoted as j_b in the table below.

Region	Selection
Preselection	one lepton: $p_{\mathrm{T}} > 25$ GeV
	$\geq$ one large-R jet: $p_{\mathrm{T}} > 200$ GeV, $\lvert\eta\rvert < 2.0$
	$E_{\mathrm{T}}^{\mathrm{miss}} > 100$ GeV
	$p_{\mathrm{T}}(\ell\nu) > 200$ GeV
	$p_{\mathrm{T}}(J)/m_{\ell\nu J} > 0.4$
	$p_{\mathrm{T}}(\ell\nu)/m_{\ell\nu J} > 0.4$
SR	W jet substructure
	$W(J)$ mass cut: $70.2 \leq m_J \leq 96.2$ GeV
	no b-tagged jets with $\Delta R(J, j_b) > 1.0$
W+jets CR	SR except W mass sidebands:
	$50 < m_J < 70.2$ GeV and $96.2 < m_J$ GeV
Top CR	SR except reverse b-tag veto:
	≥ 1 b-tagged jet with $\Delta R(J, j_b) > 1.0$

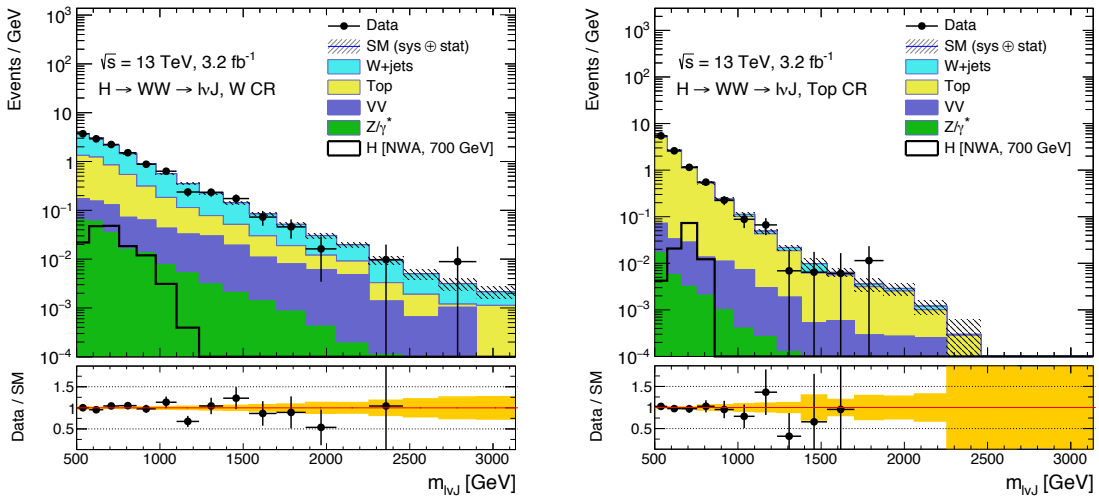

(a) $W+$jets CR **(b)** Top CR

Figure 5.2: The post-fit $m_{\ell\nu J}$ distributions for the $W+$jets control region (a) and the Top control region (b), with the 700 GeV NWA signal overlaid and the ratio of data/SM-background in the lower panel. The shaded and hatched bands in the lower and upper panels, respectively, show the total uncertainty after a background-only fit to the data. The last bin in each histogram contains the overflow.

5.3 Background Estimation

The main backgrounds are the same as the previous analysis, $t\bar{t}$ and $W+$jets, and again have their dedicated CRs (defined in Table 5.1) to constrain their normalizations in the simultaneous fit to the signal and control regions. Figure 5.2 shows the reconstructed $m_{\ell\nu J}$ distribution and data/MC agreement in the $W+$jets and Top CRs following the fit. Fairly good agreement is seen in each region.

Also shown in the figure is an overlay of the 700 GeV NWA signal distribution normalized to $\sigma_H \times \mathrm{BR}(H \to WW) = 1$ pb. The 1 pb normalization is arbitrary since there is no physical prediction of the signal cross-section, but is an easy number to rescale to any theoretical prediction.

5.4 Systematic Uncertainties

The sources of systematic uncertainties are very much the same as the previous analysis and are again dominated by the large-R JER and JES. One difference comes from the uncertainty on the modeling of the $W+$jets background. As in the previous analysis, the modeling of the $W+$jets background is observed in the $W+$jets CR by subtracting the other background contributions from the data and taking the ratio. This time, however, the slope of the ratio is consistent with unity so there is no re-weighting applied like there was for the 8 TeV analysis. The uncertainty on the $W+$jets modeling is then taken as the uncertainty on the ratio slope (15%).

5.5 Results

The same statistical methodology applied in the 8 TeV analysis, including the likelihood fit and upper limits procedure, is used here. As before, the $W+$jets and Top normalizations are left free to float in the simultaneous fit of the signal and control regions. One difference is in the binning of the discriminant, $m_{\ell\nu J}$, which this time takes on variable bin sizes chosen in order to provide adequate statistics within each bin, while maintaining the signal peak resolution.

The $m_{\ell\nu J}$ distribution in the signal region is shown in Figure 5.3a following the background-only fit. Again, the 700 GeV NWA signal is overlaid with its 1 pb normalization. The event yields are shown in Figure 5.3b for data and each background after the simultaneous background-only fit as well.

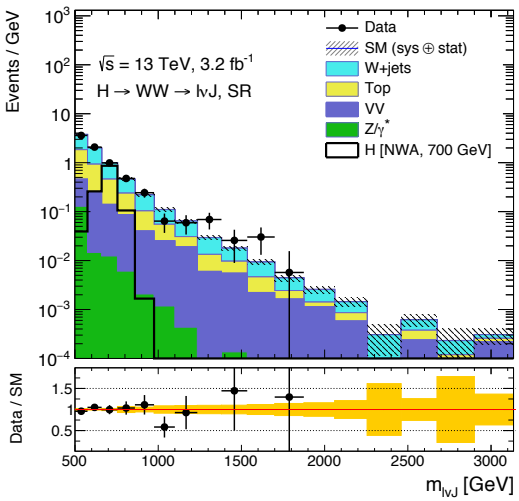

(a) Signal Region

(b) Post-fit Yields

	WW SR	W+jets CR	Top CR
W+jets	280 ± 40	643 ± 65	48 ± 14
Top-quark	180 ± 38	243 ± 55	633 ± 31
Z/γ^*+jets	7 ± 3	26 ± 7	1 ± 1
VV	68 ± 15	63 ± 14	9 ± 3
Backgrounds	535 ± 24	976 ± 30	691 ± 26
Data	533	980	690

Figure 5.3: (a) The post-fit $m_{\ell\nu J}$ distribution for the signal region, with the 700 GeV NWA signal overlaid and the ratio of data/SM-background in the lower panel. The shaded and hatched bands in the lower and upper panels, respectively, show the total uncertainty after a background-only fit to the data. The last bin in the histogram contains the overflow. (b) Event yields in the signal and control regions following the background-only simultaneous fit. The uncertainties shown contain both statistic and systematic uncertainties.

There is good agreement seen between the expected background and the data. Therefore, as in the 8 TeV analysis, 95% CL upper limits are set on the $\sigma_H \times$ BR($H \to WW$) as a function of m_H for both NWA and LWA hypotheses, which are shown in Figures 5.4a and 5.4b, respectively. The limits generally improve with increasing m_H and get progressively worse as a whole with increasing width, Γ_H. In general, the observed limits are consistent with a null (no-signal) hypothesis. In the region between 1200 GeV and 1800 GeV there is a broad excess that extends into the $+2\sigma$ band. A similar excess is not found in the control regions and, upon investigation, the excess is not attributable to any known systematic effects.

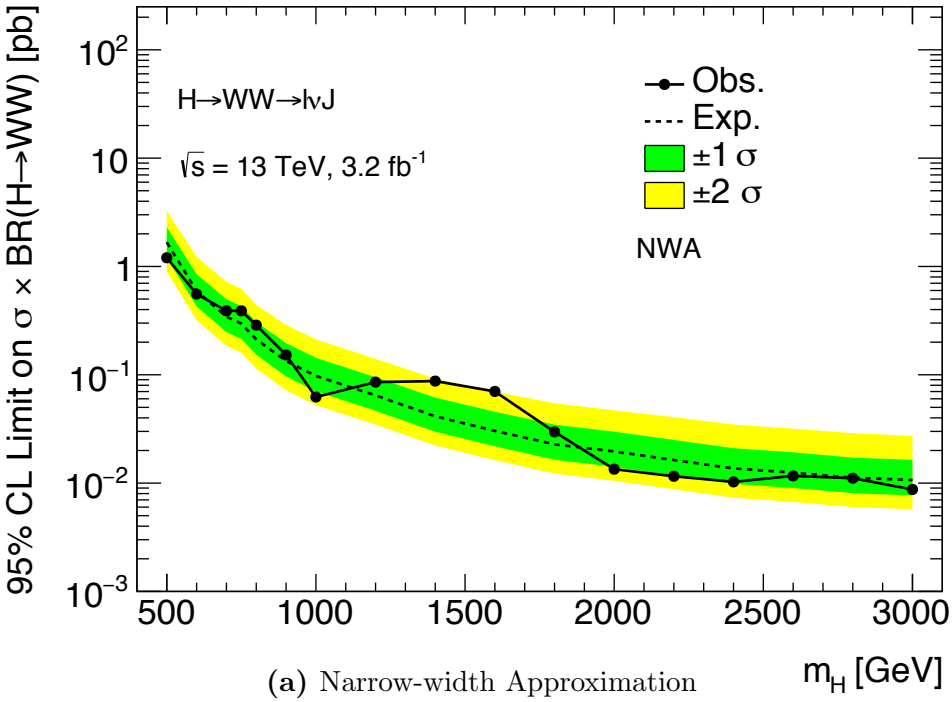

(a) Narrow-width Approximation

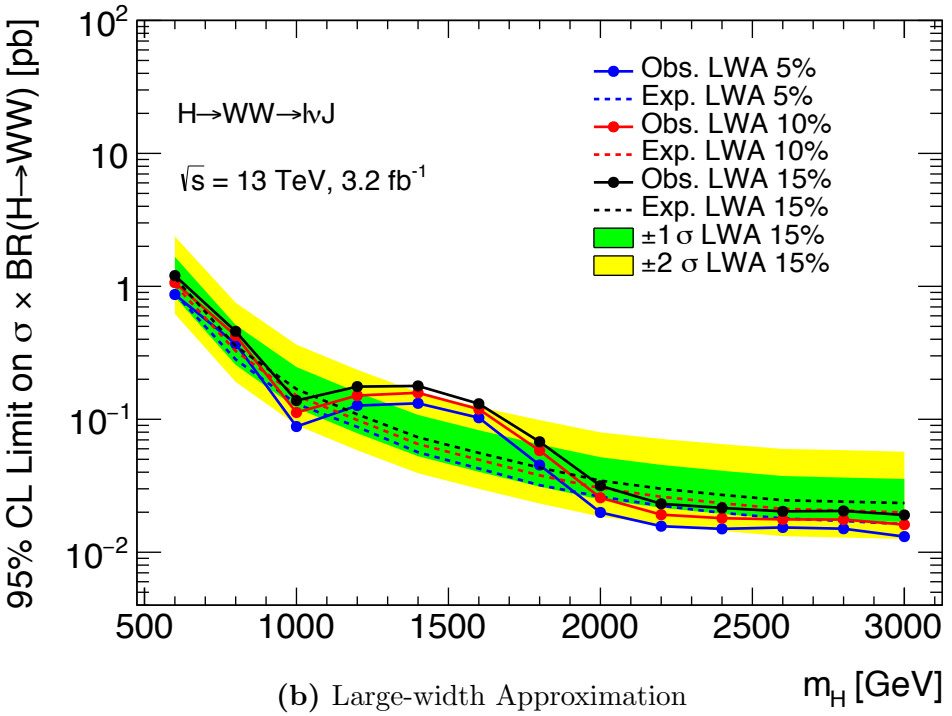

(b) Large-width Approximation

Figure 5.4: Observed and expected 95% CL upper limits on $\sigma_H \times \mathrm{BR}(H \to WW)$ as a function of m_H, for the NWA (a) and LWA (b) heavy Higgs hypotheses, where the LWA hypothesis includes all three widths: 5%, 10%, and 15% of m_H. The green and yellow bands represent the $\pm 1\sigma$ and $\pm 2\sigma$ uncertainties on the expected limits, respectively (only shown for one LWA expected limit line, 15%, for clarity).

Chapter 6

Conclusion

> *"We must not forget that when radium was discovered no one knew that it would prove useful in hospitals. The work was one of pure science. And this is a proof that scientific work must not be considered from the point of view of the direct usefulness of it. It must be done for itself, for the beauty of science, and then there is always the chance that a scientific discovery may become like the radium a benefit for humanity."*
>
> - Marie Curie (1867 - 1934)

First, a search for a high-mass Higgs boson in the $H \to WW \to \ell\nu qq$ decay channel was performed using 20.3 fb^{-1} of LHC pp collision data recorded by the ATLAS detector at a center-of-mass energy of $\sqrt{s} = 8\,\text{TeV}$. No significant deviation from the SM background-only prediction is observed. Thus, for both ggF and VBF production modes, upper limits on $\sigma_H \times \text{BR}(H{\to}WW)$ are set, as a function the Higgs mass m_H, in three different signal width scenarios of a high-mass Higgs boson with a narrow width, an intermediate width, and a SM width. The mass range of the derived limits is $300\,\text{GeV} \leq m_H \leq 1000\,\text{GeV}$, with an extension up to 1500 GeV for the narrow-width scenario.

A second, more model-independent search was performed in the same decay channel using 3.2 fb^{-1} of ATLAS recorded data from the upgraded LHC with pp collisions at a center-of-mass energy of $\sqrt{s} = 13\,\text{TeV}$. The signal widths tested in this

search include the previous narrow-width as well as three new intermediate widths at 5, 10, and 15% of m_H. Again, no significant deviations from the background-only hypothesis are observed, leading to upper limits on the $\sigma_H \times \mathrm{BR}(H \to WW)$ for the different signal width scenarios. The mass range of the limits is substantially improved, in regards to the previous search, and extends up to 3000 GeV.

The results from both searches are substantial improvements over the previous results from the ATLAS experiment in terms of both the cross-section times branching ratio values excluded and the mass range explored.

Searches in this decay channel, $WW \to \ell\nu qq$, are still alive and active! The scalar results presented in Chapter 5 are included in the recently submitted paper [89], which combines searches for heavy narrow-width resonances decaying to WW, WZ, and ZZ with final states $\nu\nu qq$, $\ell\nu qq$, $\ell\ell qq$, and $qqqq$. Also, in the course of writing this dissertation, ATLAS has already recorded another 15 fb^{-1} of data at $\sqrt{s} = 13$ TeV! Analysis of the new data is already underway in this channel, adding more data to the previous results and looking into VBF production and the resolved regime.

References

[1] MissMJ, "Standard Model of Elementary Particles." http://en.wikipedia.org/wiki/Standard Model. (document), 2.1

[2] E. Drexler, "Elementary particle interactions in the Standard Model." http://en.wikipedia.org/wiki/Standard Model. (document), 2.1

[3] LHC Higgs Cross Section Working Group Collaboration, S. Heinemeyer, C. Mariotti, G. Passarino, R. Tanaka, et al., *Handbook of LHC Higgs Cross Sections: 3. Higgs Properties: Report of the LHC Higgs Cross Section Working Group*, Tech. Rep. arXiv:1307.1347. CERN-2013-004, Geneva, 2013. https://cds.cern.ch/record/1559921. (document), 2.2, 2.3, 4.2.1, 4.10.3

[4] J. Pequenao, *Computer generated image of the whole ATLAS detector*,. http://cds.cern.ch/record/1095924. (document), 3.2

[5] J. Goodson, "Diagram of the ATLAS Magnet System." http://www.jetgoodson.com/images/thesisImages/magnetSystems.png. (document), 3.3

[6] ATLAS Collaboration, *The ATLAS Experiment at the CERN Large Hadron Collider*, Journal of Instrumentation **3** no. 08, (2008) S08003. http://stacks.iop.org/1748-0221/3/i=08/a=S08003. (document), 3, 3.4

[7] *Track Reconstruction Performance of the ATLAS Inner Detector at* $\sqrt{s} = 13$ *TeV*, Tech. Rep. ATL-PHYS-PUB-2015-018, CERN, Geneva, Jul, 2015. http://cds.cern.ch/record/2037683. (document), 3.5

[8] ATLAS Collaboration, M. Kayl, *Tracking Performance of the ATLAS Inner Detector and Observation of Known Hadrons*, in *Hadron collider physics. Proceedings, 22nd Conference, HCP 2010, Toronto, Canada, August 23-27, 2010*. 2010. arXiv:1010.1091 [physics.ins-det]. http://inspirehep.net/record/871877/files/arXiv:1010.1091.pdf. (document), 3.6

[9] M. Backhaus, *The upgraded Pixel Detector of the ATLAS Experiment for Run2 at the Large Hadron Collider*, Tech. Rep. ATL-INDET-PROC-2015-015, CERN, Geneva, Dec, 2015. http://cds.cern.ch/record/2110260. (document), 3.7

[10] J. Pequenao, *Computer Generated image of the ATLAS calorimeter*,. http://cds.cern.ch/record/1095927. (document), 3.8

[11] J. Pequenao, *Computer generated image of the ATLAS Muons subsystem*,. http://cds.cern.ch/record/1095929. (document), 3.9

[12] ATLAS Collaboration, *ATLAS Luminosity Public Results: Total Integrated Luminosity and Data Quality in 2012*,. https://twiki.cern.ch/twiki/bin/view/AtlasPublic/LuminosityPublicResults. (document), 4.3

[13] J. Donoghue, E. Golowich, and B. Holstein, *Dynamics of the Standard Model*. Cambridge University Press, Cambridge, 2014. 2

[14] S. L. Glashow, *Partial symmetries of weak interactions*, Nucl. Phys. **B 22** (1961) 579. 2.1

[15] S. Weinberg, *A model of leptons*, Phys. Rev. Lett. **19** (1967) 1264. 2.1

[16] A. Salam, *Elementary particle theory*. Almqvist and Wiksells, Stockholm, 1968. 2.1

[17] M. Peskin and D. Schroeder, *An Introduction to Quantum Field Theory*. Westview Press, Boulder, 1995. 2.1

[18] F. Englert and R. Brout, *Broken symmetry and the mass of gauge vector mesons*, Phys. Rev. Lett. **13** (1964) 321–323. 2.1

[19] P. W. Higgs, *Broken symmetries and the masses of gauge bosons*, Phys. Rev. Lett. **13** (1964) 508–509. 2.1

[20] G. S. Guralnik, C.R. Hagen and T.W.B. Kibble, *Global conservation laws and massless particles*, Phys. Rev. Lett. **13** (1964) 585. 2.1

[21] ATLAS Collaboration, *Observation of a new particle in the search for the Standard Model Higgs boson with the ATLAS detector at the LHC*, Phys. Lett. B **716** (2012) 1–29. 39 p, arXiv:1207.7214 [hep-ph]. 2.2.2

[22] CMS Collaboration, *Observation of a new boson at a mass of 125 GeV with the CMS experiment at the LHC*, Phys. Lett. B **716** (2012) 30–61. 59 p, arXiv:1207.7235 [hep-ph]. 2.2.2

[23] CMS Collaboration, *Combination of standard model Higgs boson searches and measurements of the properties of the new boson with a mass near 125* GeV,. http://cds.cern.ch/record/1542387. CMS-PAS-HIG-13-005. 2.2.2

[24] ATLAS Collaboration, *Measurements of Higgs boson production and couplings in diboson final states with the ATLAS detector at the LHC*, arXiv:1307.1427 [hep-ex]. Submitted to Phys. Lett. **B**. 2.2.2

[25] A. Hill and J. van der Bij, *Strongly interacting singlet-doublet Higgs model*, Phys.Rev. **D36** (1987) 3463–3473. 2.3

[26] M. Veltman and F. Yndurain, *Radiative corrections to WW scattering*, Nucl.Phys. **B325** (1989) 1. 2.3

[27] G. M. Pruna and T. Robens, *Higgs singlet extension parameter space in the light of the LHC discovery*, Phys. Rev. D **88** (2013) 115012. http://link.aps.org/doi/10.1103/PhysRevD.88.115012. 2.3

[28] G. Branco, P. Ferreira, L. Lavoura, M. Rebelo, M. Sher, et al., *Theory and phenomenology of two-Higgs-doublet models*, Phys. Rept. **516** (2012) 1–102, arXiv:1106.0034 [hep-ph]. 2.3

[29] L. Evans and P. Bryant, *LHC Machine*, Journal of Instrumentation **3** no. 08, (2008) S08001. http://stacks.iop.org/1748-0221/3/i=08/a=S08001. 3, 3.1

[30] ATLAS Collaboration, *ATLAS pixel detector electronics and sensors*, Journal of Instrumentation **3** no. 07, (2008) P07007. http://stacks.iop.org/1748-0221/3/i=07/a=P07007. 3.3.1

[31] A. Miucci, *The ATLAS Insertable B-Layer project*, Journal of Instrumentation **9** no. 02, (2014) C02018. http://stacks.iop.org/1748-0221/9/i=02/a=C02018. 3.3.1

[32] M. Capeans, G. Darbo, K. Einsweiller, M. Elsing, T. Flick, M. Garcia-Sciveres, C. Gemme, H. Pernegger, O. Rohne, and R. Vuillermet, *ATLAS Insertable B-Layer Technical Design Report*, Tech. Rep. CERN-LHCC-2010-013. ATLAS-TDR-19, CERN, Geneva, Sep, 2010. http://cds.cern.ch/record/1291633. 3.3.1

[33] ATLAS Collaboration, *The Silicon microstrip sensors of the ATLAS semiconductor tracker*, Nucl. Instrum. Meth. **A578** (2007) 98–118. 3.3.2

[34] T. A. T. C. et al., *The ATLAS Transition Radiation Tracker (TRT) proportional drift tube: design and performance*, Journal of Instrumentation **3** no. 02, (2008) P02013. http://stacks.iop.org/1748-0221/3/i=02/a=P02013. 3.3.3

[35] Y. Nakahama, *The ATLAS Trigger System: Ready for Run-2*, Journal of Physics: Conference Series **664** no. 8, (2015) 082037. http://stacks.iop.org/1742-6596/664/i=8/a=082037. 3.6.1

[36] ATLAS Collaboration, *Search for a high-mass Higgs boson decaying to a W boson pair in pp collisions at $\sqrt{s}$ = 8 TeV with the ATLAS detector*, JHEP **01** (2016) 032, arXiv:1509.00389 [hep-ex]. 4.1

[37] ATLAS Collaboration, *Search for the Higgs boson in the $H \to WW \to l\nu jj$ decay channel at $\sqrt{s}$ = 7 TeV with the ATLAS detector*, Phys. Lett. **B718** (2012) 391–410, arXiv:1206.6074 [hep-ex]. 4.1

[38] S. Goria, G. Passarino, and D. Rosco, *The Higgs-boson lineshape*, Nuclear Physics B **864** (2012) 530–579. 4.1, 4.2.1

[39] ATLAS Collaboration, *The ATLAS Simulation Infrastructure*, Eur. Phys. J. **C70** (2010) 823–874, arXiv:1005.4568 [physics.ins-det]. 4.2, 4.2

[40] S. A. et al., *Geant4–a simulation toolkit*, Nuclear Instruments and Methods in Physics Research Section A: Accelerators, Spectrometers, Detectors and Associated Equipment **506** no. 3, (2003) 250 – 303. http://www.sciencedirect.com/science/article/pii/S0168900203013688. 4.2

[41] J. e. a. Allison, *Geant4 developments and applications*, Nuclear Science, IEEE Transactions on **53** no. 1, (2006) 270–278. 4.2

[42] S. Alioli, P. Nason, C. Oleari, and E. Re, *NLO Higgs boson production via gluon fusion matched with shower in POWHEG*, JHEP **0904** (2009) 002, arXiv:0812.0578 [hep-ph]. 4.2.1

[43] T. Sjöstrand, S. Mrenna, and P. Z. Skands, *A Brief Introduction to PYTHIA 8.1*, Comput. Phys. Commun. **178** (2008) 852–867, arXiv:0710.3820 [hep-ph]. 4.2.1

[44] S. Actis, G. Passarino, C. Sturm, and S. Uccirati, *NLO electroweak corrections to Higgs boson production at hadron colliders*, Phys. Lett. **B670** (2008) 12–17, arXiv:0809.1301 [hep-ph]. 4.2.1

[45] C. Anastasiou and K. Melnikov, *Higgs boson production at hadron colliders in NNLO QCD*, Nucl. Phys. **B646** (2002) 220–256, arXiv:hep-ph/0207004 [hep-ph]. 4.2.1

[46] S. Catani, D. de Florian, M. Grazzini, and P. Nason, *Soft-gluon re-summation for Higgs boson production at hadron colliders*, JHEP **0307** (2003) 028, arXiv:hep-ph/0306211. 4.2.1

[47] M. Ciccolini, A. Denner, and S. Dittmaier, *Electroweak and QCD corrections to Higgs production via vector-boson fusion at the LHC*, Phys. Rev. **D 77** (2008) 013002, arXiv:0710.4749 [hep-ph]. 4.2.1, 4.10.3

[48] P. Bolzoni, F. Maltoni, S.-O. Moch, and M. Zaro, *Higgs production via vector-boson fusion at NNLO in QCD*, Phys. Rev. Lett. **105** (2010) 011801, arXiv:1003.4451 [hep-ph]. 4.2.1, 4.10.3

[49] A. Bredenstein, A. Denner, S. Dittmaier, and M. Weber, *Radiative corrections to the semileptonic and hadronic Higgs-boson decays $H \to WW/ZZ \to 4$ fermions*, JHEP **0702** (2007) 080, arXiv:hep-ph/0611234. 4.2.1

[50] J. M. Campbell and R. Ellis, *MCFM for the Tevatron and the LHC*, Nucl. Phys. Proc. Suppl. **205-206** (2010) 10–15, arXiv:1007.3492 [hep-ph]. 4.2.1

[51] K. Arnold et al., *Release Note – VBFNLO-2.6.0*, arXiv:1207.4975 [hep-ph]. 4.2.1

[52] K. Arnold et al., *VBFNLO: A parton level Monte Carlo for processes with electroweak bosons – Manual for Version 2.5.0*, arXiv:1107.4038 [hep-ph]. * Temporary entry *. 4.2.1

[53] K. Arnold et al., *VBFNLO: A parton level Monte Carlo for processes with electroweak bosons*, Comput. Phys. Commun. **180** (2009) 1661, arXiv:0811.4559 [hep-ph]. 4.2.1

[54] T. Gleisberg et al., *Event generation with SHERPA 1.1*, JHEP **0902** (2009) 007, arXiv:0811.4622 [hep-ph]. 4.2.2

[55] T. Sjöstrand, S. Mrenna, and P. Z. Skands, *PYTHIA 6.4 physics and manual*, JHEP **0605** (2006) 026, arXiv:hep-ph/0603175. 4.2.2

[56] B. P. Kersevan and E. Richter-Was, *The Monte Carlo event generator AcerMC versions 2.0 to 3.8 with interfaces to PYTHIA 6.4, HERWIG 6.5 and ARIADNE 4.1*, Comput. Phys. Commun. **184** (2013) 919–985, arXiv:hep-ph/0405247 [hep-ph]. 4.2.2

[57] ATLAS Collaboration, *Measurements of normalized differential cross sections for $t\bar{t}$ production in pp collisions at $\sqrt{s} = 7$ TeV using the ATLAS detector*, Phys. Rev. **D90** no. 7, (2014) 072004, arXiv:1407.0371 [hep-ex]. 4.2.2

[58] M. L. Mangano et al., *ALPGEN, a generator for hard multi-parton processes in hadronic collisions*, JHEP **0307** (2003) 001, arXiv:hep-ph/0206293. 4.2.2

[59] J. M. Butterworth, J. R. Forshaw, and M. H. Seymour, *Multiparton interactions in photoproduction at HERA*, Z. Phys. **C72** (1996) 637, arXiv:hep-ph/9601371. 4.2.2

[60] G. Corcella et al., *HERWIG 6: An event generator for hadron emission reactions with interfering gluons (including super-symmetric processes)*, JHEP **0101** (2001) 010. 4.2.2

[61] D. Quality, *ATLAS Data Quality Operations in 2012*, Tech. Rep. ATL-DAPR-INT-2015-001, CERN, Geneva, Jan, 2015. https://cds.cern.ch/record/1982821. 4.3

[62] ATLAS Collaboration, *Electron efficiency measurements with the ATLAS detector using the 2012 LHC proton-proton collision data*,. 4.4, 4.5.2, 4.10

[63] ATLAS Collaboration, *Performance of the ATLAS muon trigger in pp collisions at $\sqrt{s} = 8$ TeV*, Eur. Phys. J. **C75** (2015) 120, arXiv:1408.3179 [hep-ex]. 4.4

[64] ATLAS Collaboration, *Measurement of the muon reconstruction performance of the ATLAS detector using 2011 and 2012 LHC proton-proton collision data*, Eur. Phys. J. **C74** no. 11, (2014) 3130, arXiv:1407.3935 [hep-ex]. 4.4, 4.5.3, 4.10

[65] M. Cacciari, G. P. Salam, and G. Soyez, *The anti- k t jet clustering algorithm*, Journal of High Energy Physics **2008** no. 04, (2008) 063. http://stacks.iop.org/1126-6708/2008/i=04/a=063. 4.5.4

[66] ATLAS Collaboration, *Pile-up subtraction and suppression for jets in ATLAS*,. 4.5.4

[67] Y. Dokshitzer, G. Leder, S. Moretti, and B. Webber, *Better jet clustering algorithms*, Journal of High Energy Physics **1997** no. 08, (1997) 001. http://stacks.iop.org/1126-6708/1997/i=08/a=001. 4.5.4

[68] ATLAS Collaboration, *Performance of jet substructure techniques for large-R jets in proton-proton collisions at $\sqrt{s}$ = 7 TeV using the ATLAS detector*, JHEP **09** (2013) 076, arXiv:1306.4945 [hep-ex]. 4.5.4

[69] J. M. Butterworth, A. R. Davison, M. Rubin, and G. P. Salam, *Jet Substructure as a New Higgs-Search Channel at the Large Hadron Collider*, Phys. Rev. Lett. **100** (2008) 242001. http://link.aps.org/doi/10.1103/PhysRevLett.100.242001. 4.5.4

[70] ATLAS Collaboration, *Calibration of b-tagging using dileptonic top pair events in a combinatorial likelihood approach with the ATLAS experiment*,. 4.5.4, 4.10

[71] ATLAS Collaboration, *Calibration of the performance of b-tagging for c and light-flavour jets in the 2012 ATLAS data*,. 4.5.4, 4.10

[72] ATLAS Collaboration, *Performance of Missing Transverse Momentum Reconstruction in Proton-Proton Collisions at 7 TeV with ATLAS*, Eur. Phys. J. **C72** (2012) 1844, arXiv:1108.5602 [hep-ex]. 4.5.5, 4.10

[73] ATLAS Collaboration, *Performance of Missing Transverse Momentum Reconstruction in ATLAS studied in Proton-Proton Collisions recorded in 2012 at 8 TeV*,. 4.5.5, 4.10

[74] ATLAS Collaboration, *Electron and photon energy calibration with the ATLAS detector using LHC Run 1 data*, Eur. Phys. J. **C74** (2014) 3071, arXiv:1407.5063 [hep-ex]. 4.10

[75] ATLAS Collaboration, *Jet energy measurement and its systematic uncertainty in proton-proton collisions at $\sqrt{s}$ = 7 TeV with the ATLAS detector*, Eur. Phys. J. **C75** (2015) 17, arXiv:1406.0076 [hep-ex]. 4.10

[76] ATLAS Collaboration, *Improved luminosity determination in pp collisions at $\sqrt{s}$ = 7 TeV using the ATLAS detector at the LHC*, Eur. Phys. J. C **73** (2013) 2518, arXiv:1302.4393 [hep-ex]. 4.10

[77] ATLAS Collaboration, *Jet mass and substructure of inclusive jets in $\sqrt{s} = 7$ TeV pp collisions with the ATLAS experiment*, JHEP **1205** (2012) 128, arXiv:1203.4606 [hep-ex]. 4.10.1

[78] G. Passarino, *Higgs interference effects in $gg \to ZZ$ and their uncertainty*, Journal of High Energy Physics **2012** no. 8, (2012) 1–22. http://dx.doi.org/10.1007/JHEP08(2012)146. 4.10.3

[79] P. Bolzoni, F. Maltoni, S.-O. Moch, and M. Zaro, *Vector boson fusion at next-to-next-to-leading order in QCD: Standard model Higgs boson and beyond*, Phys. Rev. D **85** (2012) 035002. http://link.aps.org/doi/10.1103/PhysRevD.85.035002. 4.10.3

[80] ATLAS Collaboration, *Combined search for the Standard Model Higgs boson in pp collisions at $\sqrt{s} = 7$ TeV with the ATLAS detector*, Phys. Rev. **D86** (2012) 032003, arXiv:1207.0319 [hep-ex]. 4.12.1

[81] A.L. Read, *Presentation of search results: the CL_s technique*, J. Phys. **G28** (2002) 2693. 4.12.1

[82] G. Cowan, K. Cranmer, E. Gross, and O. Vitells, *Asymptotic formulae for likelihood-based tests of new physics*, Eur. Phys. J. C **71** (2011) 1554, arXiv:1007.1727 [physics.data-an]. [Erratum: Eur. Phys. J.C73,2501(2013)]. 4.12.1

[83] *Search for WW/WZ resonance production in the $\ell\nu qq$ final state at $\sqrt{s} = 13$ TeV with the ATLAS detector at the LHC*, Tech. Rep. ATLAS-CONF-2015-075, CERN, Geneva, Dec, 2015. https://cds.cern.ch/record/2114847. 5.1, 5.2

[84] K. Agashe, H. Davoudiasl, G. Perez, and A. Soni, *Warped gravitons at the CERN LHC and beyond*, Phys. Rev. D **76** (2007) 036006. http://link.aps.org/doi/10.1103/PhysRevD.76.036006. 5.1

[85] D. Pappadopulo, A. Thamm, R. Torre, and A. Wulzer, *Heavy vector triplets: bridging theory and data*, Journal of High Energy Physics **2014** no. 9, (2014) 1–50. http://dx.doi.org/10.1007/JHEP09(2014)060. 5.1

[86] *Search for a high-mass Higgs boson decaying to a pair of W bosons in pp collisions at sqrt(s)=13 TeV with the ATLAS detector*, Tech. Rep. ATLAS-CONF-2016-021, CERN, Geneva, Apr, 2016. https://cds.cern.ch/record/2147445. 5.1, 5.2

[87] *Search for resonances decaying to photon pairs in 3.2 fb^{-1} of pp collisions at $\sqrt{s} = 13$ TeV with the ATLAS detector*, Tech. Rep. ATLAS-CONF-2015-081, CERN, Geneva, Dec, 2015. https://cds.cern.ch/record/2114853. 5.2.2

[88] L. Asquith, C. M. Delitzsch, and R. Camacho Toro, *Identification of boosted, hadronically-decaying W and Z bosons in $\sqrt{s} = 13$ TeV Monte Carlo Simulations for ATLAS*, Tech. Rep. ATL-PHYS-PUB-2015-033, CERN, Geneva, Aug, 2015. https://cds.cern.ch/record/2041461. 5.2.3

[89] ATLAS Collaboration Collaboration, *Searches for heavy diboson resonances in pp collisions at $\sqrt{s} = 13$ TeV with the ATLAS detector*, Tech. Rep. CERN-EP-2016-106. arXiv:1606.04833, CERN, Geneva, Jun, 2016. https://cds.cern.ch/record/2161140. Comments: 29 pages plus author list + cover pages (46 pages total), 8 figures, 5 tables, submitted to JHEP, All figures including auxiliary figures are available at https://atlas.web.cern.ch/Atlas/GROUPS/PHYSICS/PAPERS/EXOT-2016-01/. 6

Appendix A

8 TeV Analysis Auxiliary Material

A.1 Reconstructed Higgs Mass Separated by Lepton Flavor and Charge

In this section, Figures A.1 - A.4 show the reconstructed Higgs mass $m_{\ell\nu jj}$ distributions separated by lepton flavor and charge in the WCR, TopCR, and SR after the ggF preselection or the VBF preselection. The upper panel of each plot shows the background processes (normalized by their theoretical cross-sections) stacked, with the data and a hypothetical CPS signal ($m_H = 500\,\text{GeV}$) overlaid. The lower panels show the ratio of data to background. The hatched gray band in the upper panel and the shaded yellow band in the lower panel show the combined statistical and systematic uncertainties on the background. Lastly, the $W+$jets and top backgrounds in all of the plots include their $m_{\ell\nu jj}$ shape reweighting, but not their normalization from the final fit.

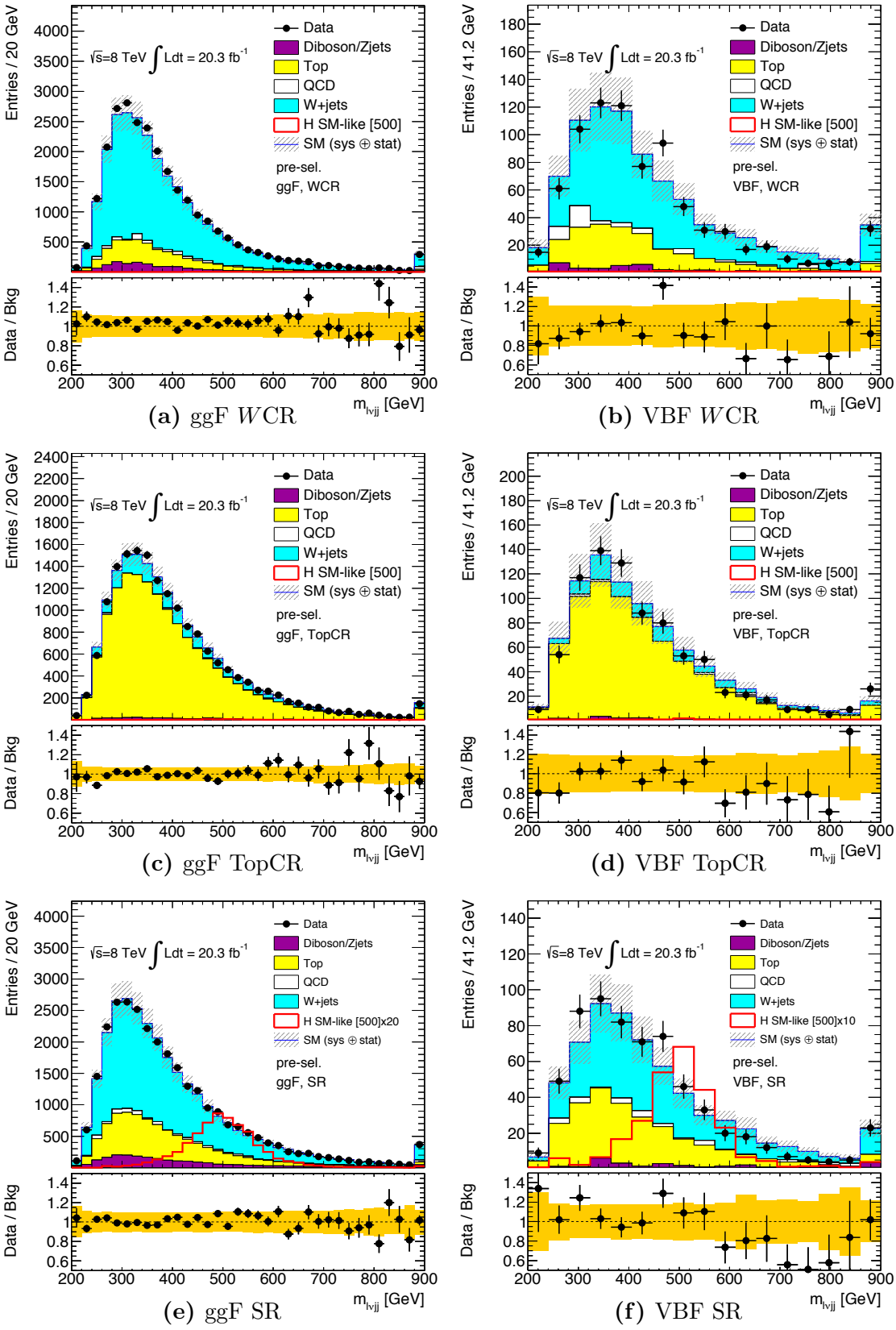

(a) ggF WCR **(b)** VBF WCR

(c) ggF TopCR **(d)** VBF TopCR

(e) ggF SR **(f)** VBF SR

Figure A.1: e^- category reconstructed Higgs mass

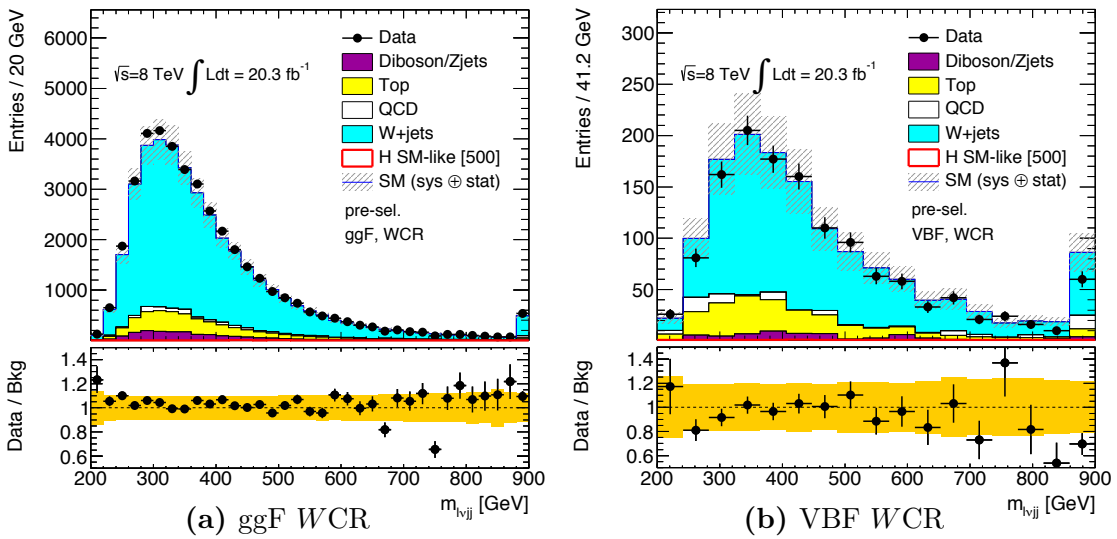

(a) ggF WCR

(b) VBF WCR

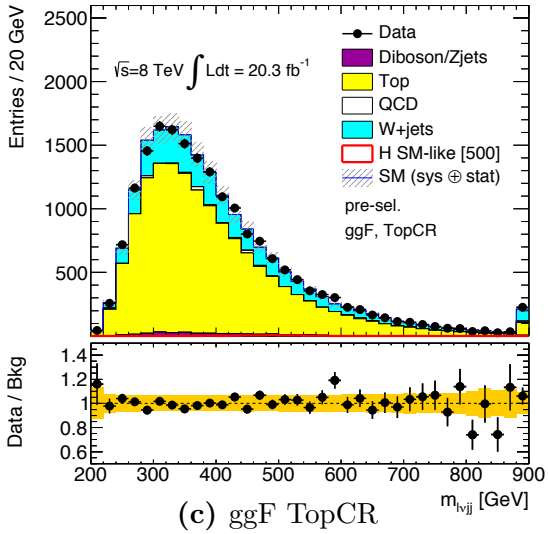

(c) ggF TopCR

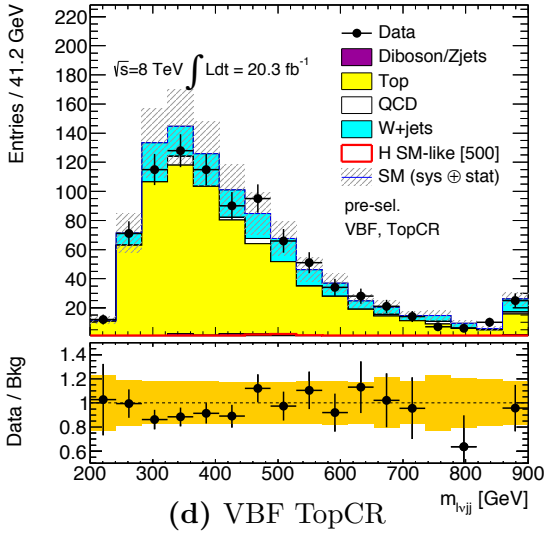

(d) VBF TopCR

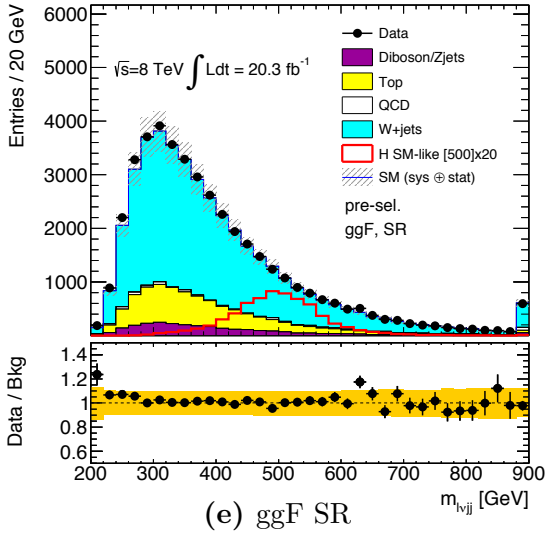

(e) ggF SR

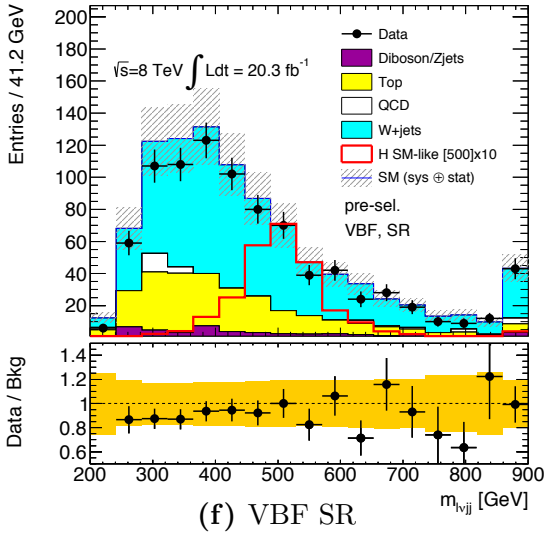

(f) VBF SR

Figure A.2: e^+ category reconstructed Higgs mass

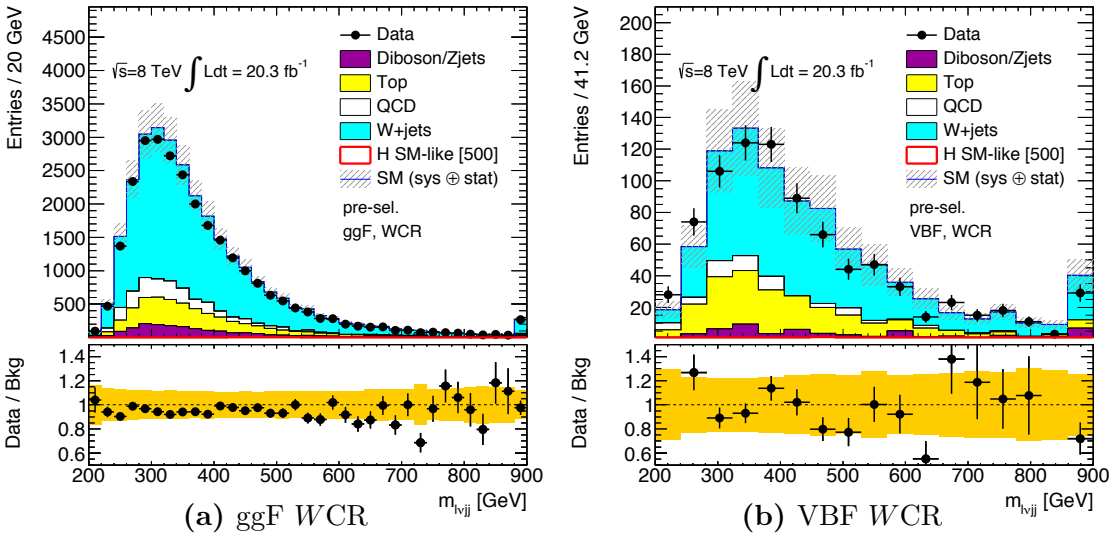

(a) ggF WCR

(b) VBF WCR

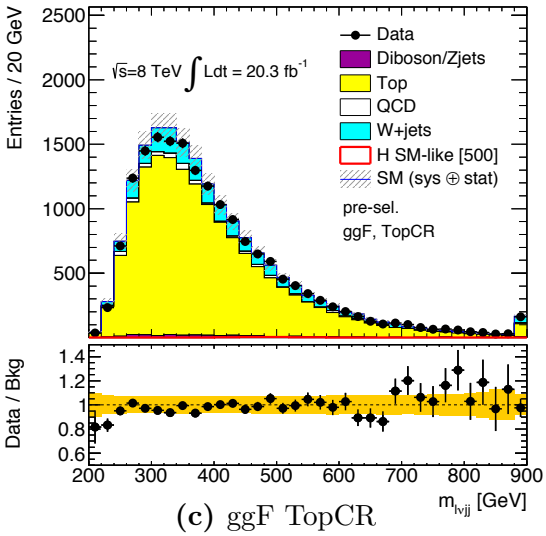

(c) ggF TopCR

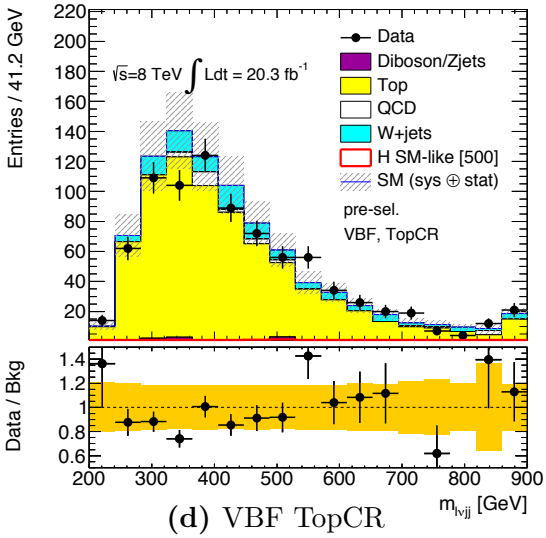

(d) VBF TopCR

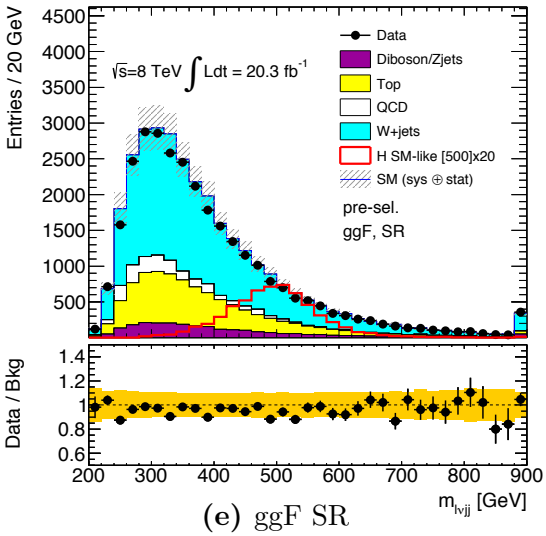

(e) ggF SR

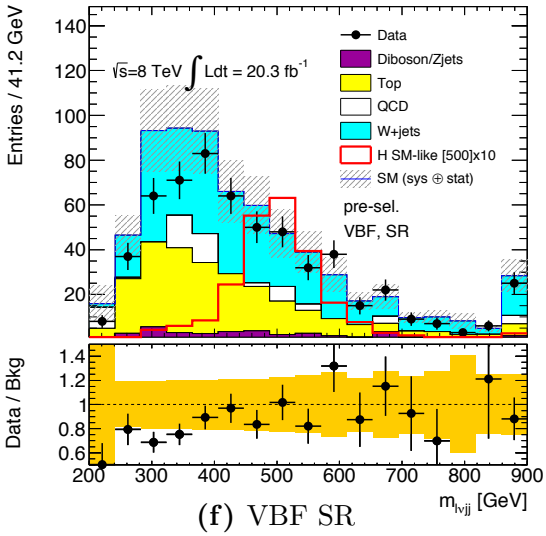

(f) VBF SR

Figure A.3: μ^- category reconstructed Higgs mass

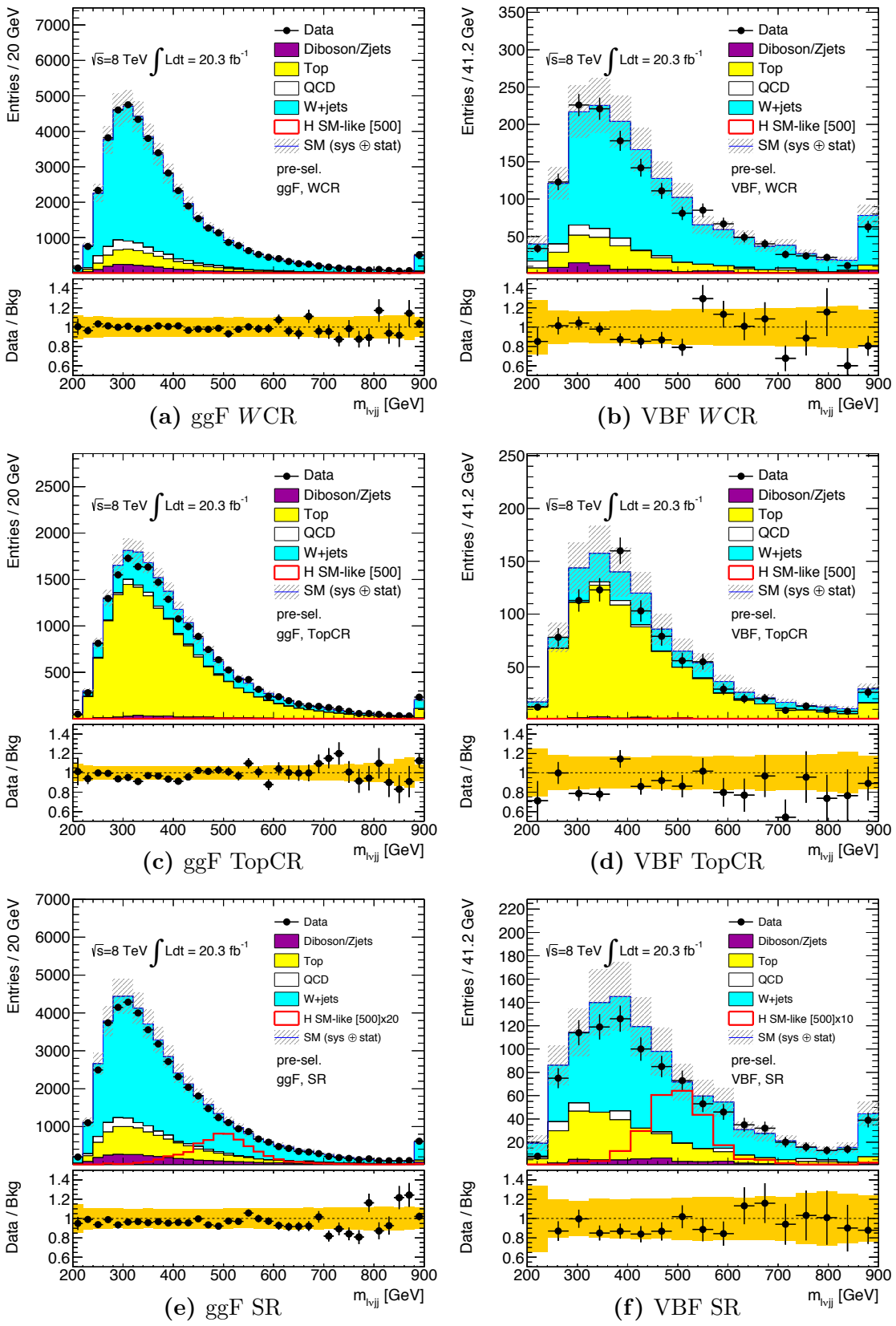

(a) ggF WCR (b) VBF WCR

(c) ggF TopCR (d) VBF TopCR

(e) ggF SR (f) VBF SR

Figure A.4: μ^+ category reconstructed Higgs mass

A.2 Kinematic Variable Modeling after Event Preselection

In this section, distributions of the kinematic variables used in the analysis selections are shown in the WCR, TopCR, and SR after the ggF preselection or the VBF preselection. All lepton flavor and charge categories are summed in each plot. A few variables only pertain to certain categories of events like the merged (resolved) category's large-R (small-R) W jet(s) and the VBF category's tagging jets.

The upper panel of each plot shows the background processes (normalized by their theoretical cross-sections) stacked, with the data and a hypothetical CPS signal ($m_H = 500\,\text{GeV}$) overlaid. The lower panels show the ratio of data to background. The hatched gray band in the upper panel and the shaded yellow band in the lower panel show the combined statistical and systematic uncertainties on the background. Lastly, the $W+$jets and top backgrounds in all of the plots include their $m_{\ell\nu jj}$ shape reweighting, but not their normalization from the final fit.

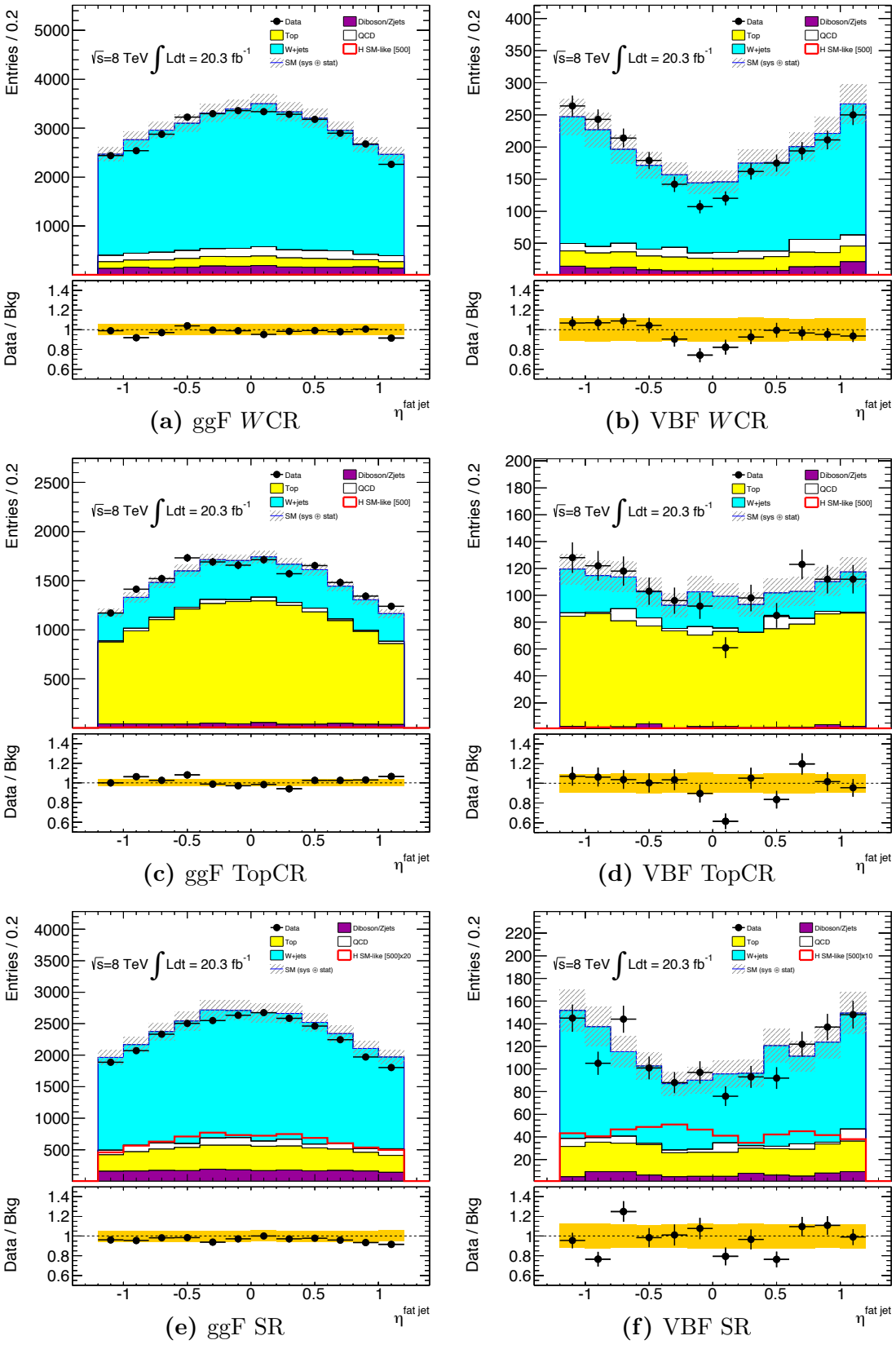

Figure A.5: Large-R W-jet η [merged only]

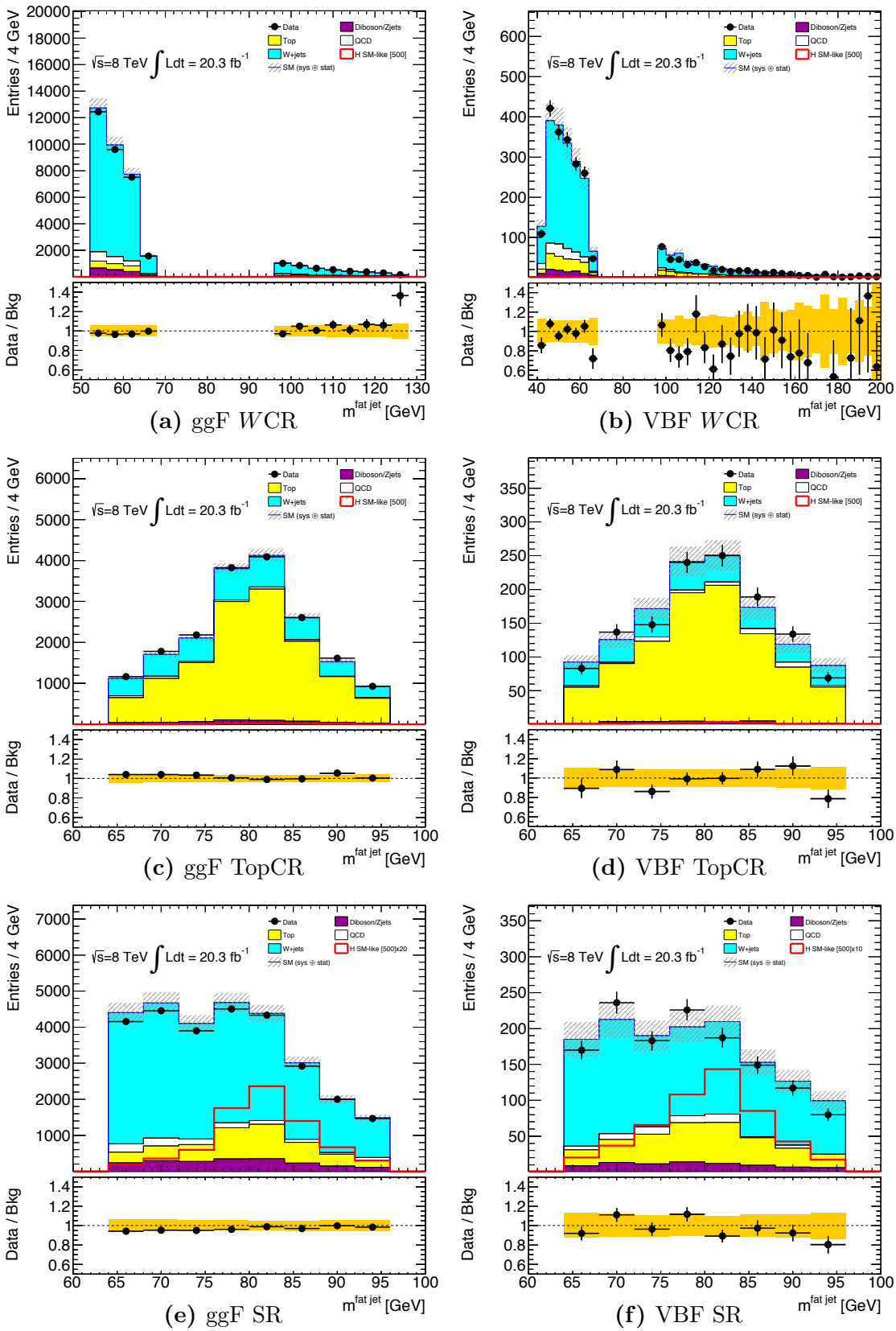

(a) ggF WCR **(b)** VBF WCR

(c) ggF TopCR **(d)** VBF TopCR

(e) ggF SR **(f)** VBF SR

Figure A.6: Large-R W-jet (merged hadronic W) mass

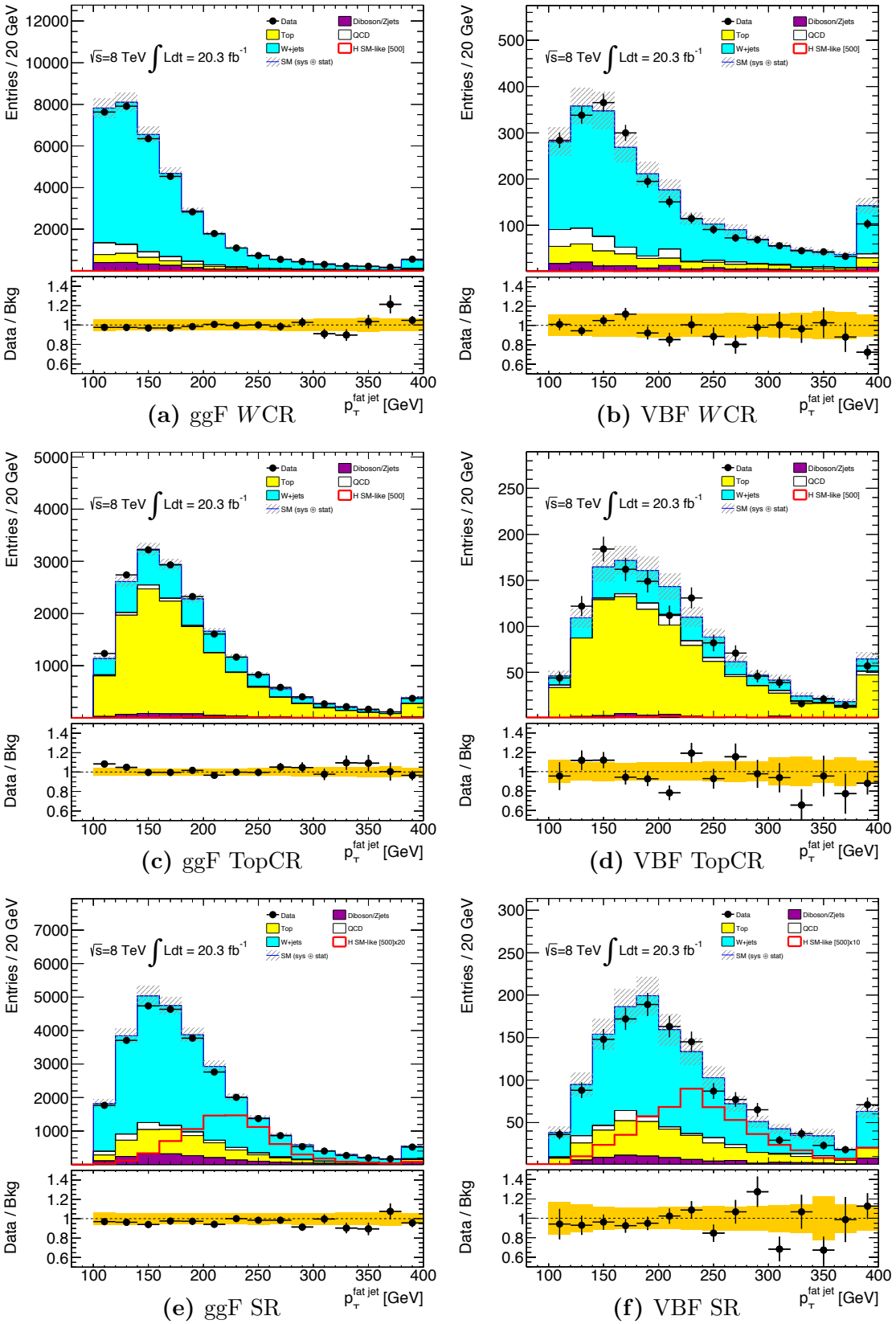

Figure A.7: Large-R W-jet (merged hadronic W) p_{T}

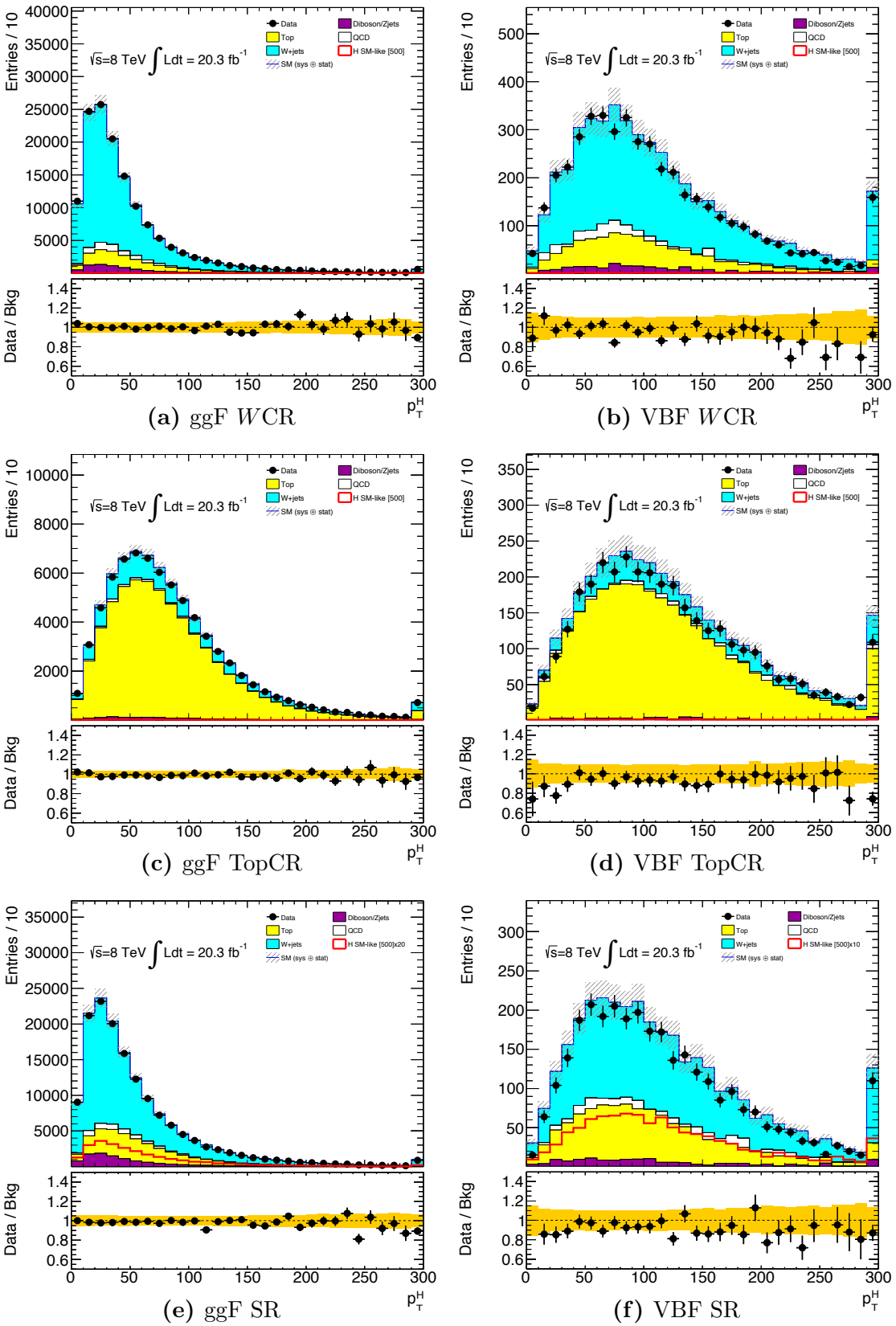

(a) ggF WCR **(b)** VBF WCR

(c) ggF TopCR **(d)** VBF TopCR

(e) ggF SR **(f)** VBF SR

Figure A.8: Reconstructed Higgs p_{T}

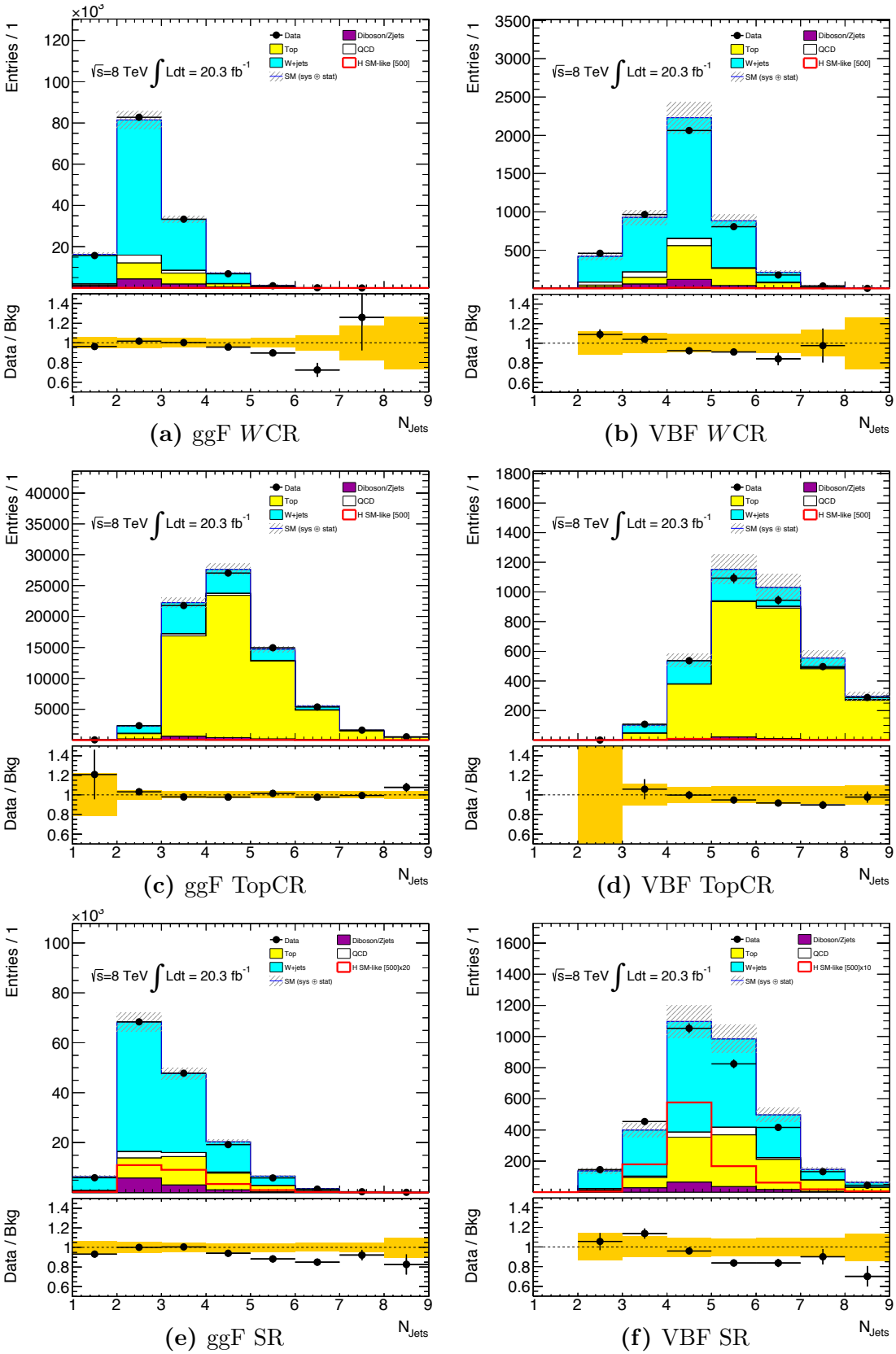

(a) ggF WCR (b) VBF WCR

(c) ggF TopCR (d) VBF TopCR

(e) ggF SR (f) VBF SR

Figure A.9: Number of small-R jets

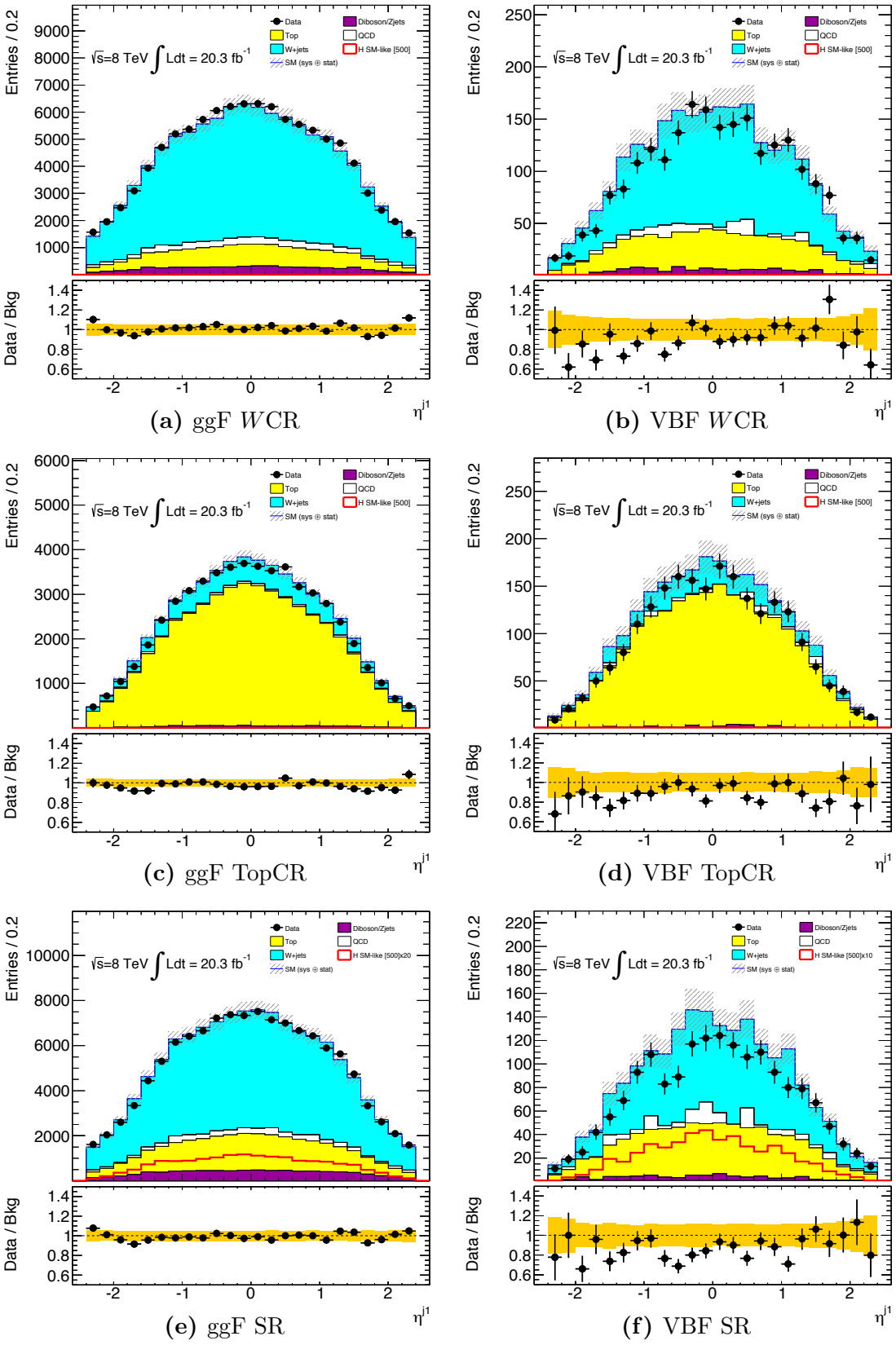

(a) ggF WCR **(b)** VBF WCR

(c) ggF TopCR **(d)** VBF TopCR

(e) ggF SR **(f)** VBF SR

Figure A.10: Leading small-R W-jet η [resolved only]

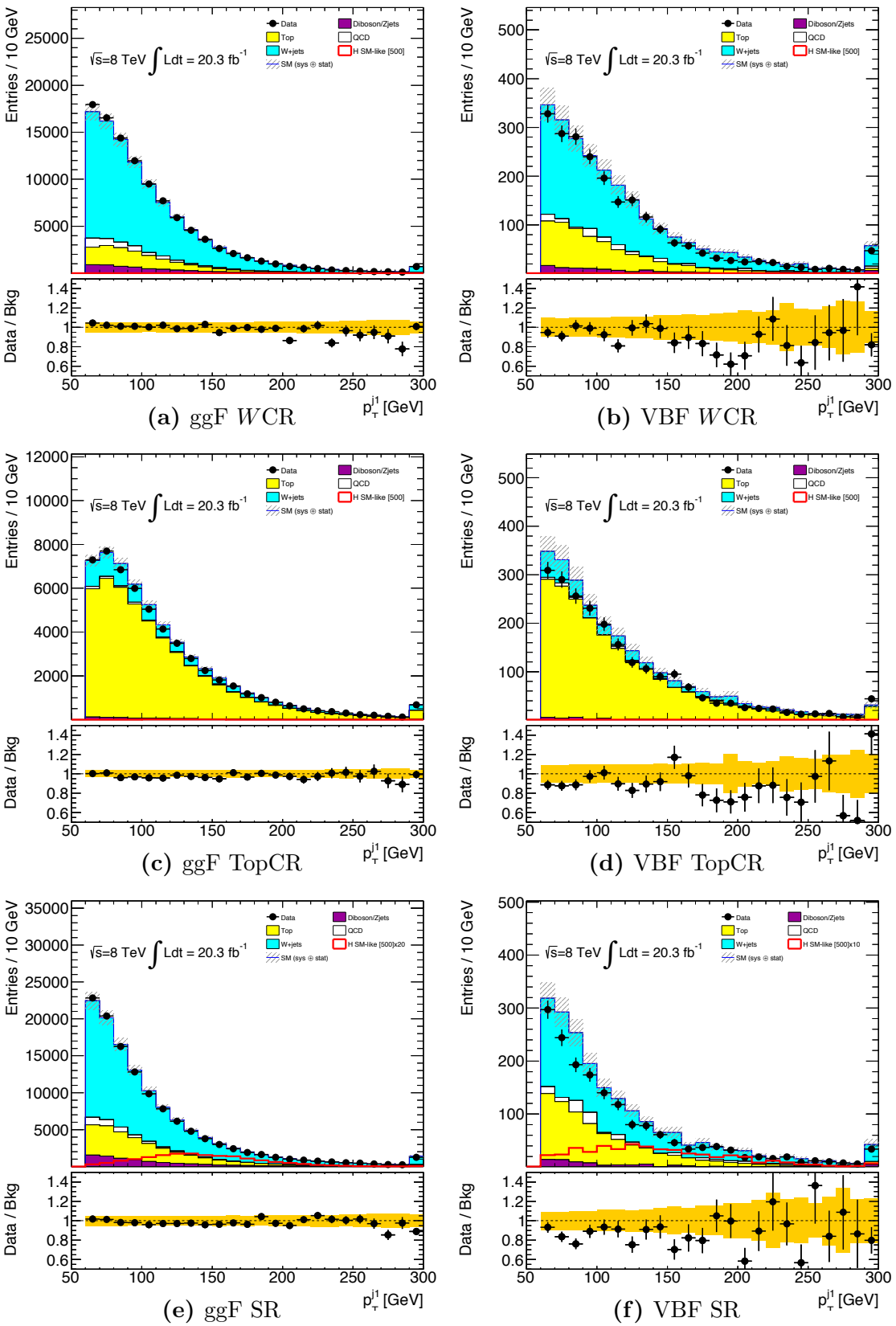

(a) ggF WCR (b) VBF WCR

(c) ggF TopCR (d) VBF TopCR

(e) ggF SR (f) VBF SR

Figure A.11: Leading small-R W-jet p_{T} [resolved only]

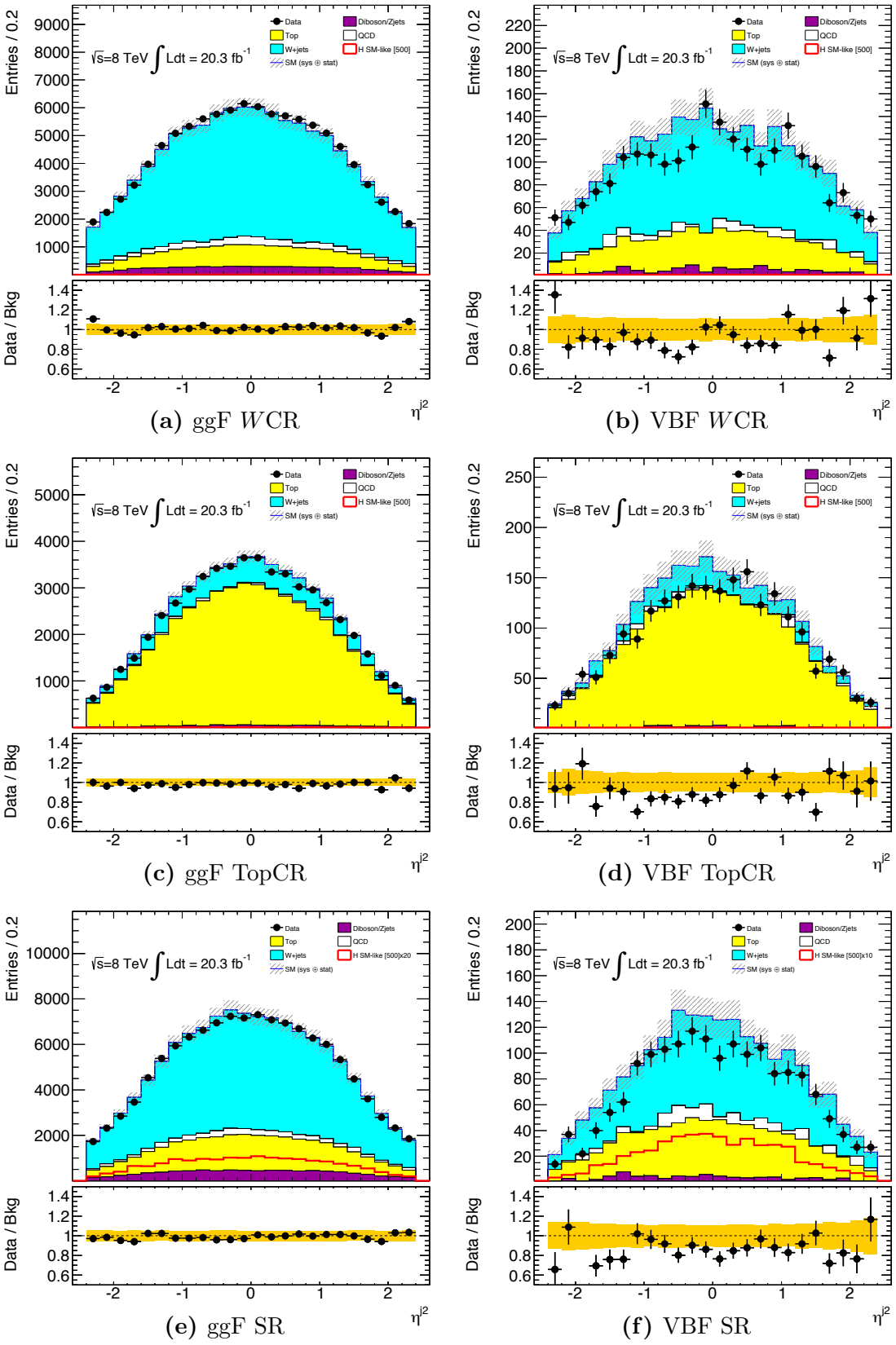

(a) ggF WCR **(b)** VBF WCR

(c) ggF TopCR **(d)** VBF TopCR

(e) ggF SR **(f)** VBF SR

Figure A.12: Sub-leading small-R W-jet η [resolved only]

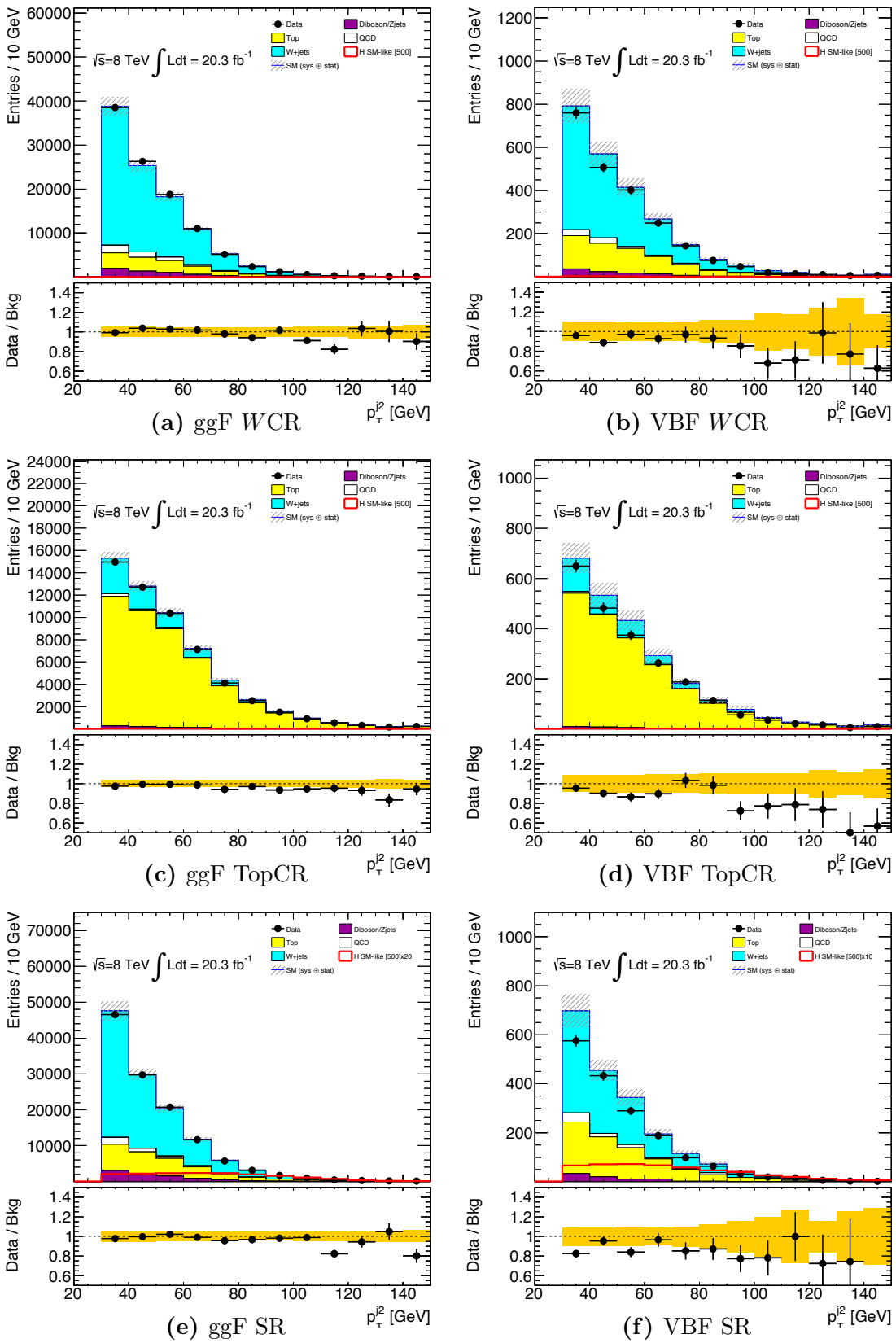

Figure A.13: Sub-leading small-R W-jet p_{T} [resolved only]

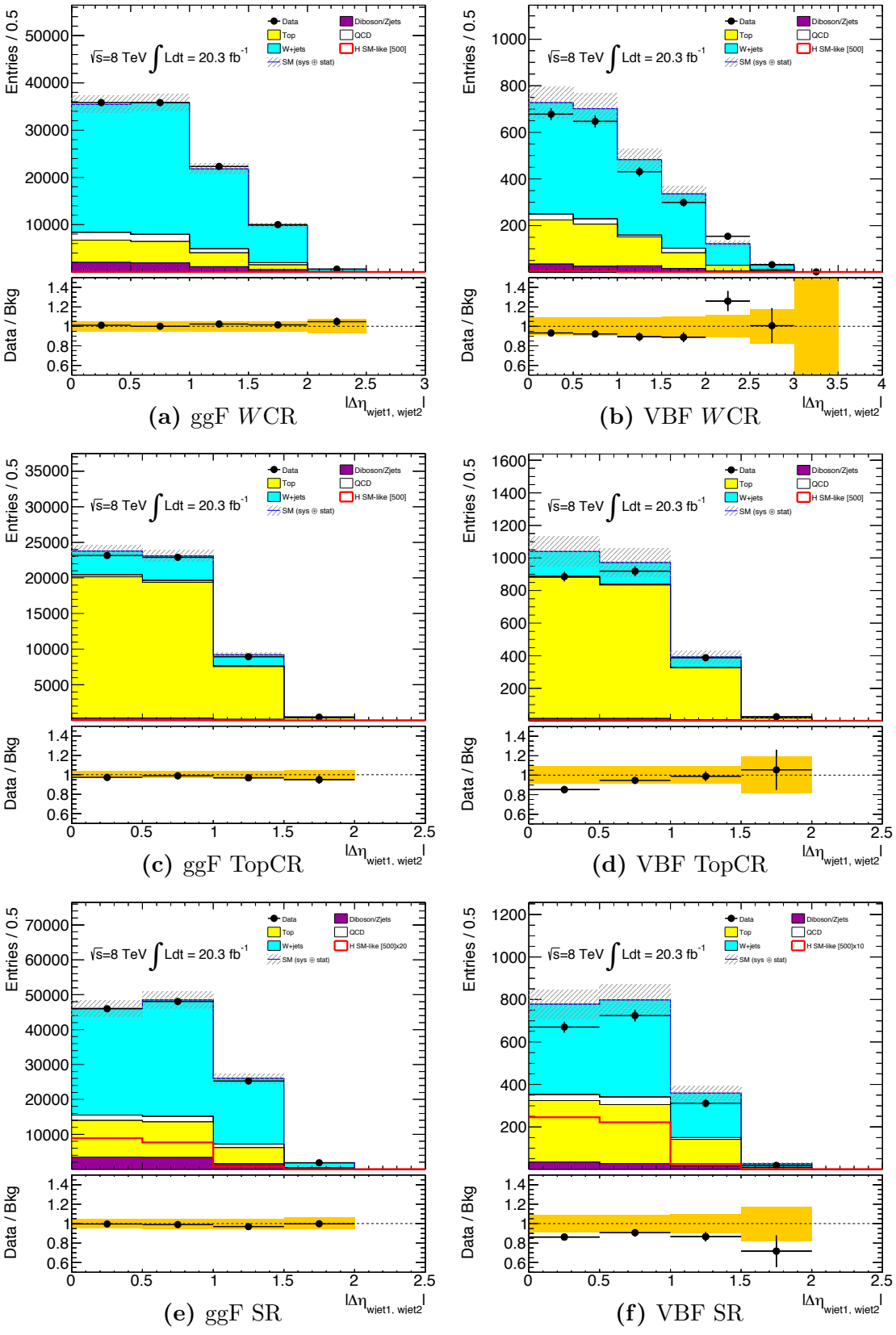

(a) ggF WCR **(b)** VBF WCR

(c) ggF TopCR **(d)** VBF TopCR

(e) ggF SR **(f)** VBF SR

Figure A.14: $|\Delta\eta|$ between small-R W-jets [resolved only]

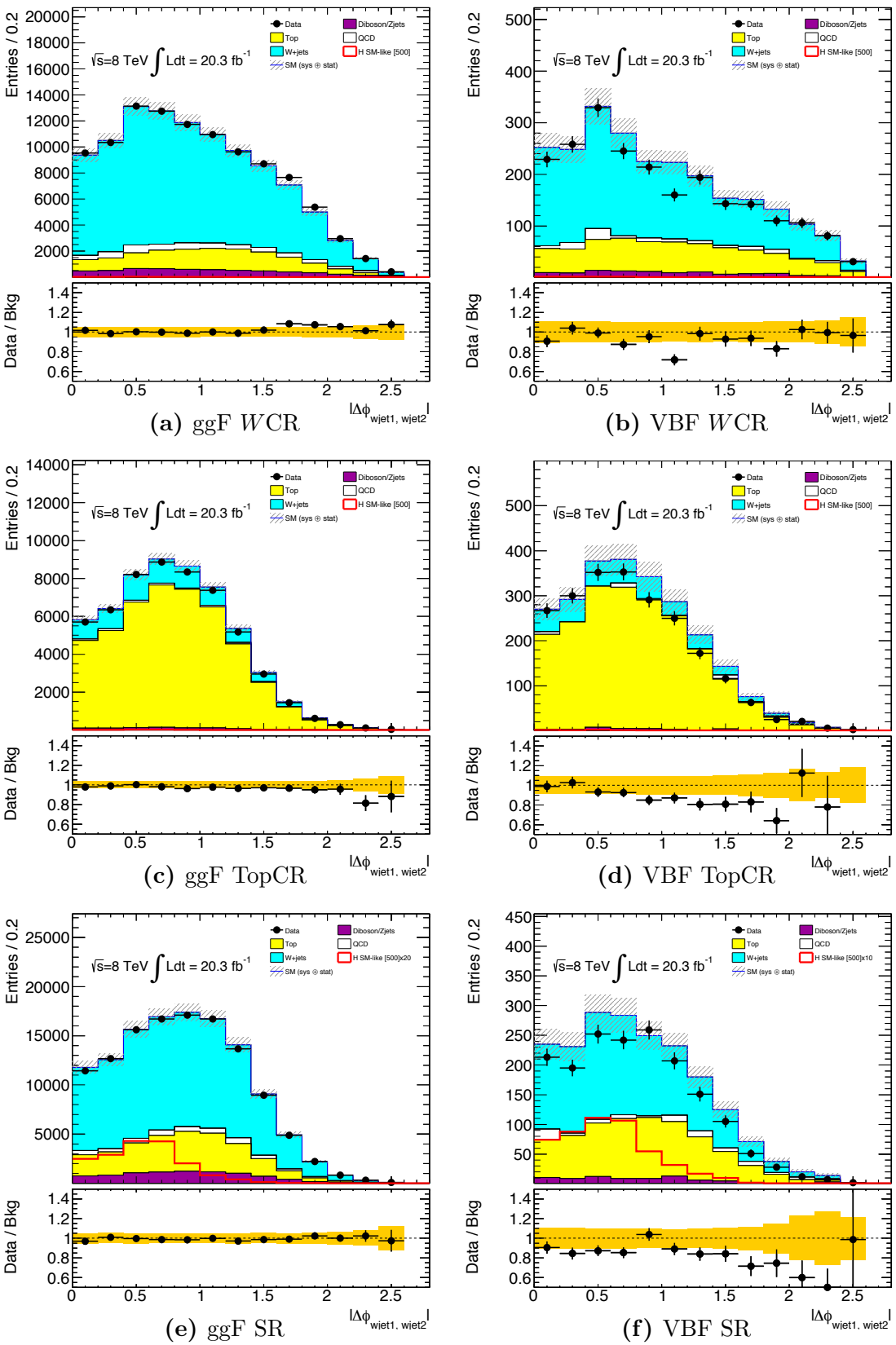

(a) ggF WCR **(b)** VBF WCR

(c) ggF TopCR **(d)** VBF TopCR

(e) ggF SR **(f)** VBF SR

Figure A.15: $|\Delta\phi|$ between small-R W-jets [resolved only]

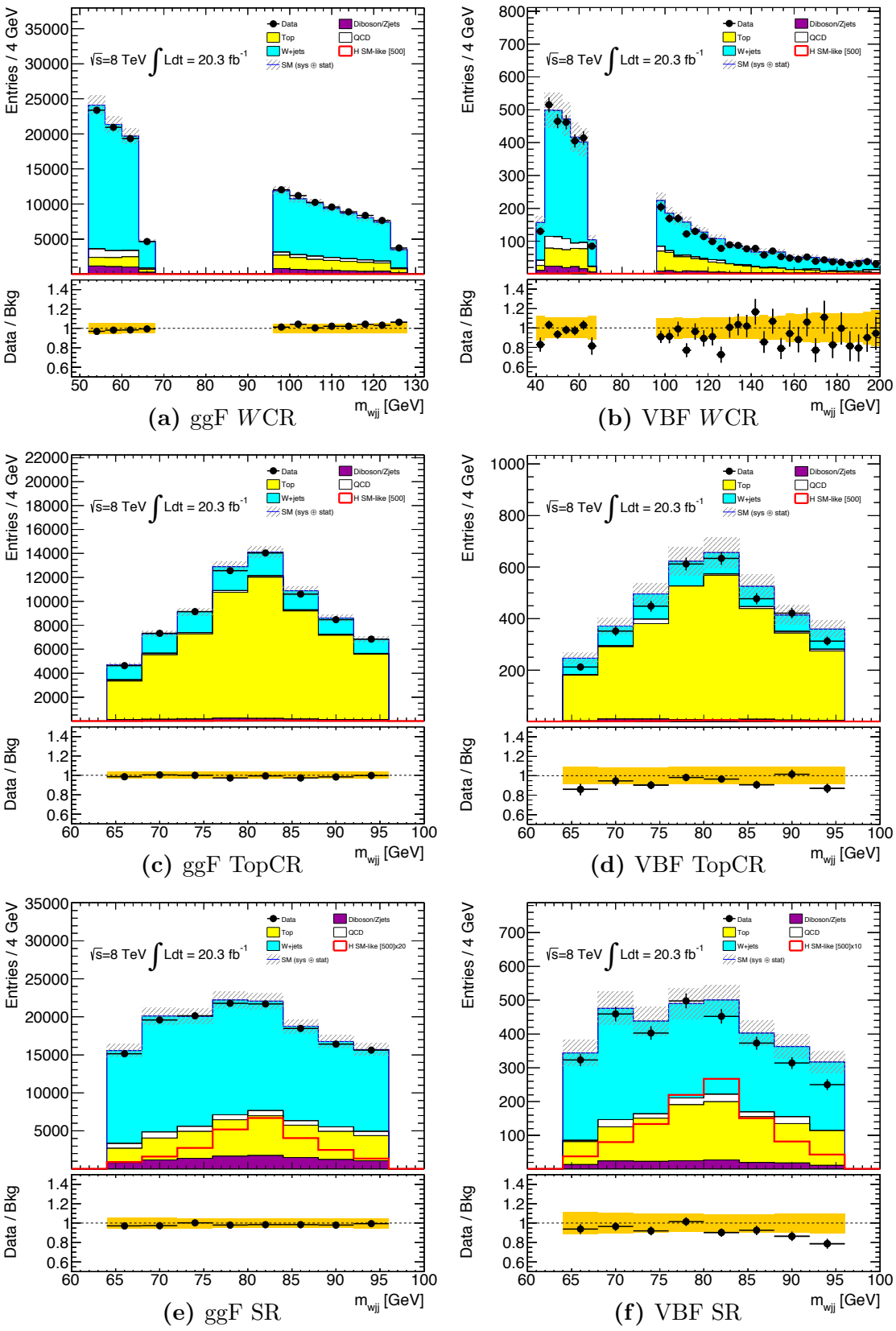

(a) ggF WCR **(b)** VBF WCR

(c) ggF TopCR **(d)** VBF TopCR

(e) ggF SR **(f)** VBF SR

Figure A.16: Small-R di-jet (resolved hadronic W) invariant mass

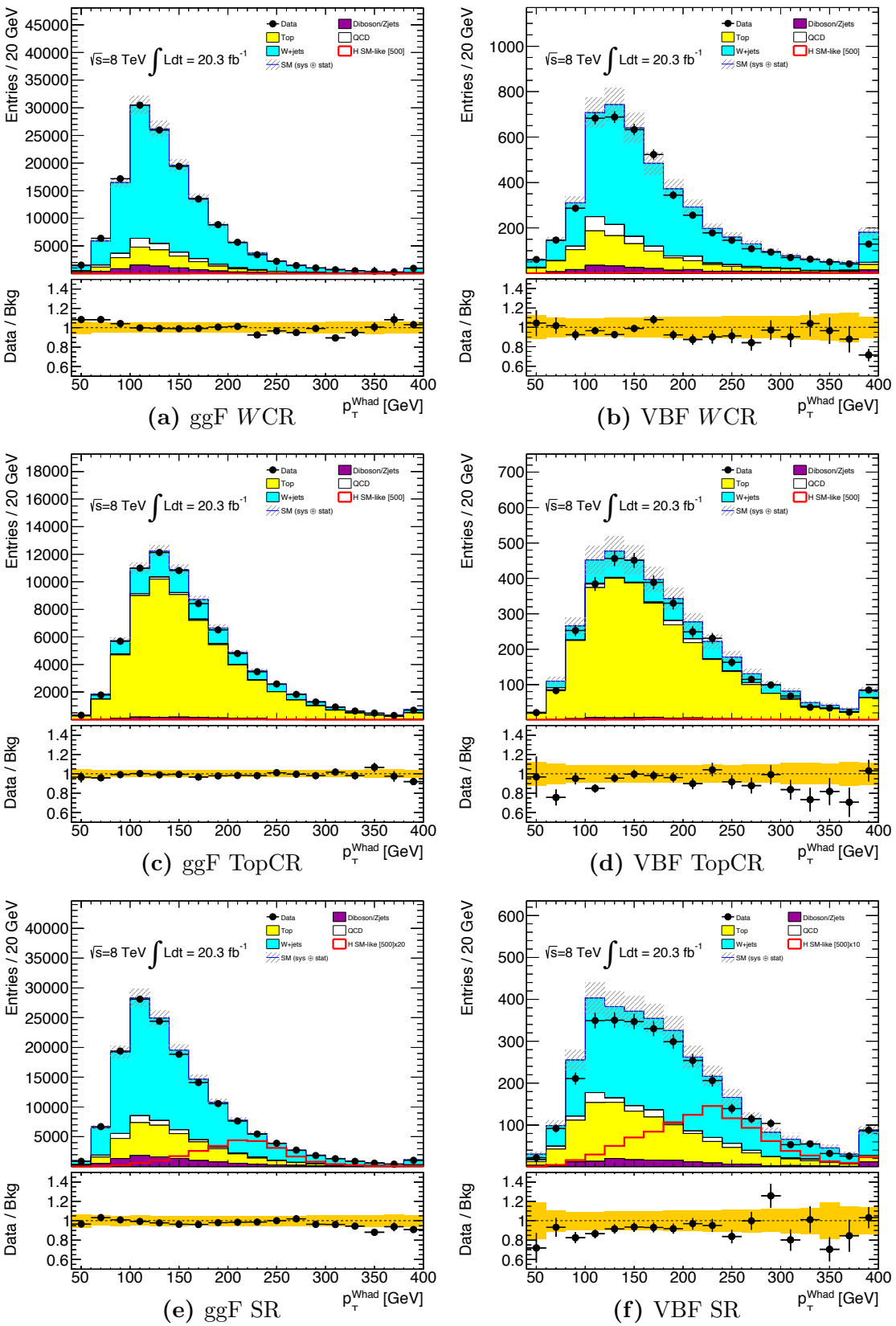

(a) ggF WCR (b) VBF WCR

(c) ggF TopCR (d) VBF TopCR

(e) ggF SR (f) VBF SR

Figure A.17: Small-R di-jet (resolved hadronic W) p_{T}

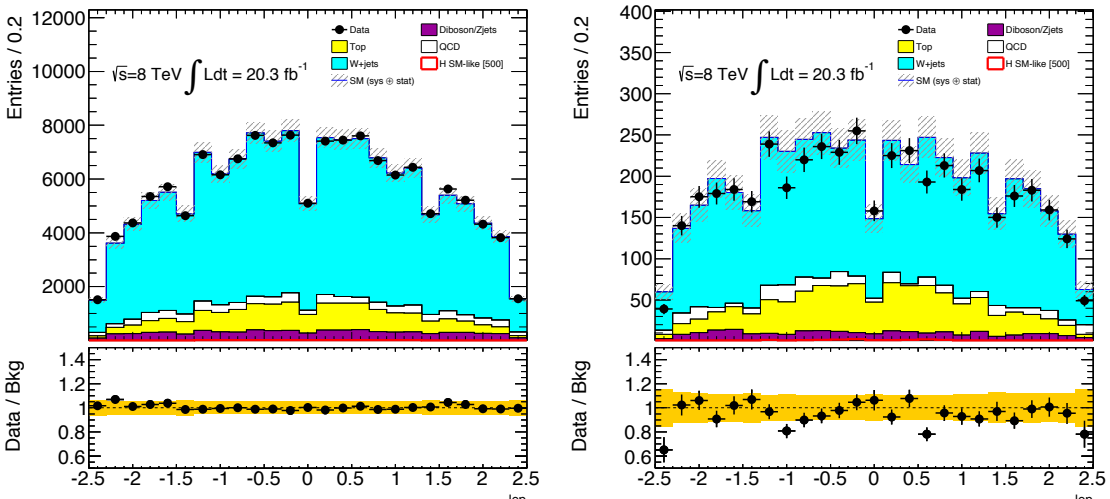

(a) ggF WCR (b) VBF WCR

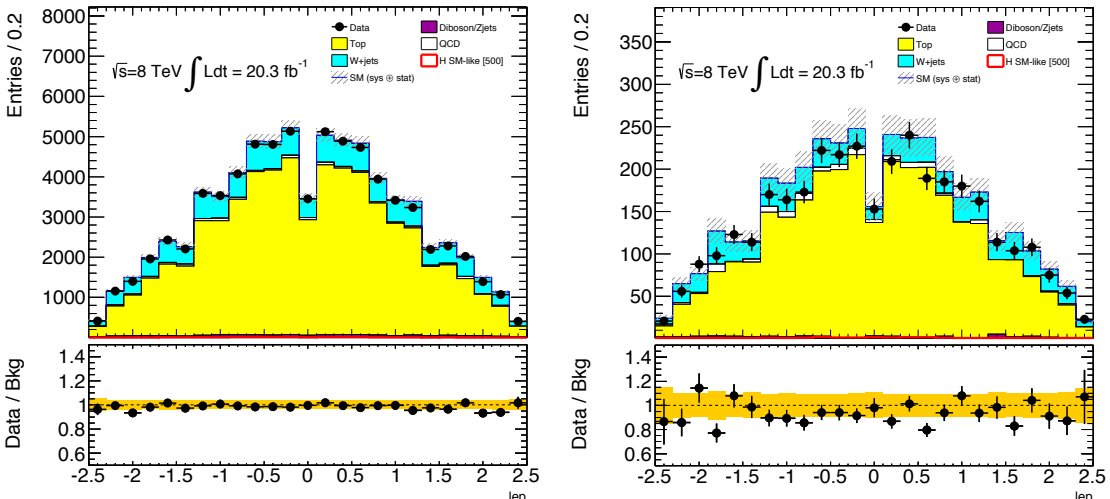

(c) ggF TopCR (d) VBF TopCR

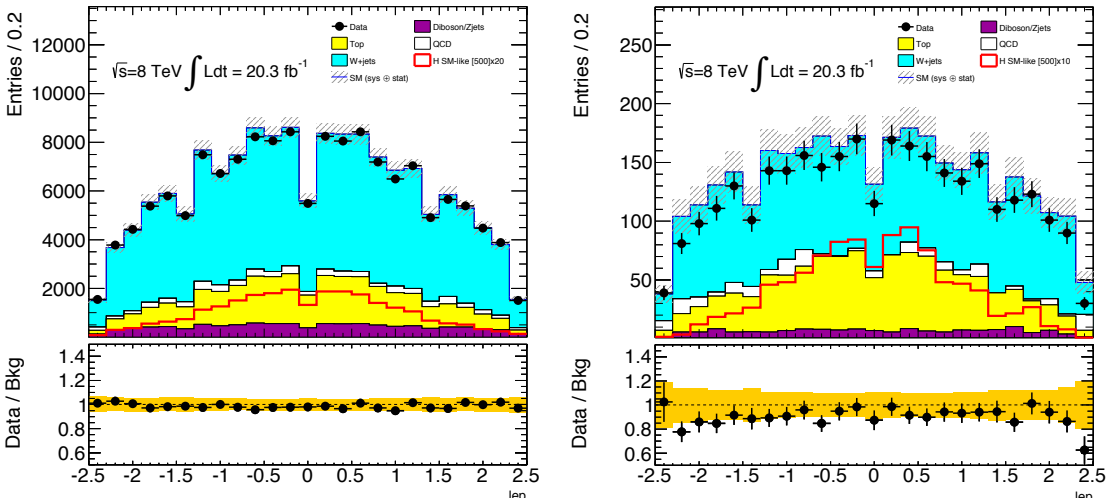

(e) ggF SR (f) VBF SR

Figure A.18: Lepton η

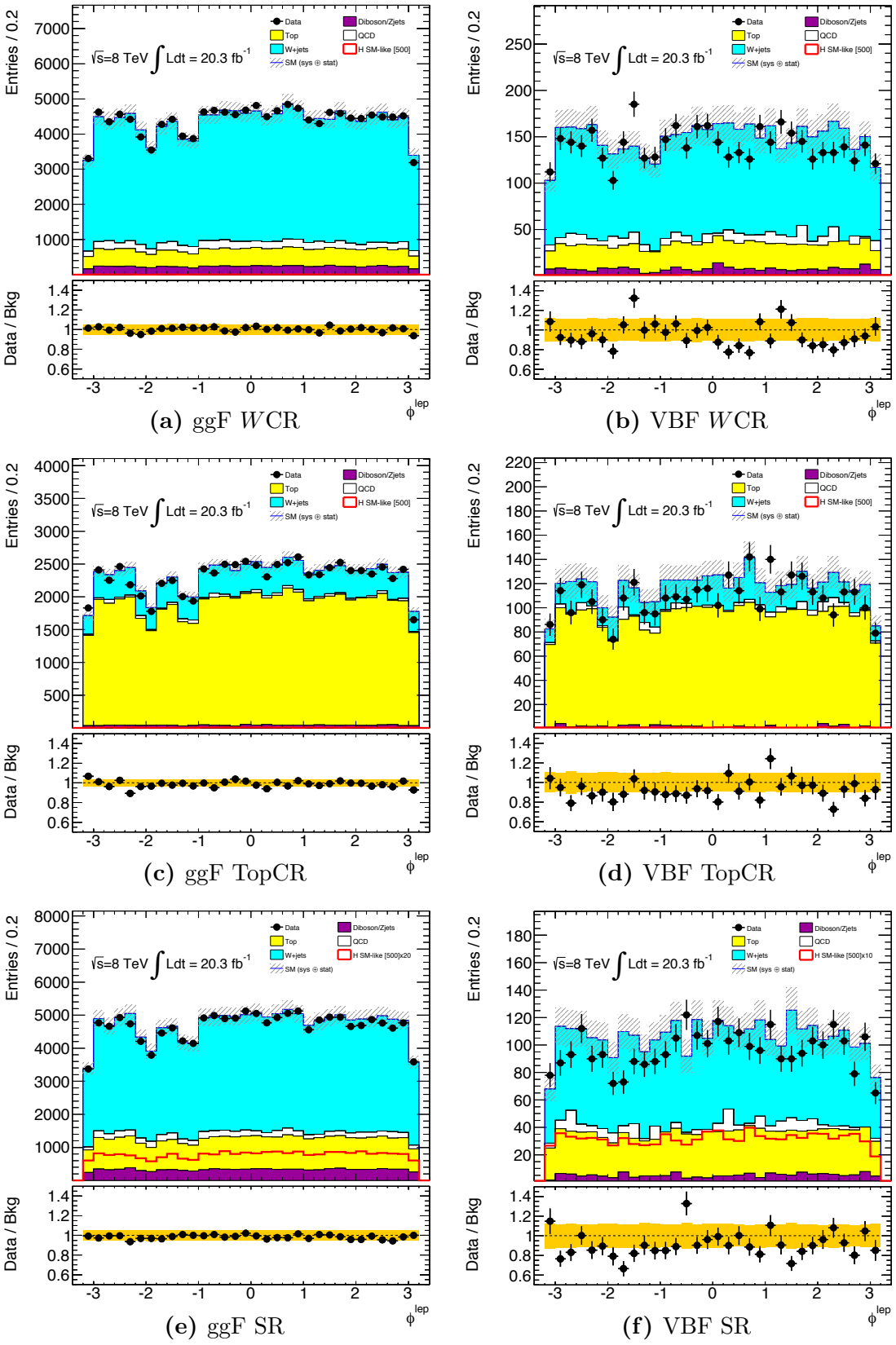

(a) ggF WCR (b) VBF WCR

(c) ggF TopCR (d) VBF TopCR

(e) ggF SR (f) VBF SR

Figure A.19: Lepton ϕ

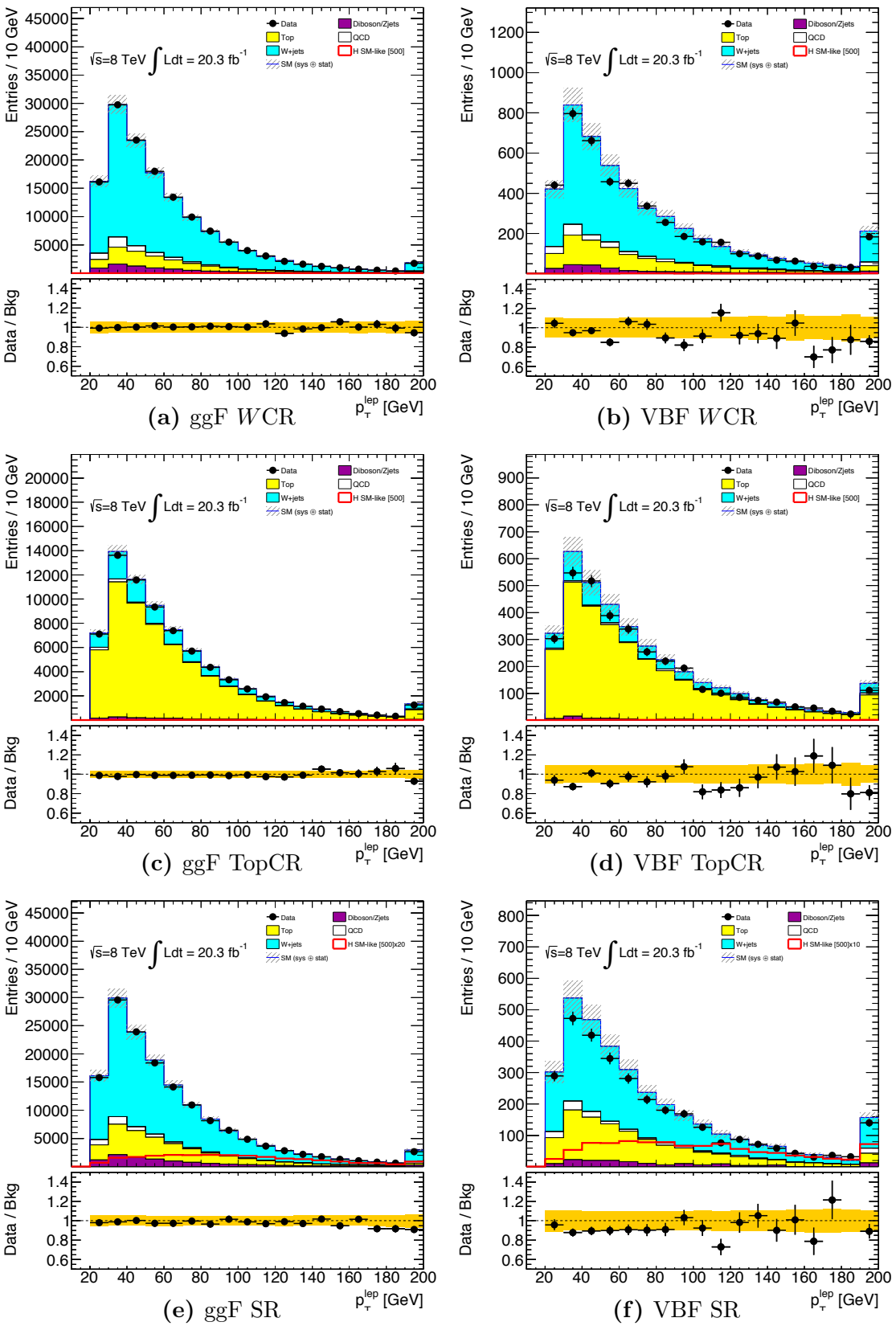

(a) ggF WCR (b) VBF WCR

(c) ggF TopCR (d) VBF TopCR

(e) ggF SR (f) VBF SR

Figure A.20: Lepton p_{T}

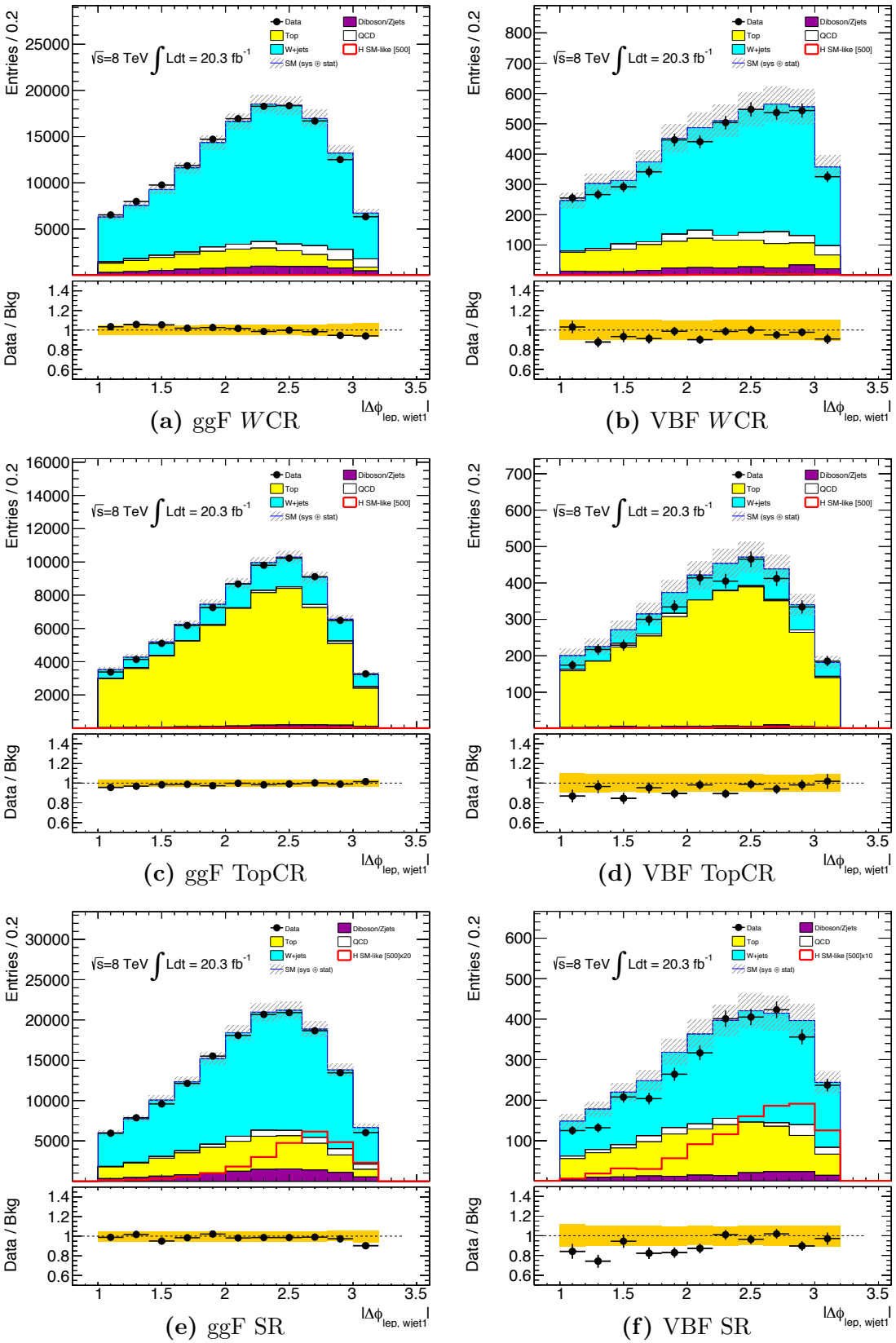

Figure A.21: $|\Delta\phi|$ between the lepton and leading small-R W-jet [resolved only]

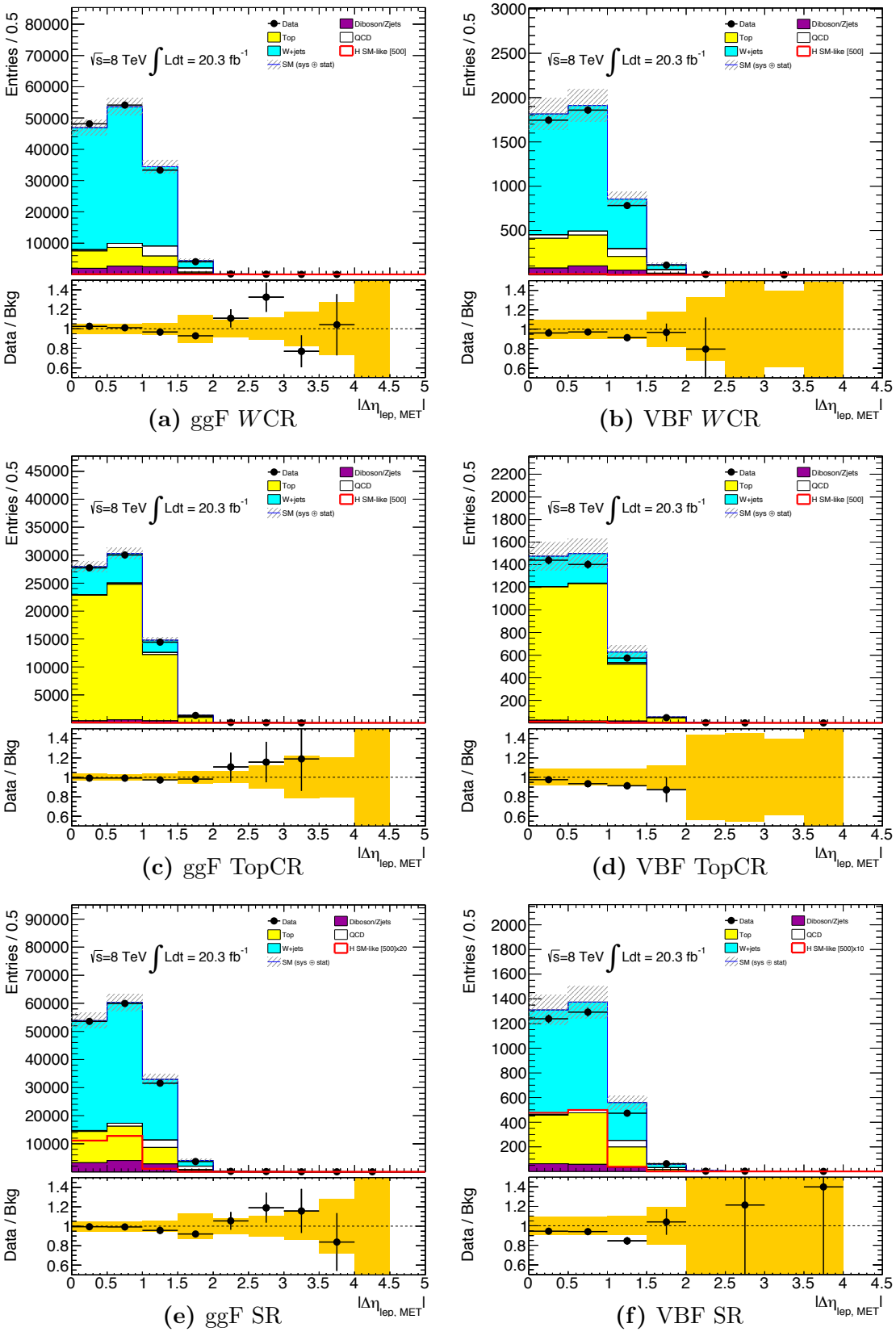

(a) ggF WCR (b) VBF WCR

(c) ggF TopCR (d) VBF TopCR

(e) ggF SR (f) VBF SR

Figure A.22: $|\Delta\eta|$ between the lepton and neutrino

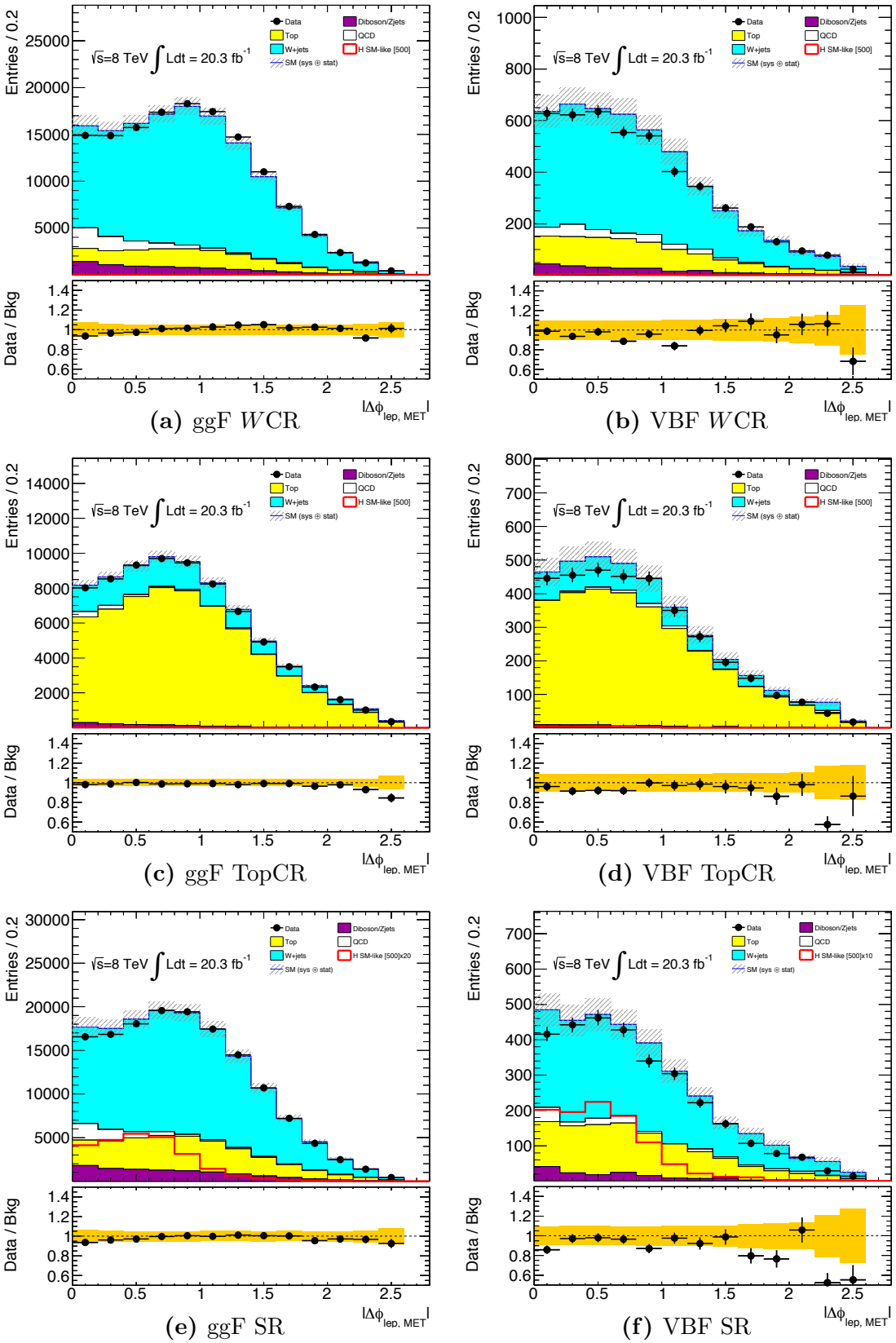

(a) ggF WCR (b) VBF WCR

(c) ggF TopCR (d) VBF TopCR

(e) ggF SR (f) VBF SR

Figure A.23: $|\Delta\phi|$ between the lepton and neutrino

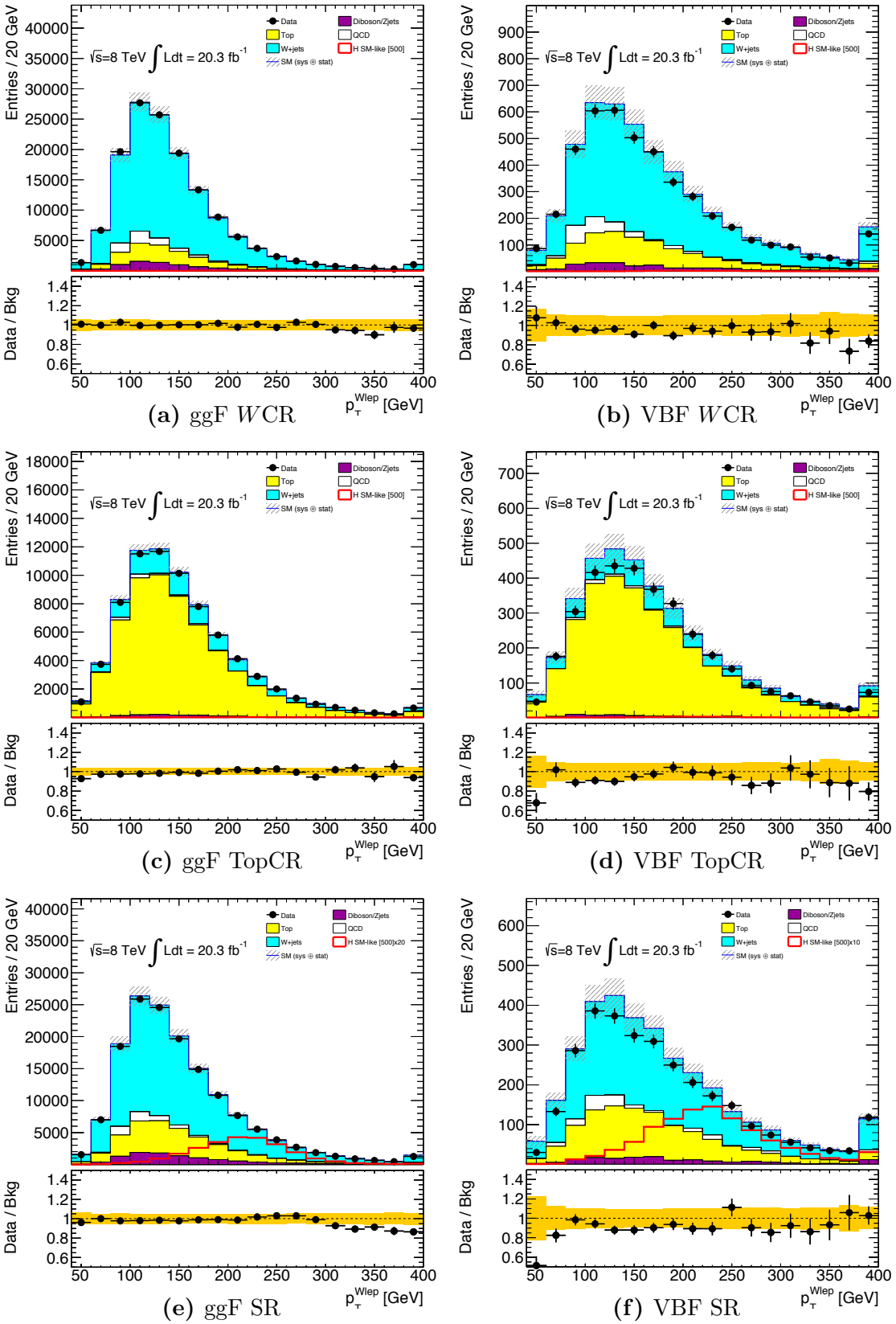

(a) ggF WCR (b) VBF WCR

(c) ggF TopCR (d) VBF TopCR

(e) ggF SR (f) VBF SR

Figure A.24: Leptonic W p_{T}

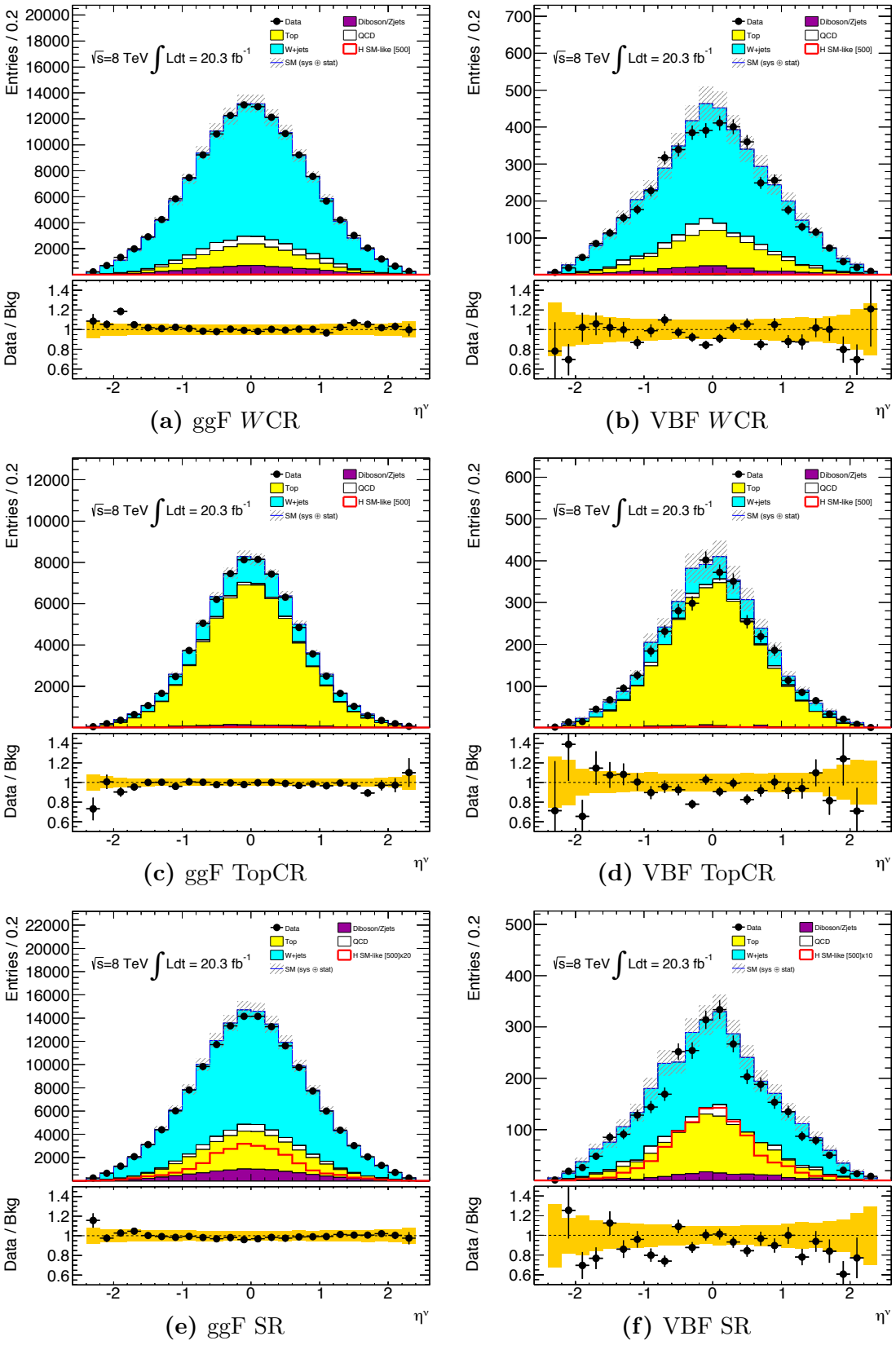

(a) ggF WCR **(b)** VBF WCR

(c) ggF TopCR **(d)** VBF TopCR

(e) ggF SR **(f)** VBF SR

Figure A.25: Neutrino η

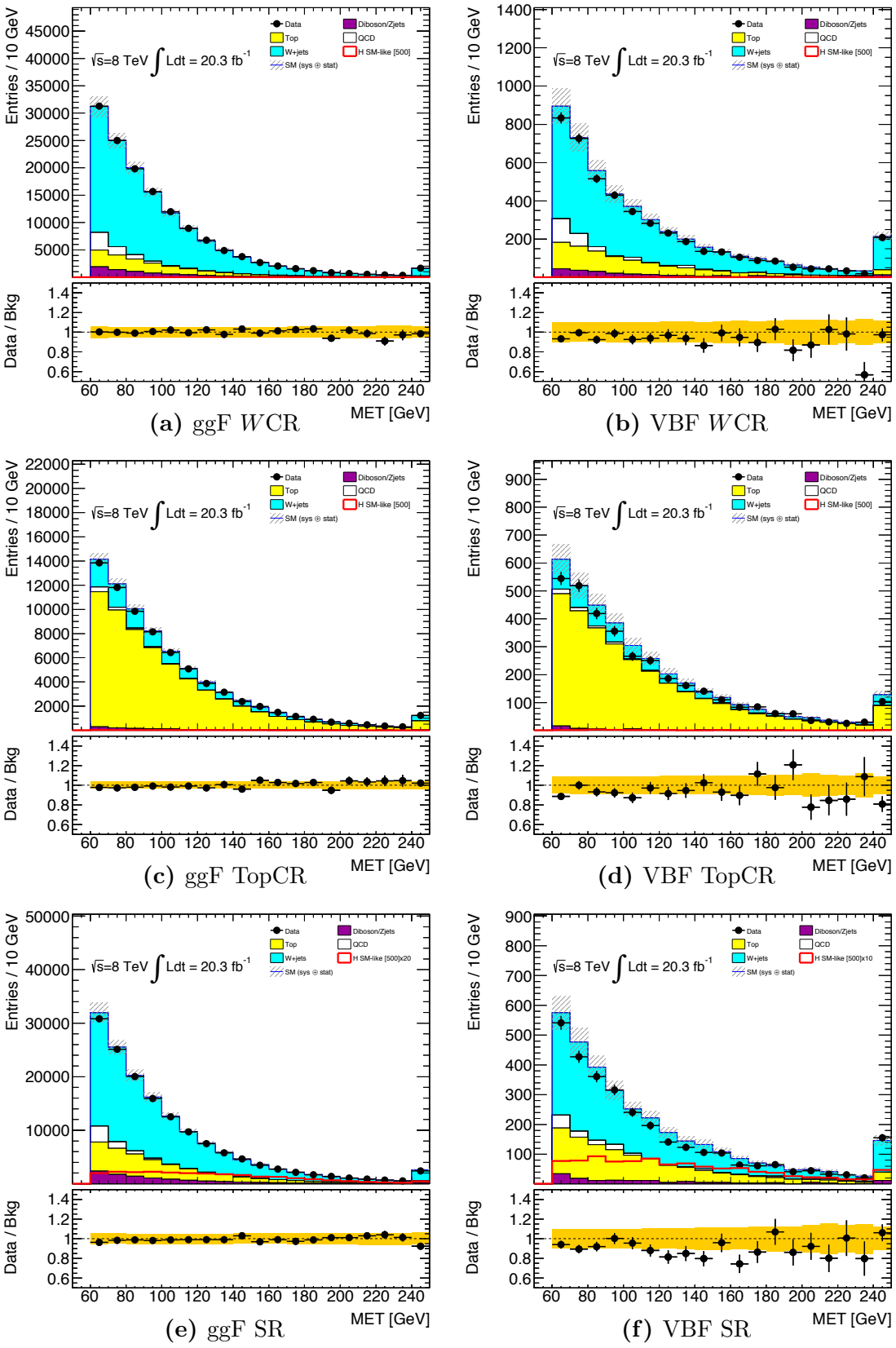

(a) ggF WCR **(b)** VBF WCR

(c) ggF TopCR **(d)** VBF TopCR

(e) ggF SR **(f)** VBF SR

Figure A.26: Missing Transverse Momentum $E_{\mathrm{T}}^{\mathrm{miss}}$ (i.e. neutrino p_{T})

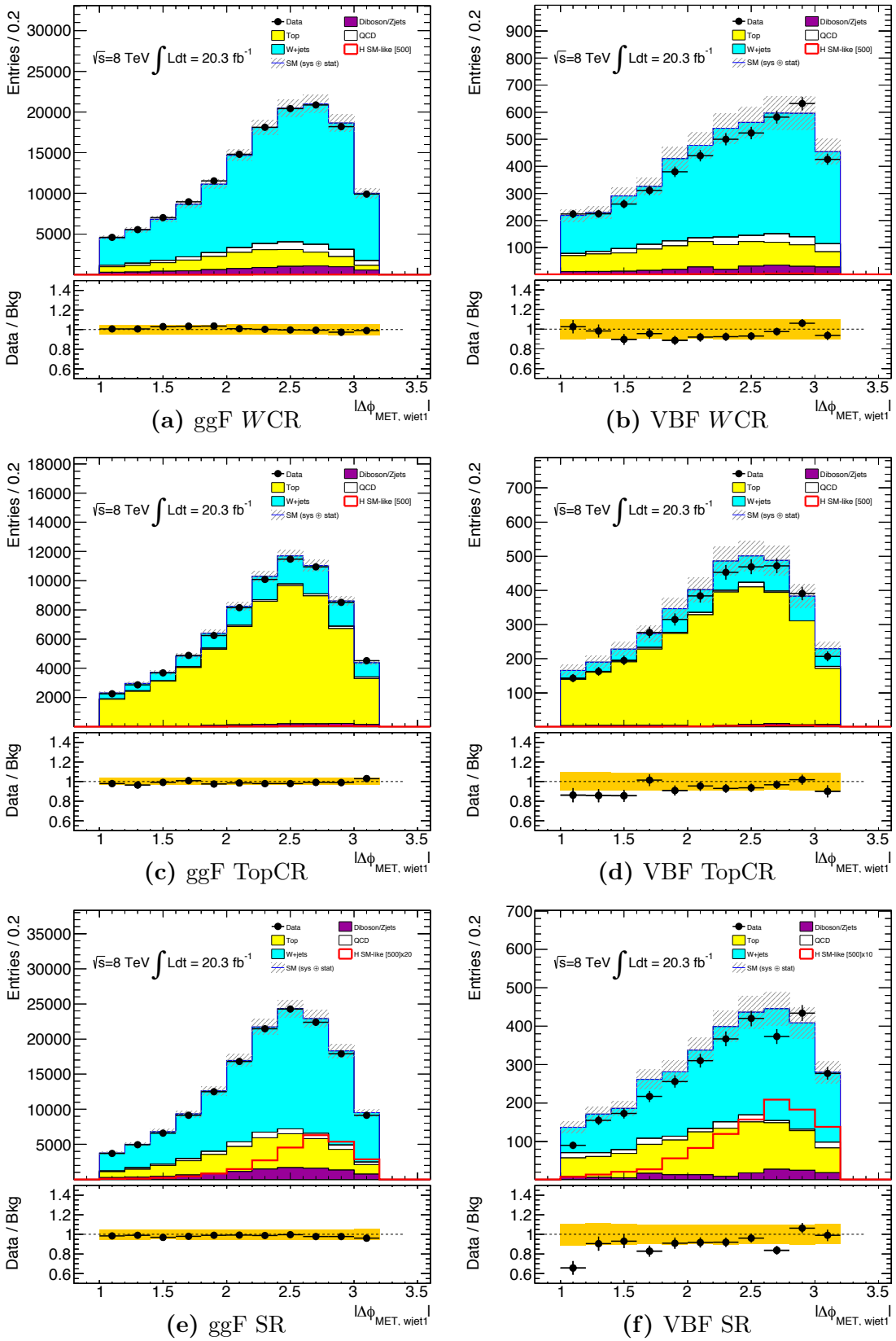

Figure A.27: $|\Delta\phi|$ between the neutrino and leading small-R W-jet [resolved only]

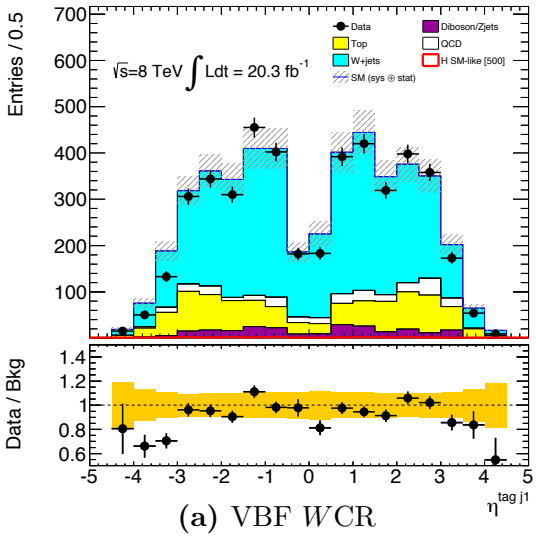

(a) VBF WCR

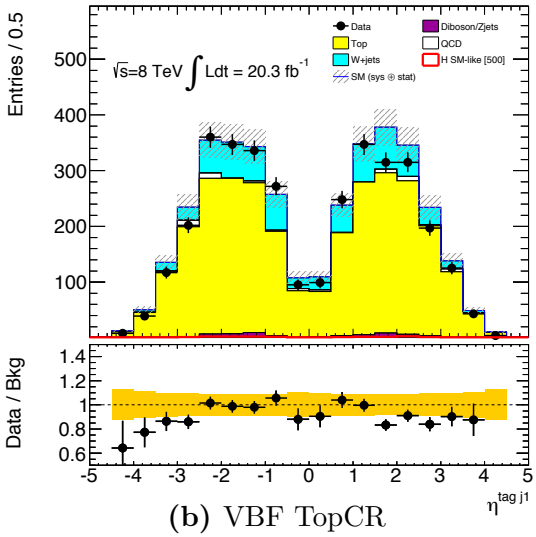

(b) VBF TopCR

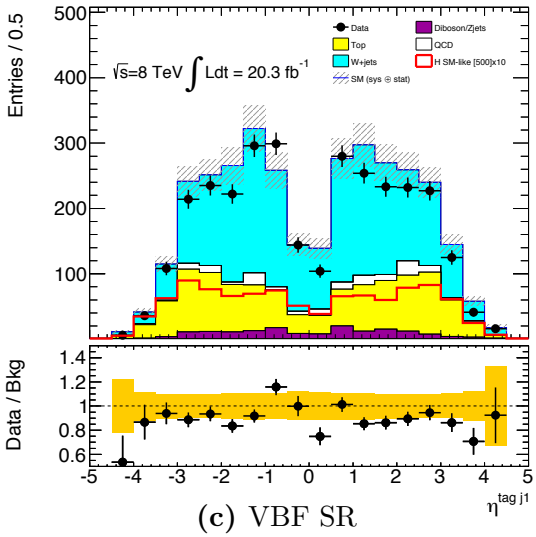

(c) VBF SR

Figure A.28: Leading VBF tagging jet η

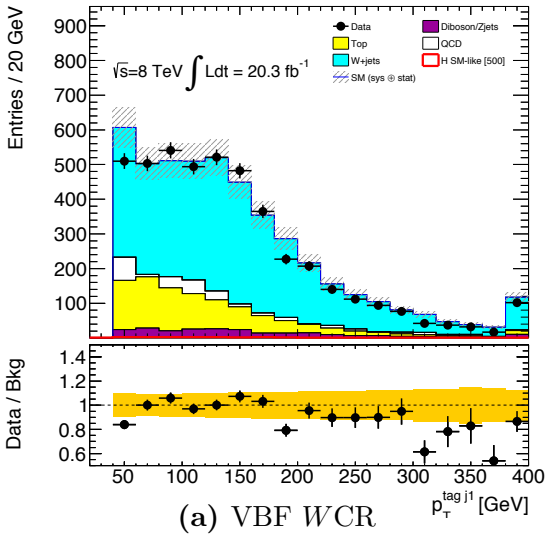

(a) VBF WCR

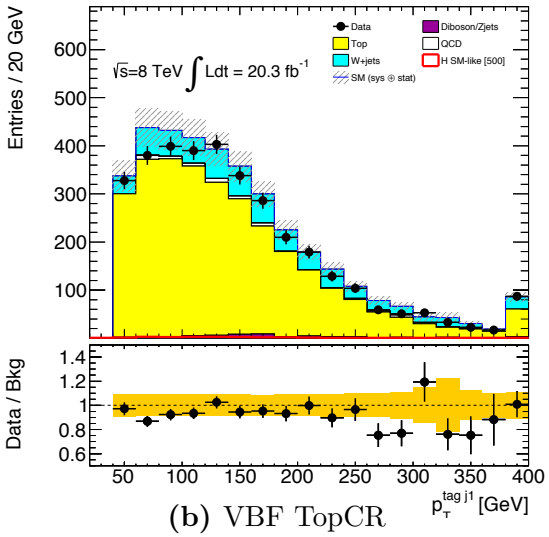

(b) VBF TopCR

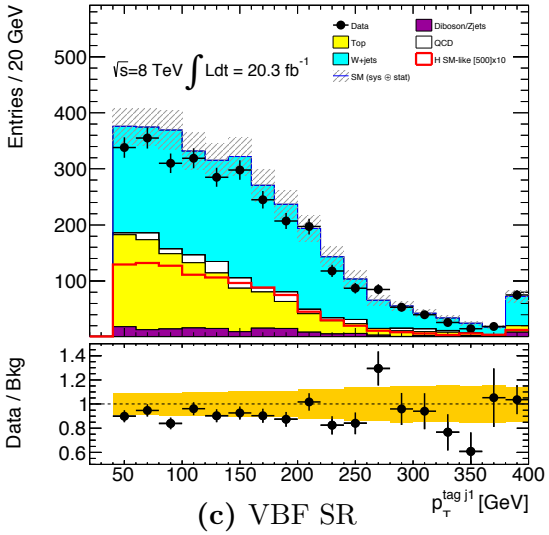

(c) VBF SR

Figure A.29: Leading VBF tagging jet p_{T}

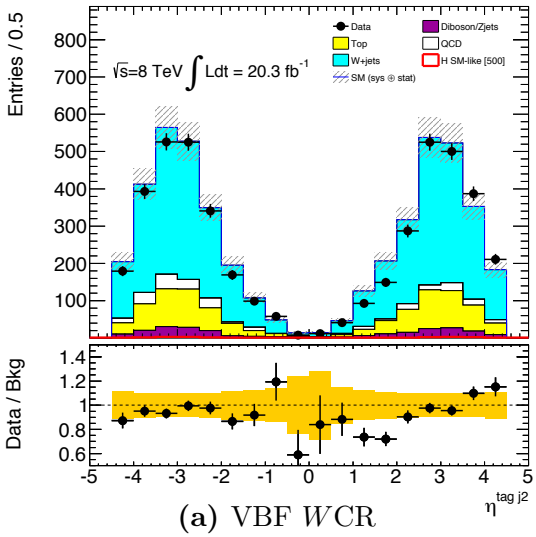

(a) VBF WCR

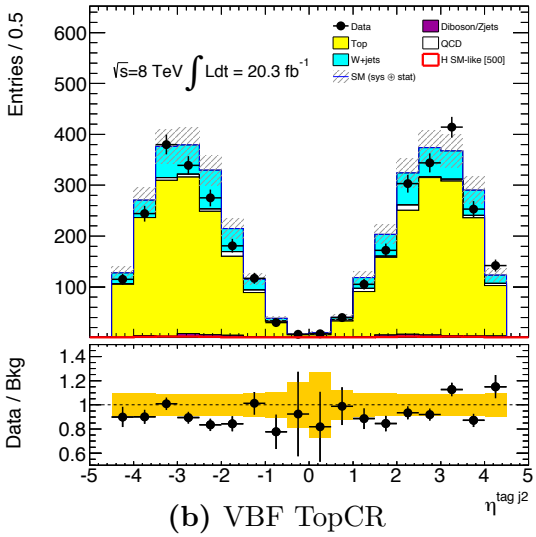

(b) VBF TopCR

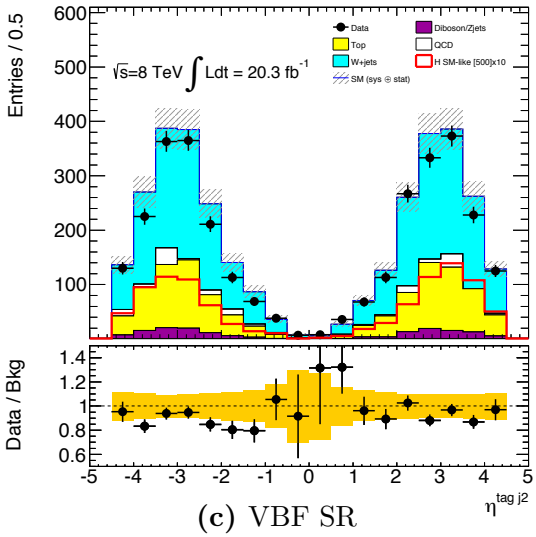

(c) VBF SR

Figure A.30: Sub-leading VBF tagging jet η

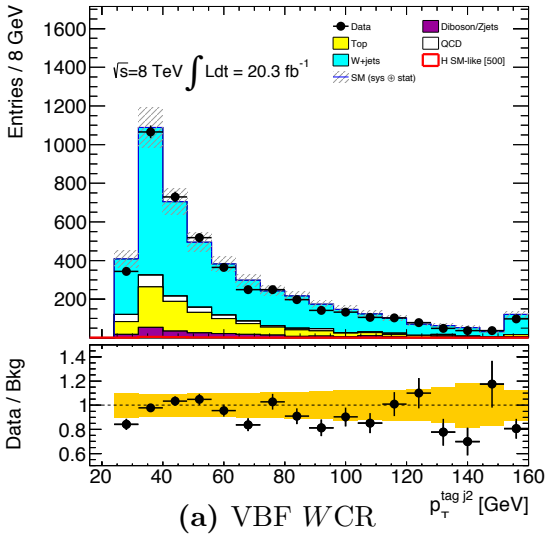

(a) VBF WCR

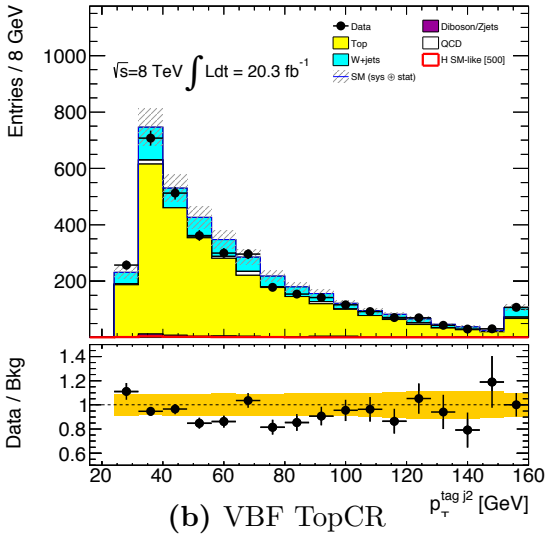

(b) VBF TopCR

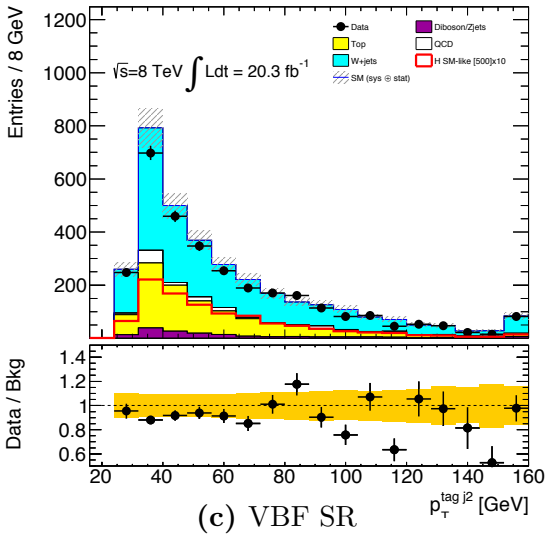

(c) VBF SR

Figure A.31: Sub-leading VBF tagging jet p_{T}

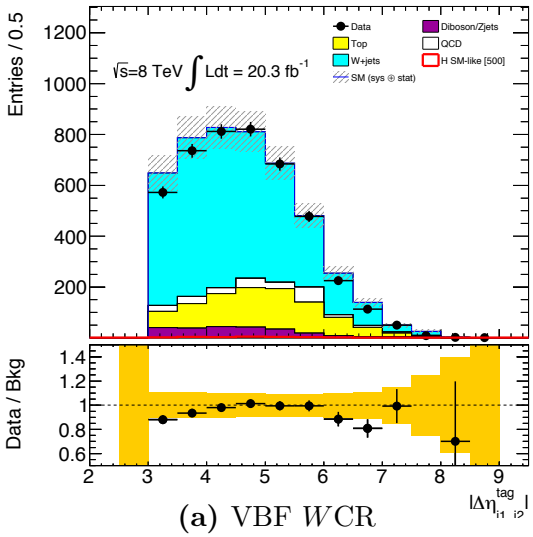

(a) VBF WCR

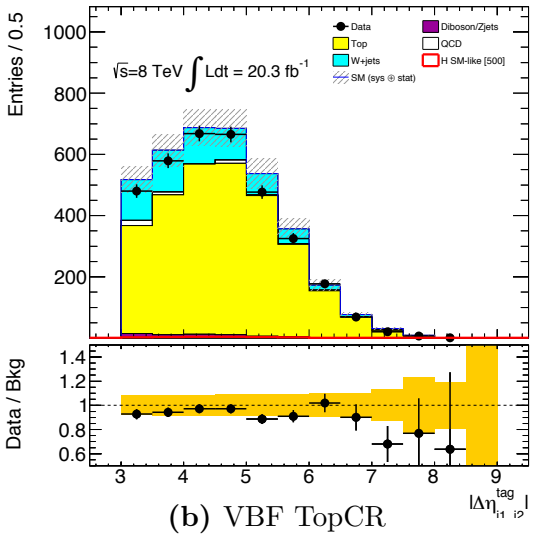

(b) VBF TopCR

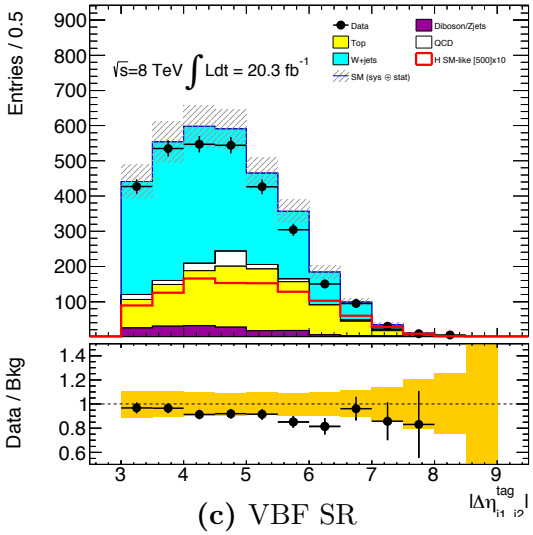

(c) VBF SR

Figure A.32: $|\Delta\eta|$ between the VBF tagging jets

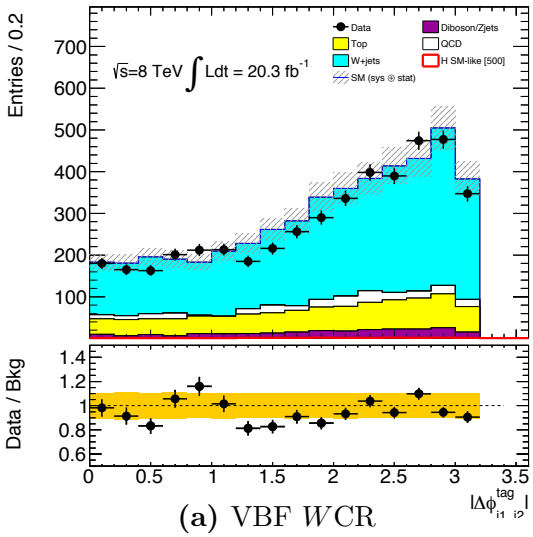

(a) VBF WCR

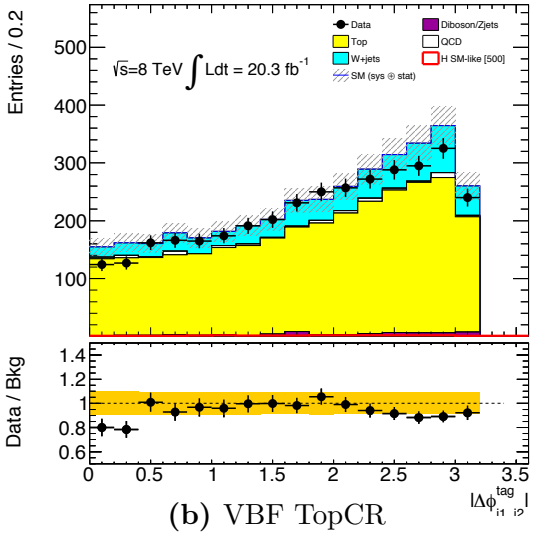

(b) VBF TopCR

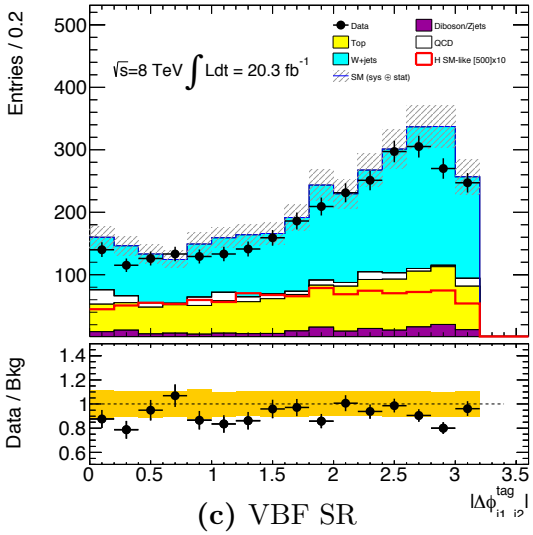

(c) VBF SR

Figure A.33: $|\Delta\phi|$ between the VBF tagging jets

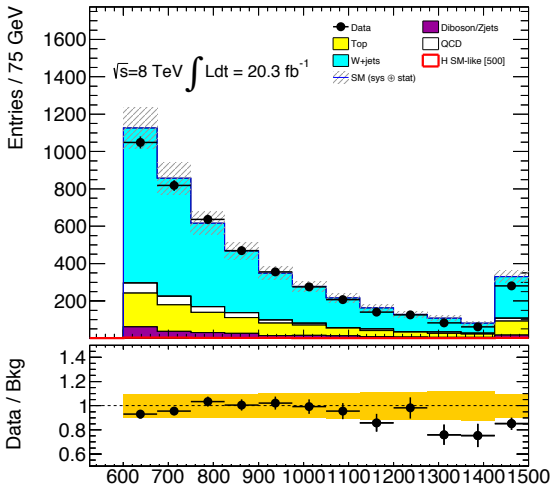

(a) VBF WCR

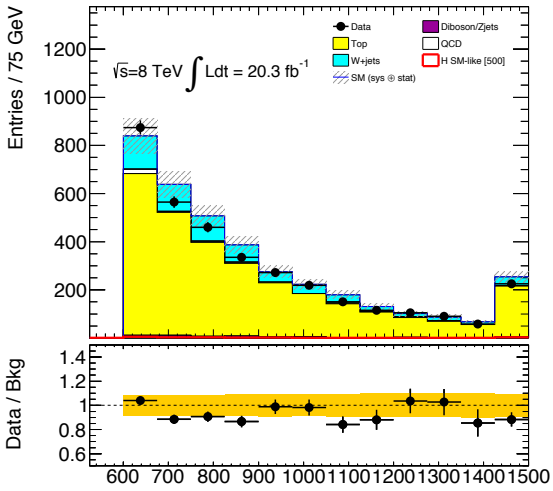

(b) VBF TopCR

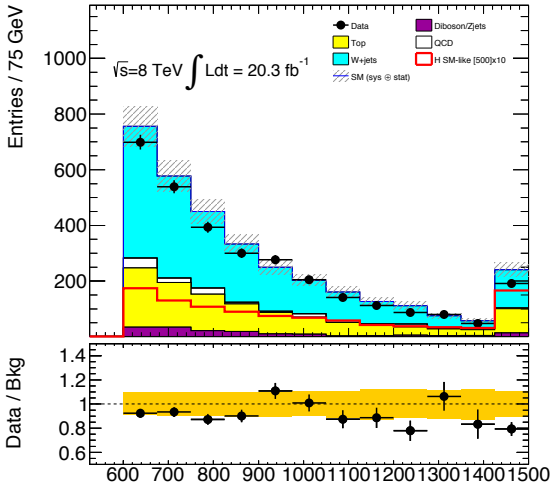

(c) VBF SR

Figure A.34: Invariant mass of the VBF tagging jets